Physical, chemical and electronic properties of hybrid supramolecular interfaces

Marc-Antoine Stoeckel

UNIVERSITÉ DE STRASBOURG

ÉCOLE DOCTORALE DES SCIENCES CHIMIQUES

UMR 7006 – Institut de Science et d'Ingénierie Supramoléculaires

THÈSE

présentée par :

Marc-Antoine STOECKEL

soutenue le : **5 Mars 2019**

pour obtenir le grade de : **Docteur de l'université de Strasbourg**

Discipline/ Spécialité : Chimie-Physique

Propriétés physico-chimiques et électroniques des interfaces supramoléculaires hybrides

THÈSE dirigée par :

M. SAMORÌ Paolo	Professeur, Université de Strasbourg, Strasbourg, France
M. ORGIU Emanuele	Professeur, Energie Matériaux Télécommunication Research Center, Varennes, Québec

RAPPORTEURS :

M. VUILLAUME Dominique	Directeur de recherche, Institut d'Électronique de Microélectronique et de Nanotechnologie, Villeneuve d'Ascq, France
M. CAIRONI Mario	Directeur de recherche, Center for Nanoscience and Technology, Genova, Italy

---

AUTRES MEMBRES DU JURY :

M. ROGEZ Guillaume	Directeur de recherche, Institut de Physique et Chimie des Matériaux de Strasbourg, Strasbourg, France
M. BISCARINI Fabio	Professeur, Università degli Studi di Modena e Reggio Emilia, Modena, Italy

Résumé de thèse

Depuis leurs apparitions en tant que matériaux actifs dans les transistors à effet de champ, dans les années 1970,[1] les semi-conducteurs organiques ont attiré de plus en plus d'attention, du fait de leur facilité d'emploi via des processus basés sur des solutions, et utilisés à température ambiante. Plus tard, les propriétés de ces matériaux ont également pu être employées dans des dispositifs tels que des diodes électroluminescentes organiques (OLED) ou les cellules photovoltaïques organiques (OPV). Un développement important a été effectué sur cette technologie, du fait de la grande polyvalence de ces matériaux actifs, pouvant être modulés à volonté par les chimistes de synthèse pour donner des propriétés innovantes, jusqu'à introduire de la multifonctionnalité.

L'étude du transport de charge dans de tels matériaux est d'une importance capitale, non seulement pour la compréhension des mécanismes inhérents à un type de composé précis, mais également pour l'optimisation des performances des dispositifs électriques formant l'électronique de demain.

Afin de parvenir à ce but, le travail de cette thèse s'est axé sur l'étude du transport de charges, en utilisant les principes de la chimie supramoléculaire afin d'obtenir un contrôle sur les propriétés électriques de matériaux, à travers la synergie existante entre des architectures moléculaires et leurs fonctions. Cette thématique a donc été étudiée sous différents aspects :

- via l'étude de l'origine du mécanisme du transport de charges selon le design moléculaire, dans des dérivés de pérylène bisimide
- en modulant les propriétés de matériaux 2D en utilisant des dopants moléculaires autoassemblés
- en contrôlant l'environnement chimique pour nuancer les propriétés électriques via les défauts cristallins de pérovskites hybrides, ou en affinant la distance intermoléculaire de petites molécules semiconductrices

Le premier projet a permis l'élucidation de l'origine des différents mécanismes de transport de charges dans deux dérivés de pérylène bisimide. L'un des composés, le PDI7-CN_2, possède un transport thermiquement activé,[2] de type *multiple trap and release* où les charges injectées sont ralenties par des pièges présent dans le gap, alors que le second, le PDIF-CN_2, les charges sont délocalisées sur plusieurs unités moléculaires.[3] Selon une analyse systématique, il a été démontré que les deux composés possèdent un empilement cristallin légèrement différent, PDIF-CN_2 forme une structure de type H alors que PDI8-CN_2 forme une structure de type J, ce qui change la directionnalitée de l'empilement moléculaire. Ces différences se répercutent sur les interactions intermoléculaires, notamment sur l'intégrale de transfert que partagent deux unités moléculaires, mais également sur les modes de vibrations cristallins (ou phonons). En effet, PDIF-CN_2 présente, d'une part, une forte interaction intermoléculaire a deux dimensions, mais également un paysage phononique restreint en dessous de 200 cm^{-1}, comme il a été montré par des mesures de diffusion inélastique de neutrons et de spectroscopie térahertz. A l'inverse, PDI7-CN_2 ne décrit majoritairement qu'une interaction intermoléculaire à une dimension, ainsi qu'une activité vibrationnelle prononcée à basse fréquence. Ces vibrations sont majoritairement décrites par les chaines latérales dans le composé. Les basses fréquences étant des vibrations responsables de la localisation des charges dans les semi-conducteurs, cela explique donc la différence observée dans le mécanisme de

transport de charges de ces deux composés.[4] Cela a notamment été démontré par une analyse théorique du système que forme ces deux composés, via l'étude par modélisation moléculaire, de l'évolution des intégrales de transfert de ces deux molécules, ainsi que de la contribution atomique de chaque vibration observées par spectroscopie térahertz et diffusion inélastique de neutrons.

Dans le second projet, une étude du dopage de matériaux 2D a été réalisée avec une approche moléculaire. Tout d'abord, une étude préliminaire a été réalisée via une analyse par spectroscopie Raman du dopage de graphène sur trois différentes molécules pouvant s'auto-assembler en couches minces sur SiO_2. La première, le trichloro(1H,1H,2H,2H-perfluorooctyl)silane (PFS) induit un dopage de type *p* dans le graphène, alors que le N-[3-(Trimethoxysilyl)propyl]éthylenediamine (AHAPS) produit un dopage de type *n*.[5] Etonnamment, la troisième molécule, le 2-(Cyanoethy)triéthoxysilane (TESPN) ne présente aucun dopage, ce qui n'est pas attendu aux vues de la composition chimique de cette molécule, ayant un fort dipôle et un groupement électroattracteur à son extrémité. Les mêmes molécules ont été ensuite utilisées pour évaluer les propriétés électriques d'une monocouche de dichalcogénure de métaux de transition, le disélénure de tungstène WSe_2. Ce composé ne présente habituellement de bonnes performances électriques qu'avec des dispositifs ayant des géométries compliquées.[6] En revanche, combiné à des SAMs de PFS, ou AHAPS, sa mobilité de trous a pu augmenter de 3 ordres de grandeurs, ou de 4 ordres de grandeurs pour les électrons. C'est, cependant, quand les molécules sont placées au-dessus du matériau 2D que les propriétés sont les plus contrastées. En effet, ces molécules ont la capacité de former des liaisons covalentes avec l'oxygène présent dans la monocouche et/ou dans les lacunes de sélénium,[7] via leur fonction silanol. De cette manière, les propriétés de transport de trous avec PFS atteignent 100 $cm^2V^{-1}s^{-1}$ et 50 $cm^2V^{-1}s^{-1}$ pour le transport des électrons avec AHAPS, après un traitement UV/Ozone de la monocouche, ce dernier ayant pour effet d'augmenter la densité d'oxygène dans le matériau, et donc le nombre de points d'ancrage. Le mécanisme de fonctionnalisation a été vérifié par une combinaison de techniques telles que la microscopie à force atomique

et la spectrométrie photoélectronique à rayons X. Une approche de double fonctionnalisation (une sur la surface du diélectrique, sous le matériau 2D et l'autre au-dessus) a également permis d'obtenir un dispositif double couche présentant une ambipolarité balancée, avec une mobilité des porteurs de charge proche de 20 $cm^2V^{-1}s^{-1}$ avec des contacts en or, qui ne sont généralement pas utilisés pour les dispositifs haute performances à base de WSe_2.

Le troisième projet s'est axé sur la modulation des performances électriques de l'iodure de plomb méthylamonium en fonction de la composition gazeuse environnante. En effet, pour la première fois, une étude détaillée des propriétés électriques de cette pérovskite vis-à-vis de l'oxygène gazeux, a été reportée. L'oxygène peut, de manière réversible, se loger dans les lacunes d'iode de la pérovskite.[8] Dans un milieu sans oxygène, ces lacunes forment des pièges pour les charges, diminuant ainsi les propriétés de conductivité électrique de la pérovskite. Lorsque l'oxygène comble ces lacunes, moins de charges injectées dans le matériau sont piégées, ce qui a pour effet d'augmenter la conductivité électrique de la pérovskite par un facteur de plus de 3000 entre 0% et 100% en volume d'oxygène. Cette sensibilité peut être réduite en traitant la pérovskite avec des vapeurs d'iodure de méthyle, qui va combler les lacunes en iode présentes à la surface de la pérovskite, sans pouvoir combler celles à l'intérieur de la structure due à l'encombrement stérique de la molécule. Par ailleurs, la sensibilité de la pérovskite peut être affinée en jouant sur la manière de former le composé. En effet, les deux approches conventionnelles basées sur des solutions, pour déposer la pérovskite, sont la méthode en une étape, où les deux précurseurs, à savoir l'iodure de plomb et l'iodure de méthylamonium, sont mélangés dans une solution unique qui est déposée par un processus de spin-coating, et la méthode en deux étapes, dans laquelle un film d'iodure de plomb est d'abord déposé sur une surface, puis celui-ci est converti en pérovskite par dépôt d'un deuxième film formé par l'iodure de méthylamonium. En contrôlant les paramètres de chaque processus, la réponse électrique à l'oxygène de la pérovskite peut être alors modulée. Une approche

en une étape forme des cristaux complets de pérovskites, alors que l'approche en deux étapes conduit à la formation de nombreux petits cristaux de pérovskites, en surface du film de PbI_2. Ainsi, un film polycristallin aura plus de défauts, notamment aux jonctions des domaines cristallins, et donc une meilleure sensibilité à l'oxygène.

Le quatrième projet, similaire au précédent, s'est concentré sur la réponse électrique qu'a un dérivé de [1]benzothieno[3,2-b]benzothiophene (BTBT) fonctionnalisé avec des chaînes latérales de type polyéthylène glycol (PEG). Ces chaines PEG ont la particularité d'absorber de manière réversible et quasi-sélective, des molécules d'eau. Ainsi, un équilibre se forme entre l'humidité environnante, et la quantité d'eau absorbée par ces chaines PEG.[9,10] Cette molécule, PEG-BTBT, lorsqu'elle est déposée sur un substrat par un procédé de type spin-coating, va adopter une conformation dont le corps BTBT se trouve orienté perpendiculaire au substrat, ce qui conduit à une modification de la distance d'empilement qui va ainsi grandement influer sur les performances d'un dispositif de géométrie latérale. Ainsi, dans un milieu à basse humidité, l'encombrement stérique lié aux chaines PEG définit une certaine distance intermoléculaire. Lorsque l'humidité augmente, les chaînes latérales vont absorber des molécules d'eau, ce qui va réduire la distance entre les molécules, du fait, notamment, de la formation de liaisons hydrogènes entre chaines latérales. Une analyse par spectroscopie Raman a été menée afin d'orienter l'hypothèse développée pour décrire ce mécanisme, qui sera sous peu complétée par une analyse structurale par diffraction des rayons X dans des environnements avec différentes humidités relatives. Le composé présente une réponse électrique de plus de 5 ordres de grandeurs entre 0% RH et 75% RH, avec un temps de réponse ultra rapide inférieur à 13 ms, faisant de lui un détecteur d'humidité à haute performance. Bien que sa sélectivité soit prédominante pour les molécules d'eau, une très faible réponse est cependant observée pour les molécules possédant une fonction alcool.

Le but de cette thèse a donc été d'explorer les effets intrinsèques et extrinsèques liés au transport de charges dans les matériaux semiconducteurs organiques, hybrides et des matériaux 2D. Ce but a été atteint sous de nombreux aspects et avec des matériaux très différents les uns des autres, en apportant une analyse détaillée et/ou une amélioration de performances des dispositifs électriques dans les différents projets. Il n'a pu être réalisé que par une stratégie d'ingénierie supramoléculaire, et par des approches non-conventionnelles dans la conception de dispositifs, ainsi que par une caractérisation multi-instrumentale précise. Ainsi, nous avons d'abord fait une étude de cas sur le mécanisme de transport de charges dans deux petites molécules organiques semiconductrices. Puis, nous avons modulé les propriétés électriques de matériaux 2D en optimisant le type d'interaction qu'ils décrivent avec des dopants molécules, et nous avons enfin développé des détecteurs haute performance, d'oxygène pour les pérovskites hybrides et d'humidité pour une molécule ayant pour base un corps BTBT.

Abstract

The first demonstration on the use of organic semiconductor as electroactive materials in field-effect transistors, reported 40 years ago, represented a major breakthrough in science.[1] Their processing from solution at room temperature made this class of materials technologically highly relevant.

Later, in virtue of their unique properties, these semiconducting materials were also exploited in other types of devices such as organic light-emitting diodes (OLED) and organic photovoltaic solar cells (OPV). The high versatility of these materials via bottom up tailoring of their physical and chemical properties opens numerous opportunities for fundamental studies and technologically innovative applications, e.g. in logic circuits and in flexible, thus portable, smart devices.

Studying charge transport properties in such materials is of paramount importance, not only for the understanding of the inherent properties of a precise class of compounds, but also in order to optimise the performances of the tomorrow's electronic devices.

In this context, the work carried out within this thesis was oriented toward the study of charge transport, using supramolecular approaches to control the electrical properties of the (semi)conducting materials through the synergy existing between the molecular architectures and their functions. This quest has been explored over different facets:

- by studying the origin of the charge transport mechanism with respect to the molecular design in perylenediimide derivatives
- by modulating the electrical and optical properties of 2D materials with the help of self-assembled molecular dopants

- by adjusting the chemical environment in order to control the electrical properties of an hybrid perovskite through its crystal vacancies and by tuning the intermolecular distance of small semiconducting molecules

The first project allows to elucidate the origin of different charge transport mechanisms in two different perylenediimide derivatives. One of the compounds, PDI8-CN_2, exhibits a thermally-activated transport mechanism,[2] where the injected charges are slowed down by localized traps within the band-gap, while the other compound, PDIF-CN_2, is reported to show band-like transport, where the charges are delocalized over a few molecular units.[3] Through systematic analysis, it was possible to demonstrate that both compounds hold a slightly different molecular packing; PDIF-CN_2 forms a H-type structure while PDI8-CN_2 is organized through a J-type aggregate, which is changing the directionality of the molecular packing. These differences have an impact on the intermolecular interactions, especially on the transfer integrals shared by two molecular units, but also on the crystalline vibrational modes called phonons. Indeed, PDIF-CN_2 presents not only a strong intermolecular interaction in two dimensions, but also a limited phononic landscape below 200 cm^{-1}, as it was demonstrated by inelastic neutron scattering and terahertz spectroscopy measurements. In contrast, PDI8-CN_2 describes an intermolecular interaction mostly dominated by one dimension, and a pronounced vibrational activity at low energies. This range of energy is characterized by vibrational modes that are responsible of the charge localization in the semiconductors, which is explaining the notable difference observed in the charge transport mechanism of these two compounds.[4] This has been also demonstrated through a theoretical analysis of the system formed by the two molecules, through the study by molecular dynamics of the evolution of the transfer integral of both compounds, as well as by the elucidation of the atomic contribution to the vibrations, detected by terahertz and inelastic neutron scattering spectroscopy.

In the second project was focused on the use of molecules to controllably dope 2D materials. Firstly, a preliminary study was made through Raman analysis of graphene flakes exfoliated on SiO_2 substrates on which three different molecules were grown, forming self-assembled monolayers. The first molecule, trichloro(1H,1H,2H,2H-perfluorooctyl)silane (PFS), is inducing a p-type doping into the graphene, while N-[3-(Trimethoxysilyl)propyl]ethylenediamine (AHAPS) is generating a n-type doping.[5] Surprisingly, the third molecule, 2-(Cyanoethy)triethoxysilane (TESPN), doesn't induce any doping. This is unexpected, considering the chemical composition of the molecule as well as its strong dipole moment due to the electro withdrawing groups present on its head. Then, the same molecules were used in order to tune the electrical properties of a monolayer of the transition metal dichalcogenide tungsten diselenide (WSe_2). This compound demonstrates good electrical performances only when integrated in complicated device geometries.[6] However, combined with PFS or AHAPS self-assembled monolayers, its hole mobility can be increased by three orders of magnitude while the electron mobility can be increased by four orders of magnitude. Nevertheless, it is when the molecules are deposited on top of the 2D material that its electrical properties are the most contrasted. Indeed, this molecule used as SAM can form covalent bonds with the oxygen present in the monolayer and/or with the selenium vacancies,[7] through their silanol function. In this way, the hole-mobility can reach 100 $cm^2V^{-1}s^{-1}$ with a PFS treatment, and a 50 $cm^2V^{-1}s^{-1}$ electron-mobility with AHAPS, after exposing the monolayer to UV/Ozone. This UV/Ozone treatment is used to increase the oxygen density of the material, and thus, to increase the number of anchoring points. The functionalization mechanism has been controlled through a combination of techniques such as the atomic force microscopy and X-ray photoelectron spectroscopy. A double-functionalization approach (one on the dielectric surface underneath the 2D material, and the other one on top of it) allows to obtain a double-layer device with a balanced ambipolarity demonstrating a mobility close to 20 $cm^2V^{-1}s^{-1}$ with gold contacts, that are in general not used for high-performance WSe_2 devices.

The third project is based on the modulation of the electrical performances of methylammonium lead iodide, with respect to the composition of the surrounding gas. Indeed, for the first time, a detailed study of the electrical performances of hybrid perovskites with a controlled amount of the oxygen present in the atmosphere has been reported. Oxygen can, in a reversible manner, fill iodine vacancies of perovskites. In an atmosphere without oxygen, these vacancies are forming charge traps, which is decreasing the electrical conductivity of the perovskite.[8] When oxygen is filling these vacancies, less injected charges in the material are trapped, which is increasing its conductivity by a factor 3000 between 0% and 100% in volume of oxygen. This sensitivity can be reduced by treating the perovskite with vapours of iodomethane that will fill the iodine vacancies in an irreversible way, but only at the surface of the perovskite crystal, due to the steric hindrance of the molecule. Moreover, the sensitivity of the perovskite can be refined by playing on the processability of the compound. The two conventional approaches based on solution processing, are the one-step approach and the two-step approach. The one-step approach consists in the spin-coating of a solution containing the methylammonium iodide and the lead iodide onto the substrate, while in the two-step approach a first layer of PbI_2 is deposited on the substrate before being converted into hybrid perovskites using a solution containing the organic part. By carefully controlling the parameters for each process, the electrical response of the perovskite to the oxygen can be modulated. The one-step approach forms crystal domains with a higher proportion of perovskites, while the two-step approach leads to the formation of a high density of small crystallites on top of PbI_2. The polycrystalline film exhibits more defects, especially at the grain boundaries, leading to a higher sensibility to oxygen.

The fourth project, building up on the projects described above, focused on the electrical response of a [1]benzothieno[3,2-b]benzothiophene (BTBT) derivative, functionalized with polyethylene glycol (PEG) as lateral chains. These PEG chains have the unique feature of absorbing water molecules, in a reversible manner and with quasi-selectivity. Hence, an equilibrium is created between the surrounding humidity and the quantity of

adsorbed water by the PEG chains. This molecule PEG-BTBT, when spin-coated on a SiO_2 support packs perpendicularly to the basal plane of the substrate. As a result, a modification of the intermolecular distance between adjacent molecules strongly affects the electrical performances of a FET device. Thus, in a humid atmosphere, the steric hindrance of the PEG chains is defining a precise intermolecular distance. When the humidity increases, the lateral chains swallow the water molecules, which is leading to a reduction of the intermolecular distance because of the molecules of water that will form bridges between two chains, through hydrogen bonding whereas the hydrophobic BTBT core will pack closer. Such interpretation relied on the Raman spectroscopy analysis to describe such mechanism, which will be soon complemented by a structural analysis through x-ray diffraction performed at variable humidity levels. This PEG-BTBT compound exhibits an electrical response exceeding five orders of magnitude between 0% RH and 75% RH, with an ultra-fast response time below 13 ms, making this compound a high-performance humidity sensor. Even if the selectivity of this sensor is mainly attributed to water molecules, a very small response can be also observed for other polar molecules, in particular for small molecules exposing alcohol function, such as methanol.

The aim of this thesis was to explore the intrinsic as well as the extrinsic effects related to charge transport in organic semiconductors, hybrid and 2D materials. This goal has been achieved in many regards with different classes of materials, by providing a detailed analysis and/or an improvement of the electrical performances of devices in different topics. It has been accomplished by adopting a supramolecular approach, through unconventional device conceptions and by providing a precise multi-instrumental characterisation. We first studied the charge transport mechanism in two small semiconductive molecules. Later, we managed to modulate the electrical properties of 2D materials by optimizing the interactions that are described by molecular dopants, and we finally developed two high-performance gas sensors, one for oxygen based on hybrid perovskites, and the other able to detect humidity with a small molecule.

References

[1] A. Tsumura, H. Koezuka, T. Ando, *Appl. Phys. Lett.* **1986**, *49*, 1210.
[2] J. Rivnay, L. H. Jimison, J. E. Northrup, M. F. Toney, R. Noriega, S. Lu, T. J. Marks, A. Facchetti, A. Salleo, *Nature Materials* **2009**, *8*, 952.
[3] N. A. Minder, S. Ono, Z. Chen, A. Facchetti, A. F. Morpurgo, *Advanced Materials* **2012**, *24*, 503.
[4] I. Y. Chernyshov, M. V. Vener, E. V. Feldman, D. Y. Paraschuk, A. Y. Sosorev, *The Journal of Physical Chemistry Letters* **2017**, *8*, 2875.
[5] Y. Li, C.-Y. Xu, P. Hu, L. Zhen, *ACS Nano* **2013**, *7*, 7795.
[6] Y. J. Zhang, T. Oka, R. Suzuki, J. T. Ye, Y. Iwasa, *Science* **2014**, *344*, 725.
[7] T. K. H. Ta, T. N. H. Tran, Q. M. N. Tran, D. P. Pham, K. N. Pham, T. T. Cao, Y. S. Kim, D. L. Tran, H. Ju, B. T. Phan, *Journal of Electronic Materials* **2017**, *46*, 3345.
[8] C. Ran, J. Xu, W. Gao, C. Huang, S. Dou, *Chemical Society Reviews* **2018**, DOI 10.1039/C7CS00868F.
[9] M. A. Squillaci, L. Ferlauto, Y. Zagranyarski, S. Milita, K. Müllen, P. Samorì, *Adv. Mater.* **2015**, *27*, 3170.
[10] M. A. Squillaci, A. Cipriani, M. Melucci, M. Zambianchi, G. Caminati, P. Samorì, *Adv. Electron. Mater.* **2017**, 1700382.

Table of contents

Symbols and Abbreviations

AFM	Atomic Force Microscopy
AHAPS	N-[3-(Trimethoxysilyl)propyl]ethylenediamine
BTBT	[1]benzothieno[3,2-b][1]benzothiophene
CB	Conduction band
$\mathbf{C_i}$	Dielectric capacitance
D	Drain electrode
DMF	Dimethylformamide
E	Electric field
$\mathbf{e^-}$	Electron
EA	Electron afinity
$\mathbf{E_c}$	Conduction band energy level
EELS	Electron energy loss spectroscopy
$\mathbf{E_f}$	Fermi level
$\mathbf{E_g}$	Band gap energy
Ev	Valence band energy
F-SAM	1H,1H,2H,2H-perfluorodecanethiol
FET	Field-effect transistor
G	Gate electrode
$\mathbf{h^+}$	Hole
$\hbar$	Reduced Planck constant
HMDS	Hexamethyldisilazane
HOMO	Highest Occupied Molecular Orbital
HOPG	Highly Oriented Pyrolytic Graphite
H-SAM	1-decanethiol
I	Current
$\mathbf{I_{DS}}$	Drain-source current
IE	Ionization energy
$\mathbf{I_{GS}}$	Gate-source current/leakage current
INS	Inelastic Neutron Scattering
$\mathbf{I_{OFF}}$	I_{DS} value with the FET OFF
$\mathbf{I_{ON}}$	I_{DS} value with the FET ON
$\boldsymbol{J_{SD}}^{max}$	Maximum current density
$\mathbf{k_B}$	Boltzmann constant
L	FET channel length
LCAO	Linear Combination of Atomic Orbitals

lin	Linear
LUMO	Lowest Unoccupied Molecular Orbital
MAI	Methylammonium iodide
$MAPbI_3$	Methylammonium lead iodide
MAS	Magic angle spinning
MD	Molecular dynamic
MTR	Multiple trap and release
NEXAFS	Near Edge X-Ray Absorption Fine Structure
N_t	Trap density
OFET	Organic Field-Effect Transistor
OTS	Octadecyltricholorsilane
PCB	Printed Circuit Board
PDFO	2,2,3,3,4,4,5,5,6,6,7,7,7,7,7-Pentadecafluoro-1-octanol
PDI	Perylenediimide
PDI7-CN_2	N-N'-bis(n-octyle)-(1,7&1,6)-dicyanoperylene-3,4:9,10-bis(dicarboximide)
PDIF-CN_2	N'-bis(perfluorobutyl)-(1,7&1,6)-dicyanoperylene-3,4:9,10-bis(dicarboximide)
PEG	PolyEthylene Glycol
PESA	PhotoElectron Spectroscopy Ambient
PFD	1H,1H,2H-Perfluoro-1-decene
P_{max}	Maximum power density
PFS	Trichloro(1H,1H,2H,2H-perfluorooctyl)silane
PL	Photoluminescence
r	Reliability factor
R	Resistance
R_c	Contact resistance
R_{chan}	Channel resistance
RH	Relative humidity
R_m	Metal resistance
S	Source electrode
SAM	Self-Assembled Monolayer
sat	Saturation
SCLC	Space-charge limited current
SIP	Solvent induced precipitation
SEM	Scanning Electron Microscopy
Si n++	Heavily n-doped silicon
ssNMR	Solid state Nuclear Magnetic Resonance
T	Temperature
TESPN	(2-Cyanoethy)triethoxysilane
TMDC	Transition Metal DiChalogenide
TLM	Transfer line method

UPS	Ultraviolet Photoelectron Spectroscopy
VB	Valence band
$\mathbf{V_{DS}}$	Drain-source voltage
vdW	van der Walls
V	Voltage
$\mathbf{V_{GS}}$	Gate-source voltage
Vol	Volume
$\mathbf{V_{TH}}$	Threshold voltage
W	FET channel width
WCA	Water Contact Angle
WF	Work function
XPS	X-ray Photoelectron Spectroscopy
XRD	X-Ray Diffraction
1S	One-step
2S	Two-step
$\boldsymbol{\tau}$	relaxation time
$\boldsymbol{\lambda}$	Reorganization energy
$\boldsymbol{\lambda_{xxx\ nm}}$	Wavelength at XXX nm
$\boldsymbol{\kappa}$	Dielectric constant
$\boldsymbol{\sigma}$	Electrical conductivity
$\boldsymbol{\mu}$	Charge carrier mobility
$\boldsymbol{\mu_e}$	Electron mobility
$\boldsymbol{\mu_h}$	Hole mobility
$\boldsymbol{\psi}$	Wave function
$\boldsymbol{\rho}$	Electrical resistivity

Statement of work

The experiments and analysis presented in this thesis were carried out by myself, unless explicitly mentioned.

Chapter 5: XRD measurements and analysis were carried out by Dr. F. Liscio and Dr. N. Demitri (Trieste). XPS, UPS and EELS measurements were performed and analysed by Prof. L. Pasquali (Modena) and Dr. M. Nardi (Trieste). INS measurements and analysis were executed by Dr. M. Zbiri (Grenoble) and Dr. A. Y. Guilbert (London). THz measurements and their analysis were made by X. Jin, Y.-H. Jeong and Prof. L. Razzari (Québec). MAS-ssNMR measurements were performed by Dr. J. Wolf and Dr. J Raya (Strasbourg). Theoretical simulations were done by Dr. D. Dudenko, Dr. Y. Olivier, Dr. D. Beljonne (Mons) and Dr. A. Y. Guilbert (London).

Chapitre 6: AFM images were recorded and treated with the help of Dr. S. Bonacchi and by M. Eredia (Strasbourg). NEXAFS has been performed and analysed by Dr. M. Nardi (Trieste). Dr. T. Leydecker and Y. Wang contributed to the preparation of some WSe_2 samples.

Chapitre 7: XRD analysis of the perovskite was performed by Dr. L. Ferlauto (Strasbourg) and Dr. F. Liscio (Trieste). The PEG-BTBT was synthesized by F. Devaux (Prof. Y. H. Geerts Group, Brussels). XRD analysis of the PEG-BTBT was carried out by F. Devaux and Dr. Chattopadhyay (Brussels). AFM images were recorded and treated by M. Eredia (Strasbourg).

Prof. P. Samorì and Prof. Emanuele Orgiu helped on designing various experiments and analysing the data, through very helpful discussion.

Chapter 1 Introduction

1.1 Context

The advent of new technologies relies on the development of new and more sophisticated components/materials and their advanced integration toward high-performance devices. For example, when considering logic circuits, which can be considered as key components for today's electronics, they are made via integration of field-effect transistors. The latter were pioneered by J. Lilienfeld[1], with further improvement brought into play by J. Bardenn, W. Brattain and W. Shockley[2] and later by J. Kilby.[3] The pace towards smaller and smaller transistor is mandatory for faster and smarter electronics, in compliance with the roadmap predicted by the famous Moore's law since 1965.[4] This law describes an exponential growth on the number of transistor implemented in processors over the years, leading in parallel to an enhancement of the computing performances described by the Dennard scaling.[5] However, such integration is more and more difficult to follow; at the horizon 2030, transistors should be within 1 nm to follow Moore's law. Up to date, transistors are already reaching 5 nm that should compose future processors in 2020. In order to become a real product, these circuits, based on semiconducting materials, need to be produced at low-cost, which goes hand in hand with up-scalable industrial processes. However, the current silicon based transistors tend to be more and more expensive, because of the high power consumption required for the manufacturing.

Organic semiconductors are perfect alternatives.[6–10] Due to their good solubility, their processability at low temperatures (typically below 100 °C) using up-scalable approaches like ink-jet or roll-to-roll printing,[11] combined with their potential in operating of low-power consumption modes[12], transparency in the visible range[13] and flexibility[14], organic semiconductors are becoming a meaningful replacement of the omnipresent silicon in the today's electronic.[15] Starting from initial modest mobilities, the scientific community devoted huge efforts to allow organic semiconductors becoming competitive with the inorganic ones, by

designing new semiconducting molecular architectures and developing novel strategies to improve the device's performances.[16] Up to date, organic semiconductors have already been widely employed in the fabrication of diodes,[17,18] solar cells,[19,20] sensors[21] or in the field of spintronics[22]. This class of compounds, feature distinct characteristics when compared to their inorganic counterpart: it usually exhibits lower degree of crystallinity,[23] allowing to be described only in a limited way by the classical band theory, which is generally applied to solids.[24–27] It is only by mastering the structure-properties relationships through a full comprehension of the physics inherent to these materials that it may be possible, one day, to fully surpass silicon properties and technologies thereof. Because the performances of semiconductors depend on their capability to transport charges carriers, the comprehension of these phenomena in organic materials is of paramount importance toward accomplishing this goal.

Thus, the aim of this work is to contribute to the understanding of physical and chemical parameters influencing the charge transport properties of different classes of materials, and the use such knowledge to engineer high-performance devices. This goal is reached by mastering the concepts of supramolecular chemistry to generate ordered structures to unravel the structure-properties relationship.

1.2 Structure of the thesis

The present manuscript is divided in 8 chapters structured as follow:

Chapter 1 puts in context the work done in this thesis.

Chapter 2 sets the basis of the physics of semiconductors, first by describing the chemical bond, and how it impacts the energy landscape of a molecule, then by reviewing the most common charge transport mechanisms in solids that are used within the thesis, and finally, by giving an overview of the interface's parameters affecting the properties of the semiconductors.

Chapter 3 introduces the classes of materials used in this work, including a brief description of small semiconducting molecules, hybrid materials such as perovskites, and atomically thin 2D materials.

Chapter 4 presents the experimental techniques used to characterize the samples as well as specific procedures employed for device preparation. Special attention is dedicated to the working principle of field-effect transistors.

Chapter 5 discusses the charge transport occurring in two different perylene diimide derivatives, each exhibiting a specific charge transport mechanism. Through a systematic investigation, the mechanisms of charge transport is exanimated with the help of structural and vibrational analysis, supported by simulations, allowing to understand their origin.

Chapter 6 focuses on the use of molecular dopant able to form self-assembled monolayer to induce drastic changes in the spectroscopic properties of graphene and in the optoelectronic performances of WSe_2 monolayers. Particular care is taken when dealing with the characterization of the interactions that describe the interface formed between the 2D materials and the molecules.

Chapter 7 presents two kinds of resistive gas sensors. The former is based on an organic-inorganic hybrid perovskite, for the detection of oxygen in the atmosphere through the defect of the compound as active sites. The latter relies on a benzothienobenzothiophene derivative, which is able to detect humidity by the reversible adsorption of water molecules the lateral chains that tune the intermolecular distance.

Chapter 8 concludes the present work by giving the major progresses achieved in the field, and the outlooks for each project.

1.3 References

[1] E. Lilienfeld, *Method and Apparatus for Controlling Electric Currents*, **1930**, US1745175A.
[2] W. Shockley, *The Bell System Technical Journal* **1951**, *30*, 990.
[3] J. S. Kilby, *Miniaturized Electronic Circuits*, **1964**, US3138743A.
[4] G. E. Moore, *Electronics* **1965**, *38*, 114.

[5] R. H. Dennard, F. H. Gaensslen, V. L. Rideout, E. Bassous, A. R. Leblanc, *IEEE Journal of Solid-State Circuits* **1974**, *9*, 256.
[6] H. Koezuka, A. Tsumura, T. Ando, *Synthetic Metals* **1987**, *18*, 699.
[7] G. Horowitz, *Advanced Materials* **1998**, *10*, 365.
[8] S. R. Forrest, *Nature* **2004**, *428*, 911.
[9] H. Sirringhaus, *Advanced Materials* **2014**, *26*, 1319.
[10] L.-L. Chua, J. Zaumseil, J.-F. Chang, E. C.-W. Ou, P. K.-H. Ho, H. Sirringhaus, R. H. Friend, *Nature* **2005**, *434*, 194.
[11] Y. Ai, Y. Liu, T. Cui, K. Varahramyan, *Thin Solid Films* **2004**, *450*, 312.
[12] M. Halik, H. Klauk, U. Zschieschang, G. Schmid, C. Dehm, M. Schütz, S. Maisch, F. Effenberger, M. Brunnbauer, F. Stellacci, *Nature* **2004**, *431*, 963.
[13] Y. Yuan, G. Giri, A. L. Ayzner, A. P. Zoombelt, S. C. B. Mannsfeld, J. Chen, D. Nordlund, M. F. Toney, J. Huang, Z. Bao, *Nature Communications* **2014**, *5*, DOI 10.1038/ncomms4005.
[14] F. Garnier, G. Horowitz, X. Peng, D. Fichou, *Advanced Materials* **1990**, *2*, 592.
[15] H. Klauk, U. Zschieschang, J. Pflaum, M. Halik, *Nature* **2007**, *445*, 745.
[16] A. Facchetti, *Materials Today* **2007**, *10*, 28.
[17] C. Groves, *Nature Materials* **2013**, *12*, 597.
[18] H. Uoyama, K. Goushi, K. Shizu, H. Nomura, C. Adachi, *Nature* **2012**, *492*, 234.
[19] Y.-J. Cheng, S.-H. Yang, C.-S. Hsu, *Chemical Reviews* **2009**, *109*, 5868.
[20] A. Facchetti, *Chemistry of Materials* **2011**, *23*, 733.
[21] J. Locklin, Z. Bao, *Analytical and Bioanalytical Chemistry* **2005**, *384*, 336.
[22] K. Ando, S. Watanabe, S. Mooser, E. Saitoh, H. Sirringhaus, *Nature Materials* **2013**, *12*, 622.
[23] C. Wang, H. Dong, W. Hu, Y. Liu, D. Zhu, *Chemical Reviews* **2012**, *112*, 2208.
[24] J. L. Bredas, J. P. Calbert, D. A. da Silva Filho, J. Cornil, *Proceedings of the National Academy of Sciences* **2002**, *99*, 5804.
[25] V. Coropceanu, J. Cornil, D. A. da Silva Filho, Y. Olivier, R. Silbey, J.-L. Brédas, *Chemical Reviews* **2007**, *107*, 926.
[26] V. Podzorov, E. Menard, A. Borissov, V. Kiryukhin, J. A. Rogers, M. E. Gershenson, *Physical Review Letters* **2004**, *93*, DOI 10.1103/PhysRevLett.93.086602.
[27] H. Sirringhaus, *Advanced Materials* **2005**, *17*, 2411.

Chapter 2 Basic concepts of semiconductor physics and device's interfaces

2.1 Introduction

This section provides an overview on the origin of the band formation, through the description of the chemical bond. The most popular charge transport mechanisms will be briefly described, starting by the conduction in a metal as an extreme case with respect to the 2D and the organic semiconducting materials. Finally, a description of the interfaces that a semiconductor can experience within a device is introduced.

2.2 Semiconductors

2.2.1 From the atomic orbital to the band

When two atoms are spatially close enough, and in a suitable electronic configuration, a chemical bond can be created, in which both atoms share electrons by overlapping their atomic orbitals. According to the linear combination of atomic orbitals theory (LCAO),[1] when two atoms A and B, whose atomic orbitals can be described by their wavefunction ψ_A and ψ_B, are interacting together to form a bond, the resulting molecular orbitals Ψ can be approximated as a linear combination of the atomic orbitals (Equation 2.1 and 2.2).

$$\Psi = c_A\psi_A + c_B\psi_B \tag{2.1}$$

$$\Psi^* = c_A\psi_A - c_B\psi_B \tag{2.2}$$

The equation (2.1) describes the bonding state while (2.2) leads to the anti-bonding state, as represented on the orbital diagram of the H_2 molecule (Figure 2-1).

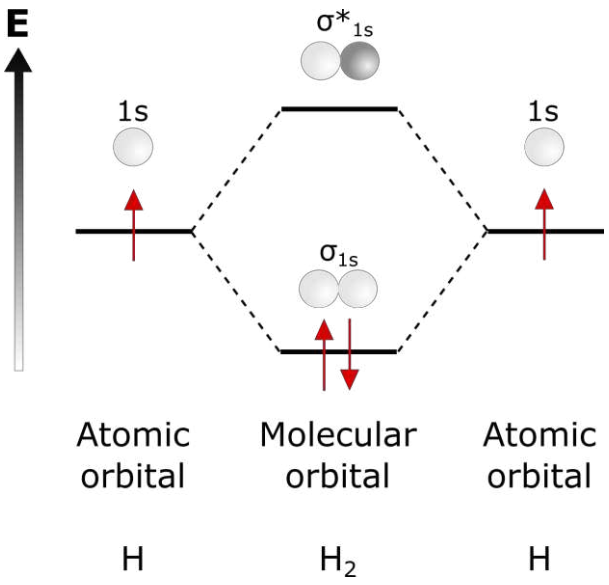

Figure 2-1 Orbital diagram of H_2.

In this precise case, the 1*s* orbitals from the hydrogen atoms, when interacting together, leads to the formation of σ_{1s} (the bonding molecular orbital, which is also in this specific case, being the highest occupied molecular orbital, or HOMO) and σ^*_{1s} (the anti-bonding molecular orbital, being the lowest unoccupied molecular orbital, or LUMO). Upon increase of the number of bonding atoms, the equation of the LCAO theory can be generalized as Equation 2.3 :

$$\Psi = \sum_n C_n \psi_n \tag{2.3}$$

Hence, in an easy view, *n* atoms bonded together will lead to n molecular orbitals with a specific energy. For infinite value of *n*, the discrete energy levels of molecular orbitals lead to two continuum distributions of energy levels, where the anti-bonding states form the so-called conduction band, while the bonding states form the valence band (Figure 2-2). Since the bonding states are the most energetically stable level, they are preferentially filled with the electrons. Hence, the valence band is the band occupied by electrons while the conduction band is empty. An empty energy level which can be filled by an electron is called a hole. In other words, that the conduction band is filled with holes. To keep the charge neutrality, since the electron are negatively charged, a hole is naturally positively charged.

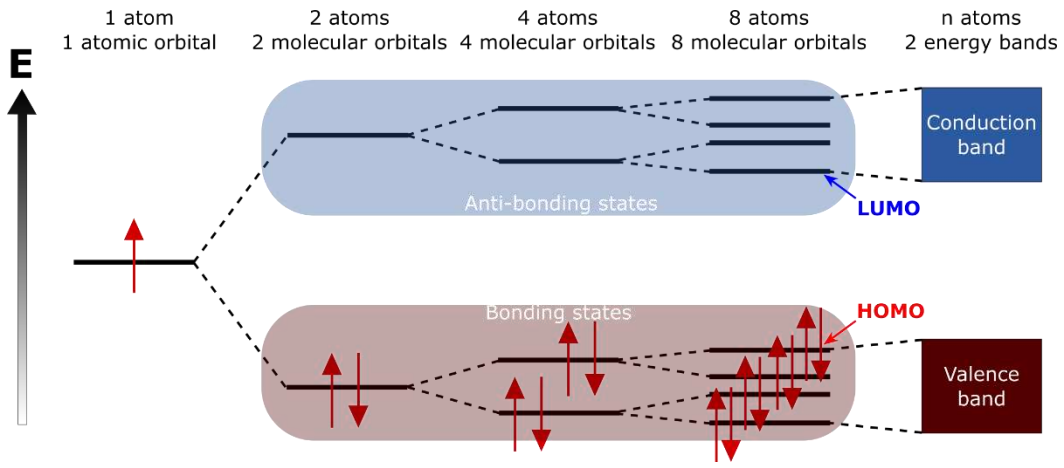

Figure 2-2 Sketch of an orbital diagram describing the formation, from the single atomic orbital, to the band structure.

It is important to note that, depending of the atoms involved in the structure, not only two bands are formed, but a multitude, at lower and higher energy than the valence band and conduction band, respectively. However, these two are among the most important to define the electronic properties of a material. Indeed, when the energy between the valence band and the conduction band (called band-gap) is not too large (typically ranging from 1 eV to 2.5 eV), under a certain stimulus, electrons can be promoted from the valence band to the conduction band, and conversely, holes can populate the valence band. In this situation, the charges are free to move within the band, which lead to the emergence of an electrical conduction. If the Fermi level (E_F, the highest energy level occupied by an electron) is in the middle of the band-gap, the semiconductor is called intrinsic, and electrons and holes have equal possibility to populate the conduction and valence band, respectively (Figure 2-3). If the Fermi level is closer to the conduction band, the electron conduction is more favoured compared to hole conduction, because of the small energy needed for the electron to be promoted to the conduction band. Such semiconductors are called *n*-type. Similarly, if the Fermi level is close to the valence band, holes will more easily access to the valence band, providing hole conduction, which can be found for the *p*-type semiconductors. However, if the Fermi level is situated in the middle of a wide band-gap (larger than 4 eV), neither electrons nor holes can access to a band; the material is thus an insulator. The opposite case is when the two bands are overlapping, and the Fermi

level is within the bands, or when the Fermi level is within a band. This leads to a complete free motion of both charges, called metallic behaviour.

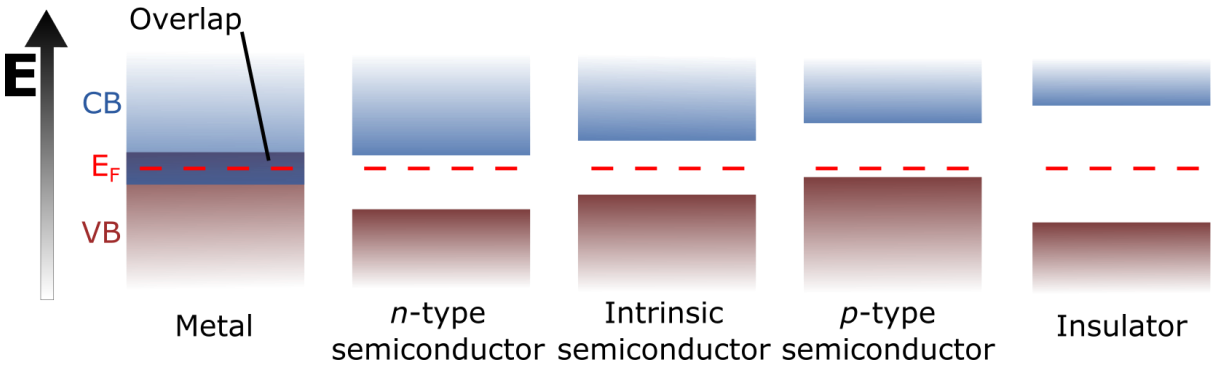

Figure 2-3 Energy diagram of a metal, the three cases of a semiconductor and an insulator.

The way that the electrons are statistically distributed around the Fermi level can be described by the Fermi-Dirac distribution[2] (Equation 2.4).

$$n_i = \frac{g_i}{\exp\left(\frac{E_i - \mu}{k_B T}\right) + 1} \tag{2.4}$$

Where n_i is the number of particles in the state with an energy E_i that as a g_i degeneration, k_B is the Boltzmann constant and T, the temperature. In (2.4), μ is the chemical potential of the electrons (or Fermi level), represented as a thermodynamic quantity reflecting the energy needed to change the number of particles in a system. Basically, if an energy state is matching with the Fermi level, this state is statistically occupied at 50%.

In a metal (Figure 2-4), the distance between the Fermi level and vacuum level is called work function (WF or Φ). For a semiconductor, the valence band (or HOMO level) is characterized by the ionization energy (IE) while the conduction band (or LUMO level) is related to the electron affinity (EA). The density of states (DOS) around these levels are described differently if the semiconductor is inorganic or organic. Indeed, the former DOS is described by a square root function of the energy while the latter is depicted by a Gaussian distribution around the HOMO and LUMO.

All these levels are estimated with respect to the vacuum level, which refers to the energy of an electron that is outside of a material, without interacting anymore with it. Hence, the work function represents the energy required to remove an electron from the metal, and similarly, the ionization energy for extracting one electron from the valence band (or HOMO) while the electron affinity correspond to the energy released by the addition of an electron into the conduction band (or LUMO).

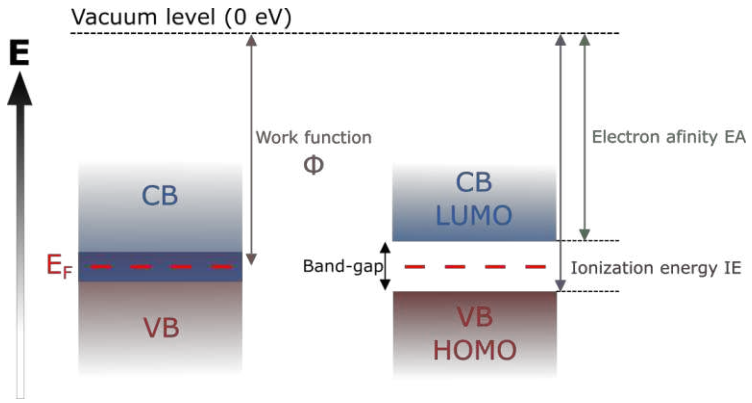

Figure 2-4 Nomenclature of the energy levels in the band structure of a metal and a semiconductor.

2.2.2 Charge transport models

2.2.2.1 Basic conduction phenomena in metals and inorganic semiconductors

The first modern description of the electrical conductivity in metals have been introduced by Drude in 1900, refined by Sommerfeld few years later, giving the free electron model. In this approach, the electron conduction is considered as a gas of particles having no long-range interaction between each other, and only subjected to collisions,[3] described by the equation 2.5.

$$\sigma = \frac{e^2}{6k_BT}.nlv \qquad (2.5)$$

Where σ is the electrical conductivity, e the elementary charge, k_B the Boltzmann constant, T the temperature, n the density of particles, v their velocity and l is their mean free path. Because of the failure of this model on the explanation of the magnetic properties and on the temperature dependence of the conductivity, new considerations had to be done to improve this model. With the emergence of the quantum theories, Bloch proposed in 1928 that the free electron gas from the Drude model can be described by eigenstates to define plane waves which are modulated by a function related to the periodicity of the crystal investigated, where the phonon spectrum has to be considered as the principal scattering event.[4] Generally speaking, the resistance of a metal is increasing while increasing the temperature, because of a higher density of phonons thermally populated at high temperature.

For inorganic semiconductors, one can apply the same theory for charge transport used for metals, at the exception that the Fermi level of a metal is within a band while for the semiconductor, it is described by the valence band which is full of electrons, a conduction band which is empty, separated by an energy gap. The conduction is happening, under an external electric field or when the charges are subject to a thermal or optical excitation, allowing to populate the empty band.

The resistance behaviour versus increasing the temperature in inorganic semiconductor is a compromise between its reduction because of an increasing probability of promoting charges in the conduction band (described by the Fermi-Dirac distribution) and its increase due to the charge scattering from intrinsic and extrinsic sources. Indeed, charge carriers interact with the atomic lattice, leading to the formation of polarons (as explained latter in section 2.2.2.3), and are also subject to different sources of scattering from defect and grain boundaries. These mechanisms are describing typical inorganic ionic semiconductor, such as GaAs[8] but can also be applied to certain hybrid materials, such as the organic-inorganic hybrid perovskite $CH_3NH_3PbI_3$.[9,10]

2.2.2.2 Charge transport in two-dimensional semiconductors

Two-dimensional semiconducting materials represent the thinnest semiconducting materials known. Due to their atomic thickness, space confinement of charges in 2D has significant consequences compared to 3D. One of the most significant implication of their 2D nature consists in its greatest sensitivity to their surrounding environment, thus being more subjected to scattering effects from different origins (Figure 2-5).

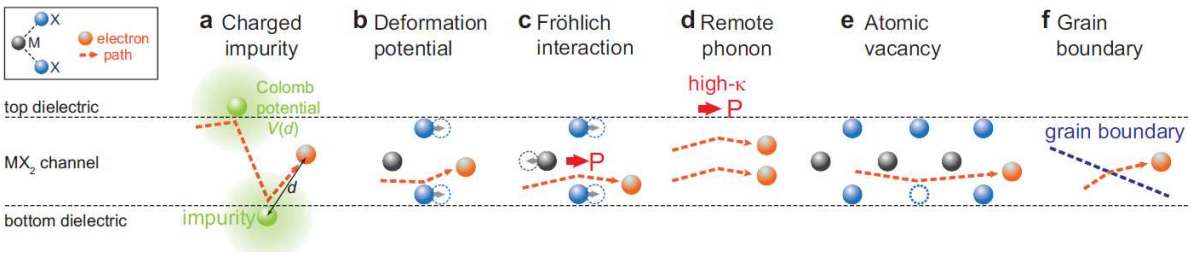

Figure 2-5 Representation of the most common scattering mechanism encountered in atomically thin MX_2 materials (Reproduced with permission from[11]).

For instance, impurities present at both interfaces of the 2D materials is one of the major reasons for charges scattering. When these impurities are charged, they create a scattering potential acting on surrounding charge carriers via long-ranged Coulomb interactions.[12] These impurities are various, from the chemical defects at the surface of the adjacent dielectric layer to the adsorbed molecule at the surface of the 2D material, such as gaseous compound or contaminant from the device processing.

Phonons (i.e. a collective vibration of atoms in a solid) play also a role in the scattering mechanisms that a charge carrier can experience. First from the interatomic displacement generated by the phonons, leading to a fluctuation of the lattice potential which rules the band structure, and then induces a perturbation of the band edges.[13] Secondly, some phonons affect the atomic lattice by interacting with the dipole moment presents between two atoms, leading to the formation of an electric field that can scatter charge carriers, known as Fröhlich interaction.[14]

Scattering events originating from lattice phonons are intrinsic to the material, which are directly related to the temperature, but it was found to not be the dominant contribution to the charge transport decrease at room temperature.[11] Undoubtedly, material defects such as atomic vacancies and grain boundaries are also scattering points for the charge carriers,[15] contributing to the decrease of the charge mobility.

2.2.2.3 Charge transport in organic semiconductors

Organic semiconducting materials are essentially composed by hydrogen, nitrogen, oxygen and sulphur, yet the main element is carbon. When two carbon atoms are involved to form a covalent bond, different scenarios are possible. If this C-C bond is saturated, a full hybridization of the atomic orbital will happen between the $2s$ and the three $2p$ orbitals, leading to the formation of four hybrid sp orbitals (Figure 2-6). The carbon is called in a sp^3 hybridization, and can form four σ bounds, with other elements. However, if this C-C bond is unsaturated, it means that not all the $2p$ orbitals are hybridized into sp ones, and can participate in the formation of a π-bond, corresponding to an overlapping between p orbitals oriented along the same axis. If the carbons are in sp^2 configuration, three p orbitals are hybridized, leading to the formation of a "double bond", and a sp configuration leaves two p orbitals not hybridized, with a "triple bond" formation. In organic semiconductor, the carbons are essentially in a sp^2 configuration, which is mostly responsible of the conduction is such systems. Indeed, the successive sequence of π bonds allows the delocalization of the electrons into these bonds over the conjugated carbon backbone, because of the degeneration of their energy levels.

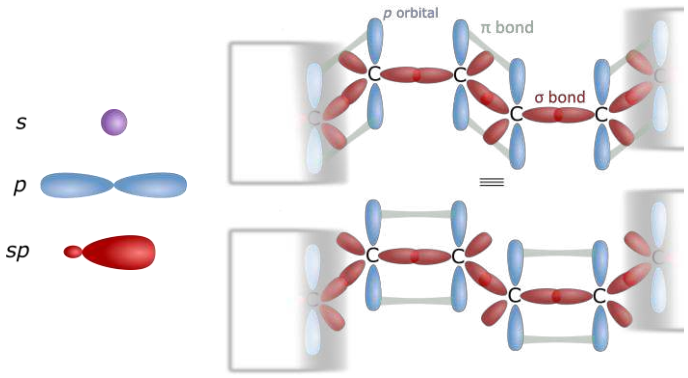

Figure 2-6 Representation of the *s* and *p* orbitals, and the result of their hybridization into a *sp* orbital (left). Representation the two states of an alkene chain where the carbon are in a sp^2 hybridization (right).

Moreover, upon increasing the size of the conjugated system, it yields to a reduction of the energy gap between the HOMO and the LUMO levels. Indeed, the equation for the energy of a particle in a one dimensional box (Equation 2.6) can be adjusted to describe the HOMO (Equation 2.7) and LUMO energy level (Equation 2.8).

$$E_n = \frac{n^2 \mathrm{h}^2}{8mL^2} \tag{2.6}$$

$$E_{\mathrm{HOMO}} = \frac{\left(\frac{N}{2}\right)^2 \mathrm{h}^2}{8m(Nd)^2} \tag{2.7}$$

$$E_{\mathrm{LUMO}} = \frac{\left(\frac{N}{2}+1\right)^2 \mathrm{h}^2}{8m(Nd)^2} \tag{2.8}$$

Where $n = 1, 2, \ldots$, h is the Planck constant, m the mass of the electron, and L the conjugation length that can be decomposed as the number of atoms N multiplied by d, the distance between two atoms. Since the band gap energy E_g is the difference in energy between the LUMO level and the HOMO level, equation 2.9 can be written, if the number of atoms N is large enough.

$$E_g = E_{LUMO} - E_{HOMO} \cong \frac{\mathrm{h}^2}{8md^2N} \tag{2.9}$$

Hence, increasing N will reduce the energy gap.

In organic semiconductor, the transport of charges can occur on three different levels (Figure 2-7).

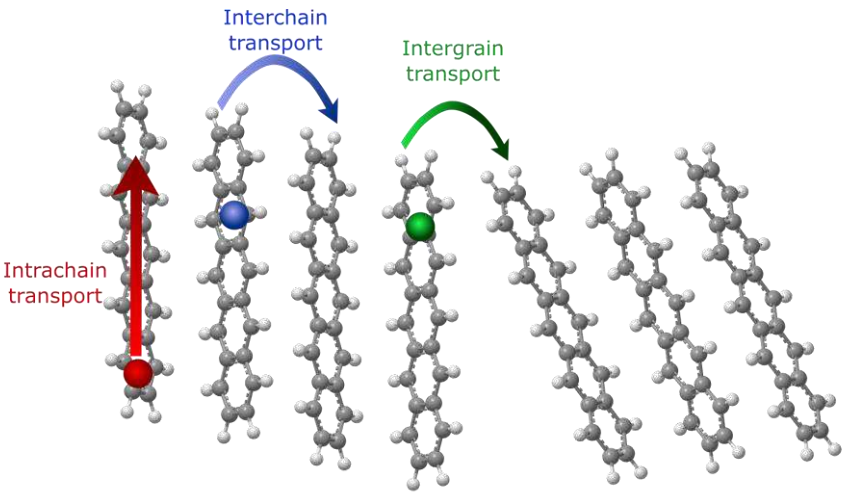

Figure 2-7 Representation of the intrachain, interchain and intergrain transports on a plane of the herringbone crystal structure of pentacene.

The charges can move through the molecule. It will be favoured for flat systems that have an extended conjugation, allowing an optimized delocalization of the charges. They can also jump from one molecule to the adjacent one, by overpassing an energy barrier described by the energy potential due to the distance between the two molecules. This is called interchain transport and will be strongly affected by the transfer integral of a molecular system, which is the overlapping of molecular orbitals between two adjacent molecules. The greater the transfer integral, the easier will the charge pass from one molecule to the adjacent one. Finally, in the case of polycrystalline films, a charge can jump from one crystalline domain to another one, crossing the so called grain boundary. Grain boundaries are a crucial parameter for the charge transport, since they act as traps for charges because of the wide physical gap open between two crystallites, and the presence of impurities. It's important to mention that when a charge is located on one molecule, the geometry of this molecule is strongly affected.

The polaronic model

When a charge is located on a molecular unit in an organic semiconductor, this charge will have the tendency to polarise its surrounding environment, forming what is called a polaron. A polaron is a quasi-particle used to picture the interaction between charges and atoms in a material. The concept of polaron was first introduced by Landau,[16] and Pekar[17] in inorganic

materials and extended to organic compounds by Holstein, with the known small-polaron model.[18] The polaron transport, thus, is described as a charge moving in an organic material, with a polarization cloud surrounding it. This polarization cloud is subjected to collective atoms oscillations with a specific mode of vibration, called phonon, leading to the formation of electron-phonon coupling. This coupling is acting on the localization length of a charge in a molecular system; a weak coupling tends to let a charge delocalized over a few molecular units while a strong coupling localizes it, hence lowering the charge carrier mobility and increasing the electron's effective mass. The stability of a polaron is dependent on a compromise between its residence time τ_{res} on a molecule and the electrical polarization time τ_{el} of the structure.[19] The former is related to the width (W) of the allowed band of the material while the latter will be affected by the energy of the band-gap (Equation 2.10 and 2.11).

$$\tau_{res} = \frac{\hbar}{W} \tag{2.10}$$

$$\tau_{el} = \frac{\hbar}{E_g} \tag{2.11}$$

Whereas the bandgap is comparable between organic and inorganic semiconductors, the bandwidth of the former is much narrower than the latter, due to the weak interaction encountered in organic structures (van der Waals, …) compared to inorganic one fully composed of strong interaction. In other words, the charge carrier is moving fast enough in inorganic semiconductor that the electrical polarization doesn't have enough time to happen.

Multiple trap and release model

The main difference between the classical band transport in inorganic semiconductor and the organic one comes from the higher degree of disorder present in the later compared to the former. In some cases, this disorder, generated by crystal defects or impurities, lead to the formation of localized states called traps, that are limiting the transport of charges. When a material is weakly disordered in the sense that the order is good enough to allow the formation of bands, but still suffer from a small amount of disorder through defect sites or impurity, traps state will be formed at an energy level located within the band-gap. In this scenario, the multiple trap and release (MTR) model can be applied to describe such system. This model,

firstly developed to describe silicon materials,[20] was later extended to organic semiconductors.[21,22] The assumption is that the traps, within the band-gap, can be close to the transport band from few k_BT (around 25 meV at 298 K) and are called shallow traps (Figure 2-8), or can be far in the band-gap (deep traps).[23] When a charge is moving through the band, under an electric field, it has a high probability of being immediately trapped in one of the localized states within the gap. If the charge is in a shallow trap, it can be released, back to the band through a thermally activated process, for the traps states that are within few k_BT.

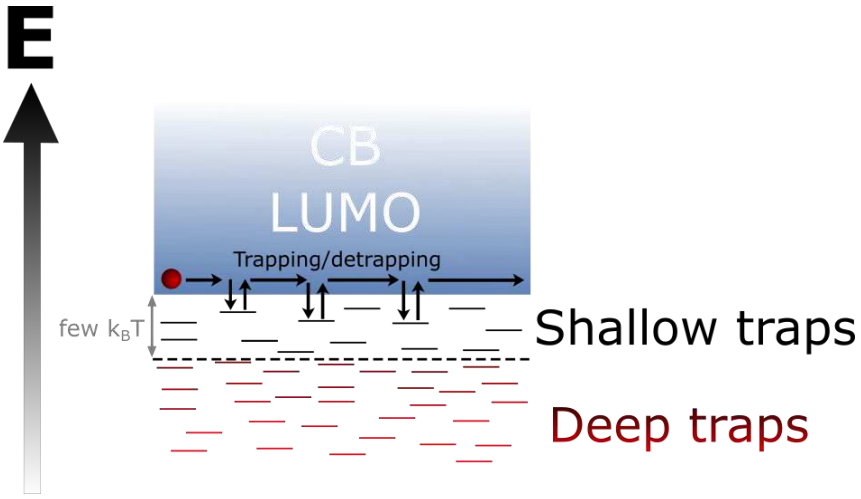

Figure 2-8 Schematic of the conduction described by the MTR model. A mobile charge can be temporary immobilize in a shallow trap.

Thus, the overall observed mobility will be defined by the number of traps states and their energy level. This type of conduction can be described in the way that the number of free charge carriers corresponds to the total charge carriers in the material, weighted by the average time that a charge will spend by being trapped. Consequently, the effective charge carrier mobility μ_{eff} can be described by the equation (2.12).

$$\mu_{eff} = \mu_0 \alpha e^{\left(-\frac{E_T}{k_B T}\right)} \tag{2.12}$$

Where μ_0 is the charge carrier mobility in absence of traps, α is a factor reflecting the trap density in the material, and E_T is the energy of an assumed single trap level.

In this view, the trapping effect can be described as μ_0 affected by the average trapping time $\tau_{tr}(T)$ with respect to the average time spent by a polaron between two trapping events $\tau(T)$ (Equation 2.13):

$$\mu_{eff} = \mu_0(T)\frac{\tau(T)}{\tau(T)+\tau_{tr}(T)} \quad (2.13)$$

This equation can be also adapted in terms of the number of carrier n contributing to the current flow (Equation 2.14):

$$n_{eff} = n\frac{\tau(T)}{\tau(T)+\tau_{tr}(T)} \quad (2.14)$$

Band-like model

The band-like transport is a type of model that has been developed to describe the high charge carrier mobilities that can be found in high purity organic crystals.[24,25] In such systems, their charge carrier transport can be described within the band framework, and are characterized by an increase of the mobility while decreasing the temperature (Figure 2-9).

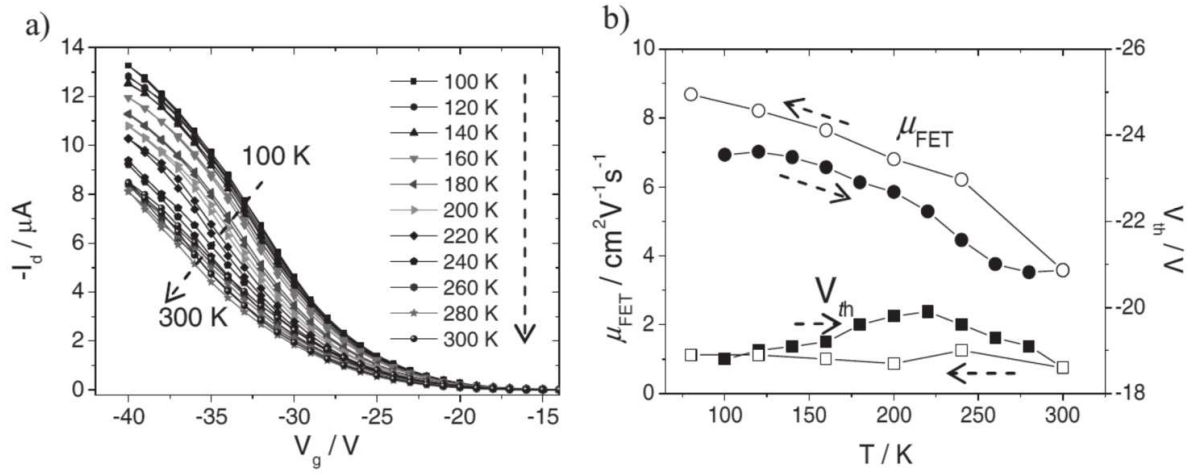

Figure 2-9 Temperature dependence of a C8-BTBT single crystal of a) the source-drain current and b) the extracted FET mobility.(Reproduced with permission from[26])

The decrease of the temperature decreases the phonon scattering that shrink the transport, thus reducing the local polarization cloud around the charge carrier and concomitantly, reducing their effective mass, in some cases close to the free electron,[27] and a broadening of the bands.[28] The exact reasons for the occurrence of this phenomenon are still not completely clear and under controversy, even if a Hall mobility, which is a sign of the extension of charge carriers over few molecular units, has been already measured on organic semiconductors.[29,30] Nevertheless, the important parameters (excluding the extrinsic disorder[31]) for the manifestation of this charge transport seems to be obviously related to the transfer integral between two adjacent molecules, but also to the vibrational/phonon landscape is such system.[32,33]

2.3 Interfaces

Whereas some materials are exhibiting certain intrinsic electrical properties, one should consider the interfaces that these materials are forming with the surrounding environment. Particularly for a FET device, the semiconducting material is in contact with a dielectric surface, charges are injected through electrodes, and measured under a certain atmospheric environment. These characteristics have to be taken into account for the careful analysis and the optimisation of the device's properties.

2.3.1 Interface between the semiconductor and the electrodes

2.3.1.1 Semiconductor-metal junction

When a metal and a semiconductor are contacted, a shift of the energy level at the interface is taking place. Indeed, the work function of the metal and the Fermi level of the semiconductor will align through a shift of the metal work function,[34,35] consequently leading to a shift of the vacuum level of one compound with respect to the other (Figure 2-10). This is due to the formation of an interface dipole barrier which results from the interaction of the electronic density of the semiconductor with the one at the surface of the metal.

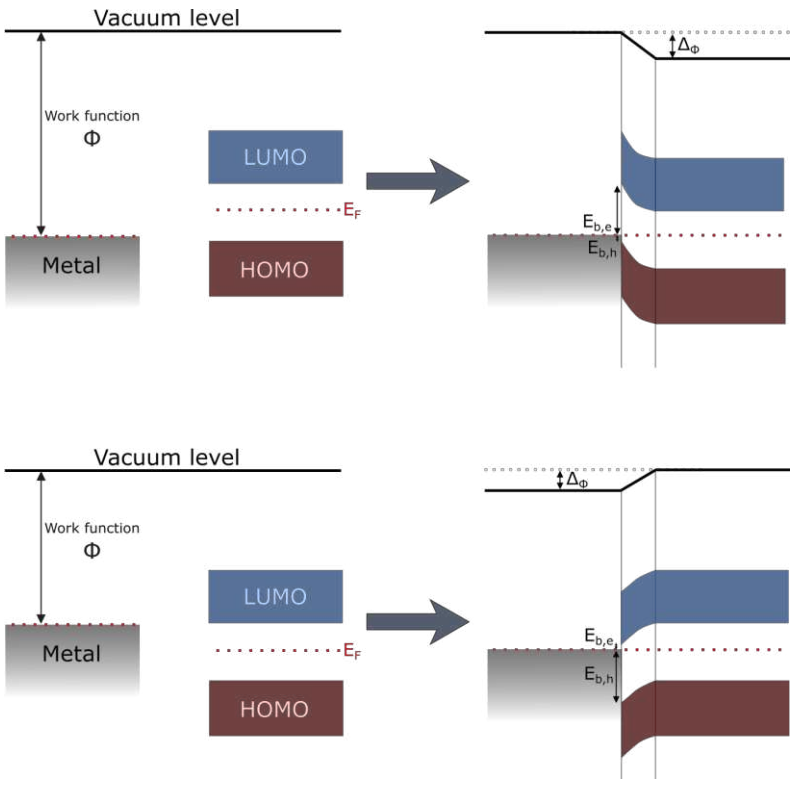

Figure 2-10 Schematic of the energy level for a semiconductor-metal junction before and after contact, with different metals.

When the work function of the metal is initially lower than the Fermi level of the semiconductor, electrons will flow from the latter to the former, commonly leading to a smaller injection barrier for holes ($E_{b,h}$) than for the electrons ($E_{b,e}$). On the contrary, if the work function of the metal is higher than the Fermi level of the semiconductor, the electrons flow is reversed, and the injection barrier for holes will be higher than for electrons. This is why, depending on the type of semiconductor used, a careful selection of the metal used for the electrodes has to be done. A *p*-type semiconductor can be used in combination with, for example, gold electrodes ($WF_{Au} \approx 5.0$ eV) compared to a *n*-type semiconductor that will preferentially be used with aluminium electrodes ($WF_{Al} \approx 4.2$ eV).

2.3.1.2 Electrode with self-assembled monolayers

As seen previously, the right match between the work function of the metal used for as electrodes in a device and the energy levels of the semiconductor is crucial for the optimization

of the properties and the performances of the device, via the engineering of the injection of charges into the semiconductor. To proceed to this optimisation, one could change the metal to fit in the best way with the energy levels of the semiconductor, but having available different sources of metal is not necessarily the case. Another possibility is to put on the metal a specific molecule with electron-donating or electron-withdrawing properties that will perturbs the electronic density at its surface, leading to a local shift of the work function. These molecules can be electron-donating such as, typically, an alkyl chain, or electron-withdrawing, like a perfluorinated chain. The effect and the magnitude of the shift in the metal work function will depend on the design of this molecule, and particularly on the elements used,[36] that will define a certain dipole at the surface of the metal (Figure 2-11).

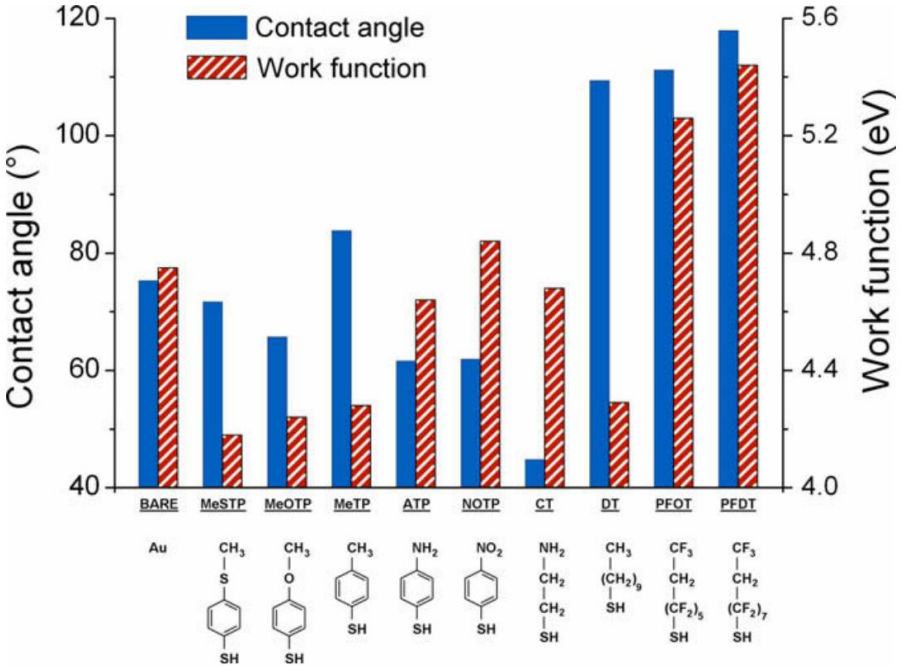

Figure 2-11 Work function of a gold surface functionalized with SAMs, depending of the dipole moment of the molecule used.(Reproduced with permission from[36])

The change of work function ΔW due to the presence of a SAM on a surface can be described by the equation 2.15, where A is the area that one molecule will occupy and Δμ is the change of dipole moment at the surface.

$$\Delta W = \frac{e\Delta\mu}{\varepsilon_0 A} \quad (2.15)$$

This last term, $\Delta\mu$ is defined as a sum of two contributions, being μ_{SAM} and μ_{Chem}. The first one corresponds to the dipole moment along the surface normal of the SAM molecule while the second one reflects the charge reordering in the molecule and in the metal surface when the bond between both is formed.[37] The shift in the work function will be effective only if the molecule described a coherent assembly (Figure 2-12), such as a self-assembled monolayer (SAM).[38] This functionalization of the surface can occur with a chemical suitability between the metal and the molecule; a molecule that possesses a thiol at one extremity will be able to form a chemical bond with a gold surface, through an oxidative addition of the S-H bond to the gold surface, and a reductive elimination of hydrogen gas.[39] When a gold surface is immersed in a solution containing such molecules, the latter will first fully functionalize the surface with a random orientation. With time, other molecules will interact with the already adsorbed one through weak interactions such as van der Waals or hydrophobic interactions, forming a tightly packed layer on the surface, which is thermodynamically favourable.[40] It is important to mention that domains exist on such films, with different packing density and angles with respect to the surface that will have a slight influence on the local work function.[41,42]

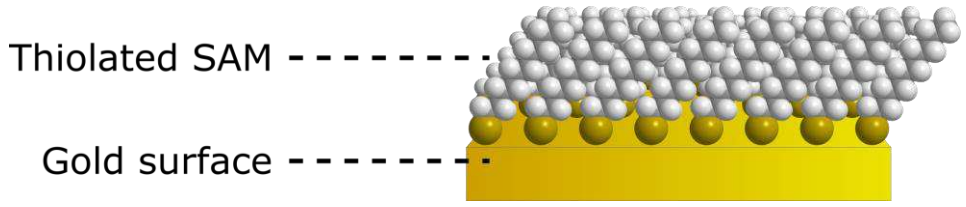

Figure 2-12 Representation of a self-assembled monolayer on a gold surface.

2.3.2 Interface between the semiconductor and the dielectric

The semiconductor/dielectric interface is a critical aspect on different parameters of the device performances. First, the roughness of the dielectric as well as its wettability will strongly affect the semiconductor properties. Indeed, for a solution deposition or a physical one, the properties

of the surface will determine the crystallinity at the interface. If the dielectric/semiconductor interaction is low (because of a high surface energy), the crystallinity of the semiconductor will be favored, leading to an enhancement of its electrical performance. Moreover, in a field-effect transistor, this interface is crucial since it's the place where charges are located for the electrical conduction. Obviously, the dielectric flatness and a reduced amount of impurities increase the performances as well. In the same way that SAMs are used to functionalize a metal surface, they can be also used to functionalize a dielectric surface. The most common dielectric used in devices is SiO_2; such material can be easily functionalized with a molecule bearing a silanol function. The use of SAMs will not only change the surface energy of the dielectric, which is changing the crystallinity of the semiconductor, but it is also passivating traps that are present at the surface, especially the one generated by hydroxyl groups, according to the following mechanism,[43] where Si is a surface atom of bulk SiO_2:

$$\text{Si-O-Si} + H_2O \leftrightarrow 2\ \text{SiOH}$$

$$\text{SiOH} + H_2O \leftrightarrow \text{SiO}^- + H_3O^+$$

$$\text{SiO}^- + H_3O^+ + e^- \rightarrow \text{SiO}^- + H_2O + \frac{1}{2}H_2$$

Whereas the charges can be trapped by the silanolate groups, the presence of these negative charges at the surface of the dielectric also induce an electric field[44] that is added to the one applied during a FET measurement, according to equation 2.16, which is also leading to a reduction of the performances,.

$$V_e = \frac{\sigma_e d_{ox}}{\varepsilon_0 \varepsilon_{ox}} \quad \textbf{(2.16)}$$

Where V_e is the resulting equivalent electric potential, σ_e is the surface charge density, and the dielectric has a thickness d_{ox} and a dielectric constant ε_{ox}.

2.3.3 Interface between the semiconductor and the environment

One additional important parameter to be considered also is the presence of impurities within the semiconducting film or on its surface. These impurities can come from side products during the synthesis of the organic compound that was poorly purified, from solvent molecules that

are trapped into the structure (especially the solvents with high boiling point) or from residues due to a lithographic process, such as traces of photoresist or developer. Most importantly, the ambient atmosphere plays a key role in the degradation of most of the organic semiconductor, because of the presence of water and oxygen. *n*-type semiconductors are much more sensitive to oxygen than *p*-type semiconductors. This is easily explained by the fact that *n*-type semiconductors have generally a higher Fermi level than the *p*-type semiconductors, with respect to the vacuum level. When the scale is reversed, the Fermi level corresponds to the reduction potential.[45] The higher the reduction potential, the higher the affinity of a chemical compound to acquire an electron, and thus, been reduced. On the contrary, a low reduction potential (i.e. a high Fermi level) leads to a high affinity to give an electron, thus, been oxidized. Therefore, the *n*-type semiconductors are more easily oxidized than the *p*-type one. Similarly, water molecules, by themselves, can induces some bias-induced trap states, leading to an increase of the voltages need to get a comparable electrical performance.[46] Different strategies are employed to face this problem. The most common one in the lab is to prepare and measure the devices in a controlled atmosphere, i.e. in an atmosphere without humidity and oxygen, containing typically nitrogen gas. Another approach is to isolate the semiconductor from the atmosphere via an encapsulation layer such as a polymeric film.[47] It is also possible to act on the sensitivity of the molecule through its design, to lower its energy levels, and then make it air-stable.[48–50] Finally, instead of limiting the interactions between the semiconductor and the environment, one can choose a compound, such as a small molecule or an ion, to intentionally tune its electrical properties. This effect is called doping, and can be *p*-type or *n*-type if holes or electrons are added into the semiconductor, to enhance one kind of charge transport or the other.[51] It's important to note that the approach to functionalize the dielectric with SAMs in order to passivate traps can also be used to induce a doping into the semiconductor. Indeed, here again, the choice of the head group of the SAM will define the type of doping induced.[52–54]

2.4 References

[1] R. S. Muilliken, *Science* **1967**, *157*, 13.

[2] M. R. A. Shegelski, *Solid State Communications* **1986**, *58*, 351.
[3] P. Drude, *Annalen der Physik* **1900**, *306*, 566.
[4] F. Bloch, *Z. Physik* **1929**, *52*, 555.
[5] J. Bardeen, *Journal of Applied Physics* **1940**, *11*, 25.
[6] E. Grüneisen, H. Reddemann, *Annalen der Physik* **1934**, *412*, 843.
[7] P. B. Allen, W. H. Butler, *Physics Today* **2008**, *31*, 44.
[8] H. Ehrenreich, *Phys. Rev.* **1960**, *120*, 1951.
[9] T. M. Brenner, D. A. Egger, A. M. Rappe, L. Kronik, G. Hodes, D. Cahen, *J. Phys. Chem. Lett.* **2015**, *6*, 4754.
[10] L. M. Herz, *ACS Energy Letters* **2017**, *2*, 1539.
[11] S.-L. Li, K. Tsukagoshi, E. Orgiu, P. Samorì, *Chem. Soc. Rev.* **2016**, *45*, 118.
[12] S.-L. Li, K. Wakabayashi, Y. Xu, S. Nakaharai, K. Komatsu, W.-W. Li, Y.-F. Lin, A. Aparecido-Ferreira, K. Tsukagoshi, *Nano Lett.* **2013**, *13*, 3546.
[13] K. Kaasbjerg, K. S. Thygesen, K. W. Jacobsen, *Phys. Rev. B* **2012**, *85*, 115317.
[14] N. Ma, D. Jena, *Physical Review X* **2014**, *4*, DOI 10.1103/PhysRevX.4.011043.
[15] A. M. van der Zande, P. Y. Huang, D. A. Chenet, T. C. Berkelbach, Y. You, G.-H. Lee, T. F. Heinz, D. R. Reichman, D. A. Muller, J. C. Hone, *Nature Materials* **2013**, *12*, 554.
[16] L. D. Landau, *Phys. Z. Sowjetunion* **1933**, *3*, 644.
[17] S. I. Pekar, *Research in Electron Theory of Crystals*, **1963**.
[18] T. Holstein, *Annals of Physics* **1959**, *8*, 343.
[19] Z. Bao, J. Locklin, in *Organic Field-Effect Transistors*, CRC Press, **2007**, p. 81.
[20] P. G. Le Comber, W. E. Spear, *Physical Review Letters* **1970**, *25*, 509.
[21] G. Horowitz, R. Hajlaoui, P. Delannoy, *Journal de Physique III* **1995**, *5*, 355.
[22] G. Horowitz, M. E. Hajlaoui, R. Hajlaoui, *Journal of Applied Physics* **2000**, *87*, 4456.
[23] V. Podzorov, E. Menard, A. Borissov, V. Kiryukhin, J. A. Rogers, M. E. Gershenson, *Physical Review Letters* **2004**, *93*, DOI 10.1103/PhysRevLett.93.086602.
[24] W. Warta, R. Stehle, N. Karl, *Applied Physics A Solids and Surfaces* **1985**, *36*, 163.
[25] W. Warta, N. Karl, *Phys. Rev. B* **1985**, *32*, 1172.
[26] C. Liu, T. Minari, X. Lu, A. Kumatani, K. Takimiya, K. Tsukagoshi, *Advanced Materials* **2011**, *23*, 523.
[27] N. Karl, J. Marktanner, R. Stehle, W. Warta, *Synthetic Metals* **1991**, *42*, 2473.
[28] Y. Li, V. Coropceanu, J.-L. Brédas, *The Journal of Physical Chemistry Letters* **2012**, *3*, 3325.
[29] H. Sirringhaus, T. Sakanoue, J.-F. Chang, *physica status solidi (b)* **2012**, *249*, 1655.
[30] N. A. Minder, S. Lu, S. Fratini, S. Ciuchi, A. Facchetti, A. F. Morpurgo, *Adv. Mater.* **2014**, *26*, 1254.
[31] N. A. Minder, S. Ono, Z. Chen, A. Facchetti, A. F. Morpurgo, *Advanced Materials* **2012**, *24*, 503.
[32] I. Y. Chernyshov, M. V. Vener, E. V. Feldman, D. Y. Paraschuk, A. Y. Sosorev, *The Journal of Physical Chemistry Letters* **2017**, *8*, 2875.
[33] A. Y. Sosorev, *Phys. Chem. Chem. Phys.* **2017**, *19*, 25478.
[34] N. F. Mott, *Mathematical Proceedings of the Cambridge Philosophical Society* **1938**, *34*, 568.
[35] H. Ishii, N. Hayashi, E. Ito, Y. Washizu, K. Sugi, Y. Kimura, M. Niwano, Y. Ouchi, K. Seki, *physica status solidi (a)* **2004**, *201*, 1075.
[36] D. Boudinet, M. Benwadih, Y. Qi, S. Altazin, J.-M. Verilhac, M. Kroger, C. Serbutoviez, R. Gwoziecki, R. Coppard, G. Le Blevennec, A. Kahn, G. Horowitz, *Organic Electronics* **2010**, *11*, 227.
[37] P. C. Rusu, G. Brocks, *The Journal of Physical Chemistry B* **2006**, *110*, 22628.
[38] R. Maoz, J. Sagiv, *Journal of Colloid and Interface Science* **1984**, *100*, 465.
[39] A. Ulman, *Chemical Reviews* **1996**, *96*, 1533.
[40] J. Sagiv, *J. Am. Chem. Soc.* **1980**, *102*, 92.
[41] S.-H. Kim, K.-S. Ock, J.-H. Kim, K.-N. Koh, S.-W. Kang, *Dyes and Pigments* **2001**, *48*, 1.
[42] F. Buckel, F. Effenberger, C. Yan, A. Gölzhäuser, M. Grunze, *Advanced Materials* **2000**, *12*, 901.
[43] W. Olthuis, P. Bergveld, in *[1991 Proceedings] 7th International Symposium on Electrets (ISE 7)*, **1991**, pp. 16–26.
[44] R. Williams, M. H. Woods, *Journal of Applied Physics* **1973**, *44*, 1026.
[45] H. Reiss, *J. Phys. Chem.* **1985**, *89*, 3783.
[46] M. Kettner, M. Zhou, J. Brill, P. W. M. Blom, R. T. Weitz, *ACS Appl. Mater. Interfaces* **2018**, *10*, 35449.
[47] S. H. Kim, W. M. Yoon, M. Jang, H. Yang, J.-J. Park, C. E. Park, *J. Mater. Chem.* **2012**, *22*, 7731.

[48] K. Takimiya, T. Yamamoto, H. Ebata, T. Izawa, *Science and Technology of Advanced Materials* **2007**, *8*, 273.
[49] L. Feng, W. Tang, J. Zhao, R. Yang, W. Hu, Q. Li, R. Wang, X. Guo, *Scientific Reports* **2016**, *6*, DOI 10.1038/srep20671.
[50] M.-Y. Kuo, H.-Y. Chen, I. Chao, *Chemistry-a European Journal* **2007**, *13*, 4750.
[51] I. E. Jacobs, A. J. Moulé, *Advanced Materials* **2017**, *29*, DOI 10.1002/adma.201703063.
[52] K. Yokota, K. Takai, T. Enoki, *Nano Lett.* **2011**, *11*, 3669.
[53] Y. Li, C.-Y. Xu, P. Hu, L. Zhen, *ACS Nano* **2013**, *7*, 7795.
[54] S. Kobayashi, T. Nishikawa, T. Takenobu, S. Mori, T. Shimoda, T. Mitani, H. Shimotani, N. Yoshimoto, S. Ogawa, Y. Iwasa, *Nature Materials* **2004**, *3*, 317.

Chapter 3 Materials

3.1 Introduction

In this chapter, an introduction on the classes of material used in this thesis is presented, followed by a description of the materials themselves. The small molecules will be presented through the examples of the n-type perylene diimide and the p-type [1]benzothieno[3,2-b][1]benzothiophene derivatives. Hybrid perovskites will be discussed in a second part whereas 2D materials such as graphene and transition metal dichalcogenides will be finally described.

3.2 Small molecules

Small molecules are of paramount importance in the field of the organic electronics. They are based on a polyaromatic core, whose chemical composition defines their electronic properties (p- or n-type), while the unsubstituted version can be processed only in the gas phase (e.g. via sublimation or evaporation). The substitution with side-chains makes them solution processable, thus opening the door to up-scalable deposition methods like spray coating ink-jet printing or roll-to-roll.

3.2.1 PDI

The formation of crystalline supramolecular assemblies via **π-π stacking** enables the generation of materials displaying high charge transport characteristics. Perylene derivatives have been widely used as industrials dyes. These compounds are presenting peculiar optical and electrical properties, including well-distinct semiconducting properties.

3.2.1.1 PTCDA and the need of a lateral chain

One of the first molecule with a perylene core that has been used in a field-effect transistor is the 3,4,9,10-perylene tetracarboxylic dianhydride (or PTCDA). With a band-gap around 3 eV, PTCDA exhibits anisotropic *n*-type properties, due to its specific crystal structure (Figure 3-1). The poor solubility of this compound was solved by the imidization of its anhydride function, leading to the formation of perylene tetracarboxylic diimide (or PTCDI). This molecular structure has the advantage to allow the functionalization in the imide position to endow solubility in common organic solvents. The most common and simple functionalization is through the grafting of an alkyl chain, which simultaneously makes it possible to tune the molecular packing without drastically perturbing the energy levels of the molecule.

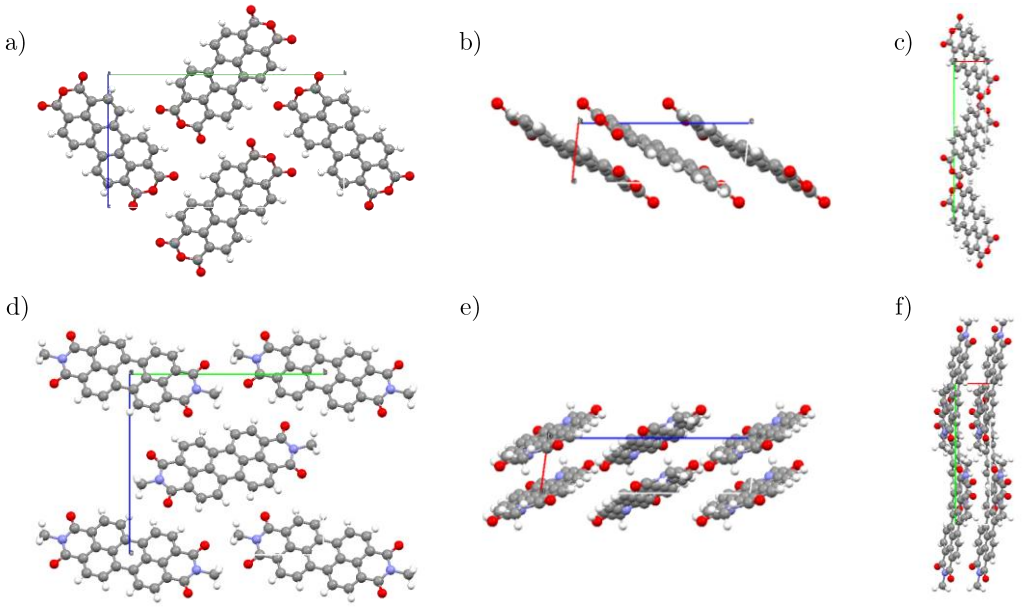

Figure 3-1 Crystal structure along a,d) a, b,e) b and c,f) c directions of α-PTCDA (Structure 196997 on Cambridge Structural Data (CSD))[1] and DiMe-PTCDI (Structure 1140279 on CSD)[2].

This approach was firstly used by Langlahs to solubilise PDI derivatives.[3] One of the most popular PDI is the PDI-8, with a lateral alkyl chain containing 8 carbon atoms (Figure 3-2), such chain is forcing the orientation of the molecules along the same direction due to steric

hindrance of this alkyl substituent. Moreover, the presence of this lateral chain is also forbidding the hydrogen bonding between two adjacent molecules; these hydrogen bonds are present in the case for α-PTCDA.

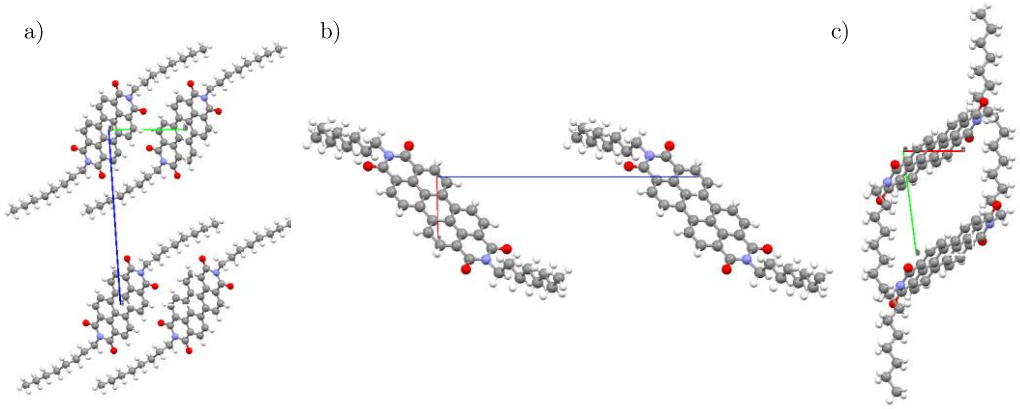

Figure 3-2 Crystal structure along a) a, b) b and c) c direction of PDI-8 (Structure 661829 on CSD)[4].

3.2.1.2 The bay position

As introduced in the chapter 2, one way to confer air-stability to a n-type semiconductor stable consist in lowering the energy levels of the molecule. This can be achieved upon functionalization of PDI derivatives in their bay positions with a suitable group. Typically, to lower the energy levels, electron withdrawing groups are used such as halides atoms, or cyano functions.[5] The number groups as well as the strength of withdrawing electrons will define the magnitude of the shift in the energy levels.[6] However, due to their steric hindrance, some functions that are too bulky determine a twist the core of the molecule, leading to an abrupt decrease of the electrical performance because of the disruption of the delocalized intermolecular π-π conjugation (Figure 3-3).[7]

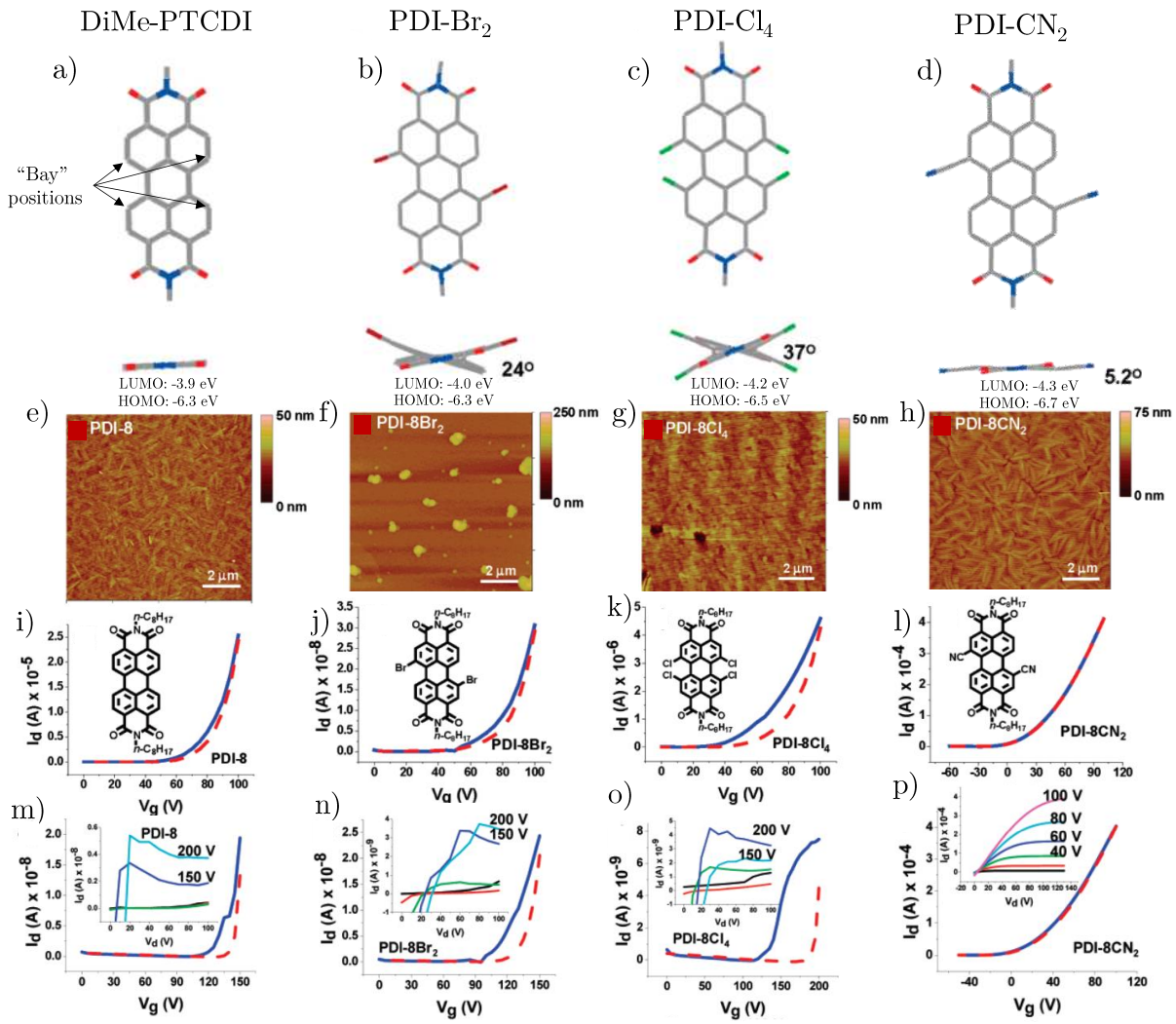

Figure 3-3 Chemical structure of a) DiMe-PTCDI, b) PDI-Br_2, c) PDI-Cl_4 and d) PDI-CN_2 showing the torsional angles of the perylene core, and e-h) their corresponding thin film morphology measured by AFM, in the C_8 lateral chain version, i-l) their transfer curves measured in vacuum and m-p) in air. The torsional angle induced by the function in bay positions can be seen on the morphology of the film, where a flat molecule has a higher probability to form big crystalline domains compared to the twisted one. The transfer curves show how these functionalization help to the air stability, through the changes in the energy levels of the molecules. (Adapted with permission from[7])

3.2.1.3 PDI8-CN_2 and PDIF-CN_2

In the chapter 5, we have focussed our attention to two PDI derivatives as ideal systems to study their charge transport properties. The ad-hoc design to guarantee good compromise in terms of solubility in a common organic solvent, electronic properties, and air-stability led us to the use of N'-bis(perfluorobutyl)-(1,7&1,6)-dicyanoperylene-3,4:9,10-bis(dicarboximide)

(also called PDIF-CN_2) and the N-N'-bis(n-octyle)-(1,7&1,6)-dicyanoperylene-3,4:9,10-bis(dicarboximide) (or PDI8-CN_2) portrayed in Figure 3-4.

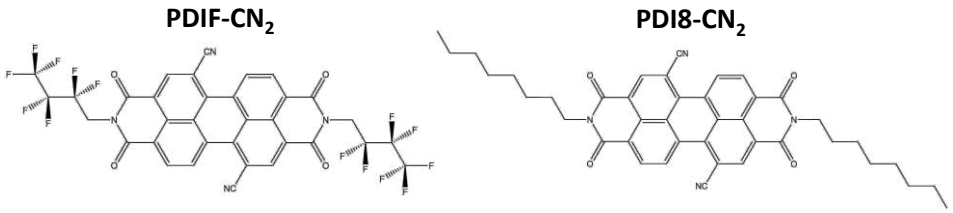

Figure 3-4 Chemical structure of PDIF-CN_2 and PDI8-CN_2.

PDIF-CN_2 [8–12] and PDI8-CN_2 [13–18] are two well-known air-stable semiconductors exhibiting electron mobilities close to 1 $cm^2V^{-1}s^{-1}$. They also do not suffer from bias stress,[19–22] thus being ideal systems for charge transport studies.

3.2.2 BTBT

Molecules derived from [1]benzothieno[3,2-b][1]benzothiophene (BTBT, Figure 3-5 a)) have demonstrated to be particularly suitable for OFET application, since they potentially exhibit mobilities higher than 10 $cm^2V^{-1}s^{-1}$.[23] These structures are known since 1950,[24] but were firstly designed to generate liquid crystalline materials.[25] It's only in early 2000 that this class of molecule was integrated as semiconducting material in a FET with high hole mobilities.[26] Their unique herringbone packing, almost independently to the substituents attached to the BTBT core, represents 2D percolation pathways for charge transport.[27,28] Early uses of BTBT derivatives relied on vacuum processing in thin films.

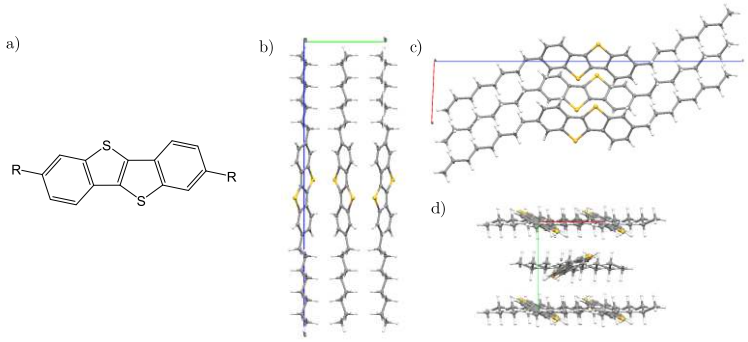

Figure 3-5 a) chemical structure of a BTBT unit. Crystal structure of C_8-BTBT along the b) a, c) b and d) c directions (structure 679293 on the CSD)[29].

Similarly to PDIs, BTBT suffers from good solubility in common organic solvents. Here also, the introduction of the adequate lateral chain leads to an improvement to their solubilisation.[30] Two of the most famous are C_8-BTBT and C_{12}-BTBT, having an 8 carbons and 12 carbons long alkyl chain, respectively. Remarkably, they exhibit hole mobilities, depending of the configuration of the device, up to 43 $cm^2V^{-1}s^{-1}$.[29,31,32]

In the chapter 8, a BTBT (Figure 3-6) with polyethylene glycol chains (PEG), synthesized by the team of Prof. Y. H. Geerts, has been employed for humidity sensing applications.

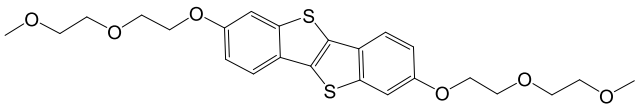

Figure 3-6 Chemical structure of the PEG-BTBT.

3.3 Hybrid materials

Hybrid materials are resulting from the combination of two or more different components, and exhibit properties which differ from those of the individual components. If the properties of both moiety are unchanged, the resulting material is classified as nanocomposite instead of hybrid.[33]

3.3.1 Organic-Inorganic perovskite structure

The word perovskite was initially used for calcium titanate $CaTiO_3$, but later it has been employed for inorganic generic ABX_3 structures, ideally displaying a cubic geometry, with A and B being cations, and X is an anion. In 1995, Wang et al. synthesized a series of hybrid organic-inorganic compounds, based on this perovskite structure, wherein A was an organic species.[34] Based on the size of this organic moiety, the dimensionality of the perovskite can be strongly affected,[35] from a 3D network when a small cation is used to lower dimensionality for the bigger cations (Figure 3-7), yielding a drastic change of the properties of the initial 3D compound.[36]

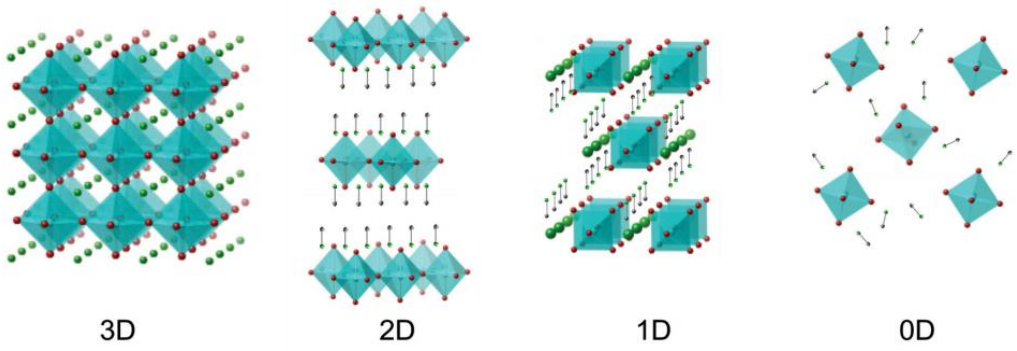

Figure 3-7 Sketch of perovskite structures with different dimensionalities.(Reproduced with permission from[35])

In the chapter 7, the electrical properties in a hybrid perovskite, the methylammonium lead iodine $CH_3NH_3PbI_3$ (Figure 3-8) were explored for oxygen sensing applications.

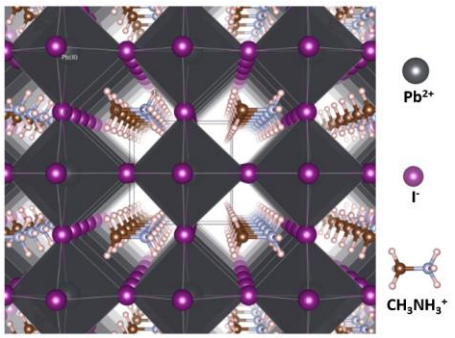

Figure 3-8 Ideal cubic structure of $CH_3NH_3PbI_3$.

3.3.2 Methylammonium lead iodide properties

With a bandgap between 1.5 eV and 2.3 eV, this perovskite is commonly used in solar cells, for the first time by Grätzel et al.[37] after the discovery of their photoelectrical properties by Miyasaka[38] in 2009, or its use in photodetectors.[39] It is noteworthy to say that Snaith employed for the first time a similar hybrid perovskite with a mix of chlorine and iodine atoms, in solar cells application, almost one year before Grätzel.[40] This compound sparked the interest of the scientific community, due to its high power conversion efficiency close to 20%, even on a large area.[41] Moreover, this hybrid organic inorganic perovskite can be easily synthesized and processed at relatively low temperature. Despite their wide use in solar cells, this compound has not been extensively employed as active semiconductor in FETs yet. Its mobility was evaluated around 50 $cm^2V^{-1}s^{-1}$ by Hall measurements,[42] and theoretical studies[43] predicts mobilities up to 10^3 $cm^2V^{-1}s^{-1}$. One important thing to deal with this compound is its instability to many boundary conditions.[44] Humidity is of paramount importance to the degradation process of this perovskite, due to the formation of the hydrated species $(CH_3NH_3)_4PbI_6.2H_2O$, which displays poor electrical properties.[45] A combination of oxygen and UV exposure is also believed to degrade the perovskite into methylamine, lead iodide, dihydrogen and iodine.[46] It is also suggested that this compound can be simply photo-degraded under UV,[47] and starts to decompose when subject to a temperature higher than 85 °C.[48] Beside this, theoretical calculations put forward the possible thermodynamically intrinsic instability of this perovskite.[49]

3.4 2D materials

2D materials are defined by a layer of atoms forming a coherent structure within a plane. They can be either an allotrope of a specific element (graphene is an allotrope of carbon), or a compound by itself, made by different elements (such as the transition metal dichalcogenides). Due to their electronic confinement and structural order, these materials potentially exhibit different properties with respect to their bulk equivalent. The strong interest of the scientific community to 2D materials mostly started in 2004, with the first exfoliation of graphene.[50]

3.4.1 Graphene

As defined by the International Union of Pure and Applied Chemistry (IUPAC), a graphene layer is "a single carbon layer of the graphite structure, describing its nature by analogy to a polycyclic aromatic hydrocarbon of quasi infinite size. The term graphene should be used only when the reactions, structural relations or other properties of individual layers are discussed".[51] Even if the word graphene was define around 1990,[52] this material was observed more than 20 years sooner[53] and explored theoretically before 1950.[54] The interest for this material reappeared at the beginning of 2000, when a simple way to produce high quality graphene has been developed through mechanical exfoliation by using scotch tape[50], for which K. Novoselov and A. Geim received the Nobel prize in Physics in 2010 for unravelling the exceptional physical properties of this material. Later on, huge efforts have been made to improve the production of high quality graphene though diverse approaches such as the liquid phase and electrochemical exfoliation[55] or by chemical vapour deposition, which still suffer from a very low rate of production.[56]

3.4.1.1 Chemical structure

Graphene is a one atom thick material composed by sp^2 carbons arranged in a 2D hexagonal lattice (Figure 3-9). The superposition of graphene flakes, driven by van der Waals interactions, leads to the well-known graphite, already used as electrode because of its low electrical resistance, or simply as pencils.[57]

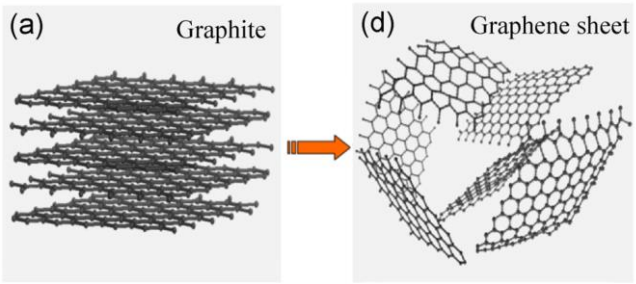

Figure 3-9 Schematic of graphite, converted to graphene sheets after exfoliation (Adapted with permission from[58]).

3.4.1.2 Electronic structure

The electronic structure of graphene can be described as a semi-metal. This means that its valence and conduction bands are meeting at the precise energy point,[59] called the Dirac point (Figure 3-10), located on six momentum space on the Brillouin zone, that can be described as two interpenetrated triangular lattice, forming the two sets of valley called *K* and *K'*.

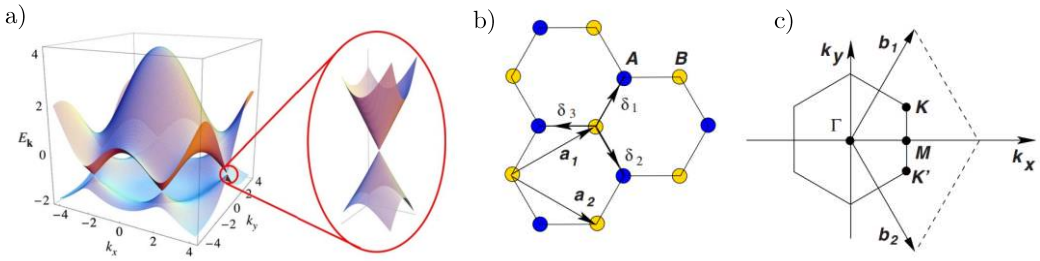

Figure 3-10 a) Electronic dispersion in the hexagonal graphene lattice. b) Sketch of the lattice structure showing the equivalent carbon atoms (A and B) in graphene and c) the corresponding Brillouin zone with the Dirac cones located at the *K* and *K'* points (Reproduced with permission from[59]).

For an undoped pristine graphene flake, the Fermi level will be located at these Dirac points, where its electrical resistance will be the highest (Figure 3-11), but a slight shift of the Fermi level will immediately populate the valence or conduction band, leading to a decrease of the material's resistance. This has a direct consequence on the electrical performances of graphene as active material into a field-effect transistor, because all the principle of a transistor is based on capability of the active material to switch from an ON state to an OFF state, forming a 2-level logic device. However, since graphene is almost never OFF, the distinction between the two states is hardly distinguishable, and thus not usable as its pristine form for such device applications, even if this material can present extremely high mobilities up to 200 000 $cm^2V^{-1}s^{-1}$ for both charge carriers at room temperature.[60]

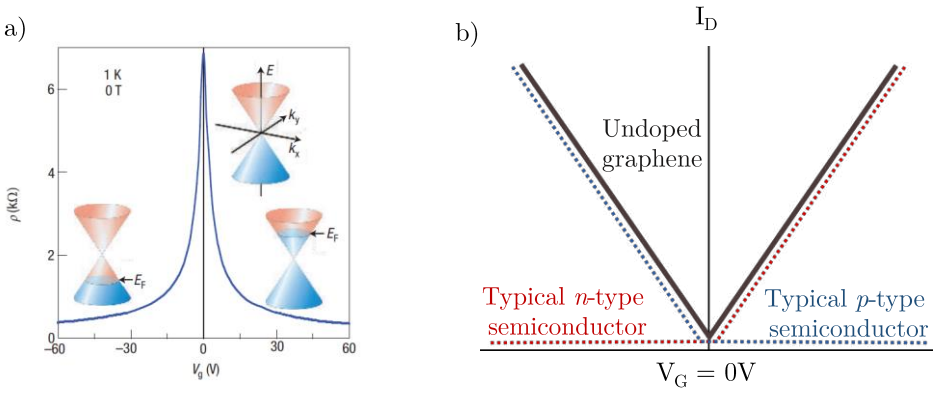

Figure 3-11 a) Field-effect induced doping of a graphene flake as function of its resistivity, showing the position of the Fermi level at the Dirac point (Reproduced with permission from[61]). b) Sketch of the decomposition of a graphene transfer curve into the overlapping of *n*- and *p*- type transports, demonstrating the absence of OFF state.

In the chapter 6, graphene has been used as a platform to study the doping induced by small molecular dopants.

3.4.2 Transition metal dichalcogenides

Following the outstanding properties measured on mechanically exfoliated graphene in 2004, this approach has been extended to the preparation of mono and multilayers from other types of layered materials such as the transition metal dichalcogenides (TMD).[62] While such class of monolayer material is known for more than 50 years it was mostly investigated as bulk materials.[63]

3.4.2.1 Structure and electrical properties

TMDs are described by a MX_2 structure, where typically M represents a transition metal atom, surrounded by two chalcogen atoms X (Figure 3-12). Among all the transition metal, only few of them can form layered structures that can be exfoliated. Depending of the chemical composition, these materials exhibit also in their bulk form diverse properties such as superconductivity, semiconductivity or metallic behaviour.[64] Due to their atomic thickness, the semiconducting TMDs are the most credible alternatives for the tomorrow's FET, because

of their high sensibility to the electrostatic environment controlled by the gate electrode. Among the TMD exhibiting semiconducting properties, MoS_2 has been the most studied after the demonstration of its excellent electrical properties as active material in a FET,[65] with rather high mobilities up to 60 $cm^2V^{-1}s^{-1}$ and high I_{on}/I_{off} ratios around 10^8.

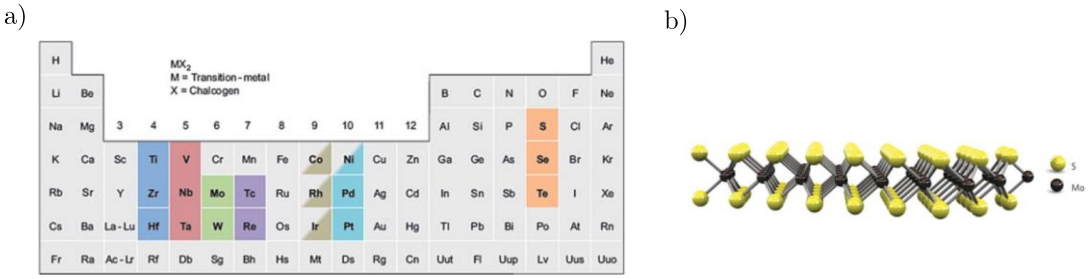

Figure 3-12 a) Periodic table where the elements favourable to describe the MX_2 structure are highlighted. b) example of the structure of a MoS_2 monolayer (Reproduced with permission from[66]).

It is important to note that different phases exist within the TMDs (Figure 3-13).[67] These structural differences can be seen as the superposition of three atomic planes, where the trigonal prismatic phase (2H) is described by an ABA stacking. If one of the layers is reversed, forming an ABC structure, such arrangement is called distorted octahedral (1T) phase. In some cases, if the distortion is too pronounced, another phase can be reached, through the formation of inter-metal bonds, resulting in the dimerized phase (1T').

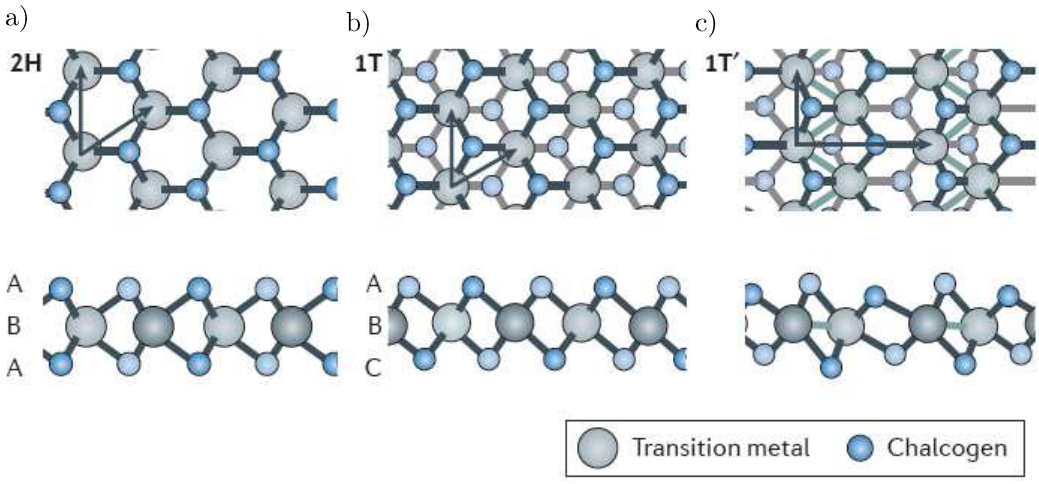

Figure 3-13 Structure of a TMD layer in a) a trigonal prismatic (2H), b) distorted octahedral (1T) and dimerized (1T') phases (Reproduced with permission from[67]).

The phase of a TMD is widely changing its properties, because affecting the whole energy landscape of the material. For example, the thermodynamically stable 2H-MoS_2 phase exhibits semiconducting properties while the 1T-MoS_2 one is metallic.[68]

3.4.2.2 Band diagram

One important difference between the bulk and the monolayer form of almost all the TMD is the transition from an indirect to a direct gap, allowing the apparition of luminescence properties (Figure 3-14).[69,70] This behaviour is due the interlayer coupling into the TMD structure.[71,72] This interlayer coupling can be, as said before, detected by photoluminescence measurements, but other techniques, such as Raman spectroscopy, can be used. Indeed, the change in interlayer coupling is slightly affecting the lattice vibration of the structure through the perturbation of the electronic density of the material.[73] These techniques are widely used to quickly characterize an exfoliated structure as a monolayer or thicker material, without the need of employing a microscopy technique such as an atomic force microscopy (AFM) analysis.[74,75] It is noteworthy to mention that it is possible to get rid of the indirect bandgap, even in multi-layers TMD, by using suitable device geometry such an electric-double-layer transistor (EDLT) configuration,[76] because of the high electric field applied through the structure, which is affecting the energy landscape of the material.

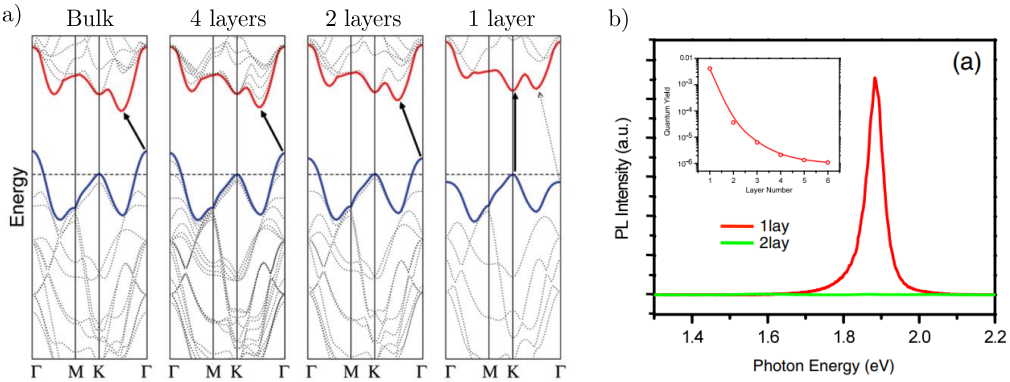

Figure 3-14 a) Band structure of MoS_2 at different thickness, showing the transition from indirect to direct band-gap (Reproduced with permission from[69]) and b) photoluminescence spectra from mono and bilayers of MoS_2. (Reproduced with permission from[70]).

3.4.2.3 Tungsten diselenide

In the chapter 6, in complement to graphene, tungsten diselenide (WSe_2) has been used to study the doping effect of molecular dopants. With a bandgap of 1.6 eV, WSe_2 is thermodynamically stable in the 2H phase.[77] Air-stable, this material exhibits good electrical performances when employed with uncommon materials or in complicated structures.[76,78–81] Potentially ambipolar, only few examples of *p* and *n* types of transport are reported on the same device.[82–85] Because of the relative position of its energy levels that are closer to the vacuum level compared to other TMD,[86] the choice of the metal for the charge injection in WSe_2 is particularly detrimental on the good performances and the type of carrier injected.[81] Typically, to get good electrical performances with WSe_2, palladium contacts are used[87], with high-*k* dielectric such as Al_2O_3 or ZrO_2,[78,80] measured on few-layered,[79,88], or with a dual-gate or liquid gating approach.[76,83]

3.5 References

[1] K. Tojo, J. Mizuguchi, *Zeitschrift für Kristallographie - New Crystal Structures* **2002**, *217*, 255.
[2] E. Hädicke, F. Graser, *Acta Cryst C* **1986**, *42*, 189.
[3] H. Langhals, *HETEROCYCLES* **1995**, *40*, 477.
[4] A. L. Briseno, S. C. B. Mannsfeld, C. Reese, J. M. Hancock, Y. Xiong, S. A. Jenekhe, Z. Bao, Y. Xia, *Nano Lett.* **2007**, *7*, 2847.
[5] J. Gao, C. Xiao, W. Jiang, Z. Wang, *Organic Letters* **2014**, *16*, 394.
[6] R. Schmidt, M. M. Ling, J. H. Oh, M. Winkler, M. Könemann, Z. Bao, F. Würthner, *Adv. Mater.* **2007**, *19*, 3692.
[7] B. A. Jones, A. Facchetti, M. R. Wasielewski, T. J. Marks, *Journal of the American Chemical Society* **2007**, *129*, 15259.
[8] A. S. Molinari, H. Alves, Z. Chen, A. Facchetti, A. F. Morpurgo, *J. Am. Chem. Soc.* **2009**, *131*, 2462.
[9] R. Colle, G. Grosso, A. Cassinese, R. Centore, *The Journal of Chemical Physics* **2013**, *139*, 114507.
[10] F. Chiarella, T. Toccoli, M. Barra, L. Aversa, F. Ciccullo, R. Tatti, R. Verucchi, S. Iannotta, A. Cassinese, *Applied Physics Letters* **2014**, *104*, 143302.
[11] K. Willa, R. Haeusermann, T. Mathis, A. Facchetti, Z. Chen, B. Batlogg, *Journal of Applied Physics* **2013**, *113*, 133707.
[12] M. Barra, D. Viggiano, P. Ambrosino, F. Bloisi, F. V. Di Girolamo, M. V. Soldovieri, M. Taglialatela, A. Cassinese, *Biochimica Et Biophysica Acta-General Subjects* **2013**, *1830*, 4365.
[13] F. Liscio, S. Milita, C. Albonetti, P. D'Angelo, A. Guagliardi, N. Masciocchi, R. G. Della Valle, E. Venuti, A. Brillante, F. Biscarini, *Adv. Funct. Mater.* **2012**, *22*, 943.
[14] J. Rivnay, L. H. Jimison, J. E. Northrup, M. F. Toney, R. Noriega, S. Lu, T. J. Marks, A. Facchetti, A. Salleo, *Nature Materials* **2009**, *8*, 952.
[15] F. Ciccullo, L. Santamaria, E. Orabona, A. Cassinese, P. Maddalena, S. Lettieri, *New Journal of Physics* **2014**, *16*, 093036.
[16] C. Keil, H. Graaf, T. Baumgärtel, I. Trenkmann, D. Schlettwein, *Organic Electronics* **2013**, *14*, 2833.
[17] M. Li, T. Marszalek, Y. Zheng, I. Lieberwirth, K. Müllen, W. Pisula, *ACS Nano* **2016**, *10*, 4268.

[18] M. Barra, F. V. D. Girolamo, F. Chiarella, M. Salluzzo, Z. Chen, A. Facchetti, L. Anderson, A. Cassinese, *J. Phys. Chem. C* **2010**, *114*, 20387.
[19] H. T. Yi, Z. Chen, A. Facchetti, V. Podzorov, *Adv. Funct. Mater.* **2015**, n/a.
[20] M. Barra, F. V. Di Girolamo, N. A. Minder, I. G. Lezama, Z. Chen, A. Facchetti, A. F. Morpurgo, A. Cassinese, *Applied Physics Letters* **2012**, *100*, 133301.
[21] F. V. Di Girolamo, F. Ciccullo, M. Barra, A. Carella, A. Cassinese, *Organic Electronics* **2012**, *13*, 2281.
[22] I. A. Grimaldi, M. Barra, A. Carella, F. V. Di Girolamo, F. Loffredo, C. Minarini, F. Villani, A. Cassinese, *Synthetic Metals* **2013**, *176*, 121.
[23] K. Takimiya, I. Osaka, T. Mori, M. Nakano, *Acc. Chem. Res.* **2014**, *47*, 1493.
[24] A. W. Horton, *The Journal of Organic Chemistry* **1949**, *14*, 761.
[25] S. Méry, D. Haristoy, J.-F. Nicoud, D. Guillon, S. Diele, H. Monobe, Y. Shimizu, *Journal of Materials Chemistry* **2002**, *12*, 37.
[26] K. Takimiya, H. Ebata, K. Sakamoto, T. Izawa, T. Otsubo, Y. Kunugi, *Journal of the American Chemical Society* **2006**, *128*, 12604.
[27] D. E. Martínez-Tong, G. Gbabode, C. Ruzié, B. Chattopadhyay, G. Schweicher, A. R. Kennedy, Y. H. Geerts, M. Sferrazza, *RSC Advances* **2016**, *6*, 22.
[28] Y. Tsutsui, G. Schweicher, B. Chattopadhyay, T. Sakurai, J.-B. Arlin, C. Ruzié, A. Aliev, A. Ciesielski, S. Colella, A. R. Kennedy, V. Lemaur, Y. Olivier, R. Hadji, L. Sanguinet, F. Castet, S. Osella, D. Dudenko, D. Beljonne, J. Cornil, P. Samorì, S. Seki, Y. H. Geerts, *Advanced Materials* **2016**, *28*, 7106.
[29] T. Izawa, E. Miyazaki, K. Takimiya, *Advanced Materials* **2008**, *20*, 3388.
[30] H. Ebata, T. Izawa, E. Miyazaki, K. Takimiya, M. Ikeda, H. Kuwabara, T. Yui, *J. Am. Chem. Soc.* **2007**, *129*, 15732.
[31] H. Minemawari, T. Yamada, H. Matsui, J. Tsutsumi, S. Haas, R. Chiba, R. Kumai, T. Hasegawa, *Nature* **2011**, *475*, 364.
[32] Y. Yuan, G. Giri, A. L. Ayzner, A. P. Zoombelt, S. C. B. Mannsfeld, J. Chen, D. Nordlund, M. F. Toney, J. Huang, Z. Bao, *Nature Communications* **2014**, *5*, 1.
[33] G. L. Drisko, C. Sanchez, *European Journal of Inorganic Chemistry* **2012**, *2012*, 5097.
[34] S. Wang, D. B. Mitzi, C. A. Feild, A. Guloy, *J. Am. Chem. Soc.* **1995**, *117*, 5297.
[35] S. González-Carrero, R. E. Galian, J. Pérez-Prieto, *Particle & Particle Systems Characterization* **2015**, *32*, 709.
[36] X. Yang, X. Zhang, J. Deng, Z. Chu, Q. Jiang, J. Meng, P. Wang, L. Zhang, Z. Yin, J. You, *Nature Communications* **2018**, *9*, 570.
[37] J. H. Noh, N. J. Jeon, Y. C. Choi, M. K. Nazeeruddin, M. Grätzel, S. I. Seok, *J. Mater. Chem. A* **2013**, *1*, 11842.
[38] A. Kojima, K. Teshima, Y. Shirai, T. Miyasaka, *J. Am. Chem. Soc.* **2009**, *131*, 6050.
[39] H.-R. Xia, J. Li, W.-T. Sun, L.-M. Peng, *Chem. Commun.* **2014**, *50*, 13695.
[40] M. M. Lee, J. Teuscher, T. Miyasaka, T. N. Murakami, H. J. Snaith, *Science* **2012**, *338*, 643.
[41] X. Li, D. Bi, C. Yi, J.-D. Décoppet, J. Luo, S. M. Zakeeruddin, A. Hagfeldt, M. Grätzel, *Science* **2016**, *353*, 58.
[42] C. C. Stoumpos, C. D. Malliakas, M. G. Kanatzidis, *Inorganic Chemistry* **2013**, *52*, 9019.
[43] Y. Wang, Y. Zhang, P. Zhang, W. Zhang, *Phys. Chem. Chem. Phys.* **2015**, *17*, 11516.
[44] Z. Zhu, Q. Sun, Z. Zhang, J. Dai, G. Xing, S. Li, X. Huang, W. Huang, *Journal of Materials Chemistry C* **2018**, *6*, 10121.
[45] A. M. A. Leguy, Y. Hu, M. Campoy-Quiles, M. I. Alonso, O. J. Weber, P. Azarhoosh, M. van Schilfgaarde, M. T. Weller, T. Bein, J. Nelson, P. Docampo, P. R. F. Barnes, *Chem. Mater.* **2015**, *27*, 3397.
[46] G. Niu, W. Li, F. Meng, L. Wang, H. Dong, Y. Qiu, *J. Mater. Chem. A* **2013**, *2*, 705.
[47] J. Schoonman, *Chemical Physics Letters* **2015**, *619*, 193.
[48] B. Conings, J. Drijkoningen, N. Gauquelin, A. Babayigit, J. D'Haen, L. D'Olieslaeger, A. Ethirajan, J. Verbeeck, J. Manca, E. Mosconi, F. D. Angelis, H.-G. Boyen, *Advanced Energy Materials* **2015**, *5*, 1500477.
[49] Y.-Y. Zhang, S. Chen, P. Xu, H. Xiang, X.-G. Gong, A. Walsh, S.-H. Wei, *Chinese Physics Letters* **2018**, *35*, 036104.
[50] K. S. Novoselov, *Science* **2004**, *306*, 666.
[51] E. Fitzer, K.-H. Kochling, H. P. Boehm, H. Marsh, *Pure and Applied Chemistry* **1995**, *67*, 473.
[52] H. P. Boehm, R. Setton, E. Stumpp, *Pure and Applied Chemistry* **1994**, *66*, 1893.

[53] H. P. Boehm, A. Clauss, G. O. Fischer, U. Hofmann, *Zeitschrift für anorganische und allgemeine Chemie* **1962**, *316*, 119.

[54] P. R. Wallace, *Physical Review* **1947**, *71*, 622.

[55] M. Yi, Z. Shen, *Journal of Materials Chemistry A* **2015**, *3*, 11700.

[56] R. Raccichini, A. Varzi, S. Passerini, B. Scrosati, *Nature Materials* **2015**, *14*, 271.

[57] F. J. Vosburgh, *Electrical Engineering* **1933**, *52*, 844.

[58] M. Xu, H. Sun, C. Shen, S. Yang, W. Que, Y. Zhang, X. Song, *Nano Research* **2015**, *8*, 801.

[59] A. H. Castro Neto, F. Guinea, N. M. R. Peres, K. S. Novoselov, A. K. Geim, *Reviews of Modern Physics* **2009**, *81*, 109.

[60] S. V. Morozov, K. S. Novoselov, M. I. Katsnelson, F. Schedin, D. C. Elias, J. A. Jaszczak, A. K. Geim, *Physical Review Letters* **2008**, *100*, 1.

[61] A. K. Geim, K. S. Novoselov, *Nature Materials* **2007**, *6*, 183.

[62] K. S. Novoselov, D. Jiang, F. Schedin, T. J. Booth, V. V. Khotkevich, S. V. Morozov, A. K. Geim, *PNAS* **2005**, *102*, 10451.

[63] R. Fivaz, E. Mooser, *Phys. Rev.* **1967**, *163*, 743.

[64] J. A. Wilson, A. D. Yoffe, *Advances in Physics* **1969**, *18*, 193.

[65] B. Radisavljevic, A. Radenovic, J. Brivio, V. Giacometti, A. Kis, *Nature Nanotechnology* **2011**, *6*, 147.

[66] M. Pumera, A. H. Loo, *TrAC Trends in Analytical Chemistry* **2014**, *61*, 49.

[67] S. Manzeli, D. Ovchinnikov, D. Pasquier, O. V. Yazyev, A. Kis, *Nature Reviews Materials* **2017**, *2*, 17033.

[68] R. Kappera, D. Voiry, S. E. Yalcin, B. Branch, G. Gupta, A. D. Mohite, M. Chhowalla, *Nature Materials* **2014**, *13*, 1128.

[69] A. Splendiani, L. Sun, Y. Zhang, T. Li, J. Kim, C.-Y. Chim, G. Galli, F. Wang, *Nano Lett.* **2010**, *10*, 1271.

[70] K. F. Mak, C. Lee, J. Hone, J. Shan, T. F. Heinz, *Phys. Rev. Lett.* **2010**, *105*, 136805.

[71] Y. Sun, D. Wang, Z. Shuai, *The Journal of Physical Chemistry C* **2016**, *120*, 21866.

[72] Z. Shi, X. Wang, Y. Sun, Y. Li, L. Zhang, *Semicond. Sci. Technol.* **2018**, *33*, 093001.

[73] L. Liang, J. Zhang, B. G. Sumpter, Q.-H. Tan, P.-H. Tan, V. Meunier, *ACS Nano* **2017**, *11*, 11777.

[74] A. C. Ferrari, D. M. Basko, *Nature Nanotechnology* **2013**, *8*, 235.

[75] X.-L. Li, W.-P. Han, J.-B. Wu, X.-F. Qiao, J. Zhang, P.-H. Tan, *Advanced Functional Materials* **2017**, *27*, 1604468.

[76] Y. J. Zhang, T. Oka, R. Suzuki, J. T. Ye, Y. Iwasa, *Science* **2014**, *344*, 725.

[77] J. Gusakova, X. Wang, L. L. Shiau, A. Krivosheeva, V. Shaposhnikov, V. Borisenko, V. Gusakov, B. K. Tay, *physica status solidi (a)* **2017**, *214*, 1700218.

[78] C.-H. Chen, C.-L. Wu, J. Pu, M.-H. Chiu, P. Kumar, T. Takenobu, L.-J. Li, *2D Materials* **2014**, *1*, 034001.

[79] H. C. P. Movva, A. Rai, S. Kang, K. Kim, B. Fallahazad, T. Taniguchi, K. Watanabe, E. Tutuc, S. K. Banerjee, *ACS Nano* **2015**, *9*, 10402.

[80] H. Fang, S. Chuang, T. C. Chang, K. Takei, T. Takahashi, A. Javey, *Nano Lett.* **2012**, *12*, 3788.

[81] W. Liu, J. Kang, D. Sarkar, Y. Khatami, D. Jena, K. Banerjee, *Nano Letters* **2013**, *13*, 1983.

[82] S. Das, J. Appenzeller, *Applied Physics Letters* **2013**, *103*, 103501.

[83] J.-K. Huang, J. Pu, C.-L. Hsu, M.-H. Chiu, Z.-Y. Juang, Y.-H. Chang, W.-H. Chang, Y. Iwasa, T. Takenobu, L.-J. Li, *ACS Nano* **2014**, *8*, 923.

[84] H.-J. Chuang, X. Tan, N. J. Ghimire, M. M. Perera, B. Chamlagain, M. M.-C. Cheng, J. Yan, D. Mandrus, D. Tománek, Z. Zhou, *Nano Letters* **2014**, *14*, 3594.

[85] V. Podzorov, M. E. Gershenson, C. Kloc, R. Zeis, E. Bucher, *Applied Physics Letters* **2004**, *84*, 3301.

[86] C. Zhang, C. Gong, Y. Nie, K.-A. Min, C. Liang, Y. J. Oh, H. Zhang, Weihua Wang, S. Hong, L. Colombo, R. M. Wallace, K. Cho, *2D Mater.* **2017**, *4*, 015026.

[87] D. Li, X. Wang, Y. Chen, S. Zhu, F. Gong, G. Wu, C. Meng, L. Liu, L. Wang, Tie Lin, S. Sun, H. Shen, X. Wang, W. Hu, J. Wang, J. Sun, X. Meng, J. Chu, *Nanotechnology* **2018**, *29*, 105202.

[88] Y. Ma, B. Liu, A. Zhang, L. Chen, M. Fathi, C. Shen, A. N. Abbas, M. Ge, M. Mecklenburg, C. Zhou, *ACS Nano* **2015**, *9*, 7383.

Chapter 4 Experimental techniques

4.1 Device fabrication

4.1.1 Substrate preparation

The substrates used for the fabrication of bottom-gate field-effect transistor were purchased from the Fraunhofer Institute. They are composed by a layer of thermally grown amorphous SiO_2 on a heavily doped Si surface. Two different SiO_2 thicknesses were used: 230 nm that results to a dielectric capacitance of 15 nF/cm^2, and 90 nm thick, leading to a 40 nF capacitance. Even if the 90 nm thick substrates would increase the probability of current leakage, the change in the optical contrast helps for the localization of exfoliated 2D materials[1,2]. Bottom-contact geometry were provided only on 230 nm thick SiO_2 substrates, through prepatterned devices with interdigitated electrodes for the source and drain. These electrodes consist of 10 nm of ITO covered by 30 nm of Au and form four groups of devices with the same channel width (W = 1 cm) but different channel lengths (L = 2.5, 5, 10 and 20 µm). In all cases, the substrates were provided with a hexamethyldisilazane (HMDS) treatment of SiO_2 and covered by a photoresist layer with the purpose to avoid silicon debris contamination during the dicing of the wafer.

The as-received substrates have first been rinsed with acetone to roughly remove the photoresist, followed by a cleaning in acetone for 20 min in an ultrasonic bath. The samples are then gently dried under a gentle nitrogen flow, and cleaned again for 20 min in isopropanol, back in the ultrasonic bath. The substrates are ultimately dried, under a flow of nitrogen. If needed, the HMDS layer can be removed through an exposure of the substrate to UV-Ozone, as discussed in the following section.

4.1.1.1 UV-Ozone cleaning

In some cases, the cleaning of the substrates can be carried out by a UV-Ozone cleaning (Novascan PSD), which consists (Figure 4-1) of their irradiation with a mercury lamp producing short UV wavelengths (λ = 184.7 nm and 253.7 nm) in presence of oxygen during 5 to 20 min. The first wavelength interacts with oxygen molecules to create free radicals and ozone while the second wavelength interacts with the formed radicals that subsequently, reacts with the adsorbed molecules on the surface thereby decomposing them into simple gaseous molecules such as CO_2 or H_2O. This technique is crucial for the substrate cleaning of adsorbed molecules as well as for pre-treated surfaces but it also allows also to activate SiO_2 via the formation of hydroxyl groups at the surface, that are critical for the growth of self-assembled monolayers, as described in the following paragraph.

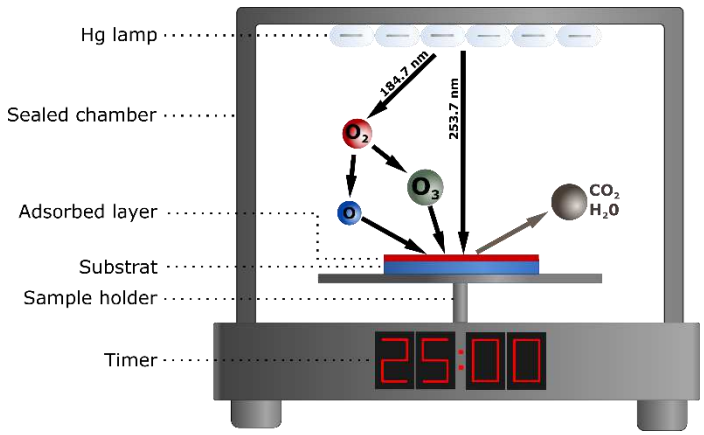

Figure 4-1 Sketch and working principle of a UV-Ozone cleaner.

4.1.1.2 Self-assembled-monolayer growth

Suitably designed molecules can be organized on solid flat surfaces to form self-assembled monolayers (SAMs). Upon operating under thermodynamic control, highly ordered polycrystalline SAMs can be produced. By design, molecules need to comprise an anchoring group capable of chemisorbing on the chosen substrate, and a core which can interact with adjacent analogues via non-covalent forces like van der Waals, to stabilise the monolayer, and

a head group to modulate the polarity and wettability of the monolayer[3] as well as its work function, because of the local dipole induced by the molecules themselves.[4,5] As anchoring group, a silane terminated moiety is needed to bind the SiO_2 surface[6] while a thiol terminated function can be used to covalent tethering to gold.

Octadecyltrichlorosilane (OTS) has been extensively used because of its high hydrophobic nature without inducing almost any doping effect the semiconductor deposited on its top.[9] (2-Cyanoethy)triethoxysilane (TESPN), trichloro(1H,1H,2H,2H-perfluorooctyl)silane (PFS) and N-[3-(Trimethoxysilyl)propyl]ethylenediamine (AHAPS) have been used similarly than OTS to functionalize the surfaces, as described in the chapter 6, yet the change of the head group can yield modification of the surface properties.

Similarly, thiolated SAMs can be used to functionalize gold electrodes because of the strong sulphur-gold interaction, leading to a change in the electrodes wettability, but most importantly, to a shift of their work function. For the gold electrodes treatment, 1H,1H,2H,2H-perfluorodecanethiol (F-SAM) and 1-decanethiol (H-SAM) were used, as described chapter 7.

4.1.1.3 Electrodes deposition

In order to deposit top-contacts on FET, metallic electrodes need to be evaporated on a semiconducting material as one of the last steps of the device fabrication. This has been done by means of a physical vapor deposition set-up (Plassys ME300B, Figure 4-2). The desired metal is placed as a pellet in a Tungsten crucible and the substrates are fixed on the sample holder with magnets with shadowmasks properly aligned on them. The chamber is then sealed, and the atmosphere is pumped with a rotary pump joints by a turbo pump until an ultra-high vacuum close to 10^{-7} mbar is reached, to ensure less gaseous contaminants adsorbed on the substrate and to prevent any oxidative process on sensible material such as Chromium or Aluminium.

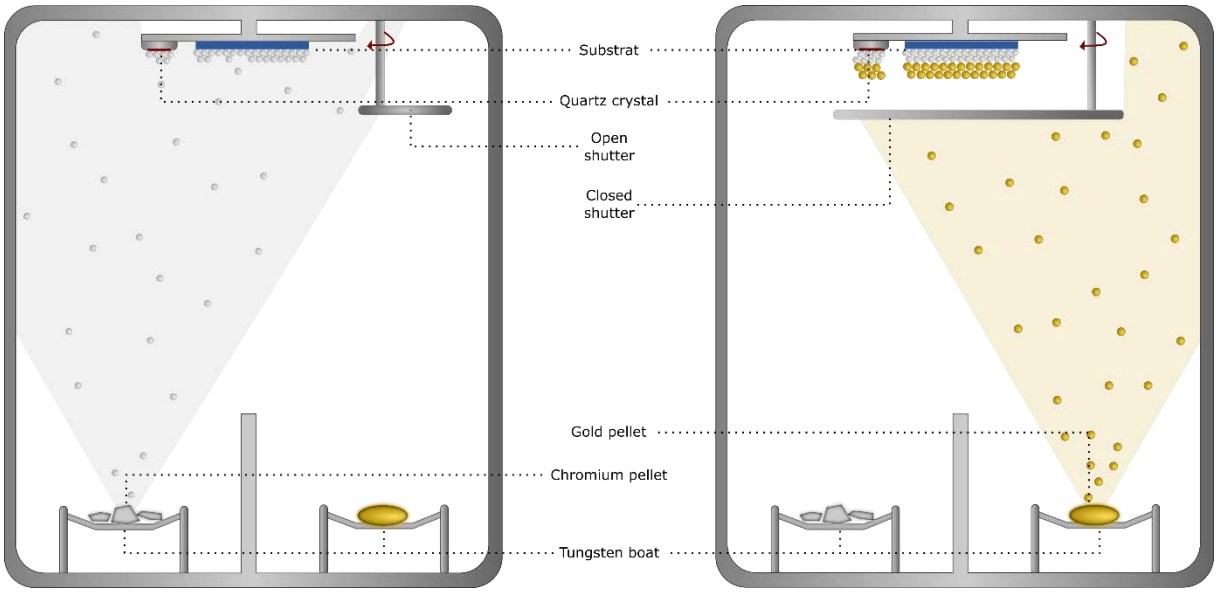

Figure 4-2 Sketch of a physical vapor deposition setup evaporating Cr with the shutter open (left) and Au with the shutter closed (right).

When the low pressure is reached, a high electric current (from 200 A to 300 A) is applied through the Tungsten boat containing the needed metal which, by Joule effect, will heat up. When the temperature is high enough, the metal is vaporized, and it starts to condensate on both the substrate and the shadowmask. The thickness of the deposited layer of metal is accurately monitored through the resonance of a quartz crystal. The evaporation rate was kept around 0.02 $nm.s^{-1}$ for Cr and 0.5 $nm.s^{-1}$ for Au in order to achieve maximum film homogeneity and crystallinity. A good adhesion of gold on SiO_2 is obtained through the evaporation of an intermediate wetting 2 nm thick layer of chromium.

4.1.1.4 Device designed by photolithography

When the commercial shadowmasks available or prepatterned devices are not suitable for the type of measurement needed, i.e. for single crystal devices, photolithography can be employed to pattern on demand unconventional motifs (Figure 4-3). To do so, a positive photoresist, which is water based (AZ1505 from MicroChemicals) is deposited on the substrate surface by spin-coating (3000 rpm, 1000 $rpm.s^{-1}$, 60 s) then annealed at 120 °C for 1 min. The resulting layer is locally irradiated with a laserwriter (LW405-A LaserWriter from Microtech, λ = 405

nm) focalized through a lens for a high precision, with a beam spot close to 2 µm. The energy of the laser beam is typically settled around 1J/cm^2 to optimise the lithography. If the energy is too small, too few photons will reach the photoresist will not be irradiated enough, and the final pattern will be under-developed. Conversely, the use of a too strong intensity will over-irradiate the photoresist, leading to the loss of the initial needed shape. The effect of the irradiation results to an isomerisation and/or cross-polymerization of the polymer composing the photoresist. Upon irradiation, the chemical structure of the molecule used as photoresist is changing, as well as its solubility. Two kinds of photoresists exist, the positive one, based on isomerisation/fragmentation, and the negative one, based on the isomerisation/cross-polymerization of the polymer. Then, for the positive photoresists, it is the irradiated area which is removed during the development step while for the negative photoresists, it is the non-irradiated part which is removed. In our case, we employed a positive photoresist where the irradiated area is soluble in the developer AZ351B Developer from MicroChemicals while the non-irradiated part remains insoluble, which is forming the desired pattern on the substrate.

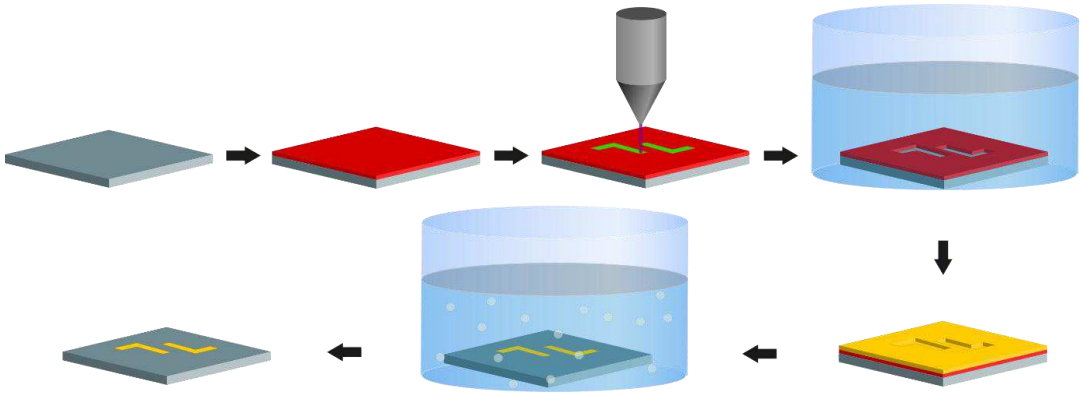

Figure 4-3 Photolithographic process to design a device with a positive photoresist. The cleaned substrate is covered by a spin-coated photoresist layer, the latter is then precisely irradiated with the laser, and the whole substrate is immersed in the developer, where the irradiated part appears, forming the wanted pattern. The needed metal is then evaporated on its surface, and the substrate is immersed in hot acetone to dissolve the remaining photoresist, leaving the wanted pattern on the substrate.

A layer of metal is then evaporated on the developed sample, and the remaining non-irradiated photoresist is washed in a bath of bubbling acetone. Only the metal in physical contact with the substrate stays attached on the substrate while the rest of the metal is removed, leading to the final pattern. If the lithography is made on semiconducting materials, it is required that the developer and the final lift-off bath are orthogonal with the semiconducting material, without damaging it.

4.1.1.5 Shadowmask designed by photolithography

When the photolithography is not compatible with the sample because of wettability problems, the laser writer can be used in infrared mode ($\lambda = 1064$ nm) to selectively heat up some area. When the material is thin enough, such as a TEM grid made of gold, it is possible to cut different shapes in the grid (G1000HSG from Ted Pella, Figure 4-4), leading to a home-made shadowmask that can be aligned with a single crystal or a monolayer of 2D material, and can be used to form two pads separated by a channel length up to 6 µm.

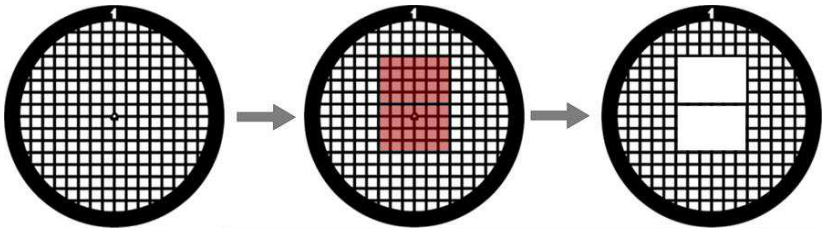

Figure 4-4 Sketch of a TEM grid irradiated (in red) to form a shadowmask.

4.1.1.6 Indium wire as electrical connector

In some cases, to prevent the scratch of the evaporated gold without adhesive layer, or to connect the electrodes with non-conventional connections such as a bare copper wire, small pieces of Indium are used. Due to its low melting point, indium is ductile at room temperature, and can be easily shaped. Pieces of typically 1 mm^2 are produced from indium wire and are pressed in contact with gold. Gold and Indium form an alloy[10] that ensure a good electrical

conduction. Indium is also sticking to Si n++ and can be used to electrically connect the gate electrode.

4.1.2 Deposition processes

4.1.2.1 Spin-coating and drop-casting

Spin-coating is the technique of choice in order to form thin and homogenous films from a wet approach (Figure 4-5). The substrate is fixed with vacuum to a rotary plate. Typically, from 80 µL to 160 µL of the solution containing the targeted molecule are deposited on a 1.5 cm x 1.5 cm substrate. Parameters are defined in the way that the plate starts to spin at a certain speed (from 100 rpm to 5000 rpm), with a precise acceleration (from 50 $rpm.s^{-1}$ to 10000 $rpm.s^{-1}$) during a defined time (from 5 s to 60 s). During the acceleration, the drop of solution that was initially placed in the center of the substrate gets spread due to the centrifugal forces initiated by the rotation while the speed will help to evaporate the solvent. The thickness of the final film is directly related to the parameters used for the spin-coating, the wettability of the substrate and the concentration of the solution used, the latter impacting the viscosity of the solution.[11]

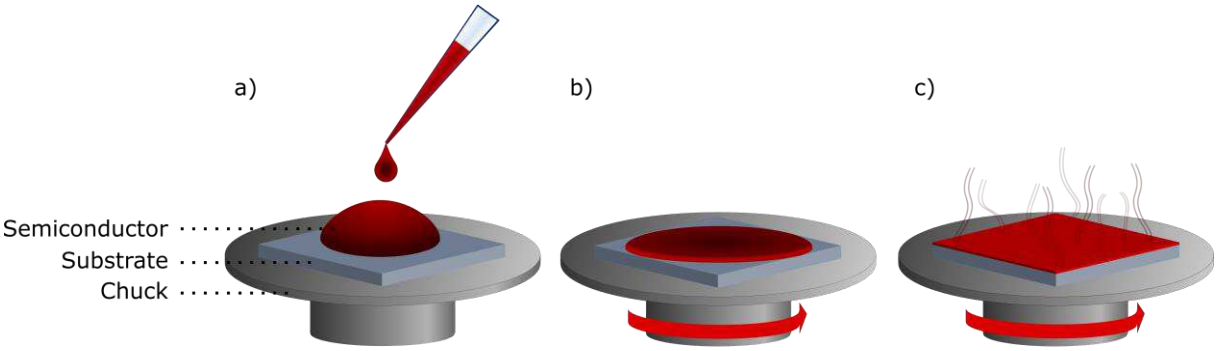

Figure 4-5 Sketch of the spin-coating approach. a) drops of the solution are deposited on the substrate, b) the sample holder starts the rotation, leading to the covering of the whole substrate and c) the solvent is evaporated during the rotation.

Drop-casting is a technique were the solution is simply dropped on the substrate in a sufficient quantity to cover its surface. While the solvent is evaporating, the concentration of the solution dropped is slowly increasing until the solidification starts, leading to the final film. This approach promotes the crystallinity of domains but often results to thick and inhomogeneous films on the hundreds of µm scale.

4.1.2.2 Solvent-induced precipitation

PDI crystals were made using solvent-induced precipitation (SIP) method, as presented in the chapter 5.[12] This method consists in the addition of a solution of the compound of interest, to a bad solvent which is miscible with the solvent used to dissolve it. This process yields in an increase of intermolecular interactions which are determining the crystallization. It is possible to modulate the kinetics of crystallization by adjusting the ratio between good solvent and bad solvent. The size of the crystals formed can also be modulated by modifying the temperature and the cooling rate.

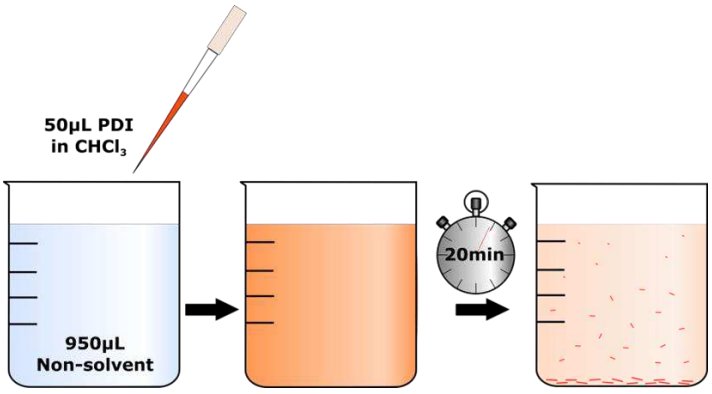

Figure 4-6 Sketch of the solvent induced precipitation process.

4.1.2.3 Mechanical exfoliation

Mechanical exfoliation is a way to produce high quality 2D materials, but usually results to a limited number of small suitable flakes per sample. One of these approaches is based on the

use of scotch tape (SPV 9205 from Nitto) with different levels of adhesiveness, depending of the targeted layered materials to exfoliate (Figure 4-7).[13–15]

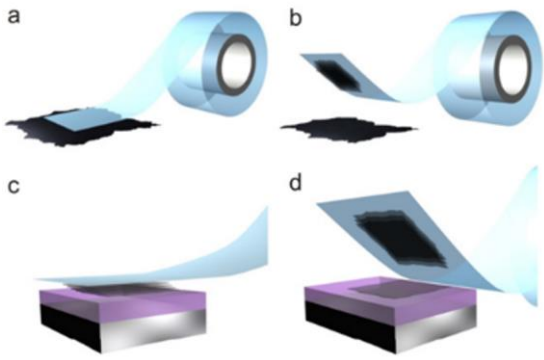

Figure 4-7 Conventional scotch-tape exfoliation of bulk to form atomically thin material. (Adapted with permission from[16])

The tape is placed in contact with the top interface of a layered material, and slowly removed to cleave it. This operation is then repeated a few times on the piece of tape itself, leading to a reduction of the material thickness present on the tape. The tape, almost fully covered by exfoliated material, is then pasted on a clean substrate, and is very slowly and carefully removed, where some partially and fully exfoliated materials remain on the substrate.

An alternative approach is a stamp-based exfoliation, where one piece of tape (Gel-Pak 4) is fixed at the end of a stamp, when another piece of tape is fixed on a rigid surface (Figure 4-8).

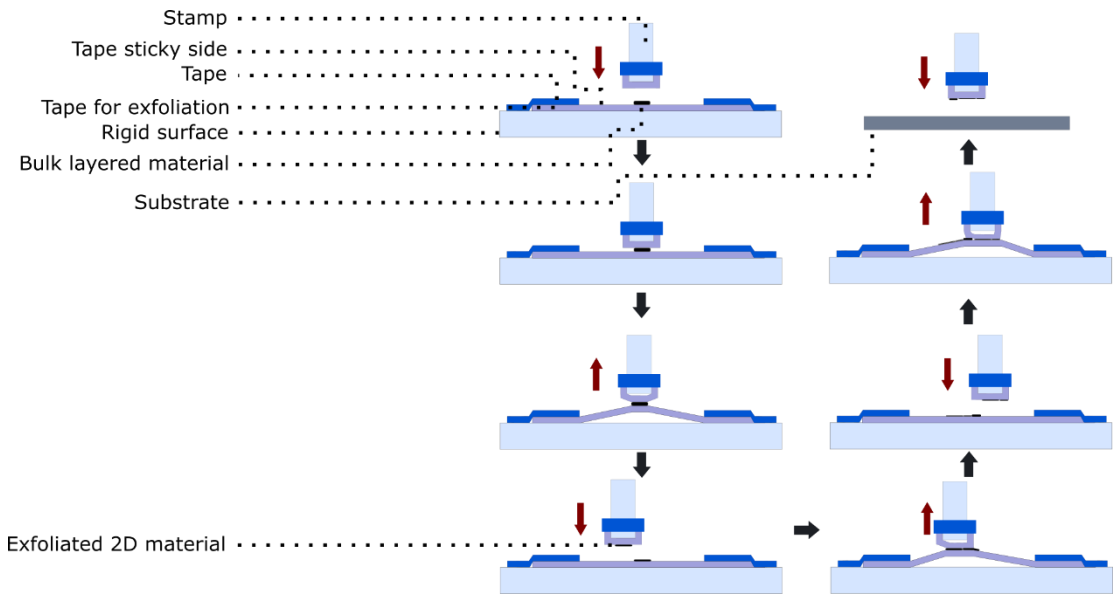

Figure 4-8 Cartoon of the stamp-based exfoliation.

A bulk piece of 2D material is placed on the piece of tape fixed on the rigid surface, and the stamp is pressed on top of it, then slowly pulled up. This action is repeated many times to lead to the thinning of the bulk material into monolayers. The stamp is then pressed on the top of the target substrate, leading to the deposition of mono- bi- and multilayers on it.

Typically, in this work, graphene monolayers have been produced in the conventional scotch-tape way while WSe_2 have been exfoliated with the stamp approach, as presented in the chapter 6.

4.2 Characterization techniques

4.2.1 Field-effect transistors

The field-effect transistor (FET) is a device first proposed by Lilienfeld[17] in 1926 and Heil in 1934,[18] and confirmed experimentally in 1948 by Shockley in the Bell Labs, who have shared in 1956 the Nobel prize in physics with Bardeen and Brattain. With the evolution of the technology, the improvement over control of the surface of the materials led to the elaboration, in 1963, to thin-film devices as we know today, through the work of Kahng.[19]

4.2.1.1 Structure and operation

An FET is a three-terminal device. In particular, the so-called source and drain electrodes are those separated by a semiconductor, and both are isolated from the gate electrode through a dielectric layer (Figure 4-9).[20,21] Typically, the most employed dielectric in research is the silicon dioxide (SiO_2, $\kappa = 3.9$), which is thermally grown on silicon in a very precise and controlled way to attain a given thickness. The remaining silicon can be heavily doped to get metallic electrical conductivity, then used as the gate electrode. Other inorganic dielectrics can be used, such as Al_2O_3 ($\kappa = 9$) or HfO_2 ($\kappa = 25$),[22,23] but organic polymer like Cytop[24] or polymethylmethacrylate[25] can also be employed, allowing other properties to the device, such as flexibility or transparency.

Concerning the electrodes' material, source and drain electrodes are made of a metal (i.e. Au, Al, Pd, etc) which is selected according to its work function, to match the energy levels of the semiconductor in the best way.[26–28] Here also, the polymer such as the poly(3,4-ethylenedioxythiophene):poly(4-styrenesulfonate) (better known as PEDOT:PSS) can be used.[29]

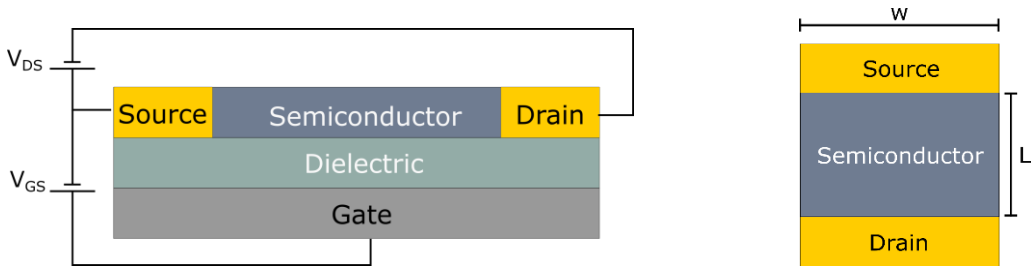

Figure 4-9 Schematic of the lateral view (left) and top view (right) of a typical bottom-gate bottom-contact field-effect transistor.

When a voltage is applied between the source and drain electrodes (V_{DS}), charges are injected into/extracted from the semiconductor, resulting in a current that flows through the device channel. The latter is defined by its length, L, and width, W. Similarly, when a voltage is applied between the source and gate electrodes (V_{GS}), charges accumulate at the top surface of

the dielectric, leading to a modulation of the charge density in the semiconductor, which is proportional to V_{GS} and to the capacitance per unit area of the dielectric (C_i) of the FET. Depending on the sign of the applied bias applied, holes or electrons can be selectively accumulated at the surface of the dielectric.

The operation of a FET can be described by two regimes, the linear and the saturation regime (Figure 4-10). After the filling of shallow traps in the semiconductor,[30] a continuous charge layer is formed throughout the device channel when a given value of V_{GS}, called threshold voltage (V_{TH}), is applied.[31] Then, a small V_{DS} is applied (typically with $V_{DS} < V_{GS} - V_{TH}$), inducing a linear gradient of charges in the channel. If a higher V_{DS} is applied in such a way that $V_{GS} - V_{TH} < V_{DS}$, a narrow depletion region is formed close to the drain electrode into the channel, and the current I_{DS} saturate and become independent from V_{DS} (saturation regime).[32]

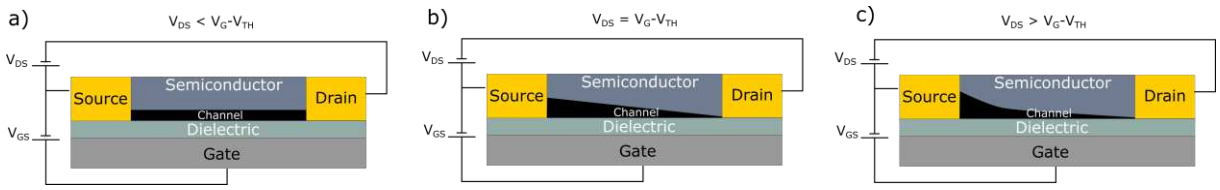

Figure 4-10 Field-effect transistor operating a) in linear regime, b) when the depletion is formed on the channel, and c) in saturation regime. (Adapted from[32])

4.2.1.2 Parameters extraction

A FET operation can be characterized in two different ways, by applying a constant V_{GS} bias while sweeping V_{DS} and recording the resulting I_{DS}, which allows to trace the so-called characteristic (output) curves (Figure 4-11 a)) and the other one corresponds to a sweep of the V_{GS} bias while applying a constant V_{DS}, and is called a transfer (output) curve (Figure 4-11 b)). From these curves, some key parameters can be extracted that are related to the good operation of an FET, but also to study the intrinsic properties of a semiconductor. In particular, these parameters are the charge carrier mobility (μ), the threshold voltage (V_{TH}), and the I_{on}/I_{off} ratio, that are discussed below.

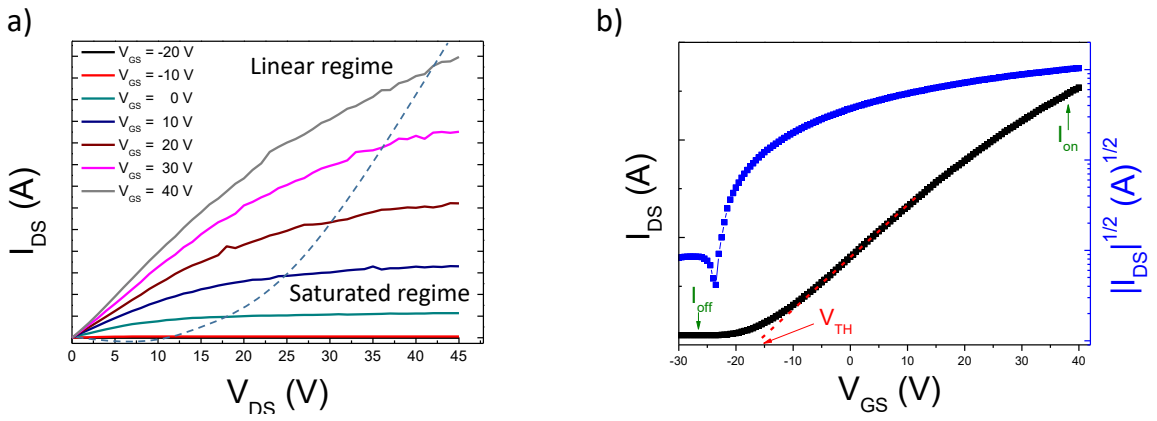

Figure 4-11 a) Output curves, and b) transfer curves measured for an n-type semiconductor.

The **charge carrier mobility** μ (in $cm^2V^{-1}s^{-1}$) is defined as the ratio between the charge drift velocity V_d and an applied electric field E (Equation 4.1).

$$V_d = \mu E \tag{4.1}$$

The charges Q, that have been induced at a V_{GS} which is higher than V_{TH}, is expressed by equation (4.2) at a certain position x in the channel.[32]

$$Q = C_i(V_{GS} - V_{TH} - V(x)) \tag{4.2}$$

The drain current I_{DS} can be expressed through the equation (4.3).

$$I_{DS} = WQ\mu E \tag{4.3}$$

Replacing the expression of (4.2) in (4.3) and knowing that the electric field $E = dV/dx$, equation (4.4) is obtained.

$$I_{DS}dx = W\mu C_i(V_{GS} - V_{TH} - V(x))dV \tag{4.4}$$

The expression of the drain current I_{DS} can be obtained for a linear regime, by using the gradual channel approximation assuming that the potential varies steadily in the channel from the drain to the source electrode, which lead to equation (4.5), that can be approximated into equation (4.6) since V_{DS} is much smaller than V_{GS} in the linear regime.

$$I_{DS,lin} = \frac{W}{L}\mu_{lin}C_i\left[(V_{GS} - V_{TH})V_{DS} - \frac{1}{2}{V_{DS}}^2\right] \tag{4.5}$$

$$I_{DS,lin} = \frac{W}{L}\mu_{lin}C_i(V_{GS} - V_{TH}) \quad (4.6)$$

Thus, from (4.6), the mobility in linear regime μ_{lin} can be extracted (Equation 4.7).[33]

$$\mu_{lin} = \frac{\partial I_{DS}}{\partial V_{GS}} \cdot \frac{L}{WC_i V_{DS}} \quad (4.7)$$

However, in the saturation regime, since the drain current changes are minimal upon increasing the drain voltage, another equation has to be considered. Since $V_{DS} > (V_{GS} - V_{TH})$, the drain current I_{DS} in this regime is expressed by the equation (4.8).

$$I_{DS,sat} = \frac{W}{2L}\mu_{sat}C_i(V_{GS} - V_{TH})^2 \quad (4.8)$$

The mobility in saturation regime μ_{sat} can be extracted in equation (4.9) from the one above.

$$\mu_{sat} = \frac{\partial \sqrt{I_{DS}}}{\partial V_{GS}} \cdot \frac{2L}{WC_i(V_{DS} - V_{TH})} \quad (4.9)$$

While some FET devices are designed, according to the doping of the semiconductor and the work function of the metal used for the electrodes, to operate with hole or electron conduction, some devices are based on ambipolar materials that are able to transport both types of charge carrier.[34] In this specific situation, the drain current measured during the operation can be seen as the sum of the contribution from holes and electrons currents, and is defined by the equation (4.10) in saturation regime.

$$I_{DS} = \frac{W}{2L}C_i\left[\mu_e(V_{GS} - V_{TH,e})^2 + \mu_h(V_{GS} - V_{TH,h})^2\right] \quad (4.10)$$

Where μ_e and μ_h correspond to the electron and hole mobilities, respectively, and $V_{TH,e}$ and $V_{TH,h}$ are the electron and hole threshold voltages.

The **threshold voltage** V_{TH} is defined by the specific V_{GS} bias where a small increase of the later results in an important increase of the drain current I_{DS}, and represents the voltage needed for filling the traps present into the semiconductor or at the surface of the dielectric.[35]

The $\mathbf{I_{on}/I_{off}}$ is the ratio between the drain current measured in ON state at a certain V_{GS}, over the one measured in OFF state, and it represents the capability of the FET to switch from the ON state to the OFF one.

The **reliability factor** r is defined by the equation (4.11) and calculated with (4.12) and (4.13) in linear and saturation regime, respectively.[36] This factor is an indicator of ideality for a FET curve, allowing to estimate if a claimed mobility is justified or overestimated because of the different regimes observed on the transfer curves.

$$\mu_{eff} \equiv r.\mu_{claimed} \tag{4.11}$$

$$r_{lin} = \frac{\left(\frac{|I_{DS}|^{max} - |I_{DS}^{0V}|}{|V_{GS}|^{max}}\right)}{\left(\frac{\partial I_{DS}}{\partial V_{GS}}\right)_{claimed}} \tag{4.12}$$

$$r_{sat} = \frac{\left(\frac{\sqrt{|I_{DS}|^{max}} - \sqrt{|I_{DS}^{0V}|}}{|V_{GS}|^{max}}\right)^2}{\left(\frac{\partial \sqrt{I_{DS}}}{\partial \sqrt{V_{GS}}}\right)^2_{claimed}} \tag{4.13}$$

Expressed in percentage, r will tend to 100% in the case of an ideal FET transfer curve and will deviate from this value for any other cases (Figure 4-12).

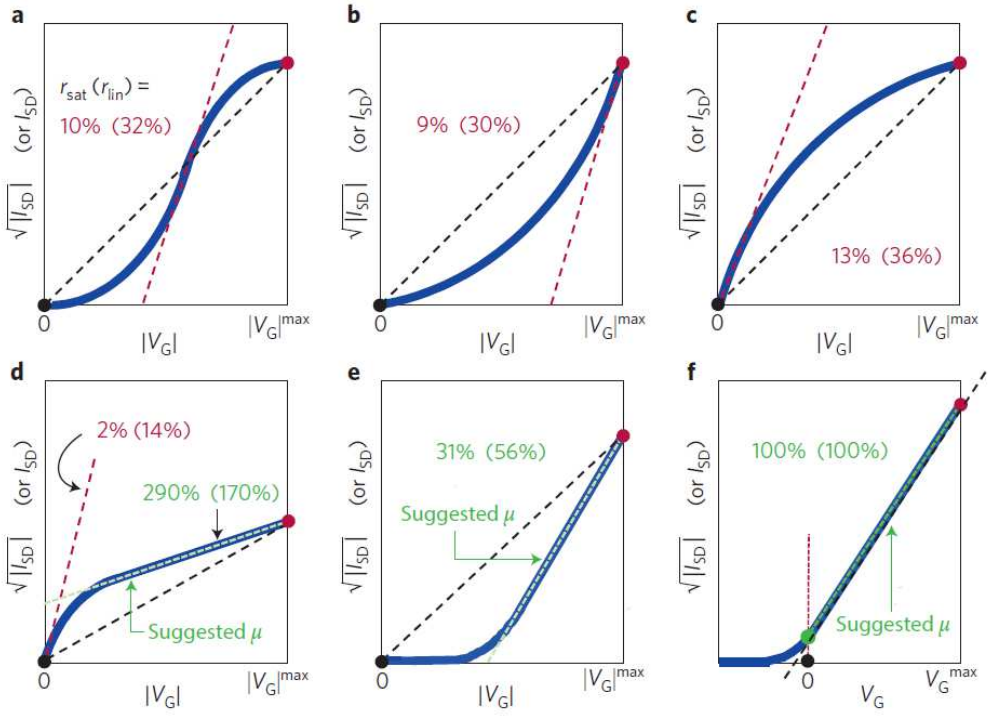

Figure 4-12 Common nonlinearities observed in FET transfer curves. The blue line represents the measured transfer curve while the red dashed line corresponds to the slope for the highest value of mobility to extract and the black dashed line correspond to the ideal transfer curve within the current measured experimentally (Reproduced with permission from[36]).

Similarly, the **maximum current density** J_{DS}^{max} and the **maximum power density** P_{max} can be calculated with the equations (4.14) and (4.15), respectively.

$$J_{DS}^{max} = \frac{|I_{DS}|^{max}}{Wd_0} \tag{4.14}$$

$$P_{max} = \frac{|I_{DS}|^{max}.|V_{DS}|}{WL} \tag{4.15}$$

Where I_{DS}^{max} is the highest drain current measured and d_0 is the thickness of the charge accumulation layer in the semiconductor. These two parameters are interesting to evaluate if the device can be subjected to thermal fluctuation when a high electric field is applied in a small volume because of the Joule effect, which leads to an instability during the electrical characterization.

The **contact resistance** R_c is an indication of how easily a charge is injected from the metallic electrode to the semiconductor.[37,38] Indeed, when charges are injected into the device, their flow will be first reduced by the resistance of the metal R_m, used as electrodes (Figure 4-13 a)). This resistance is very small and can be usually neglected. The flow of charges is then injected from the electrode to the semiconductor, into the channel. Due to the potential mismatch in energy between the energy levels of the semiconductor (i.e. the HOMO and LUMO levels for a molecule or the valence and the conductive bands for an inorganic solid) and the work function of the metal, an injection barrier is formed, leading to the contact resistance. Once injected in the semiconductor, the flow of charges will be affected by the intrinsic resistance of the semiconductor (R_{chan}). To be collected on the other electrode, the flow of charges will again experience this barrier, and the metal resistance.

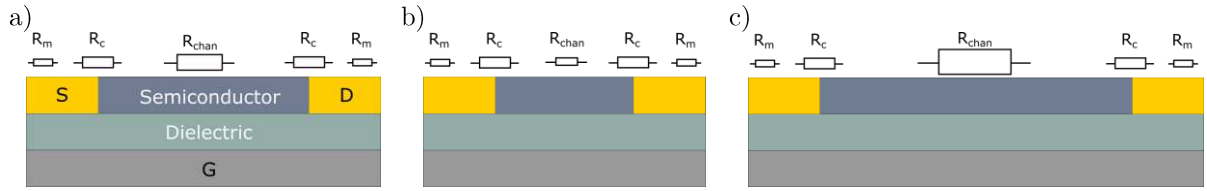

Figure 4-13 a) FET represented with the three main electrical resistances measured during operation, the resistance of the electrodes (R_m), the resistance of the semiconductor (R_{chan}) and the resistance between the electrode and the semiconductor, the so-called contact

resistance (R_c). By changing the channel length, the resistance of the semiconductor will be affected (b) and c)) while the contact resistance and the electrode resistance will remain the same.

One way to extract this contact resistance is by using the transmission line method (TLM).[39,40] By changing the channel length L of a FET, (Figure 4-13 b) and c)), the resistance of the semiconductor will be proportional to the channel length while the resistance of the electrodes and the contact resistance will remain constant. Thus, the total resistance (R_{tot}) measured can be defined by the equation (4.16).

$$R_{tot} = R_{chan} + R_c + R_m \approx \frac{L}{W\mu C_i(V_{GS}-V_{TH})} + R_c \qquad (4.16)$$

By plotting the channel length versus the total resistance measured (Figure 4-14), it is possible to extrapolate the contact resistance at $L = 0$.

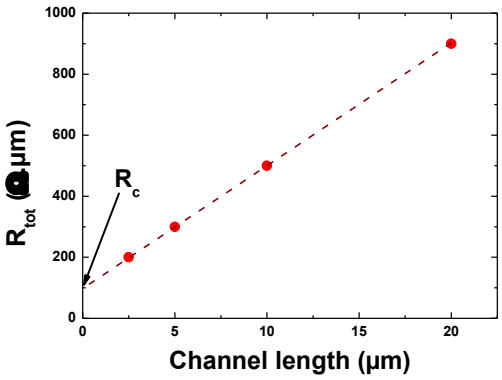

Figure 4-14 Typical Transfer Line Method plot of the channel length versus the resistance of devices, allowing to extrapolate the contact resistance.

It is possible to extract the contact resistance through other ways such as the 4-probes measurements[41] that will not be discussed here.

The **trap density** N_t in a semiconductor gives information on the number of traps present in the films. Charge traps can originate from structural defects (acting as simple scattering centers for charges) and/or can be due to electronic interactions with polarons. In the latter case, trap states can be located within the semiconductor bandgap more or less close in energy to the

HOMO or to the LUMO level. A simple way to give a rough estimate of trap density within a semiconductor in a two-terminal configuration, is represented by the use of space-charge-limited current (SCLC) method.[42,43] While increasing the voltage (Figure 4-15), the current measured increases proportionally, and define the ohmic region. After a threshold voltage V_{TH} (which is different from the threshold voltage measuring on a transfer curve), the current is proportional to the voltage-squared, and is characterized by the filling of the traps in the semiconductor. An abrupt increase of the current at V_{TFL} indicates the complete filling of the traps and defines the beginning of the trap-free regime.

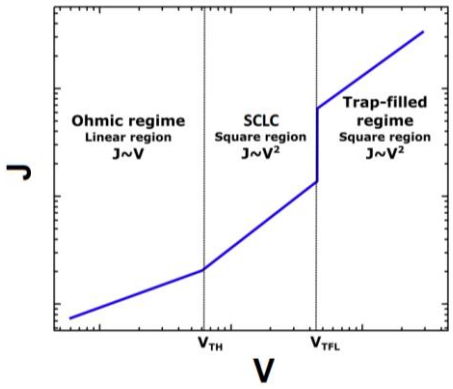

Figure 4-15 Typical double logarithm curve measured for the space-charge-limited current method, described by three succesive current regimes, the ohmic region, the SCLC, when the traps start to be filled and the trap-filled regime. The transition from the SCLC region to the trap-filled one allows to calculate the trap density.

Hence, the trap density (in cm^{-3}) can be estimated through the equation (4.17), with ε the dielectric permittivity of the semiconductor, e the elementary charge and L the inter-electrode distance.

$$N_t = \frac{\varepsilon V_{TFL}}{eL^2} \qquad (4.17)$$

4.2.2 Electrical setup

4.2.2.1 Probe-station

The devices were electrically characterized with a probe-station set-up (Cascade Microtech M150, Figure 4-16) operating in a nitrogen-filled glovebox or in air. The sample is placed on a conductive chuck, and with the help of micromanipulators, two tungsten electrodes are connected to a specific device on the sample, localized with an optical microscope. The electrical measurement is provided by a dual channel Keithley 2636B Sourcemeter controlled by Labtracer software.

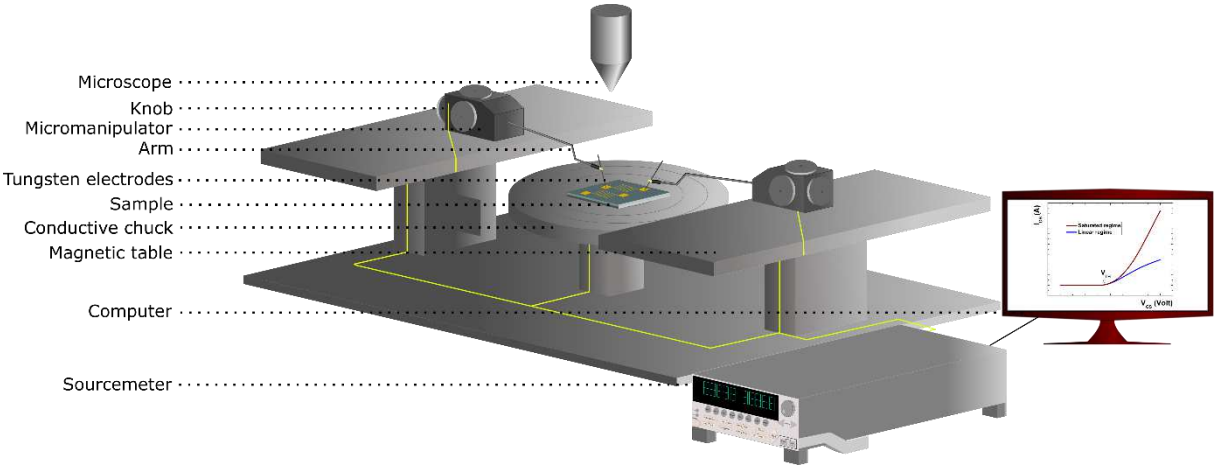

Figure 4-16 Sketch of a probe-station setup used for the characterization of FET.

4.2.2.2 Cryostat

In order to measure the evolution of the electrical performances at different temperatures, a liquid nitrogen-based cryostat (Optistat DN-V from Oxford Instrument, Figure 4-17) controlled through an ITC503S Cryogenic Temperature Controller and interfaced with a dual channel Keithley 2636A sourcemeter by a homemade Labview software.

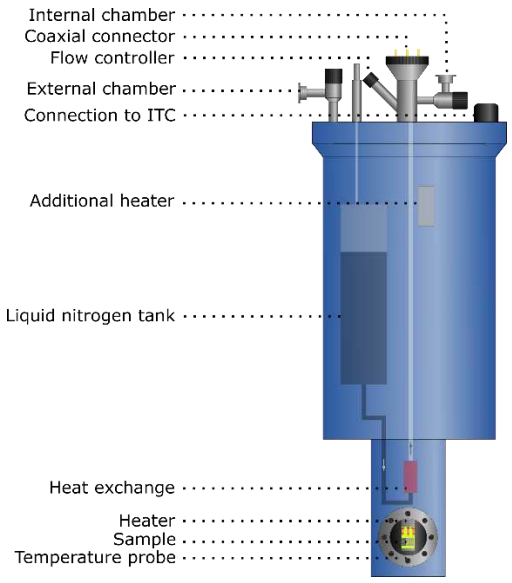

Figure 4-17 Sketch of the nitrogen-based cryostat.

The sample FET are connected in the cryostat as follow (Figure 4-18): indium is used to connect copper wires to the drain and source electrodes. The gate is connected by scratching the SiO_2 layer with a diamond pen, to access to the Si n++ layer from the top, which is then put in contact with a piece of indium, again used to be connected with a copper wire. These copper wires are fixed on metallic pads designed on a homemade PCB board, themselves connected to Manganin wire, which is an alloy of copper, manganese and nickel, known to have a very small change in its resistance over the range of temperature studied. Prior to the cooling down process, the sample chamber needs to be purged from the ambient atmosphere. To do so, the internal heater is set at 307 K to increase the desorption of water contained in the atmosphere from the surface while the chamber is pumped with a rotary pump. Since the internal heater is located at an extremity of the cryostat and in order to make this process more efficient, an additional heater has been added inside the chamber. After 4 hours of purging, both heaters are turned off, and the tank of liquid nitrogen is filled. The cooling rate is set at 0.02 $K.s^{-1}$ to prevent any thermal shock that can damage the sample. When the temperature reaches 80 K, a delay of 90 min before starting the measurement is imposed to ensure a stable and uniform temperature in the proximity of the sample. The sample is then electrically characterized for each 10 K steps until 300 K, after the same delay time of 90 min between two measurements.

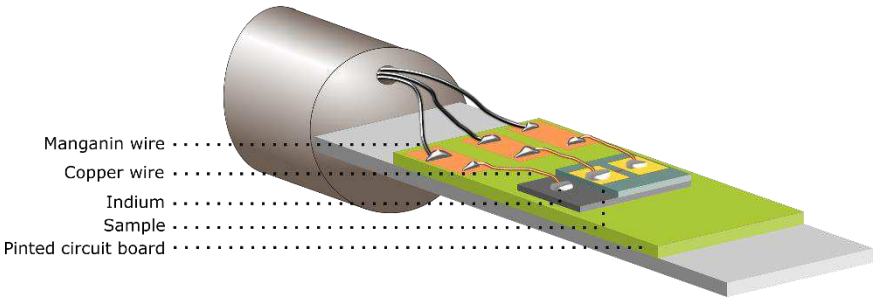

Figure 4-18 Sketch of the cryostat probe connected to the sample.

4.2.2.3 Gas chamber

The characterization of the gas sensors was feasible with the help of a sealed polycarbonate chamber. For oxygen sensing measurements (Figure 4-19), the chamber is equipped with a valve allowing to inject dry nitrogen to decrease the level of oxygen, controlled with a Dräger Pac 550 O_2 oxygen sensor. The device is electrically connected to the Keithley with two copper wires and an indium pellet which is used to connect them to the electrodes of the device. In this way, the sample can be measured in real time while changing the environment inside the chamber. This configuration only allows to probe from 1% to 20.9% in volume of O_2.

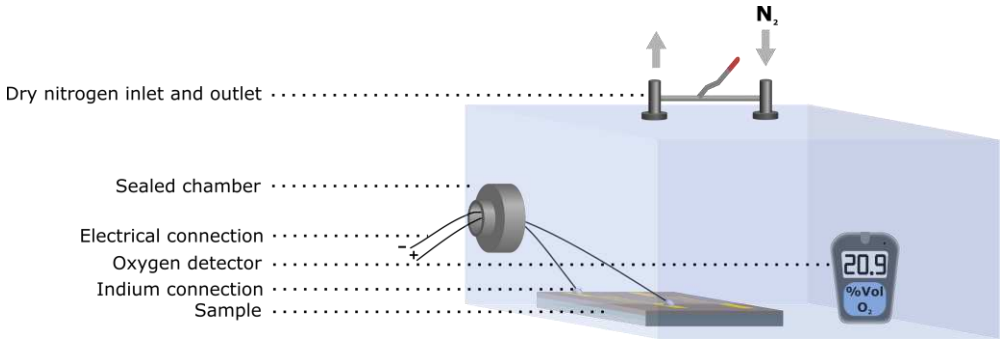

Figure 4-19 Sketch of the chamber used for the electrical measurements to control the amount of oxygen gas in the atmosphere.

Regarding the humidity sensing measurements, the same sealed chamber was used (Figure 4-20), with the same electrical connection to the sample. A Sensirion SHT31 sensor was placed inside the chamber to measure both the relative humidity and the temperature of the

environment. The humidity was controlled through the equilibrium vapour pressure of a chemical system. In this case, aqueous solution saturated in salt were used. To reach low values of relative humidity, lithium chloride salt was used, allowing to get around 14 %RH at 20 °C while sodium chloride gave the access up to 75 %RH at the same temperature. Since the chamber is a large volume, the equilibration of the environment is slow enough to proceed to electrical measurements during the increase or decrease of the humidity. Very low values of relative humidity (below 1 %RH) are not easy to get, hence the measurement under such conditions were done in a nitrogen filled glovebox.

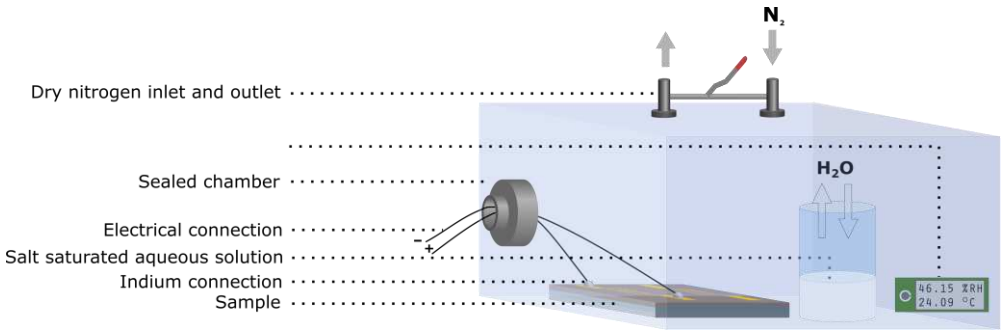

Figure 4-20 Sketch of the chamber used for electrical measurement in a controlled humidity atmosphere, with the help of aqueous solution saturated in LiCl or NaCl.

4.2.3 Spectroscopic characterization

4.2.3.1 Micro-Raman and Photoluminescence spectrometer

Raman and emission spectroscopy are powerful techniques to characterize a material. While Raman gives information on vibrations present in a material with complementary selection rules than infra-red spectroscopy, the emission spectroscopy record the photoluminescence of a material, which can be correlated to many parameters such as phase transition, doping, etc. The spectra were recorded with a Renishaw InVia spectrometer combined with a 532 nm source (Figure 4-21). The setup consists of a confocal microscope with a 100x lens objective that forms a beam spot of 800 nm for the measurement. The signal emitted by the sample is collected by the microscope lens and redirected via a rejection filter to a diffraction grating which is splitting the signal by energies, that a CCD camera will detect. A Linkam THMS600 Temperature

controlled stage and a LNP95 cooling system have been used for low-temperature characterizations. A Si reference at 520.3 cm^{-1} was used to calibrate the instrument and normalize the measurements.

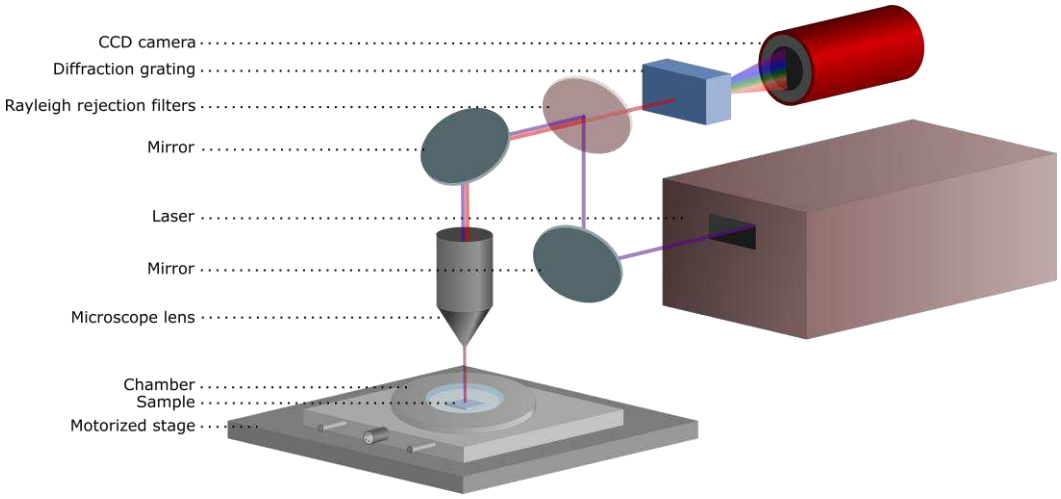

Figure 4-21 Sketch of the confocal micro-Raman.

4.2.3.2 X-ray photoelectron spectroscopy

The X-ray Photoelectron Spectroscopy (XPS, K-alpha Compact XPS from Thermo Scientific) is a powerful tool to probe, within the first 3 nm of a surface, the chemical composition and chemical states of the elements present. To do so, an X-ray beam with a known energy is interacting with atoms through the photoelectric effect. In this way, electrons from the inner shells of the atoms are ejected from the surface with a specific kinetic energy which is directly linked to the precise orbital of a specific atom in a defined chemical state.

X-rays are produced by bombarding an Aluminium anode with an electron beam produced from an electron gun and are selected in energy by using a crystal of quartz (Figure 4-22). The X-rays irradiate the sample, which is placed in an ultra-high vacuum chamber to avoid contamination and maximize the photoelectron path length created by the photoelectric effect. The photoelectrons are then focalized through a magnetic lens on a hemispherical detector that will sort the electrons by energy. Then, the resulting electrons with a known energy are counted with a detector. In this way, it is possible to plot the kinetic energy of the electrons measured

in function of their population, leading to the XPS spectrum. To prevent any charging effect of an insulating sample that would shift all the data, a flood gun is constantly bombarding the probed area with electron to neutralize the positives charges created by the photoelectric effect.

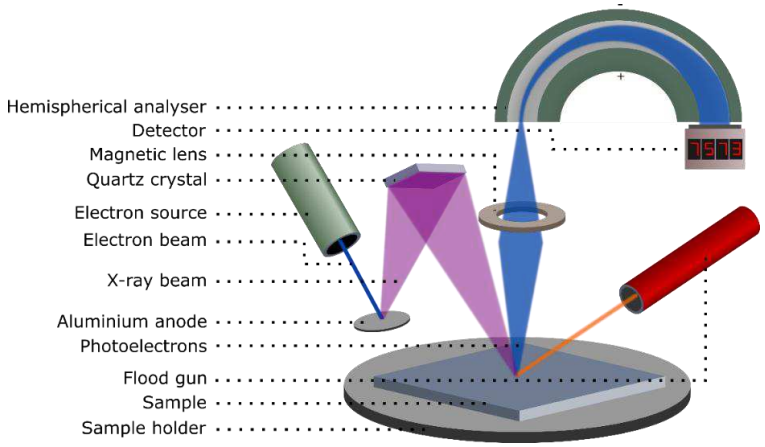

Figure 4-22 Sketch of an X-ray Photoelectron Spectrometer.

4.2.3.3 Photoelectron spectroscopy in ambient conditions

The work function (WF) of metal or Ionization Energy (IE) of semiconductor was measured with a Riken AC-2 Photoelectron spectrometer working in ambient atmosphere (Figure 4-23). A UV light, produced by a deuterium lamp, with a known energy (from 3.4 eV to 6.2 eV) is selectively irradiating a sample through an optical fiber. According to the photoelectric effect, when the energy of the beam is high enough, the molecules will eject electrons from the sample, that will be collected by a cathode linked to an electron counter. By modulating the energy of the beam versus the number of electrons collected by the cathode, it is possible to extract the precise energy where the molecules are ionized.

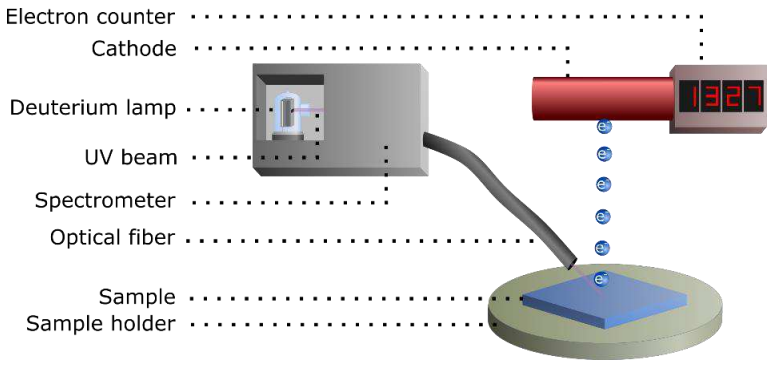

Figure 4-23 Sketch of a photoelectron spectrometer working in ambient conditions (PESA).

4.2.4 Surface characterization

4.2.4.1 Atomic force microscopy

Atomic Force Microscopy (AFM) was used in tapping mode to map the surface samples at the nanometric scale (Figure 4-24). The AFM is used to get images of the topography of the surface of a sample thus enabling to quantify its local roughness. The movement of a cantilever, on which rear-side a laser is reflected to a photodiode, is controlled by a piezo actuator. The cantilever vibrates at the proximity of the surface, at a frequency close to its resonance one. The frequency and phase of resonance changes with the interaction with the material and with its composition, depending of the strength of the interaction involved between the tip mounted on the cantilever and the material itself. A feedback loop maintains the tip at a constant height while the profile of the surface is changing. The software reconstructs line by line the profile that the tip of the AFM is experiencing. The whole setup is fixed to a table that provide an insulation from external vibrations while working in a Faraday cage, protecting the sample from the acoustic and electrostatic noise.

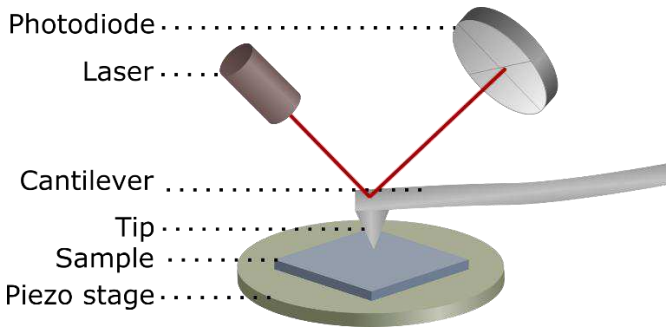

Figure 4-24 Sketch of an atomic force microscope.

4.2.4.2 Profilometer

A profilometer (KLA Tencor Alpha-Step IQ) is a convenient technique to quickly access to the thickness of a film (Figure 4-25). Prior to this measurement, the sample need to be scratched, in order to create a line by locally removing the deposited film. The line created is then localized

with a camera and aligned perpendicularly with the path of a stylus. The length of the profile as well as the speed and the force of the stylus are defined in accordance with the sample measured: a soft sample can be destroyed by a too strong force applied by the stylus which leads to the loose of the profile information since the stylus penetrate the thin-film. However, a too weak force may decrease the sensibility of the stylus and then the loose of the profile as well. This profile of the scratched line is then measured with a vertical motion sensor.

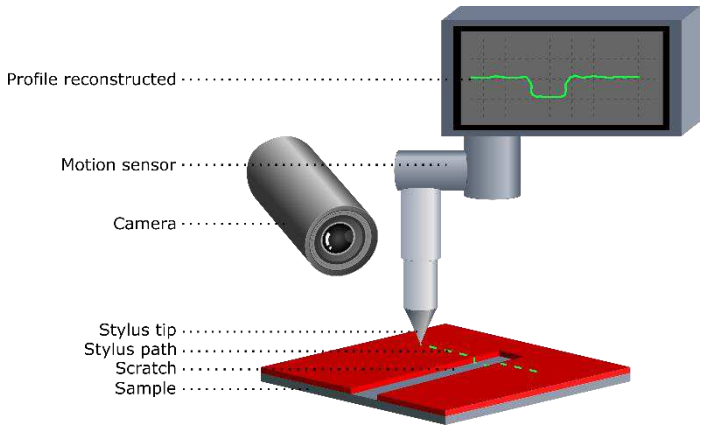

Figure 4-25 Sketch of a profilometer.

4.2.4.3 Scanning electron microscopy

In order to characterize the surfaces of samples at micrometric scale, a Scanning Electron Microsope (SEM) Quanta FEG 450 from FEI was used (Figure 4-26 (left)). In a high-vacuum chamber, an electron gun generates a high energy electron beam (from 5 keV to 30 keV) that is focus and accelerated with an anode, reduced in diameter with a spray aperture and focused on the surface of the sample with a magnetic lens. The area of the sample probed is selected via a picture of the chamber took by an optical camera prior to the measurement. Without moving the sample, a scanning coil deflect to electron beam in order to probe the whole surface of the sample. At the impact, the electron beam generate different types of products (Figure 4-26 (right)) from the surface, such as secondary electrons (SE) that are produced from the inelastic scattering of the primary electrons with the electrons in the external shells of the atomic orbits creating a vacancy, X-rays that are generated from the energetic relaxation of

an electron in higher energy to the vacancy created by the SE, or a backscattered electron (BE) corresponding to the elastic scattering of the primary electron. Each particule is collected by a specific detector, allowing the access to different information: the SE comes from the very first nanometers of the surface while the BE comes from deeper in the sample. The X-ray can be detected by an Energy Dispersive X-ray detector (EDX) and gives information on the chemical composition of the sample.

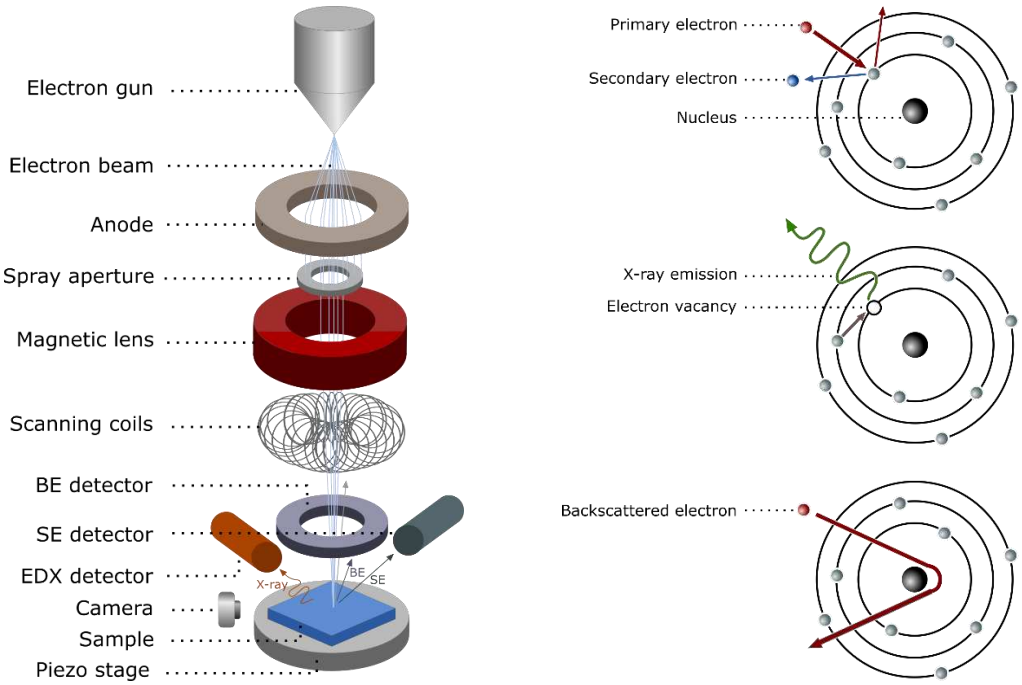

Figure 4-26 Sketch of the SEM operation (left) and type of interactions of an atom with an electron beam that can be detected by the SEM (right).

4.2.4.4 Water contact angle

The water contact angle is a useful technique to follow the changes of a surface composition. Such technique is based on the angle that a drop of water adopts when adsorb on the top of a substrate (Figure 4-27). Depending on the wettability of the surface, which is directly related to the chemical composition and roughness of the surface. The angle described by the drop of water is small for a hydrophilic surface or large for a hydrophobic surface. The setup, a Krüss DSA 100, deposits a 3 µL drop of water on the sample while the camera records the process. The software analyses the position of the drop, it defines the baseline and it fits the shape of

the drop with a tangent method leading to the final angle measured. The measure is repeated many times to ensure a reliable value of the angle measured, which can be used quantitatively to probe the changes of a surface because of a treatment, or it can be use qualitatively when the angle is compared with already reported angle value for a specific surface or treatment.

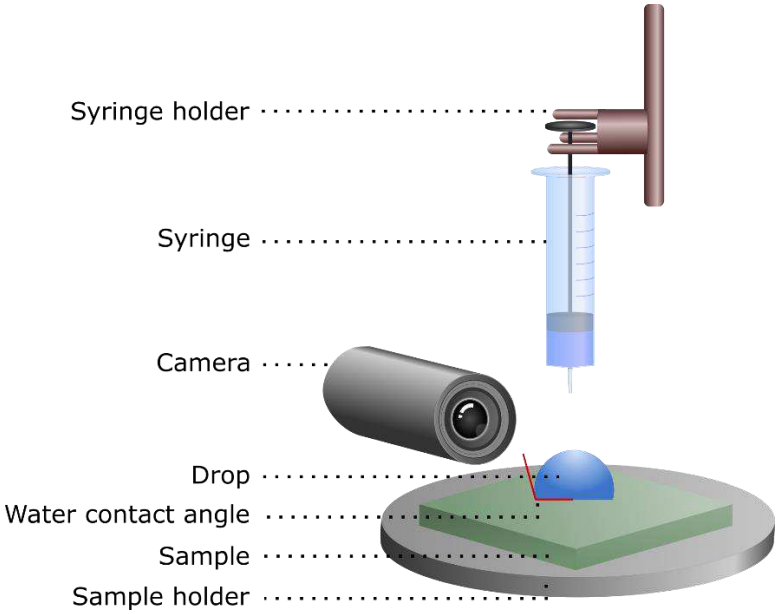

Figure 4-27 Sketch of the water contact angle setup.

4.3 References

[1] M. M. Benameur, B. Radisavljevic, J. S. Héron, S. Sahoo, H. Berger, A. Kis, *Nanotechnology* **2011**, *22*, 125706.
[2] Y. Lu, X.-L. Li, X. Zhang, J.-B. Wu, P.-H. Tan, *Science Bulletin* **2015**, *60*, 806.
[3] B. S. Lee, Y. S. Chi, J. K. Lee, I. S. Choi, C. E. Song, S. K. Namgoong, S. Lee, *J. Am. Chem. Soc.* **2004**, *126*, 480.
[4] H. Ma, H.-L. Yip, F. Huang, A. K.-Y. Jen, *Advanced Functional Materials* **2010**, *20*, 1371.
[5] G. Heimel, L. Romaner, E. Zojer, J.-L. Bredas, *Acc. Chem. Res.* **2008**, *41*, 721.
[6] Y. Wang, M. Lieberman, *Langmuir* **2003**, *19*, 1159.
[7] J. P. Folkers, P. E. Laibinis, G. M. Whitesides, *Langmuir* **1992**, *8*, 1330.
[8] L.-L. Chua, J. Zaumseil, J.-F. Chang, E. C.-W. Ou, P. K.-H. Ho, H. Sirringhaus, R. H. Friend, *Nature* **2005**, *434*, 194.
[9] C.-K. Song, B.-W. Koo, S.-B. Lee, D.-H. Kim, *Jpn. J. Appl. Phys.* **2002**, *41*, 2730.
[10] S. E. R. Hiscocks, W. Hume-Rothery, *Proc. R. Soc. Lond. A* **1964**, *282*, 318.
[11] T. Ohara, Y. Matsumoto, H. Ohashi, *Physics of Fluids A: Fluid Dynamics* **1989**, *1*, 1949.
[12] J. W. Mullin, in *Crystallization (Fourth Edition)* (Ed.: J.W. Mullin), Butterworth-Heinemann, Oxford, **2001**, pp. 289–314.

[13] K. S. Novoselov, A. K. Geim, S. V. Morozov, D. Jiang, Y. Zhang, S. V. Dubonos, I. V. Grigorieva, A. A. Firsov, *Science* **2004**, *306*, 666.
[14] A. E. Mag-isa, J.-H. Kim, H.-J. Lee, C.-S. Oh, *2D Mater.* **2015**, *2*, 034017.
[15] O. Lopez-Sanchez, D. Lembke, M. Kayci, A. Radenovic, A. Kis, *Nature Nanotechnology* **2013**, *8*, 497.
[16] K. S. Novoselov, A. H. Castro Neto, *Physica Scripta* **2012**, *T146*, 014006.
[17] E. Lilienfeld, *Method and Apparatus for Controlling Electric Currents*, **1930**, US1745175A.
[18] O. Heil, *Improvements in or Relating to Electrical Amplifiers and Other Control Arrangements and Devices*, **1935**, GB439457A.
[19] D. Kahng, *Electric Field Controlled Semiconductor Device*, **1963**, US3102230A.
[20] J. Robertson, *The European Physical Journal Applied Physics* **2004**, *28*, 265.
[21] J. M. Adhikari, M. R. Gadinski, Q. Li, K. G. Sun, M. A. Reyes-Martinez, E. Iagodkine, A. L. Briseno, T. N. Jackson, Q. Wang, E. D. Gomez, *Advanced Materials* **2016**, *28*, 10095.
[22] L. Fumagalli, D. Natali, M. Sampietro, E. Peron, F. Perissinotti, G. Tallarida, S. Ferrari, *Organic Electronics* **2008**, *9*, 198.
[23] A. Kumar, M. V. Fischetti, T. H. Ning, E. Gusev, *Journal of Applied Physics* **2003**, *94*, 1728.
[24] W. L. Kalb, T. Mathis, S. Haas, A. F. Stassen, B. Batlogg, *Appl. Phys. Lett.* **2007**, *90*, 092104.
[25] J. H. Park, D. K. Hwang, J. Lee, S. Im, E. Kim, *Thin Solid Films* **2007**, *515*, 4041.
[26] J. H. Na, M. Kitamura, Y. Arakawa, *Appl. Phys. Lett.* **2008**, *93*, 063501.
[27] S. A. McGill, S. G. Rao, P. Manandhar, P. Xiong, S. Hong, *Applied Physics Letters* **2006**, *89*, 163123.
[28] W. Liu, J. Kang, D. Sarkar, Y. Khatami, D. Jena, K. Banerjee, *Nano Letters* **2013**, *13*, 1983.
[29] M. Lefebvre, Z. Qi, D. Rana, P. G. Pickup, *Chemistry of Materials* **1999**, *11*, 262.
[30] G. Horowitz, R. Hajlaoui, H. Bouchriha, R. Bourguiga, M. Hajlaoui, *Advanced Materials* **1998**, *10*, 923.
[31] K. P. Pernstich, S. Haas, D. Oberhoff, C. Goldmann, D. J. Gundlach, B. Batlogg, A. N. Rashid, G. Schitter, *Journal of Applied Physics* **2004**, *96*, 6431.
[32] J. Zaumseil, H. Sirringhaus, *Chemical Reviews* **2007**, *107*, 1296.
[33] G. Horowitz, *Advanced Materials* **1998**, *10*, 365.
[34] H. Pfleiderer, W. Kusian, *Solid-State Electronics* **1986**, *29*, 317.
[35] U. Zschieschang, R. T. Weitz, K. Kern, H. Klauk, *Applied Physics A* **2009**, *95*, 139.
[36] H. H. Choi, K. Cho, C. D. Frisbie, H. Sirringhaus, V. Podzorov, *Nature materials* **2017**, *17*, 2.
[37] H. Sirringhaus, *Advanced Materials* **2009**, *21*, 3859.
[38] L. Bürgi, T. J. Richards, R. H. Friend, H. Sirringhaus, *Journal of Applied Physics* **2003**, *94*, 6129.
[39] G. K. Reeves, H. B. Harrison, *IEEE Electron Device Letters* **1982**, *3*, 111.
[40] J. Zaumseil, K. W. Baldwin, J. A. Rogers, *Journal of Applied Physics* **2003**, *93*, 6117.
[41] Q. T. Vu, E. Kolawa, L. Halperin, M.-A. Nicolet, *Solid-State Electronics* **1991**, *34*, 279.
[42] M. A. Lampert, *Physical Review* **1956**, *103*, 1648.
[43] M. A. Lampert, A. Rose, R. W. Smith, *Journal of Physics and Chemistry of Solids* **1959**, *8*, 464.

Chapter 5 Charge transport in perylene diimide

5.1 Introduction and scope

High charge carrier mobility is essential to ensure high performance and efficiency in opto-electronic devices such as field-effect transistors, solar cells, and light-emitting diodes.[1,2] The charge carrier mobility in organic semiconductors results from the interplay and optimization of a complex set of physical properties including chemical purity of the material, structure/morphology, energetic disorder, which ultimately are all affected by the molecular design.[3] By studying individual supramolecular assemblies displaying a high degree of crystallinity, we would like to rule out the effect of morphology and defects to charge transport referred as extrinsic disorder, and focus solely on the role of intrinsic disorder. Generally, the intrinsic disorder stems from the large fluctuations of the intermolecular charge transfer integrals.[4] The other source of disorder, called extrinsic disorder, depends on gate insulator dielectric permittivity and on polarizability of the π-conjugated core of the organic semiconductor. In particular, such kind of disorder stems from the coupling to substrate phonons, and randomly oriented distribution of dipoles at the semiconductor/dielectric interface that can negatively influence the transport of charge carriers.[5–7] The charge carrier transport in organic crystals and the relative degree of change delocalization is therefore simultaneously governed by the intrinsic and extrinsic disorder and both contributions must be considered. In the ideal case, it is believed that charge carrier mobility in organic field-effect transistors can increase upon temperature decrease due to temperature-dependent phonon scattering.[8–11] Such behaviour, whose temperature dependence from mobility resembles that observed in inorganic semiconductors such as silicon, is conventionally called band-like transport for organic semiconductors. However, band-like transport cannot be fully understood unless the two sources of disorder, extrinsic and intrinsic, are properly experimentally disentangled.[6,12,13]

Concerning the intrinsic disorder, one could confidently say that charge delocalization is typically favoured by large transfer integrals, reduced electron–phonon coupling and absence of energetic disorder. Hence, these conditions make highly ordered systems such as small-molecule based organic crystals ideal candidates to study delocalized transport. Several experimental and theoretical reports[14,15] have shown that polarons in these systems can be delocalized over a given number of molecules (typically not exceeding 10).

An organic semiconductor with a high degree of charge delocalization has to feature an intrinsically high transfer integral, allowing the charge carrier to form delocalized states. Further, it is important to eliminate (intrinsic) static disorder due to chemical impurities or crystal defects, which often account for deep trap states. It is generally accepted that in the highest mobility organic semiconductor available to date, device optimization has been done in such a way that wave function delocalization is no longer limited by static charge carrier traps but by thermal fluctuations in the transfer integrals, which is referred to as (intrinsic) dynamic disorder. Another important ingredient to characterize high-mobility molecular systems acting as the active layer in thin-film devices is also represented by the simultaneous charge injection optimization and interfacial trapping minimization of charge carrier.[16–19] Several highly-performing organic semiconductors were found to exhibit a band-like transport of the mobility near room temperature.[20–22] This is a strong evidence that dynamic disorder is certainly one of the major factors that hampers charge transport. Hence, reducing dynamic disorder represents a central strategy to be pursued in order to improve the performance of molecular semiconductors. To do so, a suitable prototypical semiconductor must be chosen that presents only subtle differences in, for instance, its lateral termini. In addition, the candidate molecules have not only to feature a very similar molecular structure but also comparable crystal packing.[13,20]

In this chapter, we use two different perylene diimide (PDI) derivatives as a suitable system to unravel the role of the intrinsic vs. extrinsic disorder on band-like transport in organic crystals. By systematic structural, electrical and spectroscopic studies of two different PDIs, we were able to isolate the intrinsic disorder degree that characterizes each single-crystal compound by a combined approach that uses field-effect transistor devices, low-wavenumber

(50-200 cm^{-1}) spectroscopy and simulations. The first derivative, N-N'-bis(n-octyle)-(1,7&1,6)-dicyanoperylene-3,4:9,10-bis(dicarboximide) known as PDI8-CN_2, exposes an alkyl chain on each side,[23] while its fluorinated derivative, N-N'-bis(perfluorobutyl)-(1,7&1,6)-dicyanoperylene-3,4:9,10-bis(dicarboximide) also called as PDIF-CN_2, has a fluorinated one.[24,25] These two molecules feature a very similar molecular structure, but they greatly differ in their charge transport properties.

5.2 Experimental methods

5.2.1 Device preparation

In order to prepare samples, SiO_2/Si-n++ substrates 230-nm exposing to thick SiO_2 surface (purchased from Fraunhofer Institute for Photonic Microsystems IPMS, Dresden, Germany) were first cleaned in ultrasonic bath of acetone followed by a further sonication cycle in propan-2-ol. The substrates were then gently dried with a nitrogen flow. To form the OTS SAM layer, the substrates were exposed to a UV/Ozone atmosphere for 30 min then immediately placed inside a glovebox filled with N_2, and soaked in a solution of 10 mL of anhydrous toluene and 40 µL of octadecyltrichlorosilane (OTS, Sigma Aldrich) in a sealed glass jar. The jar was then heated at 60 °C for 1h and left undisturbed overnight at room temperature. After that, the substrates were removed from solution, rinsed twice in anhydrous toluene following annealing for 1 h at 60 °C. 50 µL of PDI (Polyera Corporation) solution at 1 mg/mL in chloroform (a good solvent for PDIs) were poured into 950 µL of a non-solvent for PDI (acetone for PDI8-CN_2, methanol for PDIF-CN_2). After 20 min, large crystals were formed and precipitated at the bottom of the vial, while smallest crystals were suspended in the middle of the vial. 20 µL of this solution were then taken from the bottom of the vial and drop-cast on non-patterned substrates, leading to the deposition of ~100 µm long single crystals. A homemade shadow mask consisting of metallic wires of different width (25 µm to 150 µm) was placed on the top of a single crystal, with the help of an optical microscope. 40 nm of gold were evaporated through this mask, forming two electrodes over the targeted crystal (Figure 5-1).

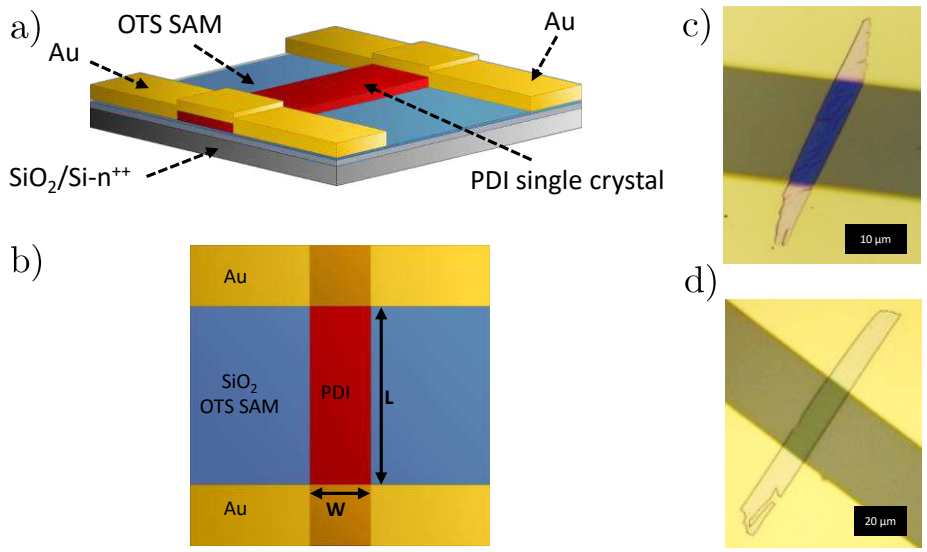

Figure 5-1 Schematic of a PDI based top-contact bottom-gate FET in a) isometric and b) top view. c) and d) are optical images of PDIF-CN_2 and PDI8-CN_2, respectively.

In some cases, longer crystals were needed. To do so, the solvent-induced precipitation process was thermally controlled over few hours. The PDI solutions were injected in an excess of their respective non-solvent, kept at 45 °C. A cooling rate was defined at -0.2 °C/min until reaching the room temperature. As seen Figure 5-2, most of the aggregation occurs within the first two hours, leading to millimetric sized crystals.

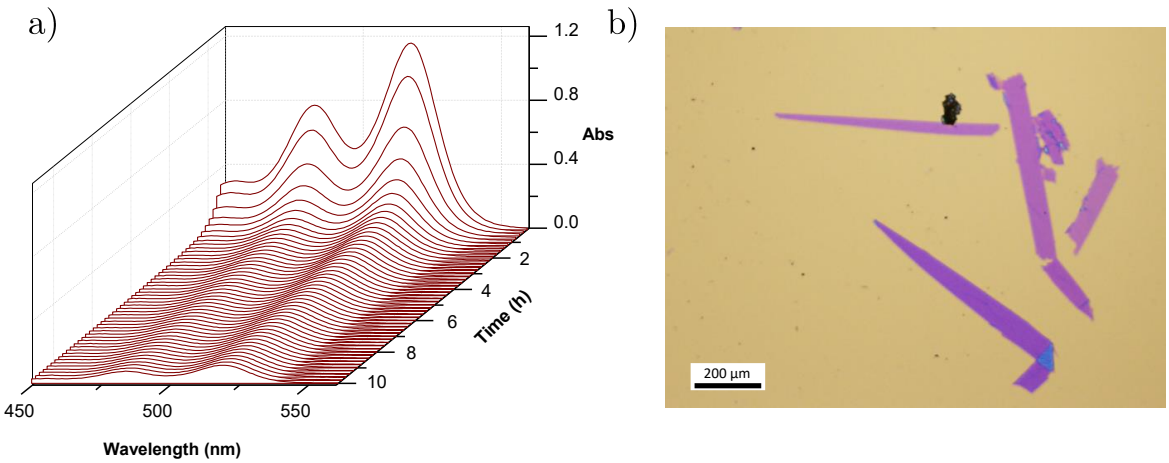

Figure 5-2 a) UV-Vis spectra recorded for PDIF-CN_2 in hot methanol (45 °C) at the beginning of the cooling process, to follow the formation of the crystals that leads to a decrease of the

absorbance. Most of the big crystals are formed after 150 minutes. b) microscopy optical image of the crystals formed with the slow cooling process, deposited on a SiO_2 substrate.

By increasing the temperature, the solubility of PDIs in the non-solvent is slightly increased, leading to less nucleation points for the formation of crystals. This has as consequence the formation of less crystals but with bigger sizes.

5.2.2 Characterization methods

Optical images were obtained with an Olympus BX51. The OTS monolayer was characterized by **water contact angle** (Krüss DSA 100) with 3 µL of milliQ water deposited on its surface. **UV-vis absorbance** in liquid vas recorded with a JASCO V-670 combined with a JASCO PAC-743R sample holder. **Photoluminescence in liquid** was acquired with a Cary eclipse fluorescence spectrophotometer from Agilent Technology. **Photoluminescence of thin-film and single crystal** was recorded with a Renishaw microscope equipped with a 100x objective, combined with a laser at λ_{ex} = 532 nm, providing a spot size around 800 nm. **Electrical measurements** were done in a nitrogen filled glovebox, on a probe station (Cascade Microtech M150) connected to a dual-channel Keithley 2636A sourcemeter. **Electrical measurements at low temperature** were done with a Nitrogen cryostat Oxford Instrument Optistat DN-V from 80 K to 300 K in steps of 10 K, controlled through an ITC503S Cryogenic Temperature Controller and interfaced with a dual-channel Keithley 2636A source-meter. The classical transistor transfer curves were acquired by sweeping the gate voltage (V_G) between -40 V to 40 V when applying a drain voltage (V_D) of 10 V and 40 V applied with a dual channel Keithley 2636A source-meter synchronized with the cryostat through Labview software. **Fluorine Solid state NMR** experiments were done on an AVANCE 500 MHz spectrometer (BrukerTM) operating at a frequency of 470.45 MHz for 19F and equipped with MAS probe designed for 2.5 mm o.d. zirconia rotors. The referencing was done by setting 19F PTFE signal at -122 ppm (room temp). The spectra were treated with Topspin software.

5.3 Results and discussion

First, the functionalization of the surface of SiO_2 substrates with the OTS SAM was monitored by means of water contact angle measurements (Figure 5-3). Previous reports[26] indicate that a contact angle around 110° is typical for OTS based-SAMs, thus it can be used as a gauge to confirm the presence of the monolayer.

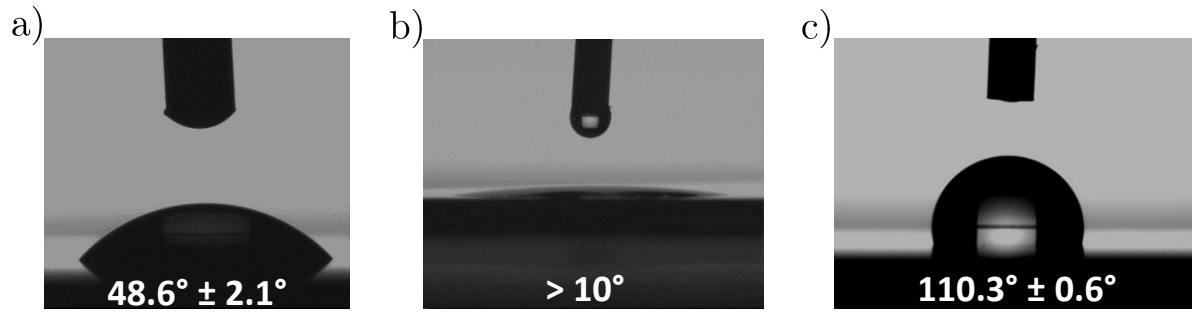

Figure 5-3 Water contact angle of a) thermally growth SiO_2,[27] b) UV/O_3 treated SiO_2 for 5 min of exposition and 25 min of incubation, leading to an increase of the wettability due to the formation of hydroxyl groups at the surface[28] and c), an octadecyltrichlorosilane (OTS) treated SiO_2 that decreases the wettability induced by the alkyl chains on the surface.[26]

To gain insight into the optical properties of both PDIs, UV-vis absorption and emission spectra were recorded in the liquid; the emission spectra was also recorded on spin-coated films and on single crystals (Figure 5-4). Absorption and emission spectra acquired in solutions of the two PDIs were similar, except for a very small red-shift of PDI8-CN_2, indicating that the lateral chains of the PDI do not crucially affect the properties of the molecules. The spin-coated films displayed roughly the same emission than in solution, even if the spectra of PDIF-CN_2 film is a bit broader compared to PDI8-CN_2, which is due to the fact that the films are composed of small crystalline domains that dominate the emission.[29]

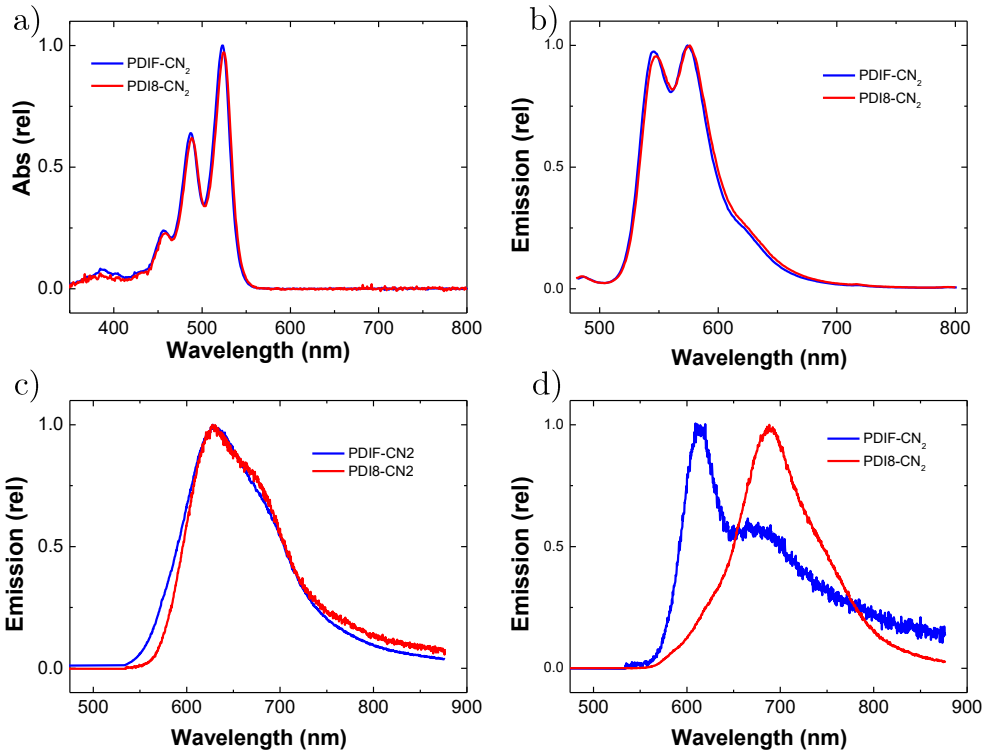

Figure 5-4 a) normalized UV-vis absorbance spectra of PDIF-CN_2 and PDI8-CN_2 in $CHCl_3$ (0.002 mg.mL-1) and b) their related emission spectra. c) normalized emission spectra of spin-coated PDIF-CN_2 and PDI8-CN_2 films on SiO_2 substrates (2 mg.mL^{-1} in $CHCl_3$ 1500 rpm 2500 rpm.sec^{-1} 30 sec) and d), normalized emission spectra of PDIF-CN_2 and PDI8-CN_2 single crystal.

The electrical properties of thin-films made with the two molecules were explored by fabricating bottom-gate top-contact OFETS. Both compounds exhibit ideal *n*-type properties, as depicted Figure 5-5 a-b), with a higher mobility for PDIF-CN_2 than PDI8-CN_2 by almost one order of magnitude. When measured at different temperatures, PDIF-CN_2 exhibited a band-like transport mechanism.[7] PDI8-CN_2, however, seems to follow a purely thermally-activated behaviour over the measurement temperature range (80 K – 300 K), which complies to a multiple trap and release (MTR) model, considering the high degree of crystallinity achieved here. Indeed, the charge transport in PDI8-CN_2 is characterized by an exponential dependence of the field-effect mobility on the temperature.[30] Such behaviour is typical when charge carriers are temporary trapped and localized on energy states within the band-gap. These states in the gap can act as charge traps with different energy; some are energetically close to the HOMO

or LUMO (typically by few k_BT) and can release a charge through thermal activation (called shallow traps) while other states are localized deeper in the gap (also called deep traps).[31] Since the transport measurements on both PDI derivatives were carried out in three-terminal devices, the contact resistance was extracted through a classical transfer line method. This value was found to be higher in PDI8-CN_2 than in PDIF-CN_2 devices. Indeed, at room temperature, the contact resistance with PDIF-CN_2 is about tens of MΩ.µm while the for PDI8-CN_2 it amounts to ca. 1 GΩ.µm. This result is in accordance with the energy diagram that will be discussed later.

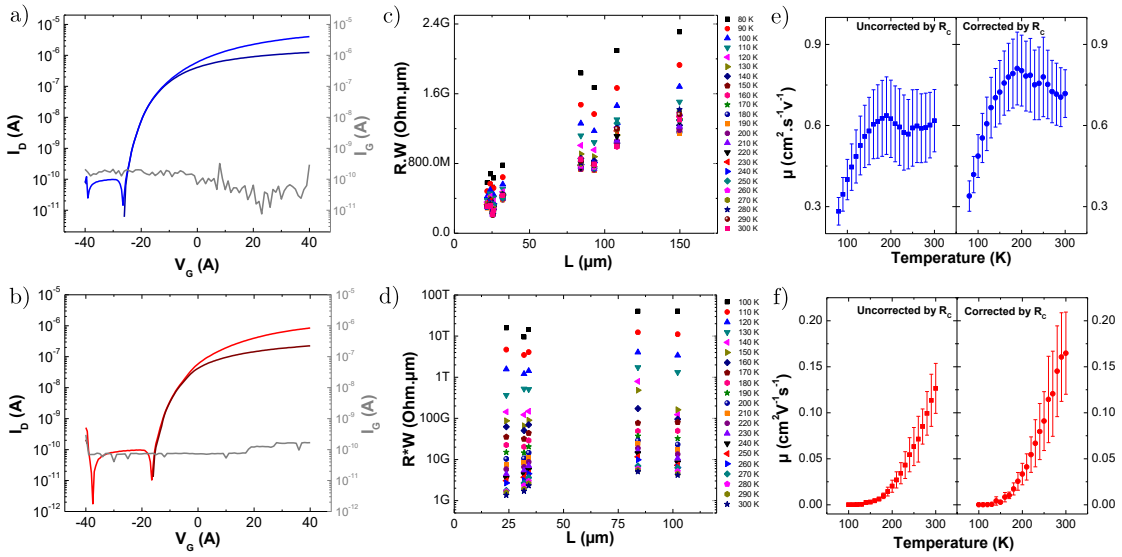

Figure 5-5 a) and b) are room-temperature transfer curves (V_D = 10 V and 40 V) of PDIF-CN_2 and PDI8-CN_2, respectively, with c) and d) their corresponding TLM plots. e) and f) display the evolution of the mobility as a function of the temperature, with and without the contact resistance correction, for PDIF-CN_2 and PDI8-CN_2.

For a careful and reliable extraction of the field-effect mobility in our devices, the resulting transfer curves of both compounds were analysed in terms of ideality as *n*-type semiconductor through the reliability factor r_{lin}, maximum power density P_{max} and maximum current density J_{SD}^{max} (Table 1).[32]

	r_{lin} (%)	P_{max} ($W.cm^{-2}$)	J_{SD}^{max} ($A.cm^{-2}$)
PDIF-CN₂	92.9	3.12	25.7
PDI8-CN₂	104	0.63	7.38

Table 1 Reliability factor in linear regime r_{lin}, maximum power density P_{max} and maximum current density J_{SD}^{max} calculated for PDIF-CN₂ and PDI8-CN₂.[32]

PDIF-CN₂ and PDI8-CN₂, in these devices, exhibit a text-book behaviour with a reliability factor close to 100% which is the ideal case, recorded at moderate maximum power and current density.

In order to analyse the intrinsic static disorder generated by the presence of trap states in the crystals, the trap density was extracted in both compounds with the help of the space-charge-limited current analysis (Figure 5-6).[33,34]

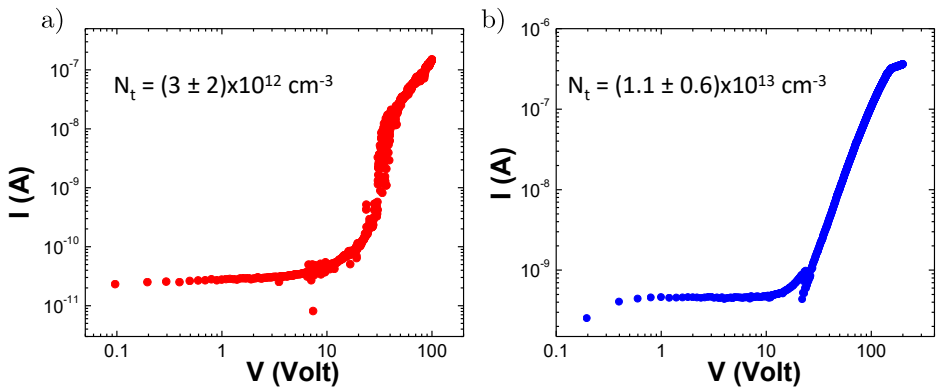

Figure 5-6 Current-voltage trace for a) PDI8-CN₂ and b) PDIF-CN₂ with different current regimes. The first one is the ohmic regime then the trap-filling transition appears leading to the Child's law region.[18,19] **The trap density N_t was extracted over a few samples with the voltage where the trap-filling transition finished. It is roughly three times more important in PDIF-CN₂ than in PDI8-CN₂.**

PDI8-CN₂ crystals were found to exhibit comparable trap density (3 times lower) to the one of PDIF-CN₂ crystals. This further experimental evidence allows to state that the significant

differences in transport regimes observed in our molecular systems do not stem from a difference in trap density while pointing out to the analysis of the intrinsic dynamic disorder as the key to understand the experimental observations.

The findings on the differences in contact resistance described above are fully consistent with the energy levels characterization performed by **Prof. L. Pasquali (Modena)** and **Dr. M. Nardi (Trento)**, through ultraviolet photoelectron spectroscopy (UPS) and electron energy loss spectroscopy (EELS) in single crystals, being therefore fully comparable with the device case, which uses single crystals as the active layer (Figure 5-7). As expected by simply looking at their respective molecular structure, the band gap of PDI8-CN_2 and PDIF-CN_2 are nearly equivalent but they were found to be shifted by 0.70 eV, making charge electron injection more favourable from PDIF-CN_2 thanks to the reduction of the energy barrier between Au work function and its LUMO.

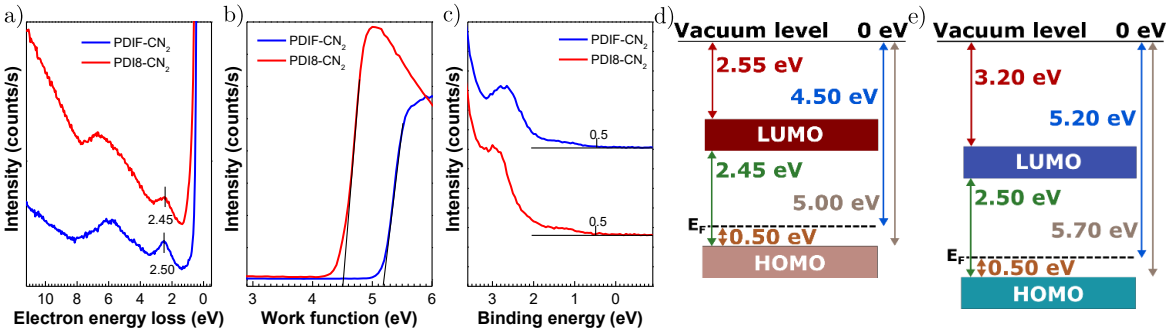

Figure 5-7 a) EELS spectra of PDIF-CN_2 and PDI8-CN_2. The numbers reported on the figure correspond to the energy difference between the primary beam and the energy of the first loss structure. The HOMO-LUMO transition correspond to 2.50 eV for PDIF-CN_2 and 2.45 eV for PDI8-CN_2. b) is the work function variation of PDIF-CN_2 and PDI8-CN_2 as measured from the low energy cutoff, and c) their valence band. d) and e) are the energy diagrams of PDI8-CN_2 and PDIF-CN_2, respectively.

Structural analysis on the crystals, performed by **Dr. F. Liscio (Bologna)** and **Dr. N. Demitri (Trieste),** confirmed the bulk structure, slipped-stacks for PDI8-CN_2 and bricklayer for PDIF-CN_2 (Figure 5-8), with only one molecule per primitive cell, which has been highlighted to be uncommon for small molecule semiconducting materials.[1,13,20]

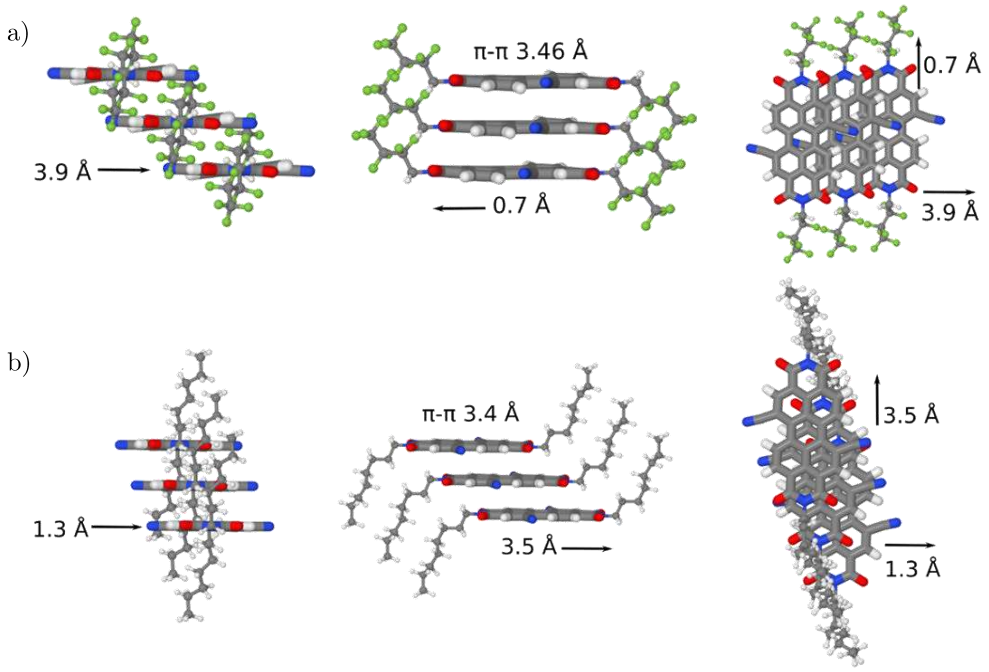

Figure 5-8 Sides and top views of the crystal structure of a) PDIF-CN_2 and b) PDI8-CN_2.

To rule out any possible phase transition upon temperature in determining the band-like behaviour of PDIF-CN_2, temperature-dependent X-ray diffraction measurements on powder (Figure 5-9) and single-crystals (Figure 5-10) were also performed.

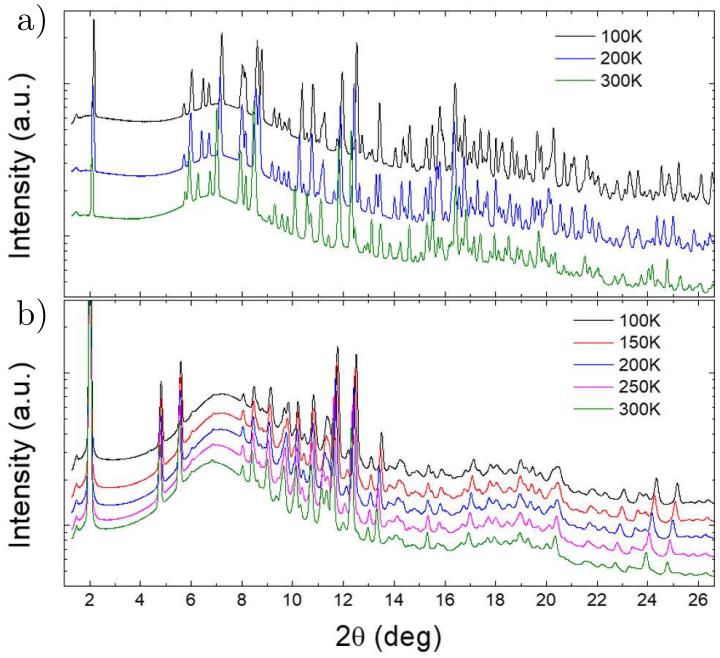

Figure 5-9 a) Diffraction patterns of a) PDIF-CN_2 and b) PDI8-CN_2 powder recorded at different temperatures, splitting and shifts of some Bragg peaks in the diffraction patterns during thermal treatment indicate a small anisotropic contraction of the unit cell.

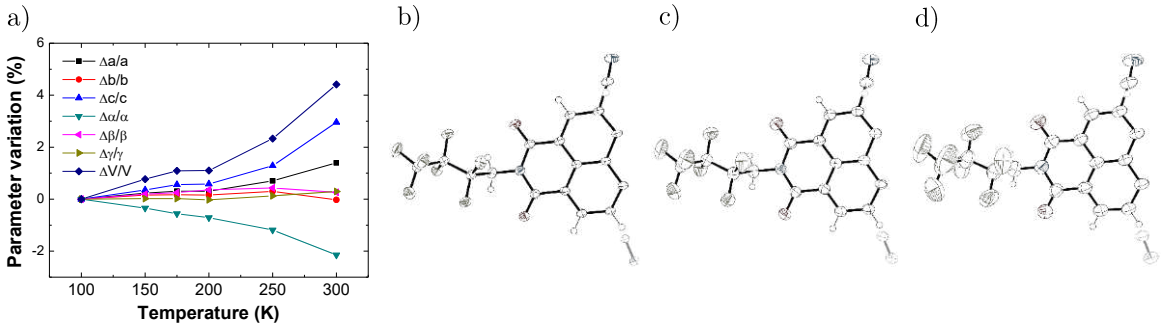

Figure 5-10 a) Variation of the lattice parameter *a*, *b*, *c*, α, β, γ, and volume (V) during the thermal annealing of PDIF-CN_2 single crystals, with the strongest variation being the expansion by 3% of the c-axis from 100 K to 300 K, which lead the volume to increase by 4.4%. Ellipsoids representation of molecular structures (50% probability) of PDIF-CN_2 at b) 100 K c), 200 K and d) 300 K.

The known triclinic crystalline form has been confirmed[24] and, excepted a thermal modification of the volume of the unit cell by 4.4%, no phase transition has been detected upon temperature ramping down to 100 K and up, back to room temperature. The same crystalline packing and

PDI side-chains conformations are preserved in the whole temperature range explored: the two molecular systems exhibit equivalent geometries of the side-chains and PDI cores, and can be perfectly superimposed, as quantified by a root-mean-square deviation (RMSD) of the atomic positions below 0.05 Å.

With the help of **Dr. J. Raya and Dr. J. Wolf (Strasbourg)**, we additionally performed temperature-dependent solid-state MAS-NMR on the fluorine atoms of the PDIF-CN_2, to bestow more information on the lateral chains (Figure 5-11).[35] The constant values of both chemical shifts indicate that the environment of the fluorine atoms is not changing when cooling down. Any phase transition would appear in the change of the chemical shift anisotropy or by the appearance/disappearance of peaks.[36] The observed increase in the noise can be ascribed to the reduction of the spinning rate below 220 K from 20 kHz to 15.140 kHz required to help for cooling down the sample.

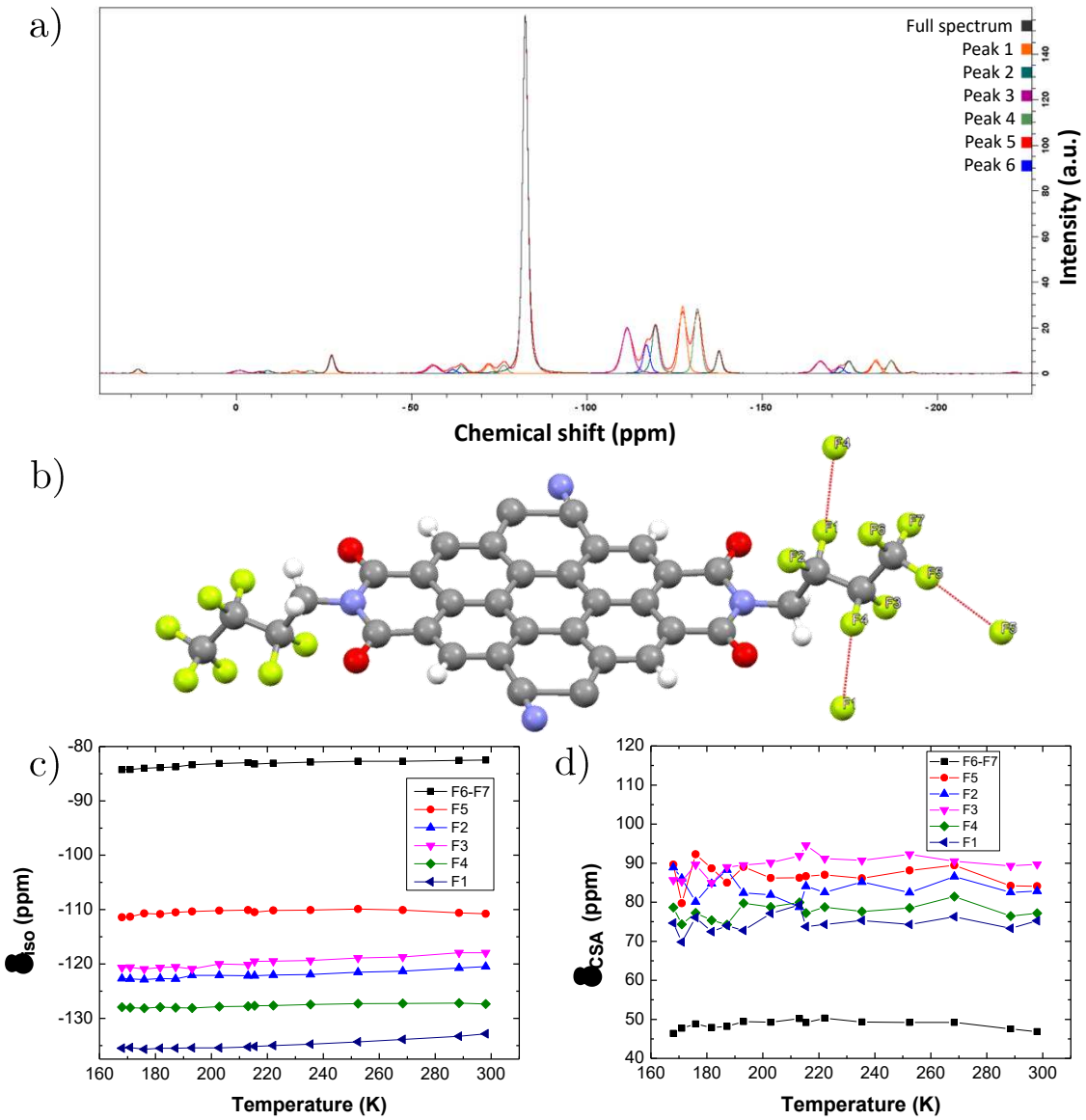

Figure 5-11 a) F^{19} Magic-angle spinning (MAS) solid-state NMR spectrum of PDIF-CN_2 at 298 K, with a spinning rate of 20 kHz, showing the deconvolution of 6 peaks. b) structure of PDIF-CN_2 with specific labels on the fluorine atoms, c) and d), evolution of the chemical shift and the chemical shift anisotropy (CSA) respectively, of the 6 groups of atoms chemically equivalent, between 298 K and 167 K, extracted from the spectra.

One strategy to reduce dynamic disorder consists in increasing the robustness of the transfer integrals to molecular vibrations which is equivalent to reducing the electron–phonon coupling.[37] To do so, one should reduce the intermolecular displacements, which could amount up to 0.5 Å at T_{amb},[38] and are able to modulate the corresponding transfer integral of about the same order of magnitude as the transfer integral itself.[39] Because the time scale at which

charge delocalization occurs is about one hundred times shorter (ca. 10 fs) than that of the intermolecular vibrations (ca. 1 ps), charge carriers can be temporarily localized in dynamically-generated molecular configurations with reduced transfer integrals. Hence, the frequency of the intermolecular vibrations, inversely proportional to the charge carrier mobility, is a crucial parameter. In particular, low-frequency (below 200 cm^{-1}) large-amplitude vibrations are the most harmful ones for charge transport.

In order to access to the vibrational landscape of both compounds at low energy (below 200 cm^{-1}), we studied the low-frequency vibrations of both compounds as a mean to understand the different transport mechanisms observed experimentally. Towards this end, we employed two complementary techniques i.e. terahertz spectroscopy (i.e., a direct vibrational spectroscopy in the terahertz frequency range, conventionally up to 10 THz / ~ 40 meV) performed by **X. Jin, Dr. Y.-G. Jeong** and **Prof. L. Razzari (Québec)** and temperature-resolved inelastic neutron scattering (INS) realised by **Dr. M. Zbiri (Grenoble)** and **Dr. A. Y. Guilbert (London),** in combination with modeling and simulations, achieved by **Dr. D. Dudenko, Dr. V. Lemaur, Dr. G. D'avino, Dr. Y. Olivier** and **Dr. D. Beljonne (Mons)**.

Despite the limitations of THz spectroscopy due to the selection rules, we used such technique to map the (dipolar optical) phonon activity. In addition, we carried out THz spectroscopy measurements on samples having the same thickness (1 µm), thus allowing a quantitative comparison between the (dipole-active) phonon response of the two different compounds. As a result, THz spectroscopy allows to access, and contains more information on carbon–carbon, and carbon–nitrogen than the associated INS spectra, for which the observed peaks have to be weighted by the motions of hydrogen atoms. INS provides the most low-energy information for all samples, but INS has the worst resolution at high energy amongst all the techniques. In summary, INS offers a better alternative when it comes to explore both the external (phonons or lattice dynamics) and internal (molecular vibrations) modes as INS covers the whole Brillouin zone without the constraint of selection rules. Neutrons interact with samples nuclei and the resulting intensities are weighted by the ratio σ/M where σ is the nuclear cross section and M the mass of the scatterer, respectively. Therefore, in hydrogenated materials, the vibrational spectrum can be expected to be dominated by the dynamical density of freedoms

(d.o.f.) involving hydrogen motions (the lightest element with the highest cross section). As a result, INS and THz spectroscopy techniques combined with theoretical simulations are optimal tools to identify the phonons responsible for charge localization.

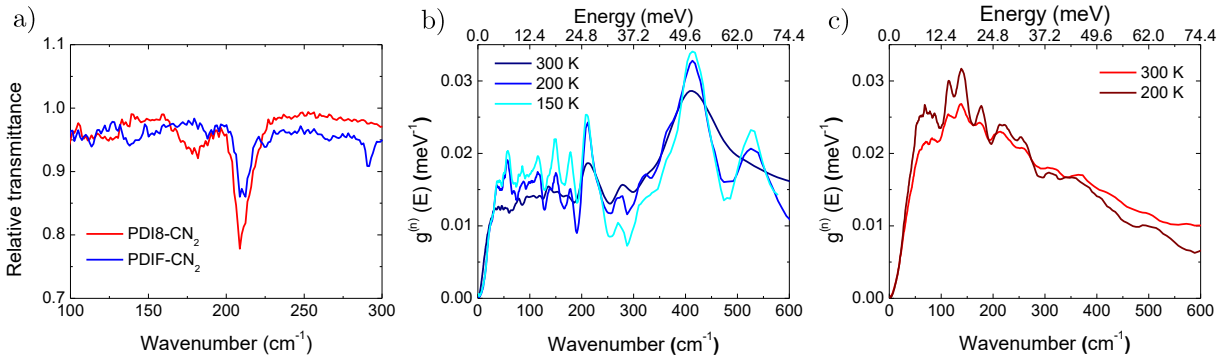

Figure 5-12 a) comparative study of PDIF-CN_2 (in blue) and PDI8-CN_2 (in red) by Terahertz spectroscopy (the spectra were normalized by the sample's thickness). b) and c) are inelastic neutron scattering spectra of PDIF-CN_2 and PDI8-CN_2 respectively, recorded at different temperatures.

As can be seen Figure 5-12 a) reveals that the transmission dips in the THz spectra in the 100-300 cm^{-1} range, corresponding to resonant vibrations, are more pronounced for PDI8-CN_2 than PDIF-CN_2. At low wavenumbers (< 200 cm^{-1}), INS revealed a more well-defined phonon structure of PDIF-CN_2 as compared to PDI8-CN_2. While it is expected that the vibrational peaks become more resolved when lowering the temperature due to a reduced effect of the Debye-Waller factor, low-energy modes below 145 cm^{-1} become distinguishable below 300 K in the case of PDIF-CN_2. Also, a new vibrational feature appears at 545 cm^{-1} in the generalized density of states $g^n(E)$ of PDIF-CN_2. It must be emphasized here that the INS spectrum of PDI8-CN_2 is going to be dominated by vibrational density of freedoms of hydrogen atoms, mainly present on the side chains that are less ordered than the conjugated part of the molecule (Figure 5-13).

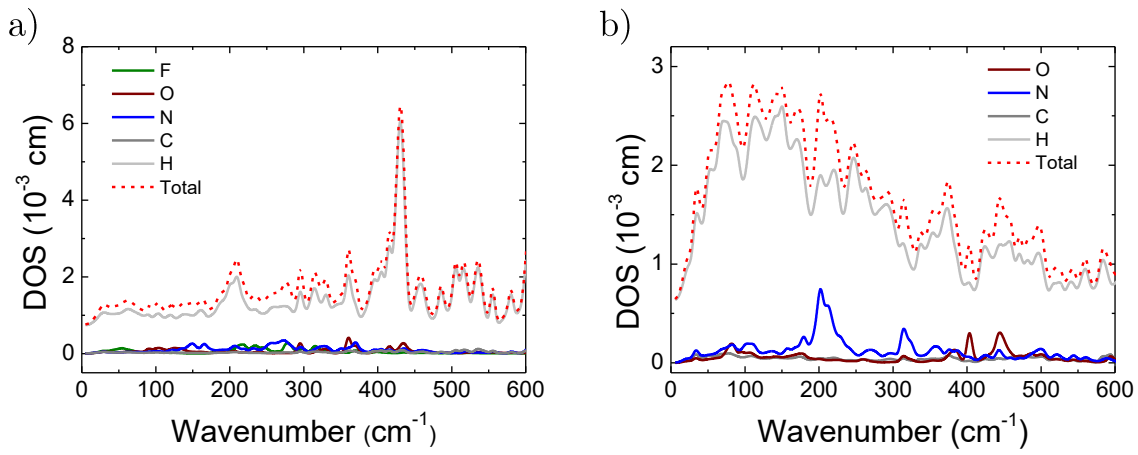

Figure 5-13 Simulated atomic contribution to inelastic neutron scattering spectra of a) PDI8-CN_2 and b) PDIF-CN_2.

Thus, it is possible to compare the temperature evolution of the INS spectra of each material, while it is hardly possible to make a direct comparison between the spectra of PDI8-CN_2 and PDIF-CN_2. Simulations were used to further understand the difference of transport between PDI8-CN_2 and PDIF-CN_2 at 300 K since neither INS nor THz spectroscopy include direct interaction of phonons with charges. At this temperature, PDIF-CN_2 exhibits band-like transport while PDI8-CN_2 exhibits temperature-activated transport. As a first step to validate the theoretical model used to describe charge transport, the INS spectra were simulated at 300 K, and compared to experimental results (Figure 5-14), showing good agreement between calculated and experimental spectra.

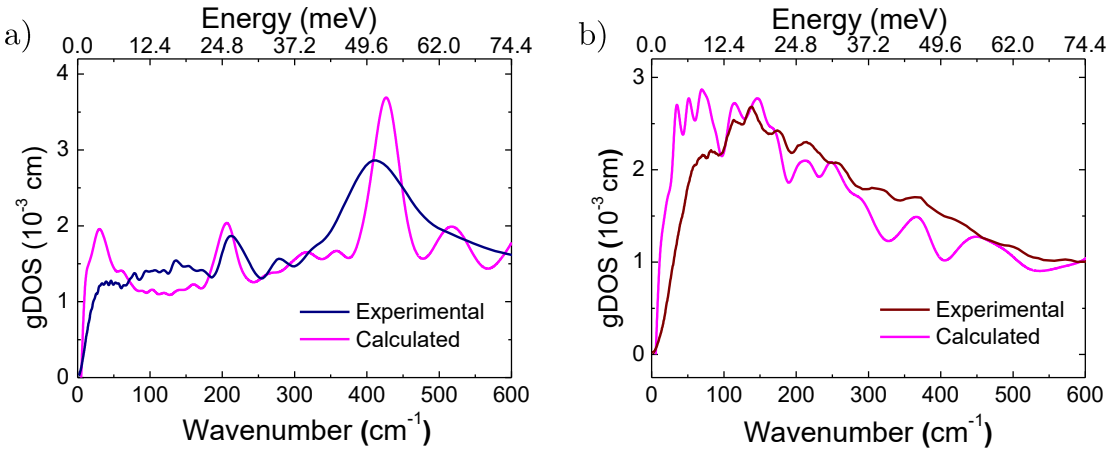

Figure 5-14 Inelastic neutron spectra of a) PDIF-CN_2 and b) PDI8-CN_2 at 300 K, and compared to simulated ones by MD that are neutron weighted.

A closer analysis of molecular displacements at low wavenumber for both PDI derivatives helps to map out the origin of this feature. The molecular displacements along the different molecular axes can be extracted from these spectra (Figure 5-15).

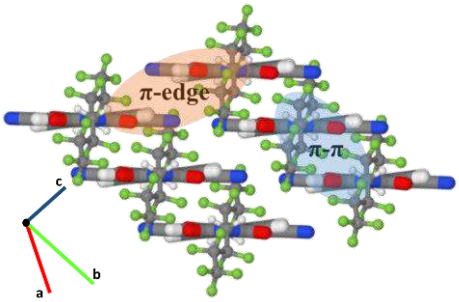

		$\langle d_a \rangle$ (Å)	σ_{d_a}(Å)	$\langle d_b \rangle$ (Å)	σ_{d_b}(Å)	$\langle d_c \rangle$ (Å)	σ_{d_c}(Å)
PDIF-CN_2	π-π	5.232	0.138	0.082	0.061	0.110	0.082
	π-edge	5.232	0.143	7.638	0.107	0.100	0.078
PDI8-CN_2	π-π	5.019	0.159	0.153	0.109	0.149	0.115
	π-edge	5.019	0.181	8.841	0.181	0.144	0.111

Figure 5-15 Representation of the π-π and π-edge directions on PDIF-CN_2 structure and the directions along the a, b and c-axes. The adjacent table is reporting the analysis in terms of molecular displacements between two dimers along the crystalline axes, recorded along the molecular dynamic trajectory for the π-π and π-edge directions for both PDIF-CN_2 and PDI8-CN_2. The standard deviations of the displacements along the different molecular axis are highlighted in colour. The largest molecular displacements occur along the π stacking direction. PDI8-CN_2 displacements exhibit larger standard deviation compared to PDIF-CN_2.

The largest ones occur along the π- π stacking direction and the largest standard deviation for all the displacements occurs for PDI8-CN_2. This can be decomposed into molecular displacements present at certain energies (Figure 5-16), showing the vibrational modes that are responsible for the charge localization. MD simulation is used to capture the molecular motions in the lattice, and charge integrals between pairs of molecules extracted from the MD simulation at constant intervals are calculated using DFT. Hence, Fourier transform of the autocorrelation function of the calculated charge integrals captures possible electron-phonon interactions. The intensity of the FFT peaks at low wavenumbers are much larger for PDI8-CN_2. This confirms that temperature-activated transport is observed when phonons are active.

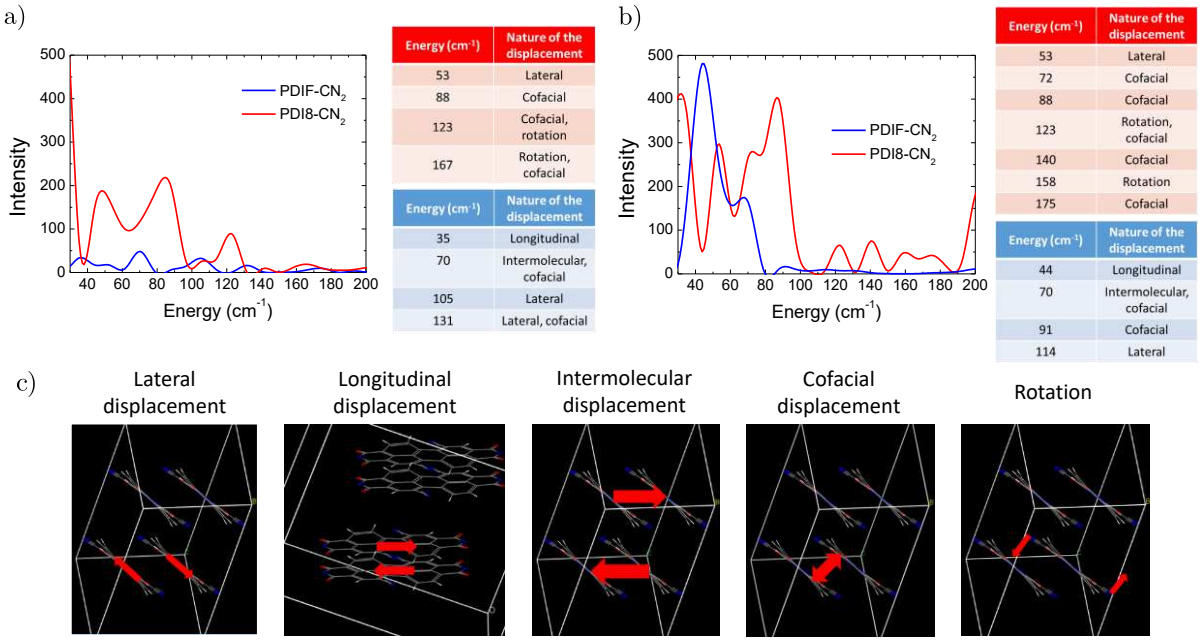

Energy (cm-1)	Nature of the displacement
53	Lateral
88	Cofacial
123	Cofacial, rotation
167	Rotation, cofacial

Energy (cm-1)	Nature of the displacement
35	Longitudinal
70	Intermolecular, cofacial
105	Lateral
131	Lateral, cofacial

Energy (cm-1)	Nature of the displacement
53	Lateral
72	Cofacial
88	Cofacial
123	Rotation, cofacial
140	Cofacial
158	Rotation
175	Cofacial

Energy (cm-1)	Nature of the displacement
44	Longitudinal
70	Intermolecular, cofacial
91	Cofacial
114	Lateral

Figure 5-16 Fast Fourier Transform (FFT) of the autocorrelation function along a) the π-π direction and b) the π-edge direction. This plot is a measurement of the remarkably different electron-phonon coupling in crystals of PDI8-CN_2 and PDIF-CN_2, respectively (room temperature). c) Representation of the different types of displacements occurring at low energy in the PDI structure.

From these results, one can see that the low-energy molecular vibrations are mostly lateral and cofacial for PDI8-CN_2 but are first longitudinal for PDIF-CN_2, with the lateral ones appearing at higher energy. This would suggest that the effect of the fluorinated lateral chains, by changing the molecular packing, is affecting the molecular vibrations; these interactions lock the molecular structure, shifting specific vibrations to higher energies and minimizing their intensity, providing a more robust and coherent molecular structure. This locking of the structure should ensure more stable transfer integral by reducing their fluctuations. These transfer integrals are computed along the π-π stacking direction but also along the π-edge one, for both compounds. π-π interactions were found to be of particular relevance for PDI8-CN_2 (Figure 5-17).

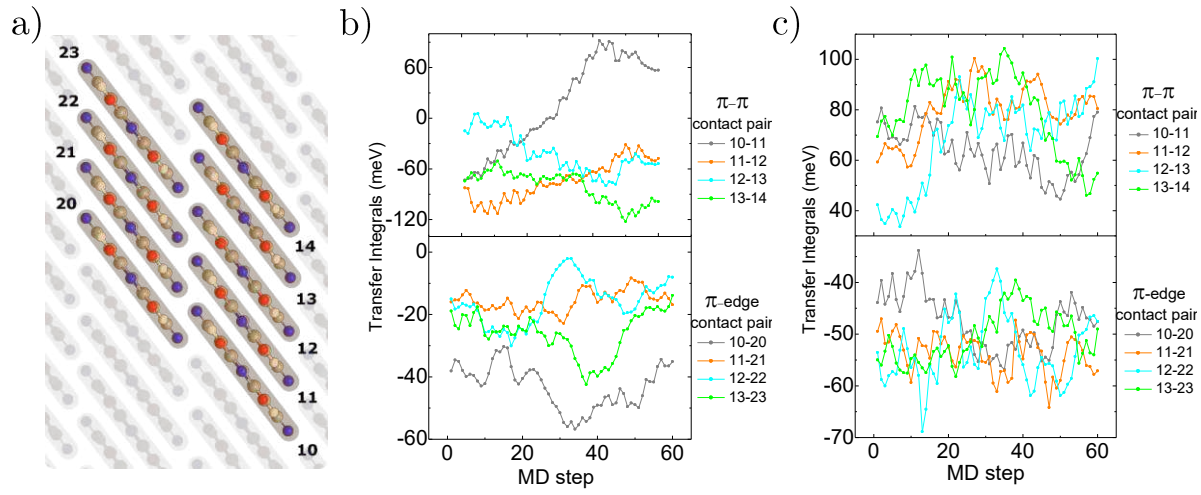

Figure 5-17 a) Representation of a typical PDI packing structure along the PDI core. The lateral chains were removed for clarity. Evolution of the transfer integral (LUMO) over time for b) PDI8-CN_2 and c) PDIF-CN_2, with a MD step of 5.0 fs.

Moreover, the fluctuations of the transfer integral in PDIF-CN_2, which are induced by the lattice vibrations, are always smaller than those measured at the equilibrium, contrary to PDI8-CN_2. This parameter is in accordance with the experimental observation; indeed, a transfer integral that punctually fluctuates at the same value of its average value leads to localized charges[40] since the characteristic time of a lattice vibration is about 100 times larger compared to the one of the charge.[4,41] Nevertheless, the localization length is estimated to be ca. 11 molecules for PDIF-CN_2 and ca. 3 for PDI8-CN_2 (Figure 5-18).

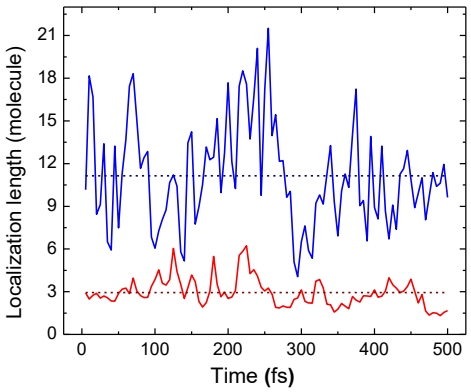

Figure 5-18 Localization length over time: charge carriers are delocalized over ca. 11 PDIF-CN_2 molecules. Conversely, charge carriers are localized only over ca. 3 molecular units in the case of PDI8-CN_2.

This is easily justified by the more intense vibrational spectra amplitude and by the larger displacements along the different molecular axis, as demonstrated above, confirming the stronger influence of the intermolecular vibration and the charge transport in PDI8-CN_2 compared to PDIF-CN_2 through the larger transfer integrals distribution of the former.

5.4 Conclusion

In summary, we performed a systematic and comparative study of charge transport in two PDI derivatives characterized by a subtle change in the side chains. The charge transport in PDIF-CN_2 and PDI8-CN_2 solution-grown single crystals was analyzed through electrical, structural, and spectroscopic characterizations such as THz spectroscopy and inelastic neutron scattering. Our findings were further supported by calculations. We have observed that the differences in transport mechanism between band-like for PDIF-CN_2 and hopping for PDI8-CN_2 can be ascribed to the different phononic activity at low energy. The more pronounced phonon modes intensity of PDI8-CN_2 described by certain molecular displacements justifies the larger transfer integral distributions and the higher degree of charge localization which results in the thermally activated charge transport. A subtle change in the packing of PDIF-CN_2 makes the intermolecular interactions robust enough to avoid fluctuations of charge transfer integral, associated with a reduced intensity of the phonon modes with the respect to PDI8-CN_2 and the shifting of some modes to higher energies, making it possible for electrons to be delocalized over a fairly large number of molecules. Hence, our experimental results coupled with simulations can be used to screen molecular semiconductors to predict a set of high-performance materials, therefore significantly contributing to a more refined chemical design for next-generation electronics materials.

5.5 References

[1] O. Ostroverkhova, *Chemical Reviews* **2016**, *116*, 13279.
[2] H. Sirringhaus, *Advanced Materials* **2014**, *26*, 1319.
[3] G. Schweicher, Y. Olivier, V. Lemaur, Y. H. Geerts, *Isr. J. Chem.* **2014**, *54*, 595.
[4] A. Troisi, G. Orlandi, *Phys. Rev. Lett.* **2006**, *96*, 086601.
[5] T. Richards, M. Bird, H. Sirringhaus, *The Journal of Chemical Physics* **2008**, *128*, 234905.

[6] I. N. Hulea, S. Fratini, H. Xie, C. L. Mulder, N. N. Iossad, G. Rastelli, S. Ciuchi, A. F. Morpurgo, *Nature Materials* **2006**, *5*, 982.

[7] N. A. Minder, S. Lu, S. Fratini, S. Ciuchi, A. Facchetti, A. F. Morpurgo, *Adv. Mater.* **2014**, *26*, 1254.

[8] S. H. Glarum, *Journal of Physics and Chemistry of Solids* **1963**, *24*, 1577.

[9] L. Friedman, *Physical Review* **1965**, *140*, A1649.

[10] V. Coropceanu, J. Cornil, D. A. da Silva Filho, Y. Olivier, R. Silbey, J.-L. Brédas, *Chemical Reviews* **2007**, *107*, 926.

[11] J.-D. Picon, M. N. Bussac, L. Zuppiroli, *Phys. Rev. B* **2007**, *75*, 235106.

[12] J. Veres, S. d. Ogier, S. w. Leeming, D. c. Cupertino, S. Mohialdin Khaffaf, *Adv. Funct. Mater.* **2003**, *13*, 199.

[13] I. Y. Chernyshov, M. V. Vener, E. V. Feldman, D. Y. Paraschuk, A. Y. Sosorev, *The Journal of Physical Chemistry Letters* **2017**, *8*, 2875.

[14] V. Podzorov, E. Menard, J. A. Rogers, M. E. Gershenson, *Phys. Rev. Lett.* **2005**, *95*, 226601.

[15] J.-F. Chang, T. Sakanoue, Y. Olivier, T. Uemura, M.-B. Dufourg-Madec, S. G. Yeates, J. Cornil, J. Takeya, A. Troisi, H. Sirringhaus, *Phys. Rev. Lett.* **2011**, *107*, 066601.

[16] G. Horowitz, P. Delannoy, *Journal of Applied Physics* **1991**, *70*, 469.

[17] N. Benson, C. Melzer, R. Schmechel, H. von Seggern, *physica status solidi (a)* **2008**, *205*, 475.

[18] H. Klauk, *Chem. Soc. Rev.* **2010**, *39*, 2643.

[19] J. Mei, Y. Diao, A. L. Appleton, L. Fang, Z. Bao, *Journal of the American Chemical Society* **2013**, *135*, 6724.

[20] Y. Krupskaya, M. Gibertini, N. Marzari, A. F. Morpurgo, *Advanced Materials* **2015**, *27*, 2453.

[21] D. He, J. Qiao, L. Zhang, J. Wang, T. Lan, J. Qian, Y. Li, Y. Shi, Y. Chai, W. Lan, L. K. Ono, Y. Qi, J.-B. Xu, W. Ji, X. Wang, *Sci Adv* **2017**, *3*, 1.

[22] X. Xu, Y. Yao, B. Shan, X. Gu, D. Liu, J. Liu, J. Xu, N. Zhao, W. Hu, Q. Miao, *Advanced Materials* **2016**, *28*, 5276.

[23] B. Yoo, T. Jung, D. Basu, A. Dodabalapur, B. A. Jones, A. Facchetti, M. R. Wasielewski, T. J. Marks, *Applied Physics Letters* **2006**, *88*, 082104.

[24] B. A. Jones, M. J. Ahrens, M.-H. Yoon, A. Facchetti, T. J. Marks, M. R. Wasielewski, *Angewandte Chemie International Edition* **2004**, *43*, 6363.

[25] A. S. Molinari, H. Alves, Z. Chen, A. Facchetti, A. F. Morpurgo, *J. Am. Chem. Soc.* **2009**, *131*, 2462.

[26] S. A. Mirji, *Surface and Interface Analysis* **2006**, *38*, 158.

[27] R. G. Frieser, *Journal of The Electrochemical Society* **1974**, *121*, 669.

[28] H. Wang, B. Yu, S. Jiang, L. Jiang, L. Qian, *RSC Advances* **2017**, *7*, 39651.

[29] B. Gieseking, T. Schmeiler, B. Müller, C. Deibel, B. Engels, V. Dyakonov, J. Pflaum, *Physical Review B* **2014**, *90*, DOI 10.1103/PhysRevB.90.205305.

[30] J. Rivnay, L. H. Jimison, J. E. Northrup, M. F. Toney, R. Noriega, S. Lu, T. J. Marks, A. Facchetti, A. Salleo, *Nature Materials* **2009**, *8*, 952.

[31] G. Horowitz, M. E. Hajlaoui, R. Hajlaoui, *Journal of Applied Physics* **2000**, *87*, 4456.

[32] H. H. Choi, K. Cho, C. D. Frisbie, H. Sirringhaus, V. Podzorov, *Nature materials* **2017**, *17*, 2.

[33] V. Podzorov, S. E. Sysoev, E. Loginova, V. M. Pudalov, M. E. Gershenson, *Applied Physics Letters* **2003**, *83*, 3504.

[34] M. A. Lampert, A. Rose, R. W. Smith, *Journal of Physics and Chemistry of Solids* **1959**, *8*, 464.

[35] Z. Liu, J. D. Goddard, *The Journal of Physical Chemistry A* **2009**, *113*, 13921.

[36] K. Aimi, S. Ando, *Polymer Journal* **2012**, *44*, 786.

[37] S. Fratini, D. Mayou, S. Ciuchi, *Advanced Functional Materials* **2016**, *26*, 2292.

[38] A. S. Eggeman, S. Illig, A. Troisi, H. Sirringhaus, P. A. Midgley, *Nature Materials* **2013**, *12*, 1045.

[39] A. Troisi, G. Orlandi, *J. Phys. Chem. A* **2006**, *110*, 4065.

[40] A. Troisi, G. Orlandi, J. E. Anthony, *Chem. Mater.* **2005**, *17*, 5024.

[41] S. Illig, A. S. Eggeman, A. Troisi, L. Jiang, C. Warwick, M. Nikolka, G. Schweicher, S. G. Yeates, Y. Henri Geerts, J. E. Anthony, H. Sirringhaus, *Nature Communications* **2016**, *7*, 10736.

Chapter 6 Fine tuning of the electrical properties of 2D materials

6.1 Introduction

2D Materials (2DMs) are emerging as a potential alternative to silicon for the next-generation electronics.[1,2] While the zero-bandgap of graphene hampers its application as a digital switch but still demonstrate high-mobilities and promising sensing properties[3,4], the family of transition metal dichalcogenides (TMDCs) includes semiconducting layered compounds with a bandgap in the visible range,[5–7] which can be exfoliated to the single-layer limit and employed as active materials in high-performance field effect transistors (FETs).

For instance, WSe_2 holds great potential for complementary digital logic applications,[8] since it is an almost intrinsic semiconductor that can sustain both hole[9–14] and electron[15,16] transport. Indeed, almost ideal ambipolar characteristics were measured in bulk WSe_2 crystals with high *p*- and *n*-type mobility.[17–19] At single or few layer limit, high performance FETs were achieved by employing unconventional metal electrodes (such as Pd,[11,14] In[15] or Ag[20]) with an optimal work function to match either the conduction or the valence band of WSe_2, ensuring almost-ohmic injection for one charge carrier type, but almost blocked injection for the other, leading to unipolar transport.[11,21] Moreover, the highest (unipolar) mobilities reported for single layer WSe_2 ($\mu_h > 200$ $cm^2V^{-1}s^{-1}$, $\mu_e > 250$ $cm^2V^{-1}s^{-1}$)[11,15] were demonstrated by using sophisticated device architectures, in which WSe_2 was interfaced with high-k dielectrics[15,19] and/or encapsulated. On the contrary, very poor performances are achieved when conventional device configurations are employed. For instance, mobility below 0.1 $cm^2V^{-1}s^{-1}$ is measured in single layer WSe_2 FET contacted by Au electrodes on standard Si/SiO_2 substrates.[22] For this reason, WSe_2 remains less investigated than the unipolar MoS_2 in field-effect devices, despite its higher intrinsic mobility and bulk ambipolarity.

In order to engineer the energy level alignment between at metal/2DM interfaces, the manipulation of the energy levels of the 2DM through molecular decoration represents a valuable strategy as alternative to the use of diverse metals.[23,24] This possibility, extensively demonstrated for graphene[25–31] and MoS_2,[32–34] has been only partially explored for WSe_2 and other Se-based TMDCs.[9,35,36] In this context, self-assembled monolayers (SAMs), i.e. ultrathin and molecular layer generated by self-assembly and covalently attached to the target surfaces,[37,38] are particularly appealing, since the highly ordered structure attained via the self-assembly ensures a parallel alignment of the molecular dipoles, causing a profound modification in the surface energy of the functionalized surface.[39,40] However, the dangling-bond-free, highly inert surface of van der Waals solids poses a problem for the choice of a suitable anchoring group.[35] Moreover, a massive covalent functionalization of single and bi layers would damage their crystalline structure,[41] eventually leading to a degradation in the electrical performances.[42,43] On the contrary, defects naturally exist in the crystal structure of TMDC which represent ideal anchoring sites for covalent functionalization.[16] For MoS_2, covalent molecular decoration at defect sites was reported to improve the electrical performances by defect healing;[44] but the low surface coverage resulted in minor effect on the energy levels of TMDCs. Analogous defect healing strategies for Se-TMDCs remain much less investigated than S-based TMDCs.[24]

Here, we firstly demonstrate the capability of different SAMs functionalisation to induce doping effect in a very well know material, the graphene. This material has been extensively studied in the past decade, and it is an ideal platform to study the doping effect through a spectroscopic characterization. We confirmed by Raman measurements that some SAMs induce a certain doping into this material, while others, unexpectedly, provide very strong undoped graphene flakes.

Secondly, we exploit SAM functionalization to demonstrate high performance *p*- and *n*- type transistors based on WSe_2 single layers on SiO_2 contacted by metals conventionally used for 2DM or organic electronics (Au for holes and Al for electrons) with mobility as high as μ_h=150 $cm^2V^{-1}s^{-1}$ and μ_e= 40 $cm^2V^{-1}s^{-1}$. Additionally, by mastering molecular modification, we provide asymmetric functions to the two surfaces of bilayer WSe_2, thereby achieving balanced

ambipolar transport at the bilayer limit using Au contacts. Our results indicate that silanol groups anchor to WSe_2 at defect sites which can be increased in number and engineered through an ozone treatment. Additionally, the molecules in the adlayer are crosslinked, which generate a large-area, uniform coverage of the WSe_2 surface, in which defect healing and energy level manipulation co-exist, resulting in programmable doping levels and high mobility for single and bi-layer WSe_2.

6.2 Experimental methods

6.2.1 Device preparation

SiO_2/Si-n++ substrates (from Fraunhofer Institute for Photonic Microsystems IPMS, Dresden, Germany) with 90 nm thick oxide were cleaned in an ultrasonic bath in acetone and isopropanol and dried under nitrogen flow. Afterwards, the substrates were treated by UV/O_3 for 20 min. **For the PFS** (Trichloro(1H,1H,2H,2H-perfluorooctyl)silane, Sigma Aldrich, Figure 6-1 a)) growth, the freshly UV/O_3 treated substrates were placed in a sealed reactor containing 20 µL of PFS, and heated at 75 °C for 90 min. Once cooled back to room temperature, the substrates were rinsed with 20 mL of toluene, sonicated 10 s in ethanol, and baked on a hotplate at 60 °C for 1 h. **For AHAPS** ((N-[3-(Trimethoxysilyl)propyl]ethylenediamine, Sigma Aldrich, Figure 6-1 b)) growth, the freshly UV/O_3 treated substrates were placed in 10 mL of toluene containing 7 µL of AHAPS. The solution was then heated at 60 °C for 1 h and then left at room temperature for 11 h. The substrates were then rinsed with 20 mL of toluene, sonicated in hexane for 5 s, and baked on a hotplate for 1 h at 60 °C. The treated substrate were then immersed in 10 mL of toluene with 50 µL of triethylamine for 5 min, and dried on a hotplate at 60 °C for 5 min. **For TESPN SAM** (2-Cyanoethy)triethoxysilane, Sigma Aldrich, Figure 6-1 c)) the substrates were treated 30 min with UV/O_3 then immediately dipped in solution of 10 mL of toluene with 23 µL of TESPN. The solution was heated at 60 °C for 1 h and left at room temperature overnight. Then, the substrates were rinsed with 20 mL of toluene, sonicated 5 s in hexane, and baked on a hotplate at 60 °C for 1 h.

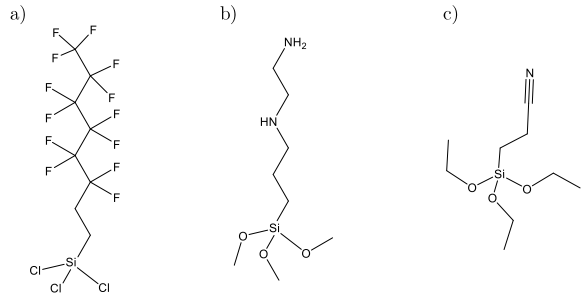

Figure 6-1 Chemical structure of a) PFS, b) AHAPS and c) TESPN used for the SAM formation.

Monolayers of graphene were produced by using a mechanical exfoliation from a pyrolytic graphite source (HOPG from Momentive Performance, ZYH grade) with a scotch-tape method (SPV 9205 from Nitto). Atomically thin **WSe_2 flakes** were produced from a stamp method, using a PF film (retention level X4, gel thickness 6.5 mil) from Gel-Pak on a synthetic WSe_2 single crystal (purchased from HQ Graphene). After using the **shadow mask approach** (homemade shadow mask from a Ted Pella G1000HSG TEM grid) or with a **photolithographic approach** (AZ1505 photoresist and AZ326 MIF developer from MicroChemicals, Laserwriter LW405B from Microtech), 30 nm of gold without adhesion layer were thermally evaporated with a Plassys MEB 300, forming the drain and sources electrodes on WSe_2. For the **vapour treatment** of WSe_2, 20 µL of PFS, AHAPS, PDFO (2,2,3,3,4,4,5,5,6,6,7,7,8,8,8-Pentadecafluoro-1-octanol, Sigma Aldrich) or PFD (1H,1H,2H-Perfluoro-1-decene, Sigma Aldrich) were poured into a sealed reactor with the samples to treat, and the system was heated at 75 °C for 90 min. When mentioned, a 3 min UV/Ozone treatment is performed with a Novascan PDS Pro Series.

6.2.2 Characterization methods

The functionalization of the surface with the SAM was characterized by **WCA** (Krüss DSA 100) depositing a drop of 3 µL of milliQ water on the surface. Graphene monolayers were identified by **Raman spectroscopy** while the monolayers and bilayers of WSe_2 were identified by optical contrast (Olympus BX51) and **PL spectroscopy** (Raman and PL measured with a Renishaw microscope equipped with a 100x objective, λ_{ex} = 532 nm, spot size of 800 nm). The devices were electrically measured with a Keithley dual channel 2636 Sourcemeter, in two-

terminal configuration with the back gate, in a glovebox filled with nitrogen gas, in dark environment. **XPS analyses** were done with a ThermoScientific K-Alpha X-ray photoelectron spectrometer equipped with an aluminium X-ray source (1.4866 keV) and working under vacuum. The X-ray spot size was 400 μm. The spectra were acquired with a repetition of 50 scans and 0.1 eV as energy step. **AFM** measurements were carried out by a Veeco Dimension 3100 atomic force microscope, under the control of a Nanoscope IV unit in ambient conditions. Topographic and phase imaging were recorded while operating in tapping mode, with an antimony *n*-doped silicon cantilever.

6.3 Results and discussion

Trichloro(1H,1H,2H,2H-perfluorooctyl)silane (PFS) and N-[3-(Trimethoxysilyl)-propyl]ethylenediamine (AHAPS) were selected for the formation of SAMs (Figure 1a and b), since F-rich PFS was demonstrated to induce p-doping effect on 2D materials,[45] while amine groups in AHAPS are expected to generate *n*-type doping.[32] Regarding TESPN, no literature is available at the moment for its use as a SAM to induce doping in semiconducting materials.

The proper functionalization of the surface was characterized, in a first approach, by water contact angle measurements (WCA, Figure 6-2). Because of the different head groups of the SAMs, a substantial change in the surface energy is described by the assemblies on the surface. This results in different interactions that a drop of water will experience on the SAM. By comparing the angle described by the water on the surface with values reported in literature, one can estimate the degree and quality of functionalization of the surface.

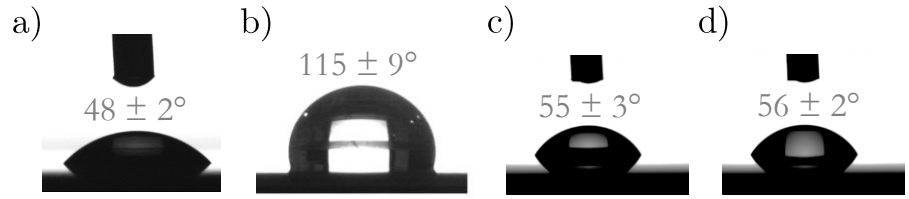

Figure 6-2 Water contact angle (WCA) of a) a SiO_2 substrate, b) a PFS treated substrate, c) a AHAPS treated substrate and d) a TESPN treated substrate.

The contact angle of water when placed on pristine SiO_2 substrate is slightly below 50°, whereas upon treatment with a hydrophobic PFS monolayer,[46] such angle becomes 115°. Both AHAPS and TESPN are defined by smaller angle, around 55°.[47,48] While Water Contact Angle (WCA) is a macroscopic surface characterization technique, AFM pictures can provide a microscopic insight into the treated surface (Figure 6-3).

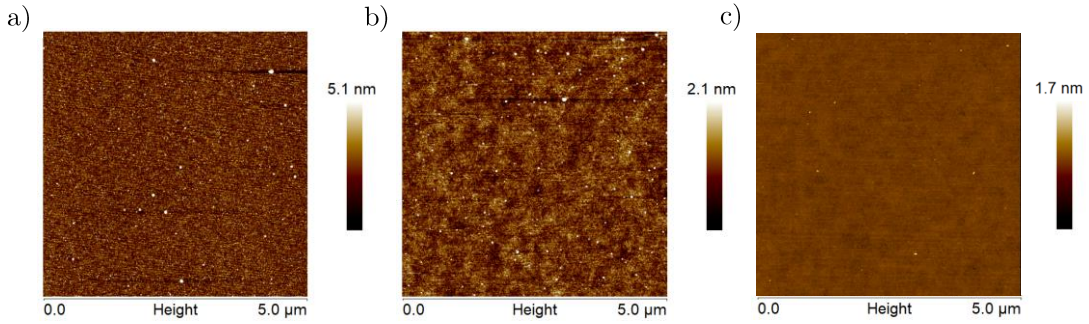

Figure 6-3 Atomic force microscopy images of a) an AHAPS, b) a PFS and c) a TESPN treated surface.

These topographic AFM images obtained with the help of **Dr. S. Bonacchi (Strasbourg)** revealed that the SAMs do not exhibit huge aggregates; only small dots scattered onto the surface are not removed by the rinsing step. From the elemental analysis provided by XPS (Figure 6-4), each surface exhibits a different feature (in addition to contaminants) corresponding to the expected composition of the surface.[47,48]

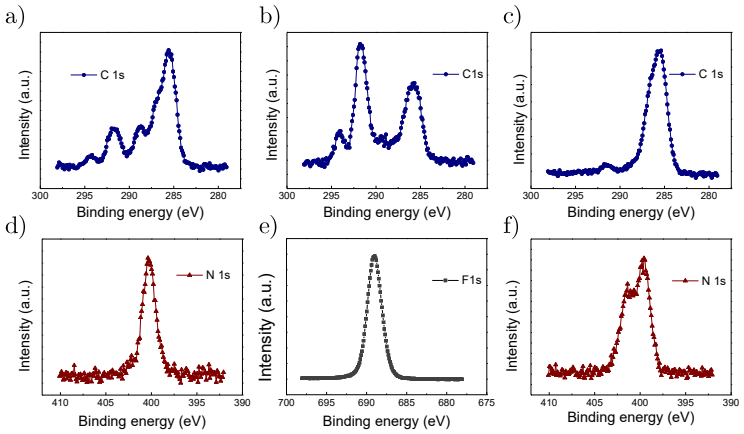

Figure 6-4 X-ray photoelectron spectra of C1s for a) TESPN, b) PFS and c) AHAPS treated surface, with their corresponding d) N1s, e) F1s and f) N1s spectra.

Another important property of the SAM is the orientation of the SAM molecules with respect to the basal plane of the surface of SiO_2. This information can be accessed with the help of Near Edge X-Ray Absorption Fine Structure (or NEXAFS), measured by **Dr. M. Nardi (Trento)**, as shown Figure 6-5. This measurement revealed that TESPN and PFS molecules adopt an angle of 45° and 27° with respect to the normal of the substrate, while AHAPS doesn't show a preferential orientation, highlighting a modest degree of order within the monolayer.

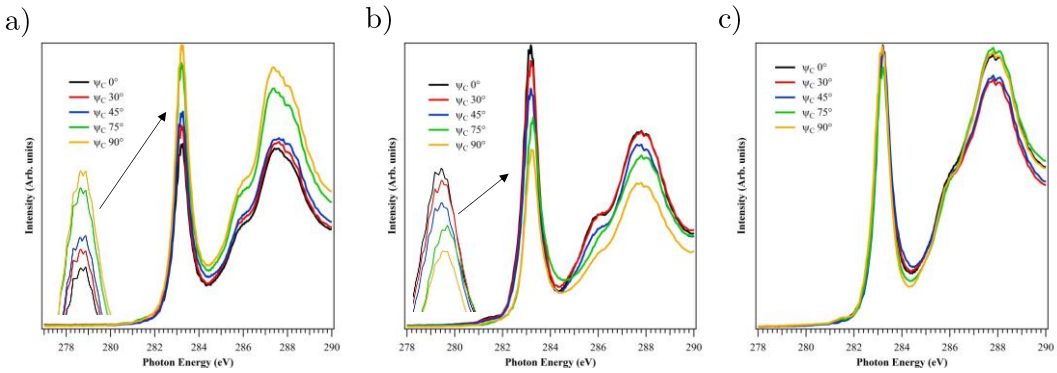

Figure 6-5 NEXAFS spectra recorded on a) TESPN, b) PFS and c) AHAPS treated substrates.

Once these SAMs characterization was completed, the effort was focused on the exfoliation of the 2D materials as described in the experimental method section. Once exfoliated, these materials were placed on the SAM and characterized (Figure 6-6) with an optical microscope. Further analysis (Raman for graphene and PL for WSe_2) were executed to ensure the monolayer nature of the studied flakes. While graphene was only analysed spectroscopically in this project, transistors based on WSe_2 have been produced through conventional photolithography. However, because of the high surface energy imposed by PFS, it was not possible to produce a decent layer of photoresist for the photolithographic process. In this case, a shadow mask approach was used, where a homemade shadow mask based on a TEM grid was employed, leading to the unsightly but nevertheless working devices, as shown Figure 6-6 d.

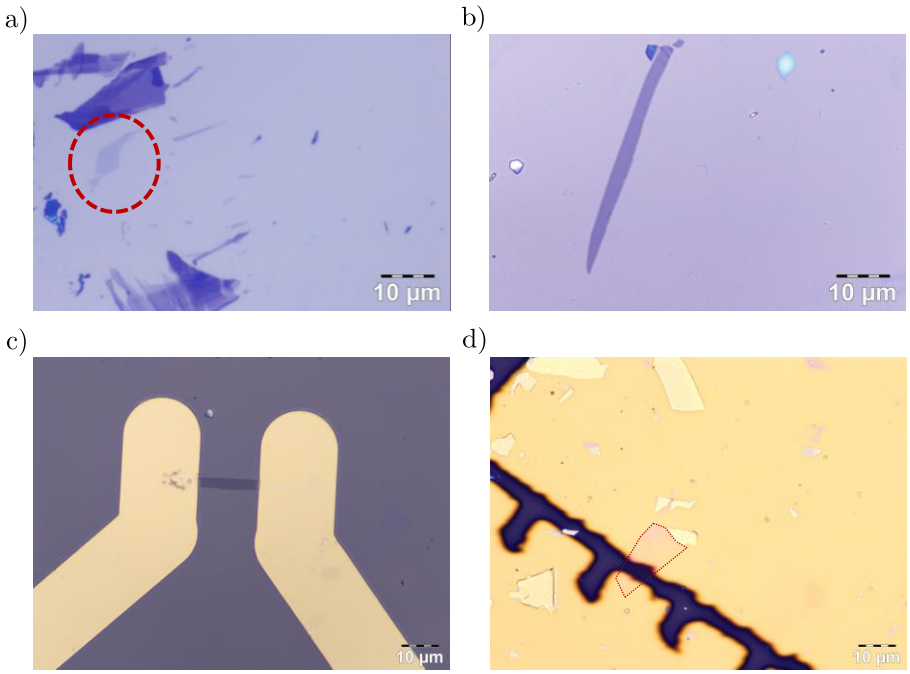

Figure 6-6 Optical images of a) a graphene flake (highlighted with a doted circle), b) a WSe_2 monolayer (note that the size of this monolayer is not representative of the average flake size) and a WSe_2-based transistor produced through c) the conventional photolithography and d) the shadow mask approach.

Raman spectrum of graphene are characteristic of this material, and are mostly defined by three important peaks. The first one is the D peak and can be found between 1300 cm^{-1} and 1350 cm^{-1}. Another one is located around 1850 cm^{-1}, and is called the G peak while the 2D peak is located near 2680 cm^{-1} (Figure 6-7 a)). The D peak usually refers to all kinds of lattice defects,[49] while the G and 2D are influenced by the level of doping and the thickness of the flake.[50–52] For instance, by mapping the G-peak and 2D-peak positions versus the G-peak FWHM and I_{2D}/I_G ratio, respectively (Figure 6-7 b) and c)), one can evaluate the degree of doping in this material. On such maps, the level of doping can be estimated by the relative position of the sample; at low wavenumbers and high G-peak FWHM or I_{2D}/I_G ratio, graphene flakes are undoped, while an increase of the wavenumber and a reduction on their respective parameters describe an augmentation of the doping level, without the possibility to make a distinction between *p*- or *n*- doping.

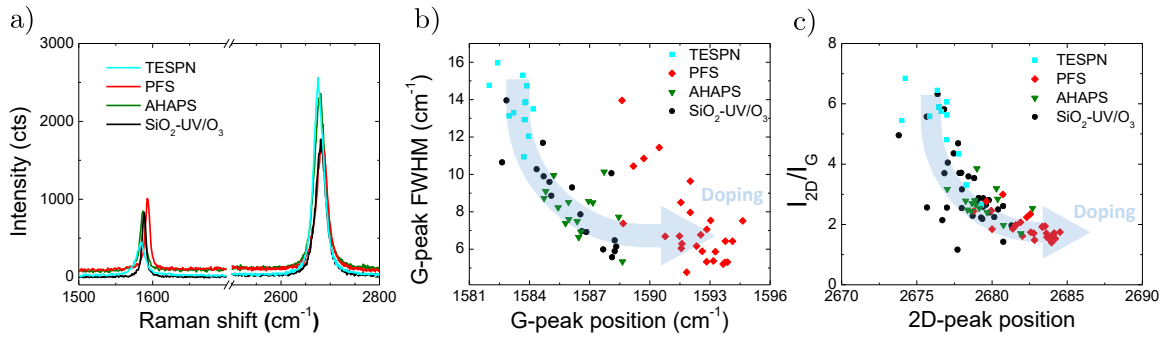

Figure 6-7 a) Raman spectra of a graphene flake on TESPN, PFS, AHAPS or UV/O$_3$ SiO$_2$-treated surface. Parameter analysis of b) the G-peak and c) the 2D-peak extracted from a). Each point corresponds to a different monolayer.

Firstly, as expected, PFS and AHAPS induces a strong doping in graphene, because of the electron withdrawing properties of the former, and the electron donating ability of the amine ending the latter through its lone pair. However, surprisingly, the TESPN induces a really strong undoping effect into the graphene, which is not expected because of the chemical structure of this molecule and in particular by its intrinsic dipole moment that it describes. Considering the significant angle that TESPN forms with the substrate and the possibility that it may be too small to formally self-assemble in a monolayer, there are for the moment no explanations for this observation. Theoretical simulations are currently running in the team of Prof. W. Wenzel (Karlsruhe), trying to elucidate the origin of this behaviour. Since the effect of TESPN is not fully understood yet, only PFS and AHAPS were selected to be used with WSe_2 monolayers, in order to enhance the electrical properties of this TMD.

In order to characterize the effect of SAMs on the electrical characteristics of WSe_2, we followed two distinct approaches. First, mechanically exfoliated WSe_2 were transferred onto SAM-functionalized SiO_2 substrates, and single layers were subsequently contacted with top metal electrodes; second, SAMs were grown onto the surface of already contacted WSe_2 single layers, transferred on un-treated SiO_2 substrates. Figure 6-8 a and b show the transfer characteristics of FETs based on WSe_2 single layers on an untreated SiO_2 substrate, as well as on WSe_2 single layers physisorbed on the surface of PFS and AHAPS SAMs. The device on the untreated SiO_2, which serves as a reference, featured poor electrical properties, with an electron mobility

on the order of 10^{-5} $cm^2V^{-1}s^{-1}$ (dashed line in Figure 6-8 a) and b)), as expected for WSe_2 on SiO_2 substrates with Au electrodes. When exfoliated on the PFS SAM, WSe_2 transistors displayed improved charge transport, with balanced ambipolarity but still relatively low hole and electron mobilities ($\mu_h \sim \mu_e \sim 0.5$ $cm^2V^{-1}s^{-1}$). Similarly, AHAPS SAM induced strong *n*-doping, displaying electron mobility approaching 0.4 $cm^2V^{-1}s^{-1}$.

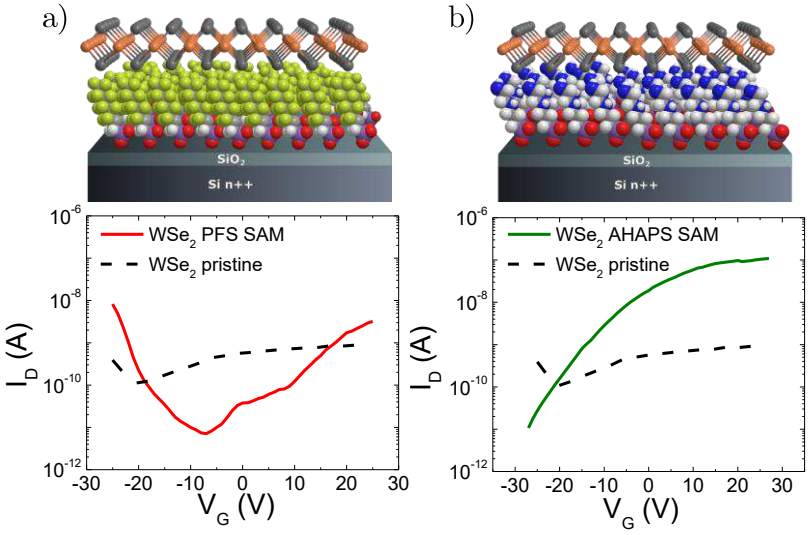

Figure 6-8 Cartoon and transfer curve (V_D = 1 V) of WSe_2 monolayer measured in two-terminal configuration with gold contacts on a 90 nm SiO_2 dielectric surface, treated with a) PFS and b) AHAPS SAMs.

A very different situation was encountered for the adlayer formation onto the surface of WSe_2. In this case, the devices were measured before and after the functionalization, so that the effect of the molecules on the electrical characteristics could be directly explored on the same device. Very poor electrical characteristics were measured for the as-fabricated devices, which are similar to the reference FET (dashed line in Figure 6-9 a) and b)). After exposure to PFS vapours, a four orders of magnitude increase in the electrical current is observed, with the device exhibiting *p*-type transport with a hole mobility of $\mu_h = 20$ $cm^2V^{-1}s^{-1}$. In the same way, exposure to AHAPS vapour causes a three orders of magnitude enhancement in the electrical mobility, with the device displaying an almost degenerated *n*-doping, with a mobility of 7 $cm^2V^{-1}s^{-1}$. While the effect SiO_2 functionalization on the electrical characteristics of WSe_2 could be expected on the basis of similar results reported for MoS_2 and graphene, the increase in

current and mobility which accompanies the formation of the adlayer onto the WSe_2 surface was unexpected.

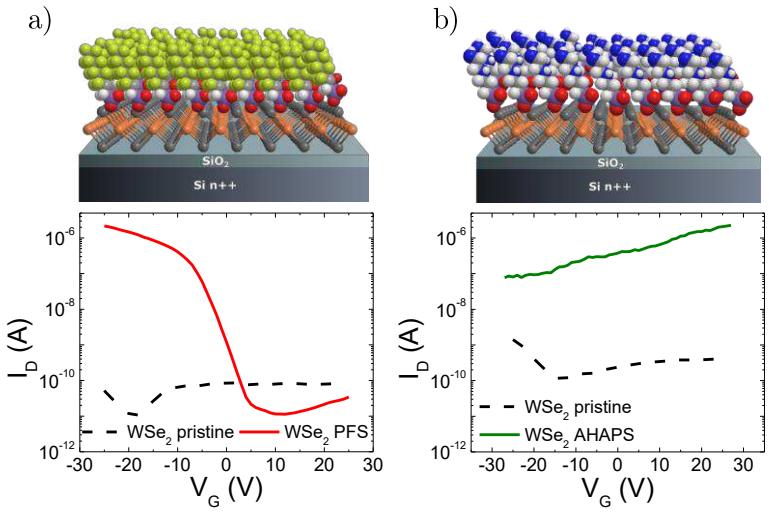

Figure 6-9 Cartoon and transfer curve (V_D = 1V) of the WSe_2 device treated with a) PFS and b) AHAPS vapours on a 90 nm thick SiO_2 dielectric.

The *p*-doping induced by the PFS vapours can partially be originated by the chlorine provided by the pre-hydrolyzed molecule. However, this doping from chlorine atoms is reported to improve the hole mobility of WSe_2 by a factor 3.5.[53] Similarly, CH_3OH is reported to n-dope WSe_2 monolayers, and increase the electron mobility by a factor 2 after 12 hours of vapour exposure.[22] In both cases, the improvement in the mobility is much lower than the one measured with PFS and AHAPS (Figure 6-10).

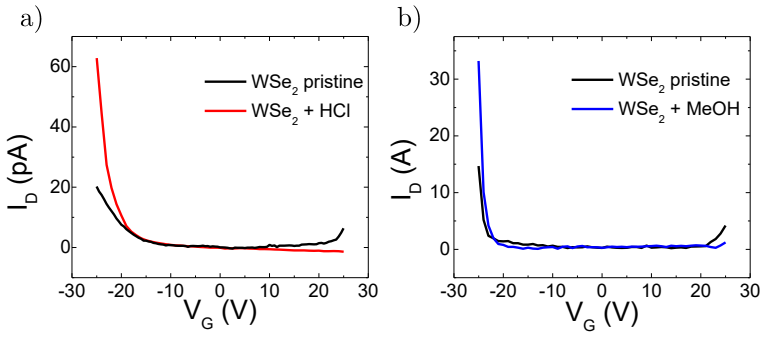

Figure 6-10 Electrical performances (V_D = 1V) of WSe_2 monolayers treated by vapours of a) HCl and b) methanol.

In order to gain greater insight into the effects of the SAMs on the surface of WSe_2, we performed additional experiments. In particular, we characterized (i) the charge carrier density of WSe_2 single layers not connected to metal electrodes through photoluminescence (PL) measurements, and (ii) the morphology of the adlayer adsorbed on the top of WSe_2 flakes. PL spectra were recorded at 77 K for WSe_2 monolayer before and after the physisorption of the molecular adlayer. The pristine WSe_2 single layer showed the typical spectral features (Figure 6-11 black line), characterized by an exciton peak X_0 at 1.73 eV and a smaller peak at lower energy (1.69 eV) corresponding to the negative trion X^-.

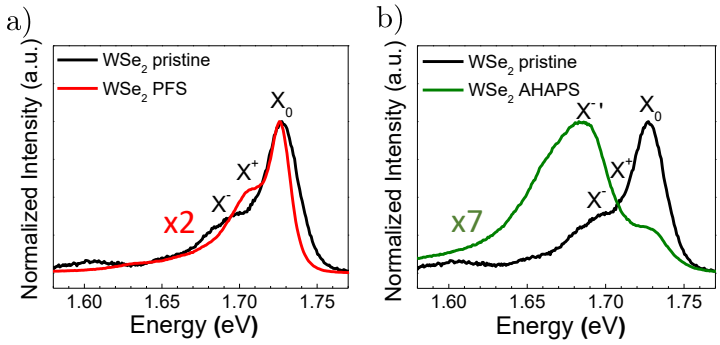

Figure 6-11: a) and b) are the photoluminescence spectra of treated WSe_2 monolayers on SiO_2, with vapours of PFS and AHAPS respectively, and measured at 77 K in nitrogen atmosphere, where the exciton X_0, positive trion X^+ and negative trion X^- peaks are labelled.

After exposure to PFS vapour (Figure 6-11 a)), the intensity of the PL spectrum of the same flake was decreased by a factor 2, and its spectral features were significantly modified. In particular, the peak corresponding to the negative trion X^- disappeared, while a new feature arose at 1.71 eV, which can be explained as a positive trion peak X^+. These findings indicate that the PFS SAM acts as an efficient hole doping layer introducing a high density of holes, in good agreement with the electrical characterization. In the case of the AHAPS treatment, the PL change after functionalization is even more dramatic. After functionalization, the PL intensity decreased almost by one order of magnitude, and the most intense peak in the spectrum is the negative trion X^-' at 1.67 eV, which indicates that the AHAPS SAM is introducing a high density of electrons.[54] The fact that the exciton peak does not shift significantly in energy for untreated and functionalized WSe_2 indicates that its band gap is not

significantly altered by the formation of the SAMs, and the modification in the WSe_2 conductance are solely due to the SAM-induced doping, which shifts the WSe_2 Fermi energy and favours the charge carrier injection.

The morphology of the SAMs grown on WSe_2 was studied by Atomic Force Microscopy (AFM) on exfoliated flakes on SiO_2. Figure 6-12 shows an AFM topographical image of the PFS adlayer on a WSe_2 multilayer deposited on SiO_2.

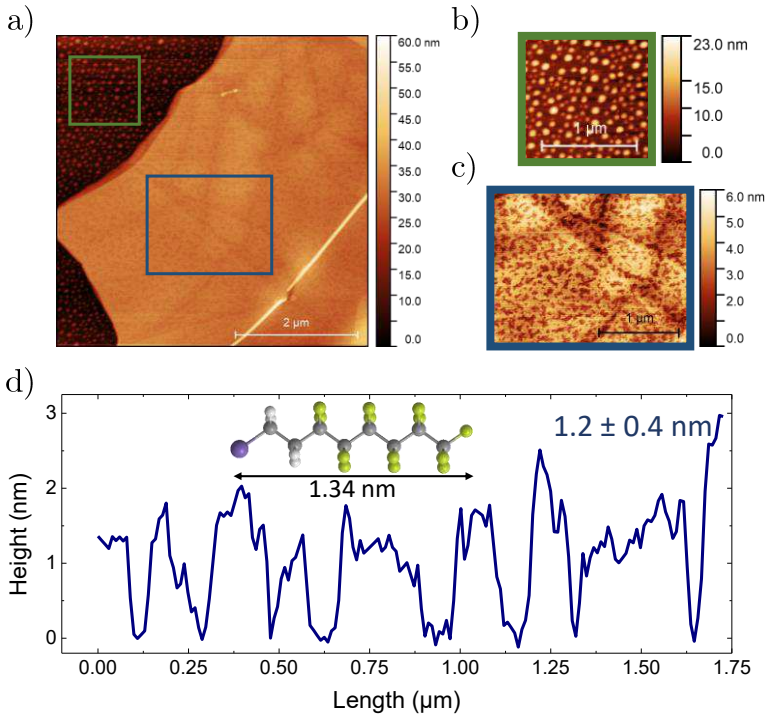

Figure 6-12 a) atomic force microscopy image of a WSe_2 multilayer treated with PFS vapour and b) and c) are magnifications on the flake and on the substrate, respectively, in the areas defined in a). d) Profile of the WSe_2 multilayer surface showing that the height of the aggregates is around 1.2 ± 0.4 nm. The molecular structure of the PFS molecule depicted in the inset displaying a contour length of 1.34 nm.

It revealed a markedly different morphology of the molecular adsorbate when adsorbed on SiO_2 and on WSe_2. On the SiO_2 substrate, several protrusions with spherical shapes are observed. These aggregates disappear from the SiO_2 surface upon rinsing the samples with toluene and sonicating them in hexane; in light of this observation, it is likely that such aggregates are physisorbed onto SiO_2. On the contrary, on the WSe_2 surface, AFM imaging revealed that the adlayer displays a rather flat morphology forming a discontinuous and ultra-thin film (Figure

6-12 c)). From this image, we can estimate that the adlayer covers the 67% of the WSe_2 surface area. The height of the adlayer amounts to 1.2 ± 0.4 nm, as evidenced in the profile displayed in Figure 6-12 d). Such a thickness is consistent with the 1.34 nm length of PFS, suggesting that the molecules are perpendicularly oriented on the surface of WSe_2.[55]

Thus far, we have presented the results obtained by exposing WSe_2 monolayers to vapours of two molecules exposing an analogous anchoring end-group (i.e. silanol) but possessing a different functional core, i.e. an electron donating amine group and an electron withdrawing perfluorinated chain. Significant and opposite effects have been introduced by the two molecules on the electrical properties of WSe_2, opening the question whether the anchoring group plays a relevant role in the determination of the electrical effects. In order to cast light onto this issue, we measured the effect of other molecules containing a similar functional core yet exposing different anchoring groups on the electrical characteristics of WSe_2 monolayers. In particular, we focused our attention on PFS, and chose two per-fluorinated molecules with the same length but with different ending groups, being 2,2,3,3,4,4,5,5,6,6,7,7,8,8,8-Pentadecafluoro-1-octanol (PDFO) and 1H,1H,2H-Perfluoro-1-decene (PFD). While PFS possesses a trichlorosilane group that can be hydrolysed into a silanol group, PDFO is terminated by an alcohol group, and PFD holds an alkene head. Figure 6-13 a-c show the effect of the different perfluorinated molecules onto WSe_2 single layers. As discussed above, the exposure of WSe_2 single layers to PFS vapour introduces significant p-doping and a remarkable increase in the WSe_2 mobility (Figure 6-13a).

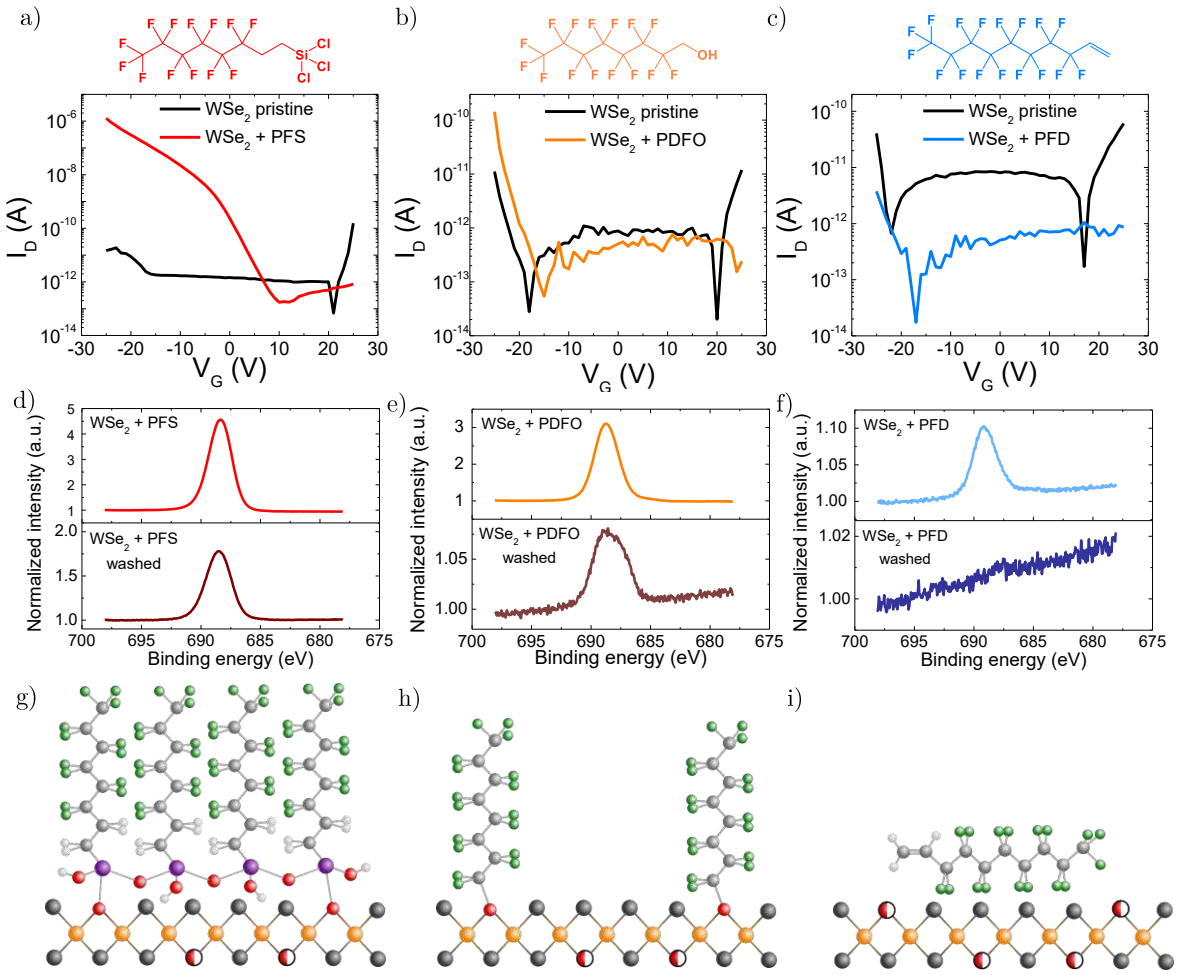

Figure 6-13 Transfer curves (VD = 1 V) of a), b) and c) pristine WSe_2 monolayers on SiO_2 (90 nm thick) without vacuum annealing treatment, and treated with vapours of PFS, PDFO and PFD, respectively. Electrical properties of PFS treated WSe_2 increase similarly regardless of thermal annealing under vacuum, while PDFO only slightly increases the p-doping of the pristine WSe_2. PFD does not improve WSe_2 performances. X-ray photoelectron spectra of F1s on a bulk WSe_2 supported by gold after d) PFS, e) PDFO and f) PFD vapour treatment, and after a washing step of the sample in an ultrasonic bath in ethanol and toluene (10 min sonication time each). A schematic of the most probable interaction with a defective WSe_2 is represented for each molecule.

Instead, the exposure to PDFO vapour only results to a minor *p*-doping, with minimal effect on the mobility, which remains in the range 10^{-5} - 10^{-6} $cm^2V^{-1}s^{-1}$ (Figure 6-13 b)). In the same way, an analogous treatment with PFD leads to a further degradation of the WSe_2 electrical performances (Figure 6-13 c)). This experiment clearly indicates that not only the functional group, but also the anchoring group plays a central role for the determination of the electrical effects.

In order to gain further insight and elucidate the nature of the interaction between the SAMs and the WSe_2 surface, we used X-ray photoemission spectroscopy (XPS) to characterize the surfaces of bulk WSe_2 crystals treated with the three different molecules. In particular, we have analysed in detail the evolution in the intensity of the F1s core level before and after washing the treated WSe_2 crystals via sonication in ethanol and toluene (Figure 6-13 d-f). Before the washing, the presence of the molecules on the three treated surfaces was confirmed by the detection of the F core level in the XPS spectra. The intensity of the peak, normalized with respect to the background, is similar for PFS and PDFO, implying an analogous number of molecules on the surface for the two compounds (Figure 6-13 d-e). Instead, the F peak corresponding to PFD displays a lower intensity as compared to PFS and PDFO, indicating the presence of less molecules on the surface (Figure 6-13 d-f).

After washing the surface, different situations are encountered in the different cases. For the PFS treated WSe_2, the intensity of the F1s peak decreases by a factor 2.5, indicating that the PFS/WSe_2 interaction is strong, since a significant amount of molecules is left on the surface after sonication (Figure 6-13 d)). On the contrary, for the PDFO treated surface, only traces of F atoms are measured after the washing step, demonstrating that the vast majority of molecules has been efficiently removed Figure 6-13 e)). The same situation is encountered for PFD, for which no F1s peak is monitored after sonication (Figure 6-13 f)). By and large, the presence of PFS molecules on WSe_2 after the aggressive washing suggests the formation of a strong bond, which could be covalent in nature. Indeed, PFS possesses a trichlorosilane group that can be hydrolysed into a silanol group in presence of residual traces of water.[37] In turn, the silanol groups can generate covalent bonds to substitutional oxygen atoms present in the monolayer[56], and/or to fill Se vacancies, which were reported to form covalent bonds with O[57]. Additionally, we suggest that polymerization takes place in the PFS adlayer, since bridges would be formed between the two silanols available and other molecules.[45] In this way, the PFS adlayer is composed of a polymerized layer of mostly physisorbed molecules, strongly anchored to the WSe_2 surface through a few covalently bound molecules at the defect sites (Figure 6-13 g)). In this regard, the modification of the electrical properties of WSe_2 after PFS treatment is mediated by a non-trivial inter-play between physisorbed and chemisorbed

molecule. A similar interpretation was put forward to explain the *p*-doping introduced in graphene by the PFS molecules.

Instead, the alcohol group of PDFO, which might bind to defects in WSe_2, does not possess additional binding sites to polymerization; hence, most molecules are simply physisorbed on the WSe_2 surface and are removed by the washing procedure, which only leaves the few molecules chemisorbed at defect sites (Figure 6-13 g)). Similarly, the alkene head of PFD prevents any covalent interaction with WSe_2, and the molecules are efficiently desorbed by sonication in solvents.

Our understanding of the anchoring mechanism for the PFS SAM allows us to further engineer the functionalization. In particular, we exploit an UV/Ozone exposure to increase the number anchoring sites, and thus to leverage the PFS and AHAPS attachment. By recording the XPS spectra of W 4f and O 1s of bulk WSe_2 treated for 3 min with UV/Ozone (Figure 6-14 a) and b), one can see an increase intensity of the W peak while the O peak is decreasing. UV/Ozone treatment is known to help in the cleaning of surface, through the oxidation and desorption of physisorbed molecules. Thus, one possible explanation of such observation consists in the desorption of contaminants on the surface of WSe_2 upon exposure to UV/Ozone. This potentially leads to a higher area available for PFS and AHAPS functionalization on WSe_2. At the same time, inclusion of oxygen in WSe_2 by UV/Ozone treatment can occur, as confirmed by XPS for longer exposure time (30 min), revealing a substantial presence of W-O bonds (Figure 6-14 c)) where oxygen can interact with the silanol groups of PFS and AHAPS.[58] The presence of holes recorded by AFM in the molecular structure reported Figure 6-12 c) is not observed anymore when an intermediate UV/Ozone treatment is used before the adlayer deposition (Figure 6-14 d)). Indeed, it is possible to see that the surface is uniform and homogeneous with this intermediate treatment. This validates the explanation of the coverage improvement of the WSe_2 surface by the adlayer due to the desorption of adsorbed contaminants on the surface of WSe_2, leaving accessible more anchoring site for the molecules.

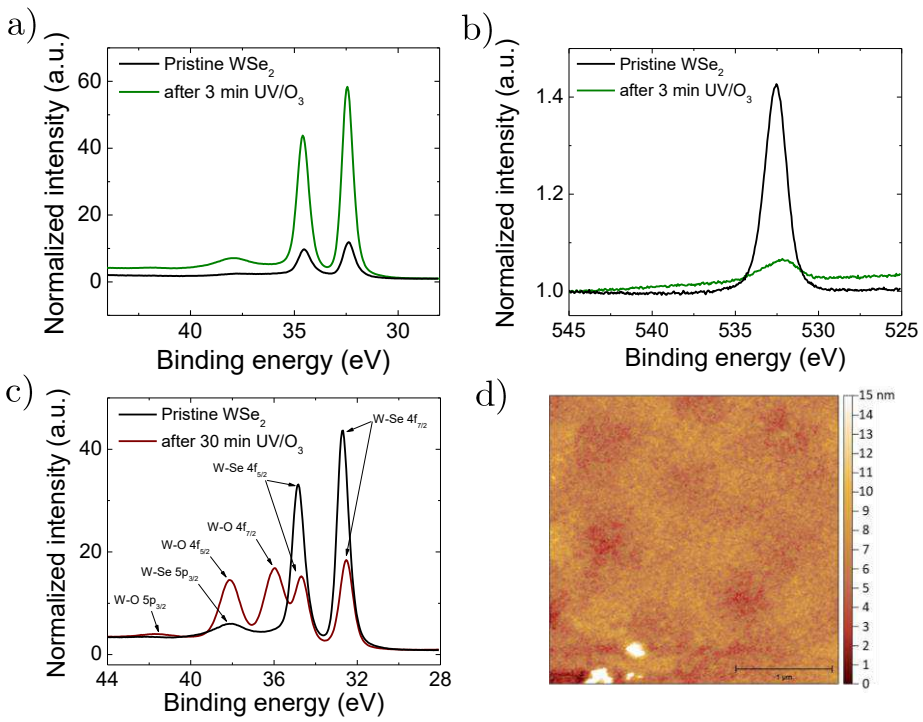

Figure 6-14 XPS spectra of a) W 4f atom for pristine WSe_2 and after 3 min of UV/O_3 treatment, b) the O 1s from the same samples and c) the W 4f after 30 min of UV/O_3 treatment. d) is a topographic AFM image of bulk WSe_2 after 3 min UV/O_3 and PFS vapour treatments.

Remarkably, hole mobilities up to 150 $cm^2V^{-1}s^{-1}$ were measured in ozone-exposed, PFS-treated WSe_2 single layers contacted by Au electrodes. Similarly, electron mobility up to 40 $cm^2V^{-1}s^{-1}$ was measured for ozone-exposed AHAPS-treated WSe_2 single layers, contacted by Al electrodes (Figure 6-15). The origin of doping can be induced by different phenomena; it can be due to the dipole moment of the molecules used with WSe_2, or to a charge transfer between the two compounds.[39,59]

It has already been reported that these SAM on SiO2, when combined 2D materials induce a doping effect originating from a charge transfer mechanism.[32] However, the same mechanism is not necessarily occurring for the adlayer. In order to unravel this mechanism behind the observed effect with the adlayer, samples will be soon analysed by angle-resolved XPS performed by **Dr. M. Nardi (Trieste)**, allowing to determine accurately the thickness of this adlayer, and the preferential orientation of the molecules at the surface of WSe_2. If the

molecules don't exhibit a preferential orientation, dipole interaction as the origin of the doping can be discarded.

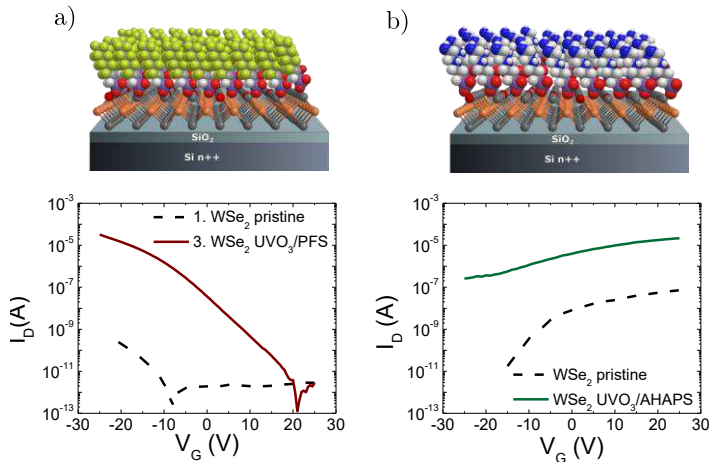

Figure 6-15 a) Cartoon and transfer curve of a WSe_2 monolayer with gold contacts, exposed to UV/Ozone for 3 min and treated with PFS vapours, while c) relates to a WSe_2 monolayer with aluminium contacts, exposed to UV/Ozone for 3 min and treated with AHAPS. Both treatments demonstrate a significant increase of the electron and hole current because of the UV/Ozone treatment.

Finally, we demonstrate that an asymmetric functionalization of the two surfaces of the same WSe_2 flake offers the opportunity to measure ambipolar transport at the bilayer limit. Toward this end, we have fabricated a device based onto a WSe_2 exfoliated bilayer which is transferred to an AHAPS-functionalized SiO_2 substrate, in order to induce *n*-type doping in the bottom layer (see Figure 6-8). Subsequently, we have exposed the same bilayer to PFS vapours, to induce *p*-type doping on the top layer (see Figure 6-9). Figure 6-16 portrays that ambipolar characteristics which were measured in the so-obtained asymmetrically functionalized device, such transfer curves revealed almost balanced mobilities.

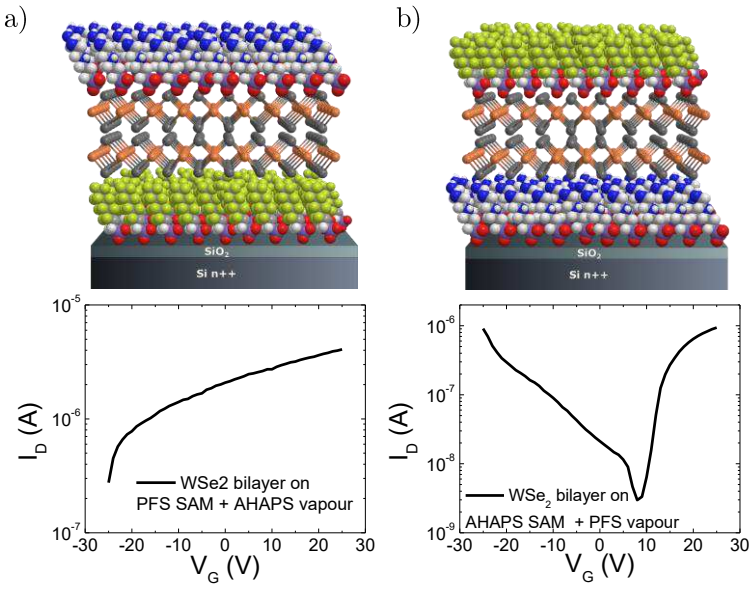

Figure 6-16 Cartoon and electrical performances of a WSe_2 bilayer a) supported on PFS SAM and treated with AHAPS vapours, and b) supported on AHAPS SAM and treated with PFS vapours.

This effect can be only seen in WSe_2 bilayers, because of the competition of both doping effect in a monolayer, leading to a partial annihilation of either one type of transport or the other (Figure 6-17).

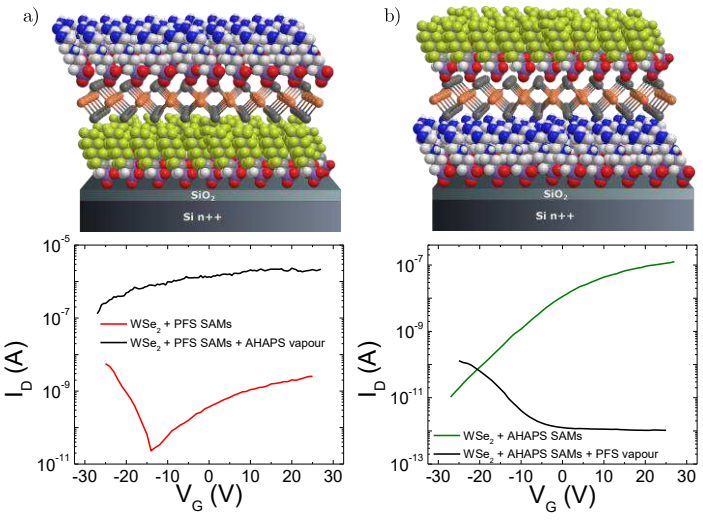

Figure 6-17 Cartoon and electrical performances of a WSe_2 monolayer a) supported on PFS SAM and treated with AHAPS vapours, and b) supported on AHAPS SAM and treated with PFS vapours.

6.4 Conclusion

In summary, we have investigated the effect of different SAM functionalization as a mean to modulate the electrical/electronic characteristics of 2D material, which manifests itself in the induction of doping of two different 2D materials. First, we provided a demonstration of the doping effect of different SAMs functionalisation by studying graphene flakes with the help of Raman spectroscopy. While PFS and AHAPS treated substrates cause a well-distinct doping of this material, TESPN provide a strongly undoped graphene, which is currently investigated by computational means.

Secondly, we have reported the analysis of the electrical and optical properties of WSe_2 monolayers in presence of the SAM. We have developed high performance *p*- and *n*- type transistors based on WSe_2 single layers with PFS and AHAPS, respectively, on SiO_2 contacted by gold or aluminium electrodes that are unconventionally used for this material to get high performances. We have found that the molecules initially used as SAM on SiO_2, can be also used to vapour treat WSe_2 monolayers exhibiting mobility as high as 150 $cm^2V^{-1}s^{-1}$ for holes and 40 $cm^2V^{-1}s^{-1}$ for electrons. Then, we exploited both interfaces that experience a WSe_2 bilayer by treating both the substrate with SAM and the top of the bilayer with vapours, to induce a balanced ambipolarity with mobilities around 20 $cm^2V^{-1}s^{-1}$. Finally, we provided indications on the functionalization mechanism of the silane groups with WSe_2, through its defect. The number of anchoring sites can be modulated by specific treatment, such as an exposure to UV/ozone for a short time. In addition, the silane groups can polymerize to form a large-area coverage of the WSe_2 surface, resulting in the doping of single and bi-layer of this material, with high performances. This approach opens the way to new uses of 2D materials, with the possibility to access to high-performance optoelectronic devices, such as light-emitting transistors.

6.5 References

[1] Q. H. Wang, K. Kalantar-Zadeh, A. Kis, J. N. Coleman, M. S. Strano, *Nature Nanotechnology* **2012**, *7*, 699.
[2] G. Fiori, F. Bonaccorso, G. Iannaccone, T. Palacios, D. Neumaier, A. Seabaugh, S. K. Banerjee, L. Colombo, *Nat Nano* **2014**, *9*, 768.

[3] Y. Dan, Y. Lu, N. J. Kybert, Z. Luo, A. T. C. Johnson, *Nano Lett.* **2009**, *9*, 1472.
[4] Y. Liu, X. Dong, P. Chen, *Chem. Soc. Rev.* **2012**, *41*, 2283.
[5] M. Chhowalla, H. S. Shin, G. Eda, L.-J. Li, K. P. Loh, H. Zhang, *Nature Chemistry* **2013**, *5*, 263.
[6] F. Xia, H. Wang, D. Xiao, M. Dubey, A. Ramasubramaniam, *Nature Photonics* **2014**, *8*, 899.
[7] K. F. Mak, J. Shan, *Nature Photonics* **2016**, *10*, 216.
[8] L. Yu, A. Zubair, E. J. G. Santos, X. Zhang, Y. Lin, Y. Zhang, T. Palacios, *Nano Lett.* **2015**, *15*, 4928.
[9] C.-H. Chen, C.-L. Wu, J. Pu, M.-H. Chiu, P. Kumar, T. Takenobu, L.-J. Li, *2D Mater.* **2014**, *1*, 034001.
[10] H. C. P. Movva, A. Rai, S. Kang, K. Kim, B. Fallahazad, T. Taniguchi, K. Watanabe, E. Tutuc, S. K. Banerjee, *ACS Nano* **2015**, *9*, 10402.
[11] H. Fang, S. Chuang, T. C. Chang, K. Takei, T. Takahashi, A. Javey, *Nano Lett.* **2012**, *12*, 3788.
[12] V. Podzorov, M. E. Gershenson, C. Kloc, R. Zeis, E. Bucher, *Applied Physics Letters* **2004**, *84*, 3301.
[13] H. Zhou, C. Wang, J. C. Shaw, R. Cheng, Y. Chen, X. Huang, Y. Liu, N. O. Weiss, Z. Lin, Y. Huang, X. Duan, *Nano Lett.* **2015**, *15*, 709.
[14] D. Li, X. Wang, Y. Chen, S. Zhu, F. Gong, G. Wu, C. Meng, L. Liu, L. Wang, Tie Lin, S. Sun, H. Shen, X. Wang, W. Hu, J. Wang, J. Sun, X. Meng, J. Chu, *Nanotechnology* **2018**, *29*, 105202.
[15] W. Liu, J. Kang, D. Sarkar, Y. Khatami, D. Jena, K. Banerjee, *Nano Lett.* **2013**, *13*, 1983.
[16] H. Schmidt, F. Giustiniano, G. Eda, *Chem. Soc. Rev.* **2015**, *44*, 7715.
[17] H.-J. Chuang, X. Tan, N. J. Ghimire, M. M. Perera, B. Chamlagain, M. M.-C. Cheng, J. Yan, D. Mandrus, D. Tománek, Z. Zhou, *Nano Letters* **2014**, *14*, 3594.
[18] J.-K. Huang, J. Pu, C.-L. Hsu, M.-H. Chiu, Z.-Y. Juang, Y.-H. Chang, W.-H. Chang, Y. Iwasa, T. Takenobu, L.-J. Li, *ACS Nano* **2014**, *8*, 923.
[19] Y. J. Zhang, T. Oka, R. Suzuki, J. T. Ye, Y. Iwasa, *Science* **2014**, *344*, 725.
[20] S. Li, S. Wang, D.-M. Tang, W. Zhao, H. Xu, L. Chu, Y. Bando, D. Golberg, G. Eda, *Applied Materials Today* **2015**, *1*, 60.
[21] S. Das, J. Appenzeller, *Applied Physics Letters* **2013**, *103*, 103501.
[22] G. P. Neupane, M. D. Tran, S. J. Yun, H. Kim, C. Seo, J. Lee, G. H. Han, A. K. Sood, J. Kim, *ACS Applied Materials & Interfaces* **2017**, *9*, 11950.
[23] M. Gobbi, E. Orgiu, P. Samorì, *Advanced Materials* **2018**, *30*, 1706103.
[24] S. Bertolazzi, M. Gobbi, Y. Zhao, C. Backes, P. Samorì, *Chem. Soc. Rev.* **2018**, *47*, 6845.
[25] S. Kobayashi, T. Nishikawa, T. Takenobu, S. Mori, T. Shimoda, T. Mitani, H. Shimotani, N. Yoshimoto, S. Ogawa, Y. Iwasa, *Nature Materials* **2004**, *3*, 317.
[26] Z. Yan, Z. Sun, W. Lu, J. Yao, Y. Zhu, J. M. Tour, *ACS Nano* **2011**, *5*, 1535.
[27] J. Park, S. B. Jo, Y.-J. Yu, Y. Kim, J. W. Yang, W. H. Lee, H. H. Kim, B. H. Hong, P. Kim, K. Cho, K. S. Kim, *Advanced Materials* **2012**, *24*, 407.
[28] B. Kang, S. Lim, W. H. Lee, S. B. Jo, K. Cho, *Advanced Materials* **2013**, *25*, 5856.
[29] W. H. Lee, J. Park, Y. Kim, K. S. Kim, B. H. Hong, K. Cho, *Advanced Materials* **n.d.**, *23*, 3460.
[30] T. Ohshiro, M. Tsutsui, K. Yokota, M. Furuhashi, M. Taniguchi, T. Kawai, *Nat Nano* **2014**, *9*, 835.
[31] Z. Liu, A. A. Bol, W. Haensch, *Nano Lett.* **2011**, *11*, 523.
[32] Y. Li, C.-Y. Xu, P. Hu, L. Zhen, *ACS Nano* **2013**, *7*, 7795.
[33] S. Najmaei, X. Zou, D. Er, J. Li, Z. Jin, W. Gao, Q. Zhang, S. Park, L. Ge, S. Lei, J. Kono, V. B. Shenoy, B. I. Yakobson, A. George, P. M. Ajayan, J. Lou, *Nano Lett.* **2014**, *14*, 1354.
[34] D. Kiriya, M. Tosun, P. Zhao, J. S. Kang, A. Javey, *J. Am. Chem. Soc.* **2014**, *136*, 7853.
[35] D.-H. Kang, J. Shim, S. K. Jang, J. Jeon, M. H. Jeon, G. Y. Yeom, W.-S. Jung, Y. H. Jang, S. Lee, J.-H. Park, *ACS Nano* **2015**, *9*, 1099.
[36] D.-H. Kang, M.-S. Kim, J. Shim, J. Jeon, H.-Y. Park, W.-S. Jung, H.-Y. Yu, C.-H. Pang, S. Lee, J.-H. Park, *Adv. Funct. Mater.* **2015**, *25*, 4219.
[37] A. Ulman, *Chem. Rev.* **1996**, *96*, 1533.
[38] S. A. DiBenedetto, A. Facchetti, M. A. Ratner, T. J. Marks, *Adv. Mater.* **2009**, *21*, 1407.
[39] W. H. Lee, Y. D. Park, *Advanced Materials Interfaces* **n.d.**, *5*, 1700316.
[40] J. Shim, H.-Y. Park, D.-H. Kang, J.-O. Kim, S.-H. Jo, Y. Park, J.-H. Park, *Advanced Electronic Materials* **n.d.**, *3*, 1600364.
[41] P. Huang, L. Jing, H. Zhu, X. Gao, *Acc. Chem. Res.* **2013**, *46*, 43.
[42] C.-J. Shih, Q. H. Wang, Z. Jin, G. L. C. Paulus, D. Blankschtein, P. Jarillo-Herrero, M. S. Strano, *Nano Lett.* **2013**, *13*, 809.

[43] D. M. Sim, M. Kim, S. Yim, M.-J. Choi, J. Choi, S. Yoo, Y. S. Jung, *ACS Nano* **2015**, *9*, 12115.
[44] S. Bertolazzi, S. Bonacchi, G. Nan, A. Pershin, D. Beljonne, P. Samorì, *Advanced Materials* **2017**, *29*, 1606760.
[45] B. Lee, Y. Chen, F. Duerr, D. Mastrogiovanni, E. Garfunkel, E. Y. Andrei, V. Podzorov, *Nano Lett.* **2010**, *10*, 2427.
[46] K. K. Rangharajan, K. J. Kwak, A. T. Conlisk, Y. Wu, S. Prakash, *Soft Matter* **2015**, *11*, 5214.
[47] H. Sugimura, A. Hozumi, T. Kameyama, O. Takai, *Surface and Interface Analysis* **2002**, *34*, 550.
[48] Z. Kong, Q. Wang, L. Ding, *Applied Surface Science* **2009**, *256*, 1372.
[49] A. C. Ferrari, J. Robertson, *Phys. Rev. B* **2000**, *61*, 14095.
[50] A. C. Ferrari, *Solid State Communications* **2007**, *143*, 47.
[51] D. M. Basko, S. Piscanec, A. C. Ferrari, *Physical Review B* **2009**, *80*, 1.
[52] Q. H. Wang, Z. Jin, K. K. Kim, A. J. Hilmer, G. L. C. Paulus, C.-J. Shih, M.-H. Ham, J. D. Sanchez-Yamagishi, K. Watanabe, T. Taniguchi, J. Kong, P. Jarillo-Herrero, M. S. Strano, *Nature Chemistry* **2012**, *4*, 724.
[53] H.-J. Nam, J. Kim, J.-H. Park, *J. Phys. Chem. C* **2017**, *121*, 14367.
[54] A. M. Jones, H. Yu, N. J. Ghimire, S. Wu, G. Aivazian, J. S. Ross, B. Zhao, J. Yan, D. G. Mandrus, D. Xiao, W. Yao, X. Xu, *Nature Nanotechnology* **2013**, *8*, 634.
[55] H. Sugimura, K. Hayashi, N. Saito, N. Nakagiri, O. Takai, *Applied surface science* **2002**, *188*, 403.
[56] T. K. H. Ta, T. N. H. Tran, Q. M. N. Tran, D. P. Pham, K. N. Pham, T. T. Cao, Y. S. Kim, D. L. Tran, H. Ju, B. T. Phan, *Journal of Electronic Materials* **2017**, *46*, 3345.
[57] P. Zhao, D. Kiriya, A. Azcatl, C. Zhang, M. Tosun, Y.-S. Liu, M. Hettick, J. S. Kang, S. McDonnell, S. Kc, J. Guo, K. Cho, R. M. Wallace, A. Javey, *ACS Nano* **2014**, *8*, 10808.
[58] M. Yamamoto, S. Nakaharai, K. Ueno, K. Tsukagoshi, *Nano Lett.* **2016**, *16*, 2720.
[59] S. Mouri, Y. Miyauchi, K. Matsuda, *Nano Lett.* **2013**, *13*, 5944.

Chapter 7 Modulating the charge transport through environmental changes: fabrication of highly sensitive gas and water sensors

7.1 Introduction and scope

The properties of a (semi)conductor can be strongly affected by its environment, as described in the chapter 2. One can take advantage of these effects to use such material for sensing. In this context, the active material acts as a transducer since it converts a non-electric signal into an electric one, and vice versa, when subject to an external stimulus such as a specific compound in the environment.[1]

Oxygen gas is the second most common component of the Earth's atmosphere and plays a fundamental role in cellular respiration as well as in industrial processes.[2] Therefore the design of oxygen sensors featuring high sensitivity and selectivity, fast response and long-term stability is essential in many fields of science and technology. A promising route to achieve this objective relies on the use of nanostructured materials, i.e. materials with at least one dimension with a characteristic length scale on the 1-100 nm scale, such as porous materials, nanowires or nanoparticles, as active components.[3–6] Thanks to their characteristic high surface-to-volume ratio, this class of materials can be extremely sensitive to specific variations in the chemical composition of their environment.[6,7] Precise control over materials' nanostructuring allows to attain fine tuning of materials sensitivity to a given analyte, and therefore optimization of the sensor performances.[8,9] Since the pioneering work of Collins et al. demonstrating extreme oxygen sensitivity of the electrical properties of carbon nanotubes,[10] several other examples have been reported of oxygen sensors and related trapping engineering based on material nanostructuring. In particular, metal oxide semiconductors[11,12] and carbon-based materials[10,13–

[16] have been used as O_2 adsobers[17] and sensitive materials,[18] in which the sensing mechanism is based on a dynamic exchange between adsorbed molecules and oxygen gas taking place on an active surface. In spite of their high sensitivity, these sensors still suffer from partial irreversibility,[19] high operating temperatures,[20] limited working range[21] and low speed[22] which hamper their technological application.

Among nanostructured materials, solution-processed hybrid organo-halide perovskites have been extensively used in the last few years as novel semiconductors for optoelectronic devices[23–29] and solar cells featuring efficiencies exceeding 23%.[30] Thanks to a suitable processing, Methyl Ammonium lead iodide perovskites ($MAPbI_3$) can feature high surface-to-volume ratio that can be exploited for different purposes, in particular for gas sensing. Indeed, recent works revealed a marked sensitivity of $MAPbI_3$ photophysical properties to moisture[31] or small gas molecules[32] such as ammonia[33,34] and oxygen.[35–39] Moreover, organo-halide perovskites are semiconducting materials with rather high charge carrier mobility,[40] offering the possibility to obtain an electrical readout as a consequence of variation in the ambient composition, which is the working mechanism of resistive sensors. Hitherto $MAPbI_3$ has never been employed as active layer in devices that can measure environmental concentration of oxygen gas through variation of an output current.

Another important component of the atmospheric environment is the water. Among all the major components, humidity (i.e. the amount of water vapour in the atmosphere or in a gas) is strongly affected by the environmental conditions, such as the temperature or the pressure. The control over the humidity is central in many aspects of everyday life. While the relative humidity (i.e. the amount of water vapour present in air expressed as a percentage of the amount needed for saturation at the same temperature) for the comfort of living should be around 50%, more dry environments are required in a clean rooms and a greater humidity is needed in hospital's operating rooms.[1,41] Thereupon, the development of hygrometers (or humidity sensors) based on different detection strategies to attain high sensitivity, selectivity and response speed combined with full reversibility was needed. Towards this end, numerous humidity sensors based on different active materials, interacting with water in different ways have been developed that led to the fabrication of capacitive,[42,43] resistive,[44–46] or optical[47,48]

devices. In particular, past activities were focussed on organic[49,50], inorganic[51,52] and hybrid [53,54], and carbon based materials,[15,55] through a specific structuration of the material and/or the device.[56] Alternatively, sensing devices using change of the weight as readout has been also developed.[57]

Suitably designed organic molecules can be self-assembled into highly organized low dimensional nanostructures. The highest degree of order is achieved by taking advantage of the reversible nature of weak (non-covalent) interactions which allow to operate under thermodynamic control. This is for example the case of **π-π** interactions holding together conjugated molecules, yielding highly ordered assemblies that act as transducer for humidity sensing. By combining a recognition receptor made of polyethylene glycol chains (PEG) that are known undergo swelling in humid environment, with a **π**-conjugated molecular core known to exhibit (semi)conducting properties, such as a polythiophene or perylene diimide unit,[58,59] it was possible to obtain materials displaying high-performance humidity sensing behaviour.[60,61]

Among the high-performance semiconducting organic materials, the [1]benzothieno[3,2-b][1]benzothiophene (BTBT) core is a well-established *p*-type semiconductor, having the highest mobility reported up to date for a small organic molecule, for its dioctyl derivative.[62] Through a wet deposition leading to a thin film with a high surface-to-volume ratio, a BTBT derivative with PEG chains has been self-assembled and exhibit all the requirements needed for the realization of a high-performance humidity sensor.

7.2 Experimental methods

7.2.1 Devices preparation

Thin-films were supported on SiO_2/Si-n++ substrates exposing 230-nm thick SiO_2 (from Fraunhofer Institute for Photonic Microsystems IPMS, Dresden, Germany). Prior to use, these substrates were cleaned in an ultrasonic bath of acetone then propan-2-ol. The substrates were then gently dried with a nitrogen flow. By using a shadow mask, 3 nm of chromium then 47 nm of gold were thermally evaporated on the substrates by using a Plassys MEB 300 set up, yielding interdigitated electrodes with a channel width of 10 mm and variable length ranging

from 60 µm to 120 µm. The substrates are then UV/Ozone treated for 5 min following 25 min of incubation in this reactive atmosphere.

Regarding the perovskite deposition, two paths were used. The first one, called ***2S***, consists of the perovskite film formation in two successive steps. To do so, 100 µL of a solution of PbI_2 (461 mg.mL^{-1} in dimethylformamide (DMF)) were spin-coated on the substrate at 3000 rpm (500 rpm.s^{-1}, 11 s) then 6000 rpm (500 rpm.s^{-1}, 11 s), followed by an annealing at 100 °C for 5 min. A second step was to spin coat 100 µL of a solution of CH_3NH_3I (15 mg.mL^{-1} in propan-2-ol) on the PbI_2 layer at 4000 rpm (500 rpm.s^{-1}, 40 s). For the other deposition method, called ***1S*** method because leading of the perovskite formation in a single step, 100 µL of a mixed solution of PbI_2 (461 mg.mL^{-1}) and CH_3NH_3I (154 mg.mL^{-1}) in DMF were spin-coated on the substrate 4000 rpm (2000 rpm.s^{-1}, 30 s). The perovskite films were completed by a solvent annealing at 100 °C for 1 h under a petri dish with 15 µL of DMF and stored inside a glovebox filled with nitrogen gas.

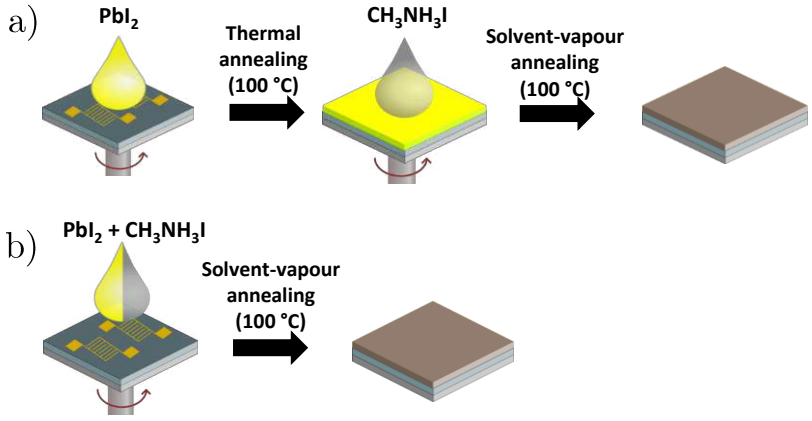

Figure 7-1 a) Schematics of the *2S* processing method to assemble $CH_3NH_3PbI_3$ thin films on SiO_2. A preformed (yellow) PbI_2 film is converted into a (dark brown) $CH_3NH_3PbI_3$ film via spin-coating of CH_3NH_3I in isopropanol. Schematics of the *1S* processing method. A solution containing both PbI_2 and CH_3NH_3I is directly spin-coated onto SiO_2.

When mentioned, the $MAPbI_3$ films were treated on a hot plate at 40 °C under a petri dish with 10 µL of CH_3I for 10 min.

The BTBT film was produced as follow: 100 µL of a solution of PEG-BTBT (synthesized by **F. Devaux from Geerts group, Brussels**) at 2, 3 or 5 mg.mL^{-1} in dichloromethane, were

spin-coated (4500 rpm, 2000 rpm/sec, 60 sec) onto a UV/Ozone treated (5 min of exposure) SiO_2/Sin++ substrates with prepatterned gold electrodes, cleaned in a ultrasonic bath successively with acetone and isopropanol for 20 min each.

7.2.2 Characterization methods

The **oxygen sensing measurements** were carried out by a chamber equipped with a valve allowing to inject dry nitrogen (5.5 grade) to decrease the level of oxygen, controlled with a Dräger Pac 550 O_2 oxygen sensor. The device is electrically connected to the 2636B Sourcemeter from Keithley. The measurement in low level of oxygen was done in a Jacomex glovebox filled with nitrogen. The **PL spectra** were recorded with an inVia confocal Raman microscope allowing photoluminescence measurements with an excitation at 532 nm. The atmosphere was controlled by injecting nitrogen or oxygen in a Linkam THMSG600 stage. The same parameters are used for the excitation of both conditions. The **SEM images** were acquired with a Quanta FEG 450 with an electron energy beam of 10 keV.

The **humidity** was controlled with the help of aqueous solution saturated in lithium chloride or sodium chloride, allowing to reach around 14% RH and 75% RH, respectively, in a sealed chamber containing a Sensirion SHT31 sensor and wires connected to a Keithley 2636B Sourcemeter, for electrical measurements. The measurement in low level of humidity was done in a Jacomex glovebox filled with nitrogen. Vapour of small organic molecules were produced by moderately heating a sealed glassware containing the needed solvent, and connected to a nitrogen line, in order to be propelled. The **AFM images** were recorded with a Dimension 3100 microscope from Bruker, by using TESPA-V2 tips. The **optical images** were taken with an Olympus BX51 combined with an X-Cite series 120Q light source. The **Raman spectra** were recorded with an inVia confocal Raman microscope allowing Raman measurements equipped with a 532 nm laser. The atmosphere was controlled by placing small containers filled with saturated aqueous solutions of LiCl or NaCl, in a Linkam THMSG600 stage.

7.3 Results and discussion

7.3.1 Perovskite

7.3.1.1 Morphology

Figure 7-2 shows the morphological characterization of $CH_3NH_3PbI_3$ films obtained on Si/SiO_2 substrates via two different solution-based deposition methods (i.e. *1S* and *2S* methods), characterized by optical and scanning electron microscopy. *2S* films are homogenous over tens of micrometers and are characterized by the presence of crystals featuring the previously reported cuboid morphology[63] with a typical length of ca. 500 nm and a thickness of ca. 400 nm estimated with the help of a profilometer. Conversely, film preparation performed by following the *1S* procedure, lead to a non-uniform substrate coverage consisting of networks of fibril-like aggregates with thickness of ca. 300 nm. A closer look into these nanostructures reveals the polycrystalline nature of the aggregates.

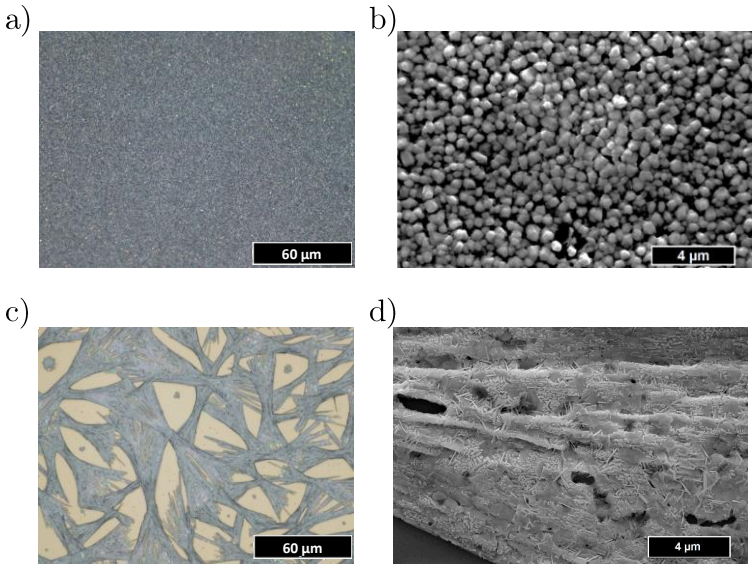

Figure 7-2 a) optical and b) SEM images of a *2S* film, and c) and d) are the corresponding images for a *1S* film, both on a SiO_2 substrate.

The different processing methods yield significant structural and morphological differences of the final perovskite films. XRD measurements, done by **Dr. L. Ferlauto and Dr. F. Liscio**

(Bologna), confirm the formation of $MAPbI_3$ structure in both cases, but a consistent amount of PbI_2 precursor was found to be still present in *2S* samples, as highlighted by the presence of intense PbI_2 peaks in the XRD diffractogram in Figure 7-3.

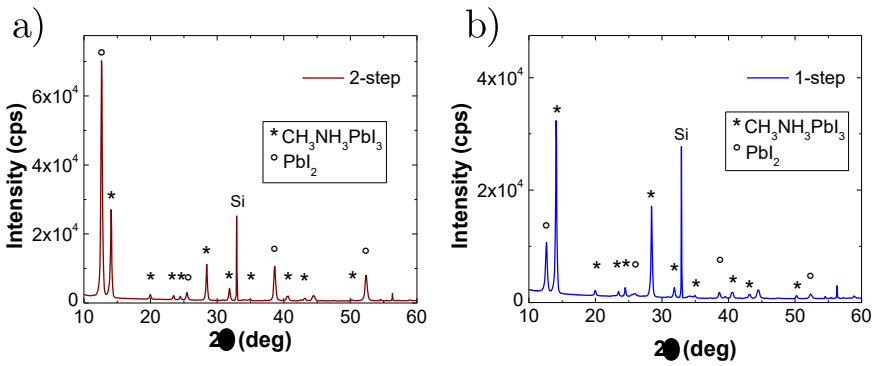

Figure 7-3 X-ray diffraction pattern of a) a *2S* film and b) a *1S* film, where the peaks corresponding to $CH_3NH_3PbI_3$ and PbI_2 are highlighted.

7.3.1.2 Oxygen response

The electrical properties of all films were recorded on samples measured inside a sealed chamber, equipped with an oxygen sensor. The devices were wired to a Keithley sourcemeter. Figure 7-4 a) shows typical current-voltage (I-V) curves of *2S* devices measured at room temperature at three different oxygen concentrations: (i) nitrogen-filled chamber (below 0.1% Vol O_2), (ii) air (20.9% Vol O_2), and (iii) oxygen-filled chamber (~95% Vol O_2). The device current revealed an over ten-fold increase upon varying oxygen concentration from (i) to (ii), and gained almost two more orders of magnitude enhancement from (ii) to (iii). In particular, during the measurement, electric current increased over the full range from approximately 90 nA in (i) up to 250 µA in (iii). Moreover, it also shows that the same resistance values could be recorded at a given O_2 concentration following repeated cycles at different oxygen/nitrogen levels inside the chamber. This experiment highlights the fully reversible character of the sensor without need of further treatments such as, for instance, a thermal annealing step in high-vacuum.[10]

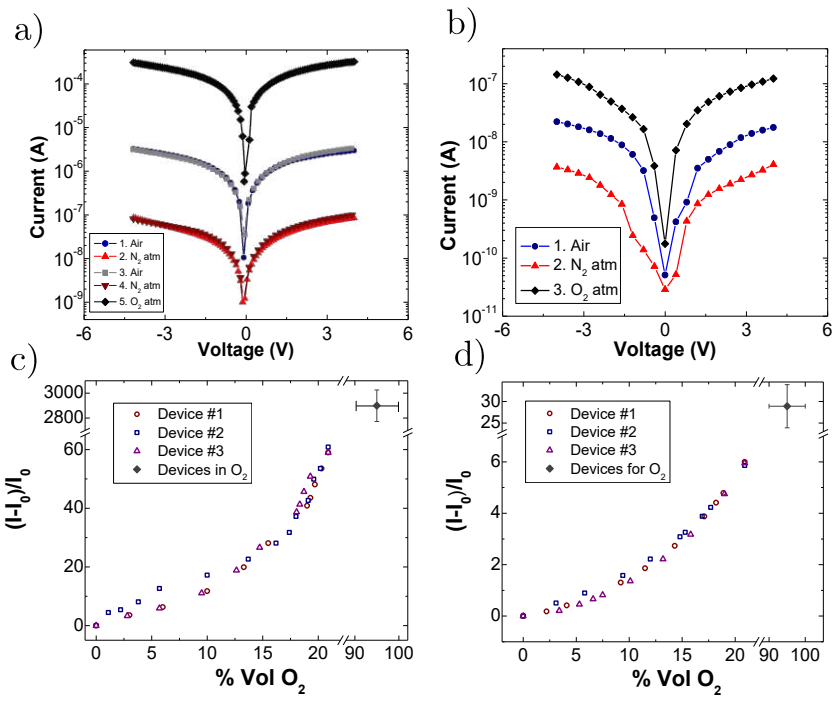

Figure 7-4 Current-Voltage traces measured at different O_2 concentrations for a) the *2S* perovskite and b), the *1S* perovskite. Sensor sensitivity versus O_2 concentration for d) *2S*, and e) *1S* perovskite, measured upon applying 4 V between the electrodes.

Analogous measurements were performed on *1S* perovskite films. Interestingly, in this case, the films showed an overall lower current passing through the junction at each gas concentration (Figure 7-4 b)). This finding can be understood on the basis of the different morphology of the perovskite films obtained by the two processing methods. In the films obtained via the *2S* method, the homogeneous surface coverage minimizes the presence of grain boundaries between adjacent crystals, which represents a basic requirement for an efficient charge transport. Instead, films obtained via *1S* method are characterized by poorly interconnected structures characterized by cracks and domain boundaries, which are detrimental for charge transport. As for the oxygen sensitivity, even in the case of the *1S* films, the device current increases significantly at higher oxygen concentrations. However, *1S* films are less sensitive to oxygen variations, as the relative change in the electrical current is much lower than in *2S* films. For the same oxygen concentrations mentioned before, the device current increased roughly four times from (i) to (ii), and a further ten-fold enhancement from (ii) to (iii). A detailed evolution of the output current in a wide range of oxygen concentration (0% - 100%) is shown in Figure

7-4 c) and d) for *2S* and *1S* films, respectively. In these graphs, the relative variation of output current, defined as $(I-I_0)/I_0$, is plotted, where I is the current measured at the different oxygen concentrations, and I_0 is the current in pure nitrogen. Importantly, while the values displayed in Figure 7-4 c) and d) were measured in three devices, they overlap onto a single curve for each deposition methods, demonstrating the high reproducibility of our sensing materials. In both cases, the current increases with oxygen concentration, as expected on the basis of the measurements shown in on the I-V curves. In particular, in the *2S* films case, the ratio $(I-I_0)/I_0$ does not linearly depend on O_2, as it increased from a value exceeding 60 in air (20.9% O_2) to almost a value of 3000 for 95% O_2. For *1S* films, current increase is up to 100 times lower than for *2S* film, reaching a $(I-I_0)/I_0$ value of 27 at 95% O_2. This finding provides further evidence that oxygen sensing properties in perovskites dramatically depend on structure and morphology, highlighting the possibility to tune the sensor sensitivity and response time by tuning material's nanostructure via different processing methods.

The electrical study was further corroborated by optical characterization of the thin films (Figure 7-5). We have performed PL measurements on *2S* and *1S* films in ambient air and in N_2, and in both cases we observe a reversible PL increase in presence of O_2, in agreement with previous works.[35,64] Interestingly, even PL intensity variation is stronger in *2S* films, again demonstrating the different O_2 sensitivity featured by different deposition methods.

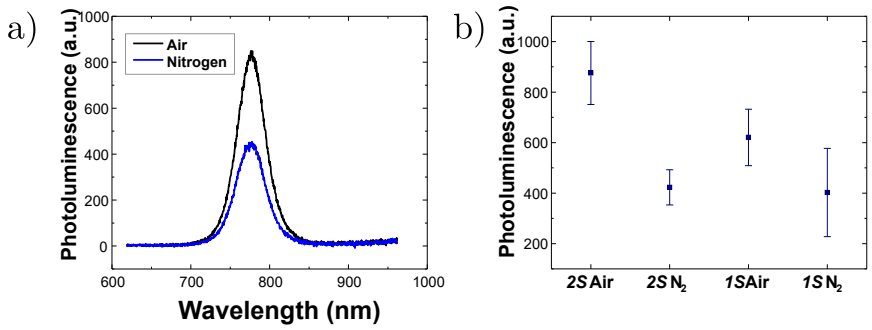

Figure 7-5 a) Photoluminescence spectra for the *2S* processed perovskite in air and in nitrogen atmosphere (λ_{ex} = 523nm) and b) averaged photoluminescence intensity at 776 nm for both morphologies, in air and nitrogen atmosphere. The difference in intensity between the air and a nitrogen atmosphere is higher for the *2S* devices than for the *1S* devices.

In order to account for the observed O_2 dependence of electrical transport and PL, we propose a trap healing mechanism according to which oxygen molecules are able to diffuse inside the perovskite crystal structure and to fill reversibly iodine vacancies that are intrinsically present inside the crystals. In turn, since iodine vacancies act as charge traps, their decreased number in presence of oxygen immediately translates into a higher number of charges available for electrical transport, i.e., higher current. In this regard, the iodine vacancies represent the sensor active sites. A similar trap healing mechanism was put forward to explain dependence of perovskite photoluminescence from O_2 concentration,[64] as well as modified Raman features upon exposure to oxygen atmosphere.[37] To obtain a more quantitative insight, I-V curves were recorded in devices where the external voltage was swept from 0 V up to 20 V at different oxygen concentrations and analysed them in the framework of the space charge limited current (SCLC) model that allows to estimate charge trap density in semiconducting materials in two-terminal devices. The results are shown in Figure 7-6 for the two processing methods. In both cases, a higher number of traps is found in pure nitrogen atmosphere, while their density decreases in presence of oxygen. Moreover, we found a significantly different trap healing efficiency for the two structures. In particular, in 1S films only 50% of the traps heal upon variation of oxygen concentration from 0% to 95%, while in *2S* films the healing process is extremely efficient, leading to an almost trap-free film at 95% O_2 atmosphere. This finding can be explained on the basis of the different morphologies of the perovskites obtained with the two deposition methods. In the *2S* case, the crystalline domain size is very small, which leads to an optimal surface-to-volume ratio that maximizes oxygen penetration in the structure. Instead, the fibril-like structures of *1S* films are relatively bulky, so that oxygen is not capable of reaching the iodine vacancies buried in the bulk.

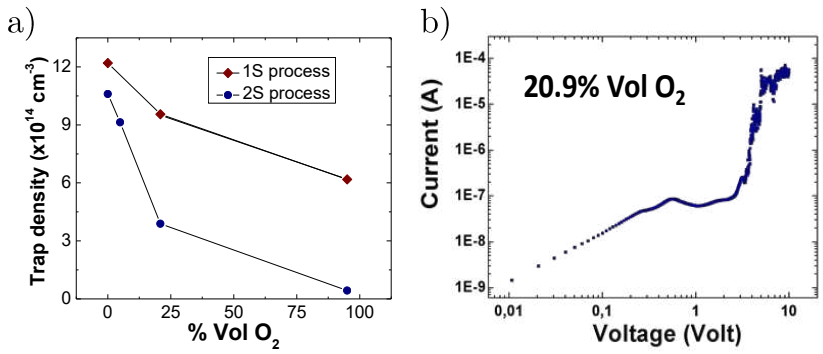

Figure 7-6 a) number of charge traps in the perovskite films at different oxygen concentration, as by fitting the I-V traces to the space charge limited current model. b) example of current-voltage trace for $CH_3NH_3PbI_3$ in different atmospheres showing different regimes from *2S* process samples.

In order to confirm that the trap healing mechanism is mediated by oxygen filling of iodine vacancies, we have performed another crucial experiment. We have employed a strategy to irreversibly fill, i.e. passivate, the part of the iodine vacancies in a pristine perovskite film via a CH_3I treatment. As we will show, since iodine vacancies represent the active sensing sites of our perovskite-based O_2 sensors, reducing their number will results in lower sensor performances. A scheme of the reported CH_3I mediated vacancies filling is shown in Figure 7-7. The iodine atom in CH_3I molecules is capable of filling an iodine vacancy while remaining attached to the CH_3 group.[65] This mechanism is only effective for iodine vacancies very close to the perovskite surface, since the steric hindrance of CH_3I prevents its penetration into the bulk. In order to characterize the effect of the iodine vacancies filling onto the sensors performances, we measured the change in the current through a *2S* film before and after the CH_3I treatment. In the pristine film, we measured a current increase by 84 times in air as compared to N_2 atmosphere. After the treatment, we observe two main effects. First, the absolute current measured in pure N_2 increases from 40 nA to 120 nA, which can be explained as a trap healing effect induced by the CH_3I-mediated vacancy filling. Second, the sensor response to O_2 is lower, as the relative change in the current measured in N_2 and air decreases to 45 times, which can be ascribed to a lower number of active sites available for O_2 sensing. While the changes are relatively small, one should consider that only a small fraction of the

iodine vacancies close to the surface are filled by the CH_3I treatment. This experiment demonstrates that iodine vacancies are indeed the active sensing sites in the perovskite layers.

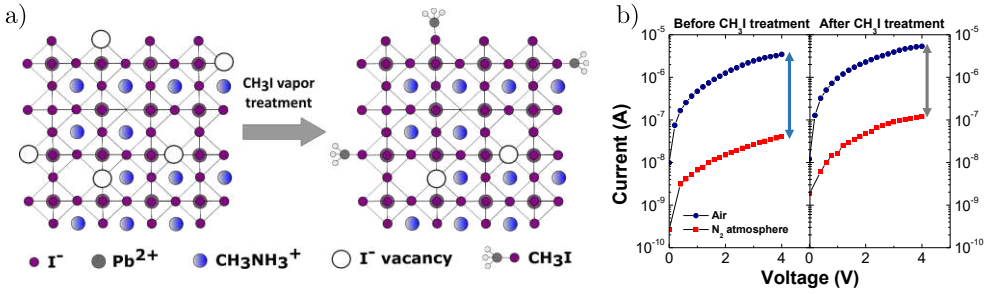

Figure 7-7 a) Mechanism for CH_3I iodine vacancies filling. Iodine vacancies, which are intrinsically present inside $CH_3NH_3PbI_3$, can be filled using CH_3I vapour. However, due to their steric hindrance, CH_3I molecules can only reach and fill vacancies close to the surface. b) Current measured in N_2 atmosphere and in air for a pristine *2S* (left) and a CH_3I-treated film (right). We highlight that for the treated sample the absolute current in N_2 is higher, while the relative current variation is lower.

However, there is an important difference between the iodine vacancies filling mechanism mediated by CH_3I gas and oxygen. While CH_3I forms covalent bonds which irreversibly passivate iodine vacancies, the O_2 mediated trap healing mechanism is reversible and in equilibrium with the O_2 concentration in the atmosphere. This property is highly beneficial, since it provides full reversibility and speed to the sensor. Figure 7-8 a) shows the real-time current of our *2S* $MAPbI_3$-based device measured by applying a constant bias of 4 V and decreasing the % of oxygen surrounding the sample from 20.9% to 7.1%. Immediately after the application of a constant bias voltage, the current flowing through the perovskite layer decreases. After a short delay time (around 150 sec) that is most likely due to the movement of ions and vacancies inside the film,[66] the current reaches a plateau which remains stable if the O_2 concentration is not varied. On the contrary, sudden steps in current appear in response to variations in the O_2 concentration, as shown in Figure 7-8. Moreover, a response speed of less than 400 ms has been measured, which represents an outstanding achievement in the field of nanostructured-based sensors.[6] We also tested the real-time reversibility of *2S* films by tuning the oxygen/nitrogen ratio flow in the chamber. Even in such broad range of oxygen exposure, our sensor shows high and fast reversibility.

A similar experiment was performed to measure the sensor sensitivity, i.e. the smallest variation of gas concentration giving rise to a detectable difference of device output current. Figure 7-8 c) shows the real-time variation of the current flowing in a *2S* film in response to 500 ppm variations in the O_2 concentration. Clear steps can be identified in correspondence with the nitrogen pulses, demonstrating that around 20.9% O_2 the sensor sensitivity is at least 500 ppm. Moreover, such 500 ppm variation of O_2 concentration represents the highest resolution of our experimental setup, which implies that the actual sensor sensitivity could be higher.

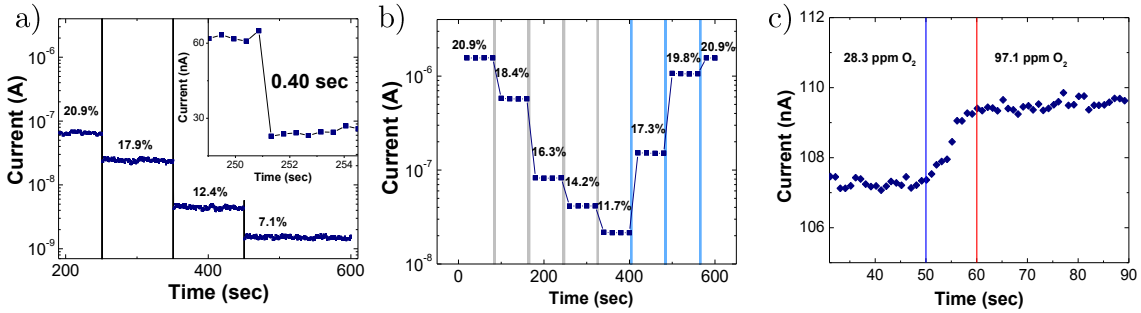

Figure 7-8 a) Real time change in the current measured in a *2S* film in response to changes in the atmosphere composition at low bias (i.e. 4V). Inset: speed of the sensor response. b) Reversibility of the sensor. The O_2 concentration is initially decreased from 20.9% to 11.7%, and then increased back to 20.9%. In this case, measurements are performed every 20 sec. c) Real time current change corresponding to a 500 ppm O_2 variation in the sample atmosphere.

As a blank experiment, we prepared a device with a thin film of PbI_2, not converted into $MAPbI_3$. The resistance of the PbI_2 layer alone is extremely high (approximately 10 GΩ, Figure 7-9 a)). When the sample is exposed to a constant flow of O_2, the current shows an instability without a clear trend, which might be explained by a degraded mechanical contact between the probe station tips and the gold pads. Irrespectively of their origin, such fluctuations do not increase significantly the current in the PbI_2 layer, which remains in the pA range. Therefore, the PbI_2 layer does not play a relevant role in the determination of the effects measured in the $CH_3NH_3PbI_3$ case. Humidity have also been tested, on a $MAPbI_3$ layer (Figure 7-9 b)). It has been found that water degrades the electrical performances of the perovskite. After one hour at relative humidity (RH) 90%, the current flowing in the device is irreversibly lowered by a factor of ca. 5, and the degradation continues with further exposure. If the sample is dropped

in water, water molecules intercalate in the perovskite structure, causing a structural change, which gives rise to a macroscopic change in the sample colour, from dark brown to yellow.[67] The water-reacted film is insulating, so the measured current irreversibly drops to zero after contact with water.

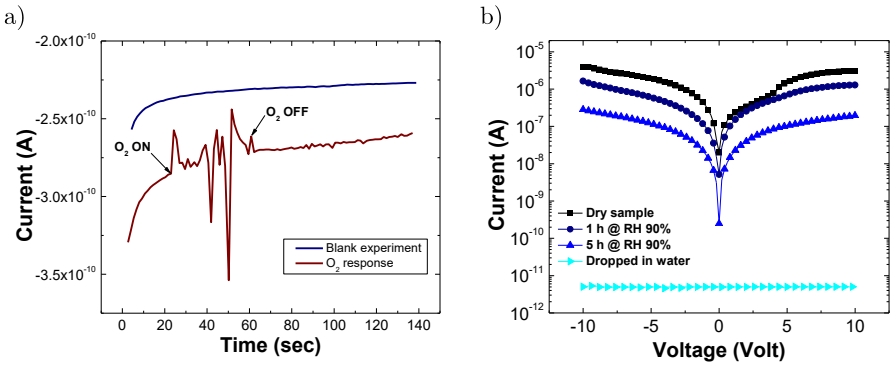

Figure 7-9 a) Electrical response of PbI_2 layer to O_2 over time under a constant bias of -4 V. The PbI_2 film was prepared by following the same procedure used in step one of the *2S* films, and we have measured its O_2 response without the second step, i.e. without converting it to $MAPbI_3$. b) I-V curves of a *2S* $CH_3NH_3PbI_3$ sample exposed to humidity.

7.3.2 BTBT

7.3.2.1 Morphology

The thickness of the organic/polymeric film produced by spin-coating can be strongly affected by rate of spin-coating and by the concentration of the solution used, potentially varying also the sensing properties of such film. In order to cast light onto this aspect, Figure 7-10 shows SEM and AFM pictures of PEG-BTBT films prepared at different concentrations (the AFM images were acquired by **M. Eredia (Strasbourg)**). The thickness of the films is estimated to around be 20 nm, 30 nm, 90 nm and 500 nm for films obtained by spin-coating 1 $mg \cdot mL^{-1}$, 2 $mg \cdot mL^{-1}$, 3 $mg \cdot mL^{-1}$ and 5 $mg.mL^{-1}$ solutions, respectively. At 1 $mg \cdot mL^{-1}$, the film does not seem to be continuous, but it is homogeneous. With the increasing concentration, a full coverage of the substrate can be seen, with the appearance of holes randomly distributed on the film.

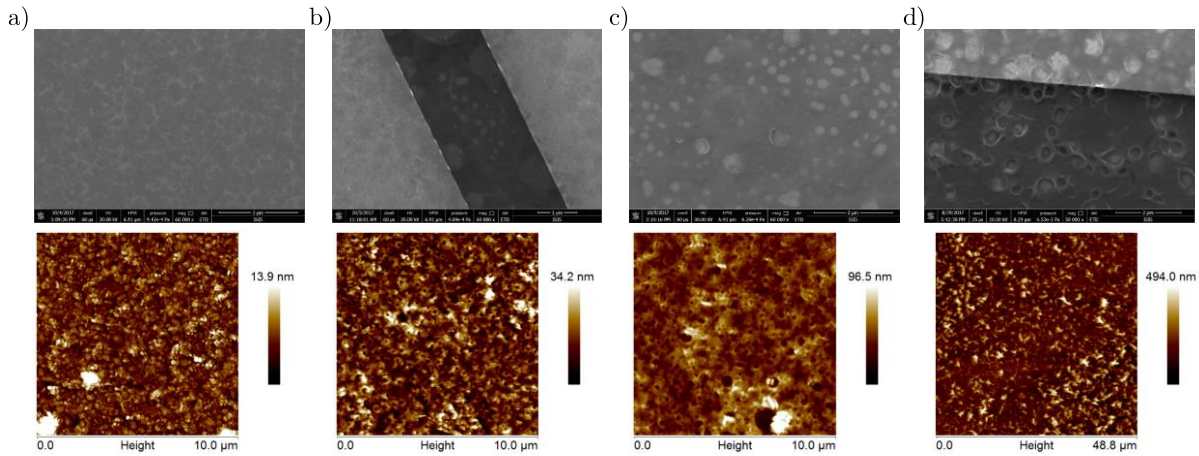

Figure 7-10 SEM and AFM pictures of PEG-BTBT film on SiO_2 spin-coated from a solution of a) 1 mg.mL^{-1}, b) 2 mg.mL^{-1}, c) 3 mg.mL^{-1} and d) 5 mg.mL^{-1} giving a film thickness of around 20 nm, 35 nm, 90 nm and 500 nm, respectively.

When explored under an optical microscope in polarization mode (Figure 7-11), the films display polycrystalline domains.

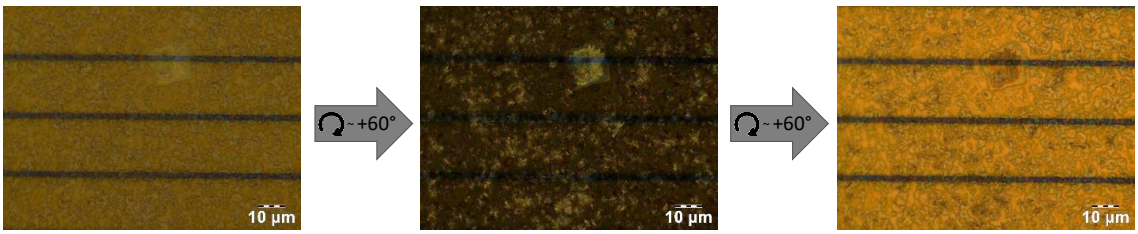

Figure 7-11 Optical images with polarized light showing the birefringence of the film, and then its polycrystallinity.

XRD analysis performed by **Dr. B. Chattopadhyay and F. Devaux (Brussels)** revealed an analogue pattern for all films, with the thickness only influencing the intensity of the peaks on the diffractogram (Figure 7-12), whereas the structure is similar than the powder one. The molecules are found to stand perpendicularly to the surface of the substrate. The analysis of the powder diffractogram with the DASH software suggests the existence of a $P2_1$ space group.

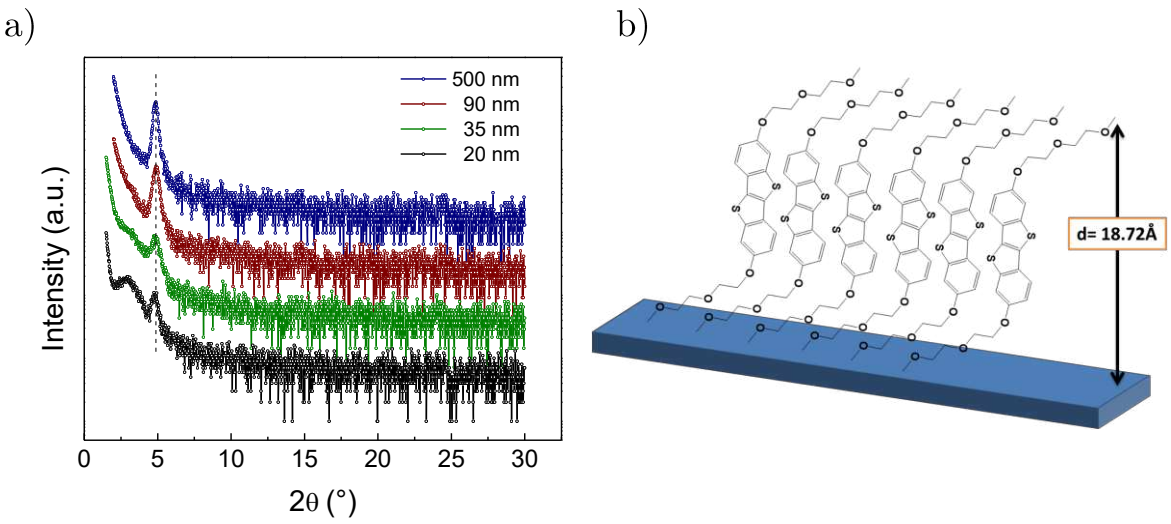

Figure 7-12 a) XRD pattern of the PEG-BTBT film at different thicknesses, showing the same structure, independently to the thickness. b) schematic of the expected orientation of the PEG-BTBT molecule on the substrate.

7.3.2.2 Electrical performances

All the sample with different film thicknesses were first measured in 2-terminal devices (L = 2.5 µm and W = 1 cm) under a constant bias of 20 V, in ambient conditions (at a temperature of 20 °C and relative humidity spanning between 35% and 50%), while the active material in the device channel is exposed to one or multiple pulses of humid air (Figure 7-13).

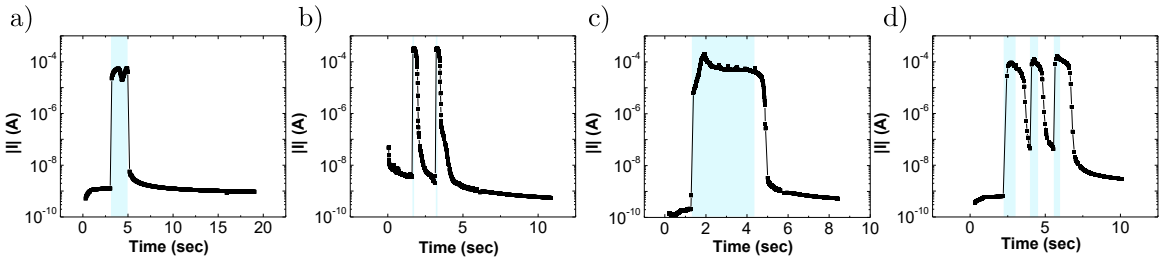

Figure 7-13 Real time response to the humidity of a PEG-BTBT film of a) 20 nm, b) 35 nm, c) 90 nm and d) 500 nm (L = 2.5 µm, V = 20 V). All the samples present almost the same response to humidity, excepted the time response to go back to the equilibrium state that can be a bit longer for thicker films.

It exhibits rather low currents (hundreds of pA) measured in ambient conditions if one considers the rather high voltage applied. However, upon pulse of humid air it is possible to observe significant increases in the measured current, reaching hundreds of µA. Interestingly, the response seems being independent on the thickness of the PEG-BTBT film. However, the response time appears being slightly slower for the thicker films, particularly for what concerns the return to the ambient state. This can be due to molecules of water getting physically trapped in the underlying film layers, slowing down the re-equilibration. The in-depth analysis of the response of the device to the humidity changes has been carried out with the thinnest (20 nm) film. Such devices exhibit a huge modulation of the current, amounting to over four orders of magnitude from 0 % RH to 75 % RH, as displayed in the Figure 7-14.

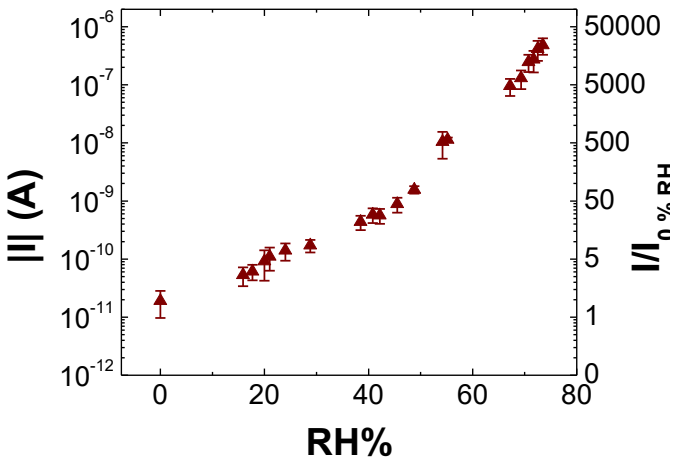

Figure 7-14 Calibration curve of a PEG-BTBT device (L = 20 µm, V = 20 V) showing a modulation of the current by more than four orders of magnitude, from 0 % RH to 75 % RH.

Excepted the existence of a small drift of the current within the first 20 sec when the device is biased, the current is stable, as portrayed in Figure 7-15 a). When exposed to short pulses of humid air, the devices display an increase of the current, and return back to the initial value, in a fully reversible process (Figure 7-15 b)). When magnified on a single peak, in Figure 7-15 c), it is possible to quantify the response time as sub-13 ms which is the limitation in such quantification determined by the instrument.

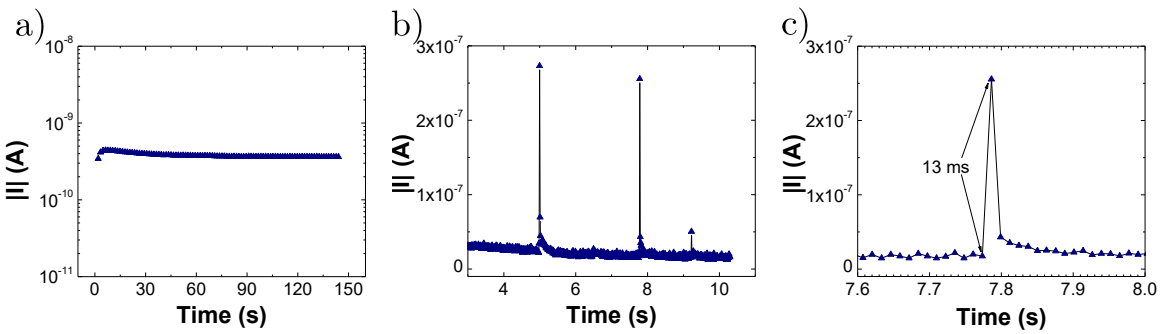

Figure 7-15 a) Blank curve in equilibrium state showing the stability of the device under biasing (L = 20 µm, V = 20 V). b) current measured in real time under 2 pulses of humid air, demonstrating a response speed below 13 ms, and a perfect reversibility, magnified in c).

The selectivity of such devices has also been tested with respect to other small and polar organic molecules (Figure 7-16). Saturated atmospheres of ethanol, methanol, chloroform and diethylether have been produced, sent on a device under constant bias with the help of a dry nitrogen flow, and compared to the effect of a pulse of humid air. One can observe a small positive response to methanol vapours, and an even smaller one with ethanol vapours. Nevertheless, these changes of current are smaller by orders of magnitude compared to the response to water vapours.

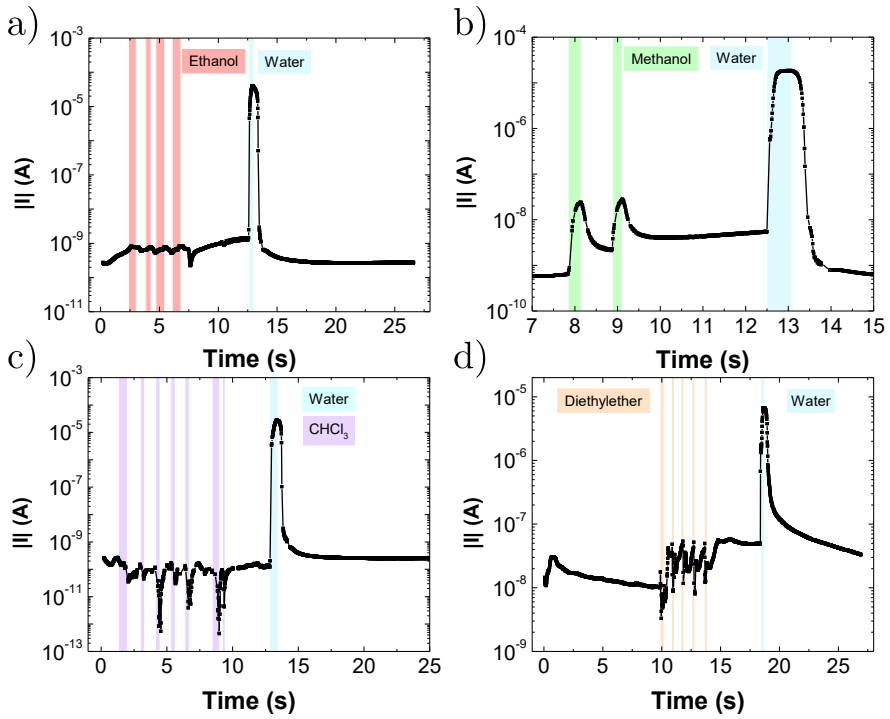

Figure 7-16 Selectivity tests of a PEG-BTBT film (L = 20 µm, V = 20 V) for a) ethanol, b) methanol, c) chloroform and d) diethylether, compared to humidity response.

Regarding the chloroform and diethylether response, negative changes are measured. This can be rationalized in terms of molecular size and proticity. We assume that the sensing mechanism is based on the hygroscopicity of the PEG chains that, through hydrogen bonding, bridges and reduces the steric hindrance of the PEG chains, which is changing the intermolecular distance and thus the conductivity of the material. Methanol and ethanol are two protic molecules, so they can, in principle, interact at the supramolecular level with PEG chains. However, they have a substantial size difference with respect to water; the latter is small enough to easily diffuse within the PEG-BTBT film while ethanol is too bulky, and methanol is in an intermediate situation, leading to different responses. Regarding the chloroform and diethylether, since these two molecules are aprotic, they are not prone to interact with the PEG chains via hydrogen bonding, thus they do not affect the intermolecular distance. However, these gases are propelled with dry nitrogen, which decrease the relative humidity locally and temporarily. The device is sensible and fast enough to be affected by this change in humidity environment, and thus, presents a negative response.

In order to validate this model for this study, a model molecule has been selected as control experiment, to attribute the change in electrical conductivity to the presence of the PEG lateral chains. This molecule is the dioctyl[1]benzothieno[3,2-b][1]benzothiophene (or C_8-BTBT, Sigma Aldrich), which has the exact chemical structure than the PEG-BTBT, except from the side chains which are alkyl based instead of PEG, yet with a similar contour length. The molecule was processed in the same way than PEG-BTBT in humidity sensing devices, the latter exhibiting the following electrical behaviour (Figure 7-17). The overall initial current is as much as nearly two orders of magnitude greater than for the PEG-BTBT. When subjected to pulses of humidity air, the current increases by less than a factor 0.5, and the molecule displays an overall current modulation lower than one order of magnitude from 0% RH to 75% RH. This demonstrate that the PEG chains are crucial for the sensing mechanism of the PEG-BTBT.

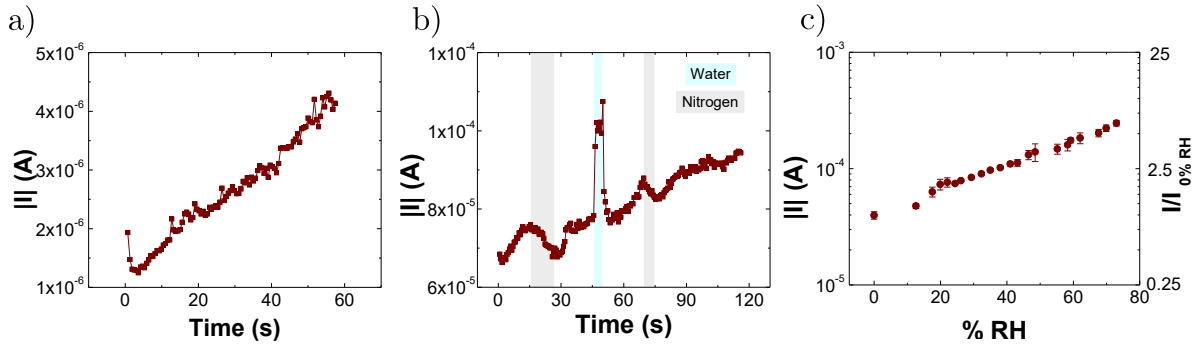

Figure 7-17 a) Blank curve, b) real time response to nitrogen and humidity pulses and c) calibration curve of a C_8-BTBT sample (L = 2.5 µm, V = 20 V), showing a poor response to humidity, with less than one order of magnitude from 0 % RH to 75 % RH.

7.3.2.3 Structural analysis vs humidity

In order to validate the mechanism presented above, a structural characterization carried out at different level of humidity is required. This analysis can be indirectly accomplished by means of vibrational spectroscopy such as Raman spectroscopy. Indeed, vibrational modes in a molecule are affected by the surrounding environment. Thus, a vibration mode, even if it only involves specific atoms in molecule, will be influenced by the coupling interactions with

surrounding molecules. Since a vibration can be, in a simplistic way, described by a harmonic oscillator, a decoupled vibrational mode from the intermolecular interaction will have a different frequency than when it is coupled with neighbours. This can emerge as a shift of a peak to a lower or higher wavenumber in the vibrational spectrum.[68]

The first step was to identify a peak corresponding to the PEG-BTBT as a thin film on SiO_2. The Raman signal of this molecule is very weak, but some peaks can be observed and easily attributed to the thin molecular layer by comparing the spectra with that recorded on a pristine SiO_2 substrate (Figure 7-18 a)). In particular, a peak at 1485 cm^{-1} can be identified as belonging to PEG-BTBT, since its signal is increasing with the film thickness. As first control experiment, to validate the occurrence of a shift of such a peak, Raman spectra were recorded at different cryogenic temperatures. By decreasing the temperature, a natural thermal contraction of the unit cell takes place, leading to a slight decrease of the intermolecular distances. As portrayed on the Figure 7-18 b), this peak is shifting by almost 3 cm^{-1} to higher energies. Then, when placed in different humidity conditions (i.e. around 30% RH and 75% RH), a shift in the same direction can be observed, indicating a reduction in the intermolecular distances.

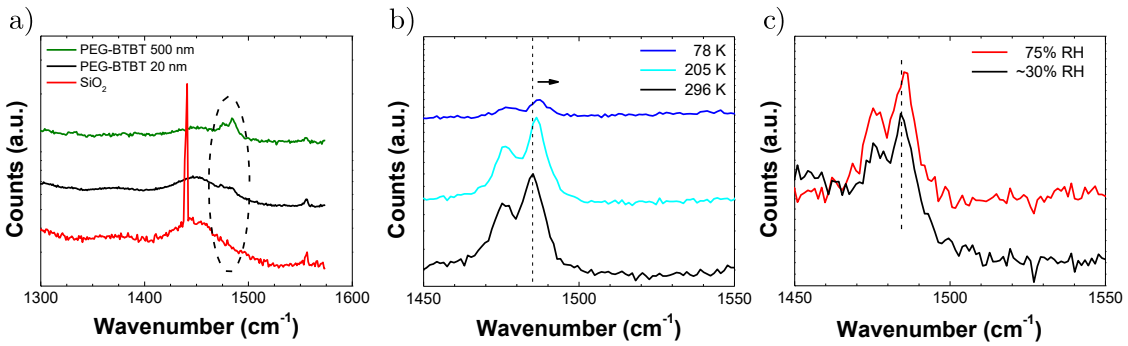

Figure 7-18 a) Raman spectra of PEG-BTBT, where a peak can be identified at 1480 cm^{-1}. b) Raman spectra recorded at different temperatures, showing a shift to a higher energy, due to the thermal contraction of the molecular unit cell. c) Raman spectra in different humidity environments, showing the same shift to higher energy than in b).

Again, as blank experiment, the same measurement was done on C_8-BTBT films. A peak belonging to the molecule can be found around 1310 cm^{-1} (Figure 7-19), and is also shifting by

almost 3 cm^{-1} when cooling down from room temperature to 78 K. However, when measured in different humidity environments, no shift of the peak can be observed, confirming that the exposure to water vapours does not affect the film structure.

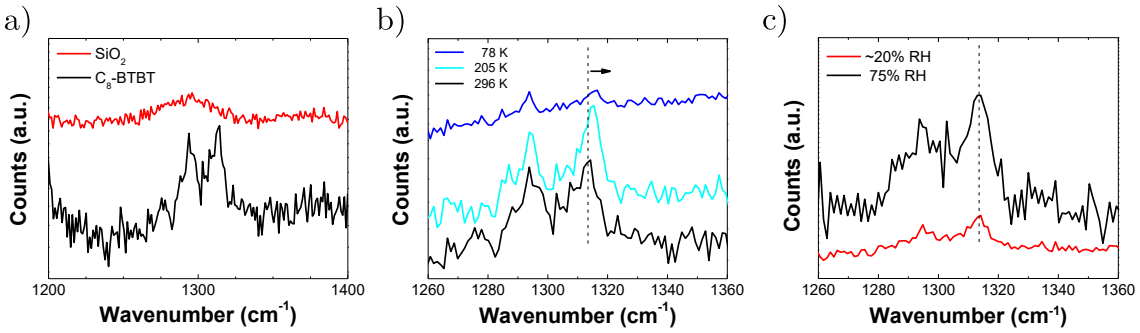

Figure 7-19 a) Raman spectra of C_8-BTBT, where a peak can be identified at 1315 cm^{-1}. b) Raman spectra recorded at different temperatures, showing a shift to a higher energy, due to the thermal contraction of the molecular unit cell. c) Raman spectra in different humidity environments, where no shift can be observed.

Another way to validate this mechanism in a more direct manner, would be by XRD analysis in different humidity environments. These measurements will be done soon by **C. Cendra and Prof. A. Salleo (Stanford)**, in order to extract the crystal structure parameters with respect to the relative humidity.[69]

7.4 Conclusion

In summary, we have investigated how the changes in the environment affect the electrical properties of two different materials. Firstly, we have provided an unprecedented experimental demonstration of the use of perovskite-based devices as O_2 sensor. We showed that device sensitivity is strongly affected by the nanoscale morphology of the perovskite films, which was controlled through the deposition method. For the most sensitive film, a more-than-three-orders of magnitude increase in the current was measured by changing the atmosphere from pure N_2 to 95% O_2. The sensor response to oxygen decreases when iodine vacancies are partially filled by CH_3I, demonstrating that the measured effect stems from a dynamic trap healing mechanism mediated by oxygen filling of I vacancies, which therefore act as the active sensing

sites. The device current variation was found to be very fast (400 ms) and completely reversible at room temperature, making nanostructured organo-halide perovskites ideal materials for oxygen sensing, and paving the way to so-far unexplored applications of this class of materials. Moreover, the effect of oxygen on the electrical characteristics of $MAPbI_3$ must be taken into deep consideration for the design and optimization of any other perovskite-based (opto-)electronic device working in ambient conditions. Our results anticipate that post-deposition oxygen treatments and optimization of the device atmosphere might further contribute to the development of this class of materials.

Secondly, we reported the analysis of the humidity response of a PEG-BTBT molecule. Independently to the film thickness, we managed to record a four-orders-of-magnitude modulation of the electrical conduction from 0% RH to 75% RH, with a full reversibility and a fast response speed below 13 ms, allowing this compound to enter in the category of high-performance humidity sensor. The sensing mechanism occurs through the adsorption of water molecules on the PEG chains which influences the intermolecular packing distance among adjacent BTBT cores. The tight packing of the BTBT within the thin films determines a highly selectivity to water molecules when benchmarked with other organic small molecules. Direct proof of this mechanism will be soon obtained through XRD synchrotron measurements in controlled environment.

7.5 References

[1] J. Fraden, *Handbook of Modern Sensors: Physics, Designs, and Applications*, Springer, New York, **2004**.
[2] I. Linnerud, P. Kaspersen, T. Jaeger, *Appl Phys B* **1998**, *67*, 297.
[3] M. Grzelczak, J. Pérez-Juste, P. Mulvaney, L. M. Liz-Marzán, *Chem. Soc. Rev.* **2008**, *37*, 1783.
[4] E. S. Cho, J. Kim, B. Tejerina, T. M. Hermans, H. Jiang, H. Nakanishi, M. Yu, A. Z. Patashinski, S. C. Glotzer, F. Stellacci, B. A. Grzybowski, *Nat Mater* **2012**, *11*, 978.
[5] E. Steven, V. Lebedev, E. Laukhina, C. Rovira, V. Laukhin, J. S. Brooks, J. Veciana, *Mater. Horiz.* **2014**, *1*, 522.
[6] J. Zhang, X. Liu, G. Neri, N. Pinna, *Advanced Materials* **2016**, *28*, 795.
[7] F. K. Perkins, A. L. Friedman, E. Cobas, P. M. Campbell, G. G. Jernigan, B. T. Jonker, *Nano Lett.* **2013**, *13*, 668.
[8] M. C. McAlpine, H. Ahmad, D. Wang, J. R. Heath, *Nature Materials* **2007**, *6*, 379.
[9] N. Liu, M. L. Tang, M. Hentschel, H. Giessen, A. P. Alivisatos, *Nature Materials* **2011**, *10*, 631.
[10] Collins, Bradley, Ishigami, Zettl, *Science* **2000**, *287*, 1801.
[11] D. E. Williams, *Sensors and Actuators B: Chemical* **1999**, *57*, 1.
[12] N. Barsan, D. Koziej, U. Weimar, *Sensors and Actuators B: Chemical* **2007**, *121*, 18.

[13] J. Kong, N. R. Franklin, C. Zhou, M. G. Chapline, S. Peng, K. Cho, H. Dai, *Science* **2000**, *287*, 622.

[14] F. Schedin, A. K. Geim, S. V. Morozov, E. W. Hill, P. Blake, M. I. Katsnelson, K. S. Novoselov, *Nature Materials* **2007**, *6*, 652.

[15] D. R. Kauffman, A. Star, *Angewandte Chemie International Edition* **2008**, *47*, 6550.

[16] J. D. Fowler, M. J. Allen, V. C. Tung, Y. Yang, R. B. Kaner, B. H. Weiller, *ACS Nano* **2009**, *3*, 301.

[17] M. Setvín, U. Aschauer, P. Scheiber, Y.-F. Li, W. Hou, M. Schmid, A. Selloni, U. Diebold, *Science* **2013**, *341*, 988.

[18] H.-C. Lee, W.-S. Hwang, *Materials transactions* **2005**, *46*, 1942.

[19] J. Eriksson, V. Khranovskyy, F. Söderlind, P.-O. Käll, R. Yakimova, A. L. Spetz, *Sensors and Actuators B: Chemical* **2009**, *137*, 94.

[20] L. Yao, G. Ou, W. Liu, X. Zhao, H. Nishijima, W. Pan, *Journal of Materials Chemistry A* **2016**, *4*, 11422.

[21] P. Jasinski, T. Suzuki, H. U. Anderson, *Sensors and Actuators B: Chemical* **2003**, *95*, 73.

[22] G. Neri, A. Bonavita, G. Micali, G. Rizzo, S. Galvagno, M. Niederberger, N. Pinna, *Chem. Commun.* **2005**, *0*, 6032.

[23] A. Kojima, K. Teshima, Y. Shirai, T. Miyasaka, *J. Am. Chem. Soc.* **2009**, *131*, 6050.

[24] J. Burschka, N. Pellet, S.-J. Moon, R. Humphry-Baker, P. Gao, M. K. Nazeeruddin, M. Grätzel, *Nature* **2013**, *499*, 316.

[25] G. Xing, N. Mathews, S. S. Lim, N. Yantara, X. Liu, D. Sabba, M. Grätzel, S. Mhaisalkar, T. C. Sum, *Nature Materials* **2014**, *13*, 476.

[26] Z.-K. Tan, R. S. Moghaddam, M. L. Lai, P. Docampo, R. Higler, F. Deschler, M. Price, A. Sadhanala, L. M. Pazos, D. Credgington, F. Hanusch, T. Bein, H. J. Snaith, R. H. Friend, *Nature Nanotechnology* **2014**, *9*, 687.

[27] Y. Lee, J. Kwon, E. Hwang, C.-H. Ra, W. J. Yoo, J.-H. Ahn, J. H. Park, J. H. Cho, *Adv. Mater.* **2015**, *27*, 41.

[28] W. S. Yang, J. H. Noh, N. J. Jeon, Y. C. Kim, S. Ryu, J. Seo, S. I. Seok, *Science* **2015**, *348*, 1234.

[29] X. Li, D. Bi, C. Yi, J.-D. Décoppet, J. Luo, S. M. Zakeeruddin, A. Hagfeldt, M. Grätzel, *Science* **2016**, 58.

[30] Best Research-Cell Efficiencies | NREL, **2018**.

[31] W. Xu, F. Li, Z. Cai, Y. Wang, F. Luo, X. Chen, *J. Mater. Chem. C* **2016**, *4*, 9651.

[32] H.-H. Fang, R. Raissa, M. Abdu-Aguye, S. Adjokatse, G. R. Blake, J. Even, M. A. Loi, *Advanced Functional Materials* **2015**, *25*, 2378.

[33] Y. Zhao, K. Zhu, *Chemical Communications* **2014**, *50*, 1605.

[34] C. Bao, J. Yang, W. Zhu, X. Zhou, H. Gao, F. Li, G. Fu, T. Yu, Z. Zou, *Chem. Commun.* **2015**, *51*, 15426.

[35] J. F. Galisteo-López, M. Anaya, M. E. Calvo, H. Míguez, *The Journal of Physical Chemistry Letters* **2015**, *6*, 2200.

[36] Y. Tian, M. Peter, E. Unger, M. Abdellah, K. Zheng, T. Pullerits, A. Yartsev, V. Sundström, I. G. Scheblykin, *Phys. Chem. Chem. Phys.* **2015**, *17*, 24978.

[37] W. Kong, A. Rahimi-Iman, G. Bi, X. Dai, H. Wu, *The Journal of Physical Chemistry C* **2016**, *120*, 7606.

[38] X. Fu, D. Jacobs, F. Beck, T. Duong, H. Shen, K. Catchpole, T. White, *Phys. Chem. Chem. Phys.* **2016**, *18*, 22557.

[39] H. Yuan, E. Debroye, G. Caliandro, K. P. F. Janssen, J. van Loon, C. E. A. Kirschhock, J. A. Martens, J. Hofkens, M. B. J. Roeffaers, *ACS Omega* **2016**, *1*, 148.

[40] Q. Dong, Y. Fang, Y. Shao, P. Mulligan, J. Qiu, L. Cao, J. Huang, *Science* **2015**, *347*, 967.

[41] H. Farahani, R. Wagiran, M. N. Hamidon, *Sensors* **2014**, *14*, 7881.

[42] T. Kuroiwa, T. Hayashi, A. Ito, M. Matsuguchi, Y. Sadaoka, Y. Sakai, *Sensors and Actuators B: Chemical* **1993**, *13*, 89.

[43] P. M. Harrey, B. J. Ramsey, P. S. A. Evans, D. J. Harrison, *Sensors and Actuators B: Chemical* **2002**, *87*, 226.

[44] X. Lv, Y. Li, P. Li, M. Yang, *Sensors and Actuators B: Chemical* **2009**, *135*, 581.

[45] S. H. Xiao, H. J. Xu, J. Hu, W. F. Jiang, X. J. Li, *Thin Solid Films* **2008**, *517*, 929.

[46] D.-I. Lim, J.-R. Cha, M.-S. Gong, *Sensors and Actuators B: Chemical* **2013**, *183*, 574.

[47] A. Tsigara, G. Mountrichas, K. Gatsouli, A. Nichelatti, S. Pispas, N. Madamopoulos, N. A. Vainos, H. L. Du, F. Roubani-Kalantzopoulou, *Sensors and Actuators B: Chemical* **2007**, *120*, 481.

[48] R. Singh, A. K. Yadav, C. Gautam, *Journal of Sensor Technology* **2011**, *01*, 116.

[49] S. Ummartyotin, H. Manuspiya, *Renewable and Sustainable Energy Reviews* **2015**, *41*, 402.

[50] M. Dokmeci, K. Najafi, *Journal of Microelectromechanical Systems* **2001**, *10*, 197.
[51] C. Wang, L. Yin, L. Zhang, D. Xiang, R. Gao, *Sensors* **2010**, *10*, 2088.
[52] Z. Wang, C. Chen, T. Zhang, H. Guo, B. Zou, R. Wang, F. Wu, *Sensors and Actuators B: Chemical* **2007**, *126*, 678.
[53] D. Patil, Y.-K. Seo, Y. K. Hwang, J.-S. Chang, P. Patil, *Sensors and Actuators B: Chemical* **2008**, *132*, 116.
[54] A. Kaushik, R. Kumar, S. K. Arya, M. Nair, B. D. Malhotra, S. Bhansali, *Chem. Rev.* **2015**, *115*, 4571.
[55] J. T. W. Yeow, J. P. M. She, *Nanotechnology* **2006**, *17*, 5441.
[56] T. Nitta, S. Hayakawa, *IEEE Transactions on Components, Hybrids, and Manufacturing Technology* **1980**, *3*, 237.
[57] P.-G. Su, Y.-P. Chang, *Sensors and Actuators B: Chemical* **2008**, *129*, 915.
[58] P. J. Brown, H. Sirringhaus, R. H. Friend, *Synthetic Metals* **1999**, *101*, 557.
[59] B. A. Jones, M. J. Ahrens, M.-H. Yoon, A. Facchetti, T. J. Marks, M. R. Wasielewski, *Angewandte Chemie International Edition* **2004**, *43*, 6363.
[60] M. A. Squillaci, L. Ferlauto, Y. Zagranyarski, S. Milita, K. Müllen, P. Samorì, *Adv. Mater.* **2015**, *27*, 3170.
[61] M. A. Squillaci, A. Cipriani, M. Melucci, M. Zambianchi, G. Caminati, P. Samorì, *Adv. Electron. Mater.* **2017**, 1700382.
[62] Y. Yuan, G. Giri, A. L. Ayzner, A. P. Zoombelt, S. C. B. Mannsfeld, J. Chen, D. Nordlund, M. F. Toney, J. Huang, Z. Bao, *Nature Communications* **2014**, *5*, DOI 10.1038/ncomms4005.
[63] J.-H. Im, I.-H. Jang, N. Pellet, M. Grätzel, N.-G. Park, *Nature Nanotechnology* **2014**, *9*, 927.
[64] Y. Tian, A. Merdasa, E. Unger, M. Abdellah, K. Zheng, S. McKibbin, A. Mikkelsen, T. Pullerits, A. Yartsev, V. Sundström, I. G. Scheblykin, *The Journal of Physical Chemistry Letters* **2015**, *6*, 4171.
[65] W. Xu, J. A. McLeod, Y. Yang, Y. Wang, Z. Wu, S. Bai, Z. Yuan, T. Song, Y. Wang, J. Si, R. Wang, X. Gao, X. Zhang, L. Liu, B. Sun, *ACS Appl. Mater. Interfaces* **2016**, *8*, 23181.
[66] Z. Xiao, Y. Yuan, Y. Shao, Q. Wang, Q. Dong, C. Bi, P. Sharma, A. Gruverman, J. Huang, *Nature Materials* **2014**, *14*, 193.
[67] J. Yang, B. D. Siempelkamp, D. Liu, T. L. Kelly, *ACS Nano* **2015**, *9*, 1955.
[68] H. L. Cheng, W. Y. Chou, C. W. Kuo, Y. W. Wang, Y. S. Mai, F. C. Tang, S. W. Chu, *Advanced Functional Materials* **2008**, *18*, 285.
[69] U. Mogera, A. A. Sagade, S. J. George, G. U. Kulkarni, *Scientific Reports* **2015**, *4*, 4013.

Chapter 8 Conclusion

In this thesis, we have studied charge transport, by mastering supramolecular approaches in order to control the electrical properties of the (semi)conducting materials by unravelling the subtle interplay between the molecular architectures and their functions.

The first experimental chapter describes to a systematic and comparative study of charge transport in two PDI derivatives only differing from their side chains. PDIF-CN_2 and PDI8-CN_2 single crystals were produced from solution process, and their charge transport characteristics were analysed through electrical, structural, and spectroscopic characterizations such as THz spectroscopy and inelastic neutron scattering, complemented by theoretical simulations. The differences in transport mechanism between both compounds are significant: PDIF-CN_2 exhibits a band-like behaviour while PDI8-CN_2 is characterized by a thermally-activated process. These differences can be ascribed to the different phononic landscape at low energy. Phonon modes are more pronounced for PDI8-CN_2, because of the larger transfer integral distributions and the higher degree of charge localization which results in the thermally activated process. PDIF-CN_2 exhibits a subtle change in the its packing compared to PDI8-CN_2, which is described by stronger intermolecular interactions preventing fluctuations of charge transfer integral. This is associated with a reduced intensity of the phonon modes with the respect to PDI8-CN_2, allowing the electrons to be delocalized over few molecular units. Together, all the complementary techniques used within our study led to insights that would be purely conjectures if based on charge transport measurements alone. Vibrational modes/phonons are crucial on the type of charge transport observed for each compound. Pushing the detailed analysis of these modes, through the simulation of the precise atomic movement involved for each vibration is a relevant way to complete the story in order to get a clearer picture of what induces the observed vibrational landscape. The same study on the same PDI core, but with other kind of lateral chains, to disentangle the contribution of the chain length, its atomic composition could be needed to get a general comprehension on the

appearance or the inhibition of specific vibrational modes involved in the charge carrier localization, and then on the type of charge transport, that reflects the electrical performances.

Then, we have used molecules able to form self-assembled monolayers as means to dope monolayers of graphene, and monolayers and bilayers of WSe_2. First, we have employed different SAMs functionalisation combined with graphene flakes where the doping was probed by Raman spectroscopy. On the one hand, PFS and AHAPS SAMs were found to induce a significant doping into this material. On the other hand, TESPN doesn't dope graphene, which was expected, and is currently under theoretical investigations. Secondly, we analysed the electrical and optical properties of WSe_2 monolayers in presence of the SAM. High-performance p- and n- type transistors based on WSe_2 single layers with PFS and AHAPS were produced on SiO_2 contacted with gold or aluminium electrodes. Those metals are unconventionally used in the literature with this 2D material to obtain high performance devices. We also report the use of these molecules as vapour to treat WSe_2 monolayers. Such devices exhibit field-effect mobilities as high as 150 $cm^2V^{-1}s^{-1}$ for holes and 40 $cm^2V^{-1}s^{-1}$ for electrons. Then, by acting on both surfaces of WSe_2 bilayers by treating the substrate with SAM and the top of the bilayer with vapours, a balanced ambipolarity with mobilities around 20 $cm^2V^{-1}s^{-1}$ have been observed. Finally, we investigated on the functionalization mechanism of the silane groups with WSe_2. The number of anchoring sites which is defined by the WSe_2 defects, is possible to be modulated by specific treatment, such as an exposure to UV/ozone. Moreover, the silane groups can interact with the neighbouring molecules to cover the WSe_2 surface, resulting in the doping of single and bi-layer of this material, with high performances. This strategy paves the way to new thoughts on the use of 2D materials, with the possibility to obtain high-performance optoelectronic devices. One way to continue this work is by changing molecules composing the adlayer, providing the reinforcement of the properties observed, or by using a specific molecular design in order to introduce multifunctionality in such system. The other way is to use the same adlayer approach, on other types of unexplored 2D material. The use of complementary molecules, leading to the formation of more complex structure such as a p-n junction can be appealing as well for light-emitting devices. 2D semiconducting materials have already exhibited their impressive performances when implemented in FET. The results provided here

allows to consider of such class of material as credible substitute for silicon in the tomorrow's electronic. With these materials, there is always a compromise between easy-processability and high performances. This shows that with the right choice of constituents for a device, supramolecular chemistry is a suitable approach for improving the properties of conventional materials, opening new perspectives, from the academic and industrial point of view.

In the last chapter, we have examined how the environment affects the electrical properties of two different materials. Firstly, we gave an experimental demonstration of the use of perovskite-based devices as oxygen sensor. We showed that the film morphology of the perovskite film is strongly affecting the device sensitivity, which can be precisely controlled through the deposition method. For the most sensitive film, a more-than-three-orders of magnitude increase in the current was measured by changing the atmosphere from pure N_2 to 95% O_2. We have demonstrated that iodine vacancies are responsible to the sensor response to oxygen. The measured effect stems from a dynamic trap healing mechanism mediated by oxygen filling of I vacancies. Fast current response was measured on the device, with a complete reversibility at room temperature, making this organo-halide perovskite an ideal material for oxygen sensing, and offers unexplored possibilities for applications of this class of materials. The defect density was demonstrated to play a crucial role in the sensing properties of this compound. Other morphologies produced by alternative deposition techniques or compound formation strategies can lead to an improvement of the sensing. For instance, 2D confined perovskite exhibits very high surface-to-volume ratio, that may be interesting to explore as sensors. On the long term, the presence of oxygen and more generally the presence of defects have to be considered, not only as a source of degradation and property limitations of this compound, respectively, but also as parameters to consider during working operation of perovskite-based devices such as LED or solar cells, and as a way to tune and engineer their properties.

Secondly, we employed a PEG-BTBT molecule as humidity sensors. We found that the thickness of the film doesn't affect the sensing properties of the film, and we were able to record a four-orders-of-magnitude modulation of the electrical conductivity from 0% RH to 75% RH, with a full reversibility and a fast response speed below 13 ms. Through the adsorption of water

molecules on the PEG chains, the intermolecular packing distance among adjacent BTBT cores is affected. Besides the structural investigation that will be done in the following months, an improvement of the electrical performances of the BTBT-based device is needed for a credible applicability in real life because of the high-voltage needed for the operation. Currently as a polycristallines active film, the formation of a single crystal or a film composed by bigger crystallites can be potentially achieved, that could reduce the operation voltage. Humidity is an important parameter in our daily life, but many others analytes need also to be detected and quantified, from the simple presence of pollutant in the environment to the complex biology of a human body, for following its health condition. Our work shows the potential of combining a supramolecular approach with small semiconducting molecules with a chemical structure that can be tuned, replacing the PEG chains presented here by other functions that can interact specifically with a precise target, or changing the molecular core to obtain different readouts that could be optic, or by integrating other properties such as flexibility or transparency.

In summary, we gave some insights on the comprehension of the charge transport mechanism and/or in strategies to tune the properties of different semiconducting materials which are contributing to defining protocols for the design and engineering of new compounds with better performances and multifunctionality for advanced electronic devices.

Most of the intrinsic charge transport studies in organic compounds were realized so far on devices prepared through physical deposition methods, allowing to obtain less defective materials compared to a solution-based approach, which is a crucial parameter for such study. We demonstrated that solution-processing can form highly-crystalline low-defective materials suitable for charge transport study. We managed to attribute the origin of charge transport mechanism to chemical, molecular and supramolecular concepts to describe the compound used. This examination of the charge transport mechanism is of particular interest as it provide new insights into the molecular design in organic compounds as a major step toward the development of new high-performance organic semiconductors.

2D materials are, due to their atomically thin structures, strongly affected by their surrounding environment. Some semiconducting compounds belonging this class of material exhibit pertinent electrical performances when integrated into complex geometrical devices or

employed with exotic materials. Our approach demonstrated that desired doping and mobility enhancement can be achieved via the formation of heterostructures made of organic molecules, with precise physicochemical properties, that are able to form self-assembled monolayers. The control of the doping of such devices exhibiting high mobilities is particularly appealing for logic circuits or light-emitting devices.

The fabricated oxygen sensor showed remarkable performances. Among all the oxygen sensors reported in the literature, the hybrid-perovskite based sensor exhibit decent characteristics allowing it to be defined in the high-performance category, because combining a good response speed, a wide sensitivity and easily processed. Through this work, we also provided key points (i.e. the effect of oxygen in the environment) to consider when using this compound for the design and optimization of any other devices processed or working in atmosphere containing oxygen.

The humidity sensor that we described exhibits super-fast responses, wide range of detection and high selectivity. Because we employed supramolecular assembly to form these sensors, we also provided a fundamental study on the structure-properties relationship involved in this system, highlighting the potential of such system, not only for sensing applications, but for organic electronic devices in general.

In conclusion, the achievements of this thesis provided a contribution to the understanding of the charge transport in organic semiconductors, to the engineering of 2D materials properties and the development of high-performance sensors.

List of publications

High-performance phototransistors based on PDIF-CN_2 solution-processed single fiber and multifiber assembly
W. Rekab, M.-A. Stoeckel, M. El Gemayel, M. Gobbi, E. Orgiu, P. Samorì
ACS Appl. Mater. Interfaces, **2016**, *8*, 9829

High, anisotropic, and substrate-independent mobility in polymer field-effect transistors based on preassembled semiconducting nanofibrils
S. Bonacchi, M. Gobbi, L Ferlauto, M.-A. Stoeckel, F. Liscio, S. Milita, E. Orgiu, P. Samorì
ACS Nano, **2017**, *11*, 2000

Hybrid copper nanowire-reduced graphene oxide coatings: a "green solution" towards highly transparent, highly conductive and flexible electrodes for (opto)electronics
A. Aliprandi, T. Moreira, C. Anichini, M.-A. Stoeckel, M. Eredia, U. Sassi, M. Bruna, C. Pinheiro, C. Laia, S. Bonacchi, P. Samorì
Adv. Mater., **2017**, *29*, 1703225

Periodic potentials in hybrid van der Waals heterostructures formed by supramolecular lattices on graphene
M. Gobbi, S. Bonacchi, J. X. Lian, Y. Liu, X. Wang, M.-A. Stoeckel, M. A. Squillaci, G. D'Avino, A. Narita, K. Müllen, X. Feng, Y. Olivier, D. Beljonne, P. Samorì, E. Orgiu
Nat. Commun., **2017**, *8*, 14767

Reversible, fast and wide range oxygen sensor based on nanostructured organo-metal halide perovskite
M.-A. Stoeckel, M. Gobbi, S. Bonacchi, F. Liscio, L. Ferlauto, E. Orgiu, P. Samorì
Adv. Mater., **2017**, *29*, 1702469, **Cover page**

Current crowding issues on nanoscale planar organic transistors for spintronics applications
T. Verduci, G. Chaumy, J.-F. Dayen, N. Leclerc, E. Deveaux, M.-A. Stoeckel, E. Orgiu, P. Samorì, B. Doudin
Nanotechnology, **2018**, *29*, 365201

Molecule-graphene hybrid materials with tunable mechanoresponse: highly-sensitive pressure sensors for health monitoring
C. Huang, S. Witomska, A. Aliprandi, M.-A. Stoeckel, M. Bonini, A. Ciesielski, P. Samorì
Adv. Mater., **2018**, 1804600

Doping of monolayer transition metal dichalcogenides via physisorption of aromatic solvent molecules
Y. Wang, A. Slassi, M.-A. Stoeckel, S. Bertolazzi, J. Cornil, D. Beljonne, P. Samorì
J. Phys. Chem. Lett., **2019**, Just accepted

100 cm²/Vs mobility and balanced ambipolarity in molecularly engineered single- and bi- layer WSe_2 with gold contacts
M.-A. Stoeckel, M. Gobbi, T. Leydecker, Y. Wang, M. Eredia, M. Nardi, S. Bonacchi, E. Orgiu, P. Samorì
Manuscript in preparation

General observation on band-like transport in organic semiconductors
M.-A. Stoeckel, M. Gobbi, D. Dudenko, M. Zbiri, A. Y. Guilbert, F. Liscio, N. Demitri, X. Jin, Y.-G. Jeong, M.-V. Nardi, L. Pasquali, Y. Olivier, L. Razzari, D. Beljonne, P. Samorì, E. Orgiu
Manuscript in preparation

High-performance humidity sensor formed by self-assembled benzothienobenzothiophene derivative
M.-A. Stoeckel, F. Devaux, C. Cendra, M. Eredia, B. Chattopadhyay, A. Salleo, Y. H. Geerts, P. Samorì
Manuscript in preparation

Molecules-gold nanoparticles hybrid 3D networks: mechanoresponsive chemistry for on-demand performances in electrical humidity sensing
M. Squillaci, M.-A. Stoeckel, P. Samorì
Manuscript in preparation

An alternative synthetic pathway to dinaphto[2,3-b:2',3'-f]thieno[3,2-b]thiophene (DNTT) derivatives.
A. Leliège, B. Chattopadhyay, A. R. Kennedy, M.-A. Stoeckel, P. Samorì, G. Schweicher, H. Sirringhaus, Y. H. Geerts
Manuscript in preparation

List of communications

Poster

On the modulation of WSe2 electrical performances through molecular dopant
M.-A. Stoeckel, M. Gobbi, T. Leydecker, M. Eredia, S. Bonacchi, E. Orgiu, P. Samorì
Optoelectronics on 2D materials, Davos, Suisse, 20-25/08/2018

Effect of different hybrid perovskite/self-assembled monolayer interfaces on electrical device performances
M.-A. Stoeckel, M. C. Momblona Rincón, M. Gobbi, M. Nardi, L. Pasquali, M. Sessolo, H. Bolink, E. Orgiu, P. Samorì
EMRS Spring Meeting, Strasbourg, France, 18-22/06/2018

Fine tuning of the opto-electronic properties of 2D materials via self-assembled monolayers
M.-A. Stoeckel, M. Gobbi, S. Bonacchi, A. Klekachev, E. Orgiu, P. Samorì
Chem2DMat, Strasbourg, France, 25/08/2017

Organo-metallic hybrid perovskite for oxygen sensing
M.-A. Stoeckel, M. Gobbi, S. Bonacchi, F. Liscio, L. Ferlauto, E. Orgiu, P. Samorì
ICP, Strasbourg, France, 16-21/07/2017

Charge transport in single-crystal perylene bisimide derivatives devices
M.-A. Stoeckel, M. Gobbi, F. Liscio, D. Dudenko, Z. Mics, A. Guilbert, M.-V. Nardi Y. Oliver, L. Pasquali, M. Bonn, J. Nelson, D. Beljonne, E. Orgiu, P. Samorì
SoMaS Summer School, Mittlewihr, France, 2-7/07/2017

Engineering charge transport physics from hopping to band-like through molecular design
M.-A. Stoeckel, M. Gobbi, F. Liscio, D. Dudenko, Z. Mics, A. Guilbert, M.-V. Nardi Y. Oliver, L. Pasquali, M. Bonn, J. Nelson, D. Beljonne, E. Orgiu, P. Samorì
EMRS Spring Meeting, Strasbourg, France, 22-26/05/2017

Oral

General observation on band-like transport in organic semiconductor
M.-A. Stoeckel, M. Gobbi, F. Liscio, D. Dudenko, M. Zbiri, L. Razzari, A. Guilbert, M.-V. Nardi, Y. Olivier, L. Pasquali, J. Nelson, D. Beljonne, E. Orgiu, P. Samorì
EMRS, Strasbourg, France, 18-22/06/2018

On the importance of molecular design and order in organic semiconductors
M.-A. Stoeckel, M. Gobbi, F. Liscio, D. Dudenko, A. Guilbert, M.-V. Nardi Y. Oliver, L. Pasquali, D. Beljonne, E. Orgiu, P. Samorì
ISIS Young scientist seminar, Strasbourg, France, 08/03/2018

Organo-metallic hybrid perovskite for oxygen sensing
M.-A. Stoeckel, M. Gobbi, S. Bonacchi, F. Liscio, L. Ferlauto, E. Orgiu, P. Samorì
Journée des doctorants, Strasbourg, France, 10/11/2017

Organo-metallic hybrid perovskite for oxygen sensing
M.-A. Stoeckel, M. Gobbi, S. Bonacchi, F. Liscio, L. Ferlauto, E. Orgiu, P. Samorì
EMRS Spring Meeting, Strasbourg, France, 22-26/05/2017

Awards

European Material Research Society (E-MRS) Spring meeting 2017
Best poster award of the Symposium *Novel transport phenomena in organic electronic devices*

Scientific Art Exhibition: Art in Micro- Nano World 2017
Best scientific image award

Acknowledgements

In the first instance, I give all my gratitude to the jury members, Prof. F. Biscarini, Dr. M. Caironi, Dr. G. Rogez and Dr. D. Vuillaume for accepting and dedicating time to judge my work.

The last years spent at the Nanochemistry lab seems to have started only few months ago, time where I enjoyed this amazing working environment that allowed me to learn, grow up, and meet exceptional people.

I want first to thank Paolo Samorì who accepted me as a master student and later as a PhD student in his lab, and gave me the possibility to attend to many conferences. He is an impressive scientist and supervisor, and gave relentless efforts to help and guide me through all the things that I faced during these almost four years.

Already a remarkable teacher when I was a bachelor student, Emanuele Orgiu, my second supervisor, introduced me to the world of organic electronics when I joined the lab. With an extreme patience, intelligence and benevolence, he was always able to find the interesting leads in the messy results that I was presenting to him. I truly thank him for all the efforts that he invests in me and in this work.

I want also to thank Marco Gobbi, who was always present to comment or answer from the smallest doubt to the stupidest question that I had. With an absolute kindness and understanding, he helped me in my everyday work, and taught me how to survive in a room full of gloveboxes, Keithley and other scary instruments that you never heard about when you start for the first time in a lab.

Because without them, this work would not have been the same, I want to thank all my collaborators from Brussels, Grenoble, London, Modena, Mons, Québec, Stanford, Trento, and Trieste for their hard work and their contributions that made the science during the past few years even more stimulating and exciting.

Sara Bonacchi and Tim Leydecker played also an important role during my time in the lab, by helping me in many occasions, and sharing precious moments.

To my other colleagues, starting from the office 327 (which is undeniably the best office of the lab) shared with Marco and Yifan. I would like also to thank the Chinese, Italian, and other communities of the lab, for the time spent together. In particular, Agostino, Alessandro, Artur, Cosimo, Lei, Lili, Marco S., Matilde, Oliver, Rafael, Songlin, Stefano C.-D.B.-I., Thomas, Wassima, Ye and Zhaoyang. Thanks also to Corinne, Fabienne and Fanny for their good mood and precious help during all these years.

Of course, I cannot forget the amazing (crazy?) Changbo; we shared very good moments in France and China, and this is just a start…

Because the lab was just on side of my life, I also want to acknowledge the other side, starting with my friends who never hesitate to bring me the fun needed at every moment. I am also deeply thankful to my family, particularly my mother, my aunt and my uncle, for the endless support and love they provided me since so many years. I owe you everything.

Very special thanks goes to Babou, because without her, my life would be different.

To finish, I dedicate all my work to Justine, for her tenderness and love, her full support in every situation, always pushing me to make me a better person. Je t'aime d'un amour inconditionnel.

Marc-Antoine

Université de Strasbourg

Marc-Antoine STOECKEL

EDSC École Doctorale des Sciences Chimiques

Propriétés physico-chimiques et électroniques des interfaces supramoléculaires hybrides

Résumé

Le travail réalisé durant cette thèse s'est axé sur la compréhension des mécanismes de transport de charges impliqués dans l'électronique organique ainsi que sur l'ingénierie des propriétés semiconductrices d'interfaces supramoléculaires hybrides. Tout d'abord, l'origine intrinsèque des propriétés de transport de charges a été étudiée dans de petites molécules semiconductrices, similaires en structure chimiques, mais présentant des propriétés électriques nettement différentes. Puis, les propriétés électroniques de matériaux 2D ont été modulées à l'aide de monocouches auto-assemblées induisant des propriétés de dopage antagonistes. Enfin, des pérovskites hybrides ainsi que des petites molécules semiconductrices ont été utilisées comme matériaux actifs dans la détection d'oxygène et d'humidité, respectivement, formant alors des détecteurs à haute performance.

L'ensemble de ces projets utilise les principes de la chimie supramoléculaire dans leur réalisation.

Mots-Clés : Transport de charges, Transistors à effet de champ organique, assemblage supramoléculaire, Matériaux 2D, Détecteur de gaz

Abstract

The work realized during this thesis was oriented toward the comprehension of the charge transport mechanism involved in organic electronics, and on the engineering of the semiconducting properties of hybrid supramolecular interfaces. Firstly, the intrinsic origin of the charge transport properties was studied for two semiconducting small molecules which are similar in terms of chemical structure but exhibit different electrical properties. Secondly, the electronic properties of 2D material were modulated with the help of self-assembled monolayers inducing antagonist doping properties. Finally, hybrid perovskites and semiconducting small molecules were used as active materials in oxygen and humidity sensing respectively, forming high-performance sensors.

All the project employed the principles of the supramolecular chemistry in their realisation.

Keywords: Charges transport, Organic field-effect transistors, Self-assembly, 2D materials, Gas sensors